PH.D. THESIS

Localization and Tracking in Imperfect *mm*wave systems with Lower Bound Benchmarks

Author:
DEEB ASSAD TUBAIL

Supervisor:
DR. SALAMA SAID IKKI

Department of Electrical and Computer Engineering
LAKEHEAD UNIVESITY

A thesis submitted to the Lakehead University in accordance with the requirements of the degree of DOCTOR OF PHILOSOPHY in the Electrical and Computer Engineering.

OCT. 2023

Abstract

Radio localization and tracking have enormously grown in the fifth generation (5G) of cellular systems and are no longer limited to emergencies. Furthermore, the data obtained from these processes proves highly beneficial for cellular networks, offering advantages such as enhanced network control and more efficient resource management. Accordingly, this thesis investigates localization and tracking in 5G and beyond. In particular, it targets realistic circumstances where the theoretical assumptions of a perfect synchronous system and ideal transceivers no longer exist. In this thesis, we undertake the task of localizing and tracking objects in progressively challenging scenarios. Subsequent to each localization and tracking process in these scenarios, we offer a performance analysis tool, accompanied by the derivation of benchmark metrics. Notably, we establish the Cramer-Rao Bound (CRB) as the benchmark for localization assessment and introduce the Bayesian Cramer-Rao Bound (BCRB) as the benchmark for tracking evaluation.

In the context of localization, the initial scenario involves localizing a mobile station (MS) equipped with a single antenna within a perfectly synchronized millimeter-wave (mmwave) multiple-input single-output (MISO) system implementing the orthogonal frequency division multiplexing (OFDM), taking into account hardware impairments (HWIs) occurring at both the base station (BS) and the MS. Subsequently, the localization task advances to a more intricate environment, where localization accuracy is compromised by non-line of sight (NLoS) effects caused by unknown position scatterers, in addition to the presence of HWIs. Continuing the exploration, the localization process is extended to an environment where it is implemented within an asynchronous reconfigurable intelligent surface (RIS) aided mmwave MISO system. Here, our focus shifts to achieving localization alongside synchronization in a RIS-aided mmwave MISO system that is subject to HWIs. As for tracking, we also delve into this aspect within both a perfectly synchronized mmwave MISO system and a RIS-enhanced mmwave MISO system. In the first system, tracking performance is notably hampered by the presence of HWIs. Specifically, we engage in range-direction tracking of the MS relative to the reference BS. Subsequently, we proceed to track the MS's position concerning the reference BS. However, in the second RIS-aided mmwave MISO system, tracking accuracy experiences a decline owing to both HWIs and synchronization errors, as we focus on monitoring the MS's position in this particular configuration.

From a technical standpoint, the process of localization, tracking, and even joint localization-synchronization is carried out on the MS board. This is achieved by estimating the downlink channel parameters using a maximum likelihood (ML) estimator. Subsequently, the localization and the joint localization-synchronization tasks are finalized by inputting these estimated parameters into specific geometric equations that establish a connection between the estimated values and the MS's position and clock drift relative to the reference BS. Regarding the tracking process, the estimated parameters are subjected to processing using the Kalman filter (KF) when the rela-

tionships between the measurements and tracked elements exhibit linearity. Conversely, when these connections display nonlinearity, the extended Kalman filter (EKF) is utilized to manage these parameters. Both KF and EKF execute tracking by combining the estimated parameters, which represent the measurements, with prior information pertaining to the transition model of the MS.

During the evaluation phase, we determine the localization and synchronization boundaries by calculating the position error bound (PEB) and synchronization error bound (SEB) using the CRB as a reference. Therefore, the CRB serves as a mathematical benchmark for assessing both the localization and the joint localization-synchronization procedures. This benchmark is derived by mathematically inverting the Fisher information matrix (FIM) associated with these processes. To initiate this procedure, we first construct a model for the received pilot signal, which is utilized in the estimation of the downlink channel parameters. Subsequently, we compute the FIM for the estimation of these downlink parameters and then transform it into the FIM for the localization and joint localization-synchronization tasks. The assessment of tracking performance involves a comparison with the BCRB, which results in tracking error limits. The BCRB takes into account not only the valuable information obtained from received pilots but also the valuable information derived from understanding the transition model of the MS. As a result, we follow a similar series of steps as those outlined for localization to compute the FIM related to the measurements. Subsequently, we calculate the FIM matrix associated with the MS's transition model. The combination of these two FIMs forms the Bayesian information matrix (BIM), which is mathematically inverted to yield the BCRB benchmark.

In conclusion, we perform numerical experiments to assess our processes. The results obtained from these computer simulations analyze the level of accuracy achieved in localization and tracking across various suggested scenarios. This accuracy measured by simulation is juxtaposed with the established benchmarks. The findings from both the simulation accuracy and the benchmarks reveal the detrimental effects of HWIs on localization and tracking performance, and this deterioration is inversely proportional to the transceiver quality. An analogous negative effect is observed as a result of the reflected NLoS paths from scatterers with unknown positions. Furthermore, the asynchronous scenarios demonstrate that assuming perfect synchronization masks a portion of the degradation observed in localization and tracking accuracy. However, in these numerical experiments, we achieve the theoretical accuracy presented by CRB for localization and by BCRB for tracking when these processes are implemented with perfect transceivers conditional to negligible NLoS reflections. On the other hand, with non-ideal conditions, the numerical experiments show that applying the proposed Monte Carlo (MC) approach with KF and EKF leads to a significant enhancement in accuracy. Furthermore, we leverage the capabilities of the proposed machine learning techniques (MLT) to offer a streamlined and highly accurate solution that does not rely on prior models and statistics around the MS.

List of Acronyms

AoA	Angle-of-Arrival
AoD	Angle-of-Departure
BCRB	Bayesian Cramer-Rao Bound
BIM	Bayesian Information Matrix
BS	Base Station
CRB	Cramer-Rao Bound
EKF	Extended Kalman Filter
ELM	Extreme Learning Machine
EVM	Error Vector Magnitude
FIM	Fisher Information Matrix
HWIs	Hardware Impairments
KF	Kalman filter
LoS	Line-of-Sight
MC	Monte Carlo
MISO	Multiple Input Single Output
ML	Maximum Likelihood
MLT	Machine Learning Technique
mmwave	Millimeter wave
MS	Mobile Station
MSE	Mean Squared Error
MVU	Minimum Variance Unbiased
NLoS	Non-Line-of-Sight
OFDM	Orthogonal Frequency Division Multiplexing
PDF	Probability Density Function
PEB	Position Error Bound
RIS	Reconfigurable Intelligent Surfaces
RMSE	Root Mean Squared Error
SNR	Signal-to-Noise Ratio
ToF	Time-of-Flight
ULA	Uniform Linear Array
2D	Two Dimensions
3D	Three Dimensions
5G	Fifth Generation

NOTATIONS AND SYMBOLS

j	$\sqrt{-1}$
e	Euler's number (e ≈ 2.718281828)
a	Scalar
$\mathbf{a}$	Column vector
$\mathbf{A}$	Matrix
$[\mathbf{A}]_{ij}$	The element of a matrix $\mathbf{A}$ in the i^{th} row and the j^{th} column
$\mathbf{I}_M$	Identity matrix of size M
tr[$\mathbf{A}$]	Trace of a square matrix $\mathbf{A}$
$\mathbf{A}^{-1}$	Inverse of a square matrix $\mathbf{A}$
$(\cdot)^*$	The complex conjugate operator
$(\cdot)^{\text{H}}$	Hermitian operator
$(\cdot)^{\text{T}}$	Transpose operator
$\mathbb{E}\{\cdot\}$	Statistical expectation
$\overset{a}{\sim}$	Asymptotically distributed
$CN(\mu,\sigma^2)$	Complex Gaussian random variable with mean μ and variance σ^2
P($\mathbf{x};\theta$)	The PDF function of the data $\mathbf{x}$ given to θ
atan2$(\cdot,\cdot)$	The four-quadrant inverse tangent function

List of Figures

Figure **Page**

Table of Contents

CHAPTER 1

INTRODUCTION

This chapter provides a brief overview of the key points discussed in this work. It introduces the localization and tracking processes and presents their well-known systems, categories and techniques. In the following section, it addresses hardware efficiency and outlines the most common types of non-idealities existing in practical communication systems. Additionally, this chapter provides a brief overview of millimeter wave (mmwave) communication systems before focusing on localization and tracking in mmwave systems, as well as highlighting previous work in the field. Finally, it summarizes the contributions, considerations, and justifications of this thesis, followed by a concise overview of the remainder of the thesis.

1.1 Localization and Tracking

Location and time are two of the most important factors that govern our daily lives. Interestingly, the term *position* refers to a spatial location in the real world. It is usually expressed by means of two-dimensional (2D) or three-dimensional (3D) coordinates, which are given as a vector of numbers, each of which represents a position in one dimension [1]. Therefore, the synonyms localization and positioning refer to the determination of the coordinates of a certain object in the real world based on known references [2]. In this thesis, the base stations (BS) serve as the reference points, and the specific object under consideration is the mobile station (MS). Beyond merely pinpointing the target's location, the tracking of its trajectory becomes imperative and holds substantial significance in today's digital era. This localization and tracking endeavour serves a multitude of purposes and finds applications in diverse domains, encompassing telecommunications, navigation, security, and marketing.

Presented below are several compelling rationales underscoring the importance of localization and tracking MS [3–7]:

- *Location-Based Services:* Localizing and tracking MS enables the provision of location-based services, such as navigation, location-based advertising, and emergency services. It enhances user experiences and can be crucial in emergency situations, allowing rapid response when someone requires assistance.

- *Telecommunications Optimization:* Mobile network operators rely on localization and tracking to optimize network performance. By monitoring the movement of MSs, carriers can manage network congestion, allocate resources efficiently, and improve call quality.

- *Asset Management:* In the business and logistics sectors, localizing and tracking MSs is essential for efficient asset management. This includes tracking the location and condition of vehicles, equipment, and inventory. It can lead to cost savings, improved productivity, and better customer service.

- *Security and Law Enforcement:* Localization and tracking are crucial for law enforcement agencies to locate missing persons, track criminals, and prevent illegal activities. It can also be used for surveillance and monitoring in situations that require heightened security.

- *Healthcare and Elderly Care:* In healthcare, mobile localizing and tracking are used to monitor patients, especially those with chronic illnesses. It can also assist in elderly care by ensuring the safety and well-being of senior citizens through tracking devices.

- *Traffic Management:* Localizing and tracking MSs are vital for managing traffic congestion in smart cities. It can provide real-time traffic data, helping commuters make informed decisions and enabling traffic authorities to optimize traffic flow.

- *Disaster Response:* During natural disasters and emergencies, mobile localizing and tracking help authorities locate and assist affected individuals. It aids in coordinating relief efforts and ensures a timely response.

Numerous systems/infrastructures are used and exploited in the positioning and tracking processes. For example [8]:

- *Global positioning systems and other positioning approaches including acoustic-based and light-based systems:*
  These systems demonstrate effectiveness when deployed in open and level outdoor settings. Nonetheless, their performance significantly diminishes when utilized in non-line-of-sight (NLoS) environments, such as regions characterized by hills, mountains, or dense urban construction. This diminished performance is primarily attributed to the necessity for a consistent and robust signal propagation to enable localization and tracking using these methods. Moreover, these systems can exclusively determine the location and track objects within the geographical area covered by signals like sound, light, or RF waves. Additionally,

the methodologies employed tend to be constrained by the need for specialized hardware, which can entail substantial costs related to labor, spectrum licensing, and capital investments required for establishing dedicated indoor infrastructure. Furthermore, these systems can only facilitate localization and tracking when the specialized hardware is operational, location data is continually transmitted to a central server, and there are no interruptions or outages in the system signal.

- *Cellular position systems:*
  Here, cellular position systems utilize broadcast radio waves from BSs to determine position. These systems are valid for estimating a rough position in both outdoor and indoor environments. The most common signal parameters used here in these systems for localization and tracking are the angle of arrival (AoA), time of flight (ToF), time difference of arrival (TDoA), and amplitude (signal strength). However, the localization and tracking in these systems pose several problems due to multipath and NLoS conditions, small-scale and large-scale fading, low signal-to-noise ratios (SNR), and interference by other systems entities. These affect the radio signal parameters used as input data for locatization and tracking algorithms. To process the noisy signal parameters and improve the accuracy, location tracking algorithms use additional intelligence and information. NLoS mitigation techniques use more robust estimators or simply discard the NLoS component.

- *Wi-Fi positioning systems:*
  These systems have been widely deployed around the world and are considered as localization and tracking enablers in both indoor and outdoor environments.

These different systems deployed for the purpose of localization and tracking have a common factor which is the existence of reference points such as navigation satellites in global positioning systems or BSs in cellular networks. Aside from these reference points, measurements are conducted to accomplish the positioning process. Examples of this are given in cellular systems as [2]:

- *Mobile-based:*
  When the MS itself calculates its position by downlink signal measurements from the reference BSs.

- *Network-based:*
  When the localization is carried out by the network side by means of signal measurements performed by the network with respect to the MS, or signal measurements performed and sent by the MS to the network.

Regardless of the type of positioning and tracking system and the entity that performs the processes, different techniques can be used to execute the localization and tracking by considering

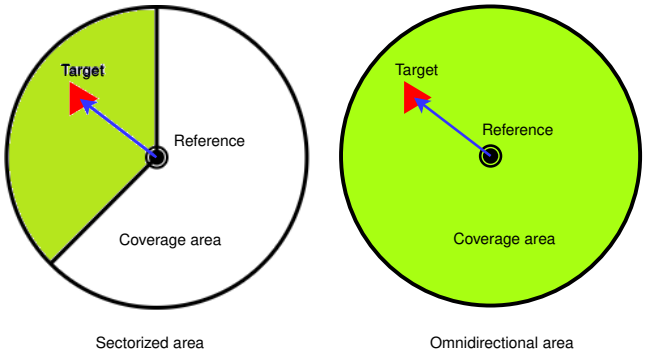

Figure 1.1: Proximity positioning.

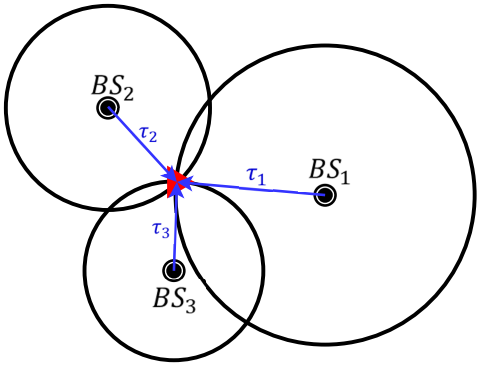

Figure 1.2: Trilateration positioning.

different measurements or references. These fundamental techniques can be summarized as [1, 2, 9]:

- *Proximity:*
  The estimated position of the target is the position of the reference that the target locates in its coverage area. The reference here can be ultrasonic sensors, light sensors, BS, RFID, etc. The known position reference sends or receives the predetermined pilot signals, after which its position is assigned as the target position. Fig. 1.1 shows types of proximity positioning methods. As illustrated in Fig. 1.1, the plot on the right shows a configuration with omnidirectional radiation, while the plot on the left illustrates proximity sensing with sectorized/directional radiation.

- *Lateration:*
  Fig. 1.2 presents the lateration concept. The tracked position is obtained by computing the intersection between geometric forms, e.g., circles, created by distance measurements between the target and the references. Here, three references construct three circles, thus called trilateration, and intersect at one point and provide 2D location, while for 3D location, four references are required. Moreover, several types of measurements can be used to construct the circles, such as time of flight (ToF), or received signal strength (RSS).

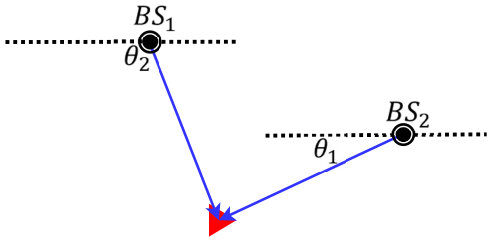

Figure 1.3: Angulation positioning.

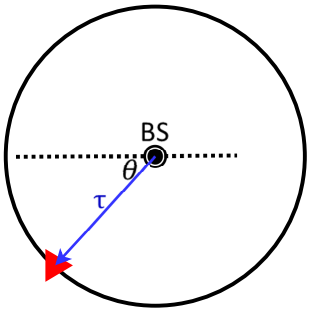

Figure 1.4: Hybrid lateration and angulation positioning.

- *Angulation:*
  The intersection of two known directions or angles from at least two references towards the target is used to track and localize the target as Fig. 1.3 depicts. The angulation concept is implemented in a cellular network when the BS is equipped with an antenna array. Specifically, the BS measures the phase difference of signals arriving at different antennas in the array to estimate the target direction. Then it defines a straight line, where the intersection of two lines determines the target position as shown in Fig. 1.3.

- *Hybrid:*
  Implementation of a combination of two or more localization algorithms to improve overall performance or to support an algorithm that cannot be computed stand-alone. For example, the combination of lateration and angulation in cellular systems as Fig. 1.4 demonstrates. In this example, the range is estimated by measuring ToF which forms the circle in the figure, while the AoA is estimated by the BS equipped with an antenna array which forms the direction θ. The UE position is then taken as the intersection of the direction and the circle.

- *Scene analysis:*
  This approach is also known as fingerprinting and pattern matching. Essentially, this technique begins by constructing a fingerprint database that includes location-based features such as received signal strength, time delay, and channel delay spread. The localization process is performed by matching the measurements of the location-based features with those stored in the fingerprint database [1].

1.2 Hardware Efficiency

Considering ideal transceivers is a theoretical assumption that underlies many challenges. This theoretical condition supposes that the transmitter is able to generate the correct modulated pass-band signal from the complex baseband samples, and the receiver can demodulate and sample the received signal correctly. Furthermore, this assumes that the transmitter and receiver are in perfect synchronization in terms of time and frequency. Unfortunately, none of these conditions are fully satisfied in practice. The following are some of the non-idealities that exist in practical transceivers, which are mentioned in [10] and referenced therein:

- *Phase noise:*
  Phase noise is the time-varying drift and the resulting frequency deviations at the transceivers caused by imperfections in the employed oscillators due to thermal noise. Oscillators that operate at higher frequencies, such as mm-waves (30-300 GHz), are more susceptible to phase noise, making stabilization more difficult. Moreover, phase noise causes phase rotation from one signal to another in the constellation.

- *Nonlinear power amplifiers:*
  Power amplifiers that boost the power level of the transmitted signal to overcome the possible path loss have a nonlinear behaviour causing distortions in the amplitude and phase of the output signal. Ideally, the power amplifier is considered to have a linear relationship between the input and output power, as more input power generates more output power. Nevertheless, in practice, with a low-power input signal, the power amplifier acts as a linear filter, but when the input signal power increases and reaches the threshold point, the power amplifier saturates. Nonlinear power amplifier deterioration can be classified into two categories: amplitude modulation/amplitude modulation (AM/AM) and amplitude modulation/phase modulation (AM/PM). The first one discusses the input and output signal's amplitude relationship, while the latter describes the input signal's amplitude and output signal's phase relationship.

- *I/Q imbalance:*
  Quadrature amplitude modulation is widely deployed in modern communication systems such as mmwave systems. This modulation involves two components, the in-phase and the quadrature components, that should be perfectly matched. In other words, the phase difference between the two components should be 90 degrees, and their amplitudes should be consistent. However, practical systems lack this targeted perfect match, known as I/Q imbalance, which leads to performance degradation, including positioning. There are two common types of models for I/Q imbalance: the frequency-independent model which examines quasilinear impairments of the input signals, and the frequency-selective model which evaluates the analog components' behaviour more precisely.

- *Antenna array calibrations:*
  The antenna array is the prime component of angulation positioning, as the electrical and geometrical characteristics of the antennas in the array must be known to achieve precise results. Practically, these features may alter over time and not be feasible to maintain each factor as designed. This necessitates a process called antenna calibration that involves transmitting known pilots from known locations.

- *Timing synchronisation:*
  Aiming at accurate localization, the transmitter and receiver should be perfectly synchronized. However, in practice, there is often a time offset between the clocks of the transceivers that is disruptive to the estimation process.

- *Doppler effect:*
  This impairment involves non-stationary transceivers, where the movement of the target relative to the BS results in distortion called the Doppler effect which causes fast time-varying multi-path fading channels and issues with frequency synchronization.

It is apparent that the ideal conditions for transceivers are not fully satisfied in practice. Moreover, enhancing the hardware efficiency of components and moving closer to ideality are more challenging to implement, more expensive, and consume more power. This introduces a cost-quality trade-off in practical systems, especially in systems employing large-size arrays. The cost of such an implementation will be roughly several times higher than that of a single-antenna transceiver, necessitating a reduction in the quality of individual components.

As a solution, analog or digital compensation algorithms have been proposed to mitigate the deterioration in hardware efficiency. Unfortunately, these algorithms heavily rely on modelling distortions, which could be inaccurate. Detailed modelling and compensation of hardware impairments (HWIs), for example, are discussed in [11–14] and referenced therein. Finally, residual impairments will still exist due to modelling inaccuracies and the destructive nature of some impairments.

This work will not cover detailed modelling, and rather, it will focus on the impact that residual HWIs have on estimation, localization, and tracking by modelling the non-ideal hardware as non-linear memoryless filters as coming in section 2.1.

1.3 The *mm*wave Communication System

In modern history, mobile communication is considered one of the most successful and popular technological innovations. Due to technological advancements and appealing features, mobile communication has become an indispensable part of billions of people's lives. Therefore, unprecedented growth of mobile data traffic is expected, with some predictions indicating that mobile data will grow exponentially over the coming years. This incredible increase in demand

makes the use of the 300 MHz - 6 GHz frequency range in most wireless communication systems today increasingly crowded, while the spectrum from 6-300 GHz is comparatively empty. This is primarily due to the very advantageous propagation characteristics at low frequencies that allow radio waves to penetrate buildings, reflect multiple times, and bend around corners [11, 15].

The empty frequency band of the range 30-300 GHz with wavelengths ranging from 1-10 mm, referred to as *mm*wave, is a promising carrier frequency for fifth generation (5G) cellular systems, as it is expected to provide the large spectrum bandwidth required to support a drastic capacity increase for 5G cellular systems. Further, the *mm*wave cellular systems can achieve a similar spectral efficiency to that obtained at a lower frequency while providing orders of magnitudes more data rate thanks to the larger bandwidth [16, 17].

Unfortunately, *mm*wave systems suffer from high atmospheric absorption, rain and foliage attenuation, significant penetration and reflection losses, and little diffraction. As a result, the use of this band is restricted to the line of sight (LoS) outdoor-to-outdoor or indoor-to-indoor communications over relatively short distances. Although it is currently employed in the wireless backhaul, recent channel measurements and theoretical considerations have confirmed the feasibility of using *mm*wave not only for the backhaul but also for the access link. These theoretical considerations and measurement campaigns have proven the possibility of deploying *mm*wave communication in outdoor "small-cells" with up to 200 m cell radii if the transmitters and receivers are equipped with sufficiently large antenna arrays to compensate for the otherwise prohibitive propagation losses [11, 15].

It is evident that the feasibility of the *mm*wave mobile communications is associated with active techniques in combating the unfavourable propagation loss observed in the high frequencies. As a result, efficient beamforming techniques are crucial in *mm*wave systems. In general, the formation of a directive beam could be applied in the digital domain or the analog domain. In the digital domain, digital beamforming is done in the same way as digital precoding which multiplies a particular coefficient to modulated baseband symbols per radio-frequency (RF) chain. On the other hand, in analog beamforming, complex coefficients are applied to manipulate RF signals through controlling phase shifters and/or variable gain amplifiers [16].

The combination of analog and digital beamforming, hybrid beamforming, is derived as a trade-off between flexibility/performance and simplicity, especially in the case of a multitude of antenna systems. Typically, digital beamforming provides a higher degree of flexibility in manipulating transmit/receive signals for improved performance. However, this flexibility is at the expense of increased complexity and cost due to digital-to-analog converters and analog-to-digital converters per RF chain. On the other hand, analog beamforming is simple and effective in generating high beamforming gains from a large number of antennas but is less flexible than digital beamforming. There has been considerable interest in hybrid beamforming when the orthogonal frequency division multiplexing (OFDM) is implemented with the *mm*wave systems as in [16–18]. This conviction comes from the expectation of operating the *mm*wave systems on

broadband channels with frequency selectivity.

1.4 Localization and Tracking in Literature

The *mm*wave communication system has been identified as one of the most promising candidates by research innovation and industrial communities for satisfying the proliferating demands of new generations of wireless applications, including multi-sensory extended reality, connected robots, wireless brain-computer interactions, digital twins, industrial internet of things, tactile IoT, internet of underwater things, self-driving ground and air vehicles, and others. To achieve the promised performance excellence, these applications are restricted to predetermined specifications in terms of throughput, latency, and reliability, within acceptable transmission distances. Despite the unprecedented bandwidth that high-frequency systems offer, both the transmitter and the receiver require knowledge of each other's relative position and orientation.

As a consequence, localization and tracking are expected to become a vital component of high-frequency wireless systems [19]. Due to the use of unprecedented levels of bandwidth and higher carrier frequencies with the deployment of large antenna arrays in *mm*wave communication systems, location accuracy is expected to be provided in the order of centimetres [20, 21]. As a result, *mm*wave is considered the first generation to integrate the location information into the network design and optimization, for example, through beamforming, pilot assignment, and resource allocation. Moreover, it makes location-aware applications more attractive than ever before. Among these applications are the industrial Internet of Things, emergency services, targeted content delivery, vehicular communication, assisted living systems, connected autonomous vehicles (CAVs), and air-ground communication with unmanned aerial vehicles [22, 23].

Estimation, localization, mapping, and many other processes have been investigated in *mm*wave systems, as demonstrated in works[24–30]. Typically, these processes have been associated with the performance analysis presented through the theoretical performance bounds in the Cramer-Rao Bound (CRB) term. Work in [24] confirmed that *mm*wave technology for 5G systems is capable of providing so robust an indoor localization scheme that centimetre accuracy can be ensured. Besides, the authors in [25] derived the 3D position error and orientation error in terms of the position error bound (PEB) and the orientation error bound (OEB), respectively. These bounds were performed for the uplink and the downlink localization with arbitrary array geometries in multipath environments. Moreover, work in [26] provided estimations for the channel parameters and the angle of departure (AoD) of the *mm*wave channels. Furthermore, the authors demonstrated proof of estimation accuracy by showing that the estimation error was small enough to approach the CRB. Similarly, the authors of the work in [27] proposed a two-stage algorithm for position and rotation angle estimation in the presence of scatters. Next, they verified the accuracy of the proposed strategy by deriving the CRB of the positioning and rotation angle estimation. Their results showed that the estimation errors attained the CRB for

an average to high SNR. Performance enhancement and complexity reduction of the localization process in mmwave are also considerable investigation points. For example, the CRB was used to evaluate the accuracy of the estimation in case of reducing estimation complexity as investigated in [28]. In this work, two low-complex estimation approaches were proposed, and the resulting reduction in estimation accuracy was analyzed and evaluated by comparing the achieved accuracy with the CRB. Moreover, in [29], a closed form of the CRB for the localization and channel estimation process was obtained. Here, the closed-form CRB was derived not only to provide a performance benchmark for the localization process but also to optimize the beamforming vector that will be utilized in enhancing the localization process later. It is not limited to the localization process since the mmwave systems are a rich environment for such impressive applications. For instance, mapping the radio environment was demonstrated in [30], and the CRB was derived as a benchmark for evaluation purposes.

More interestingly, deploying reconfigurable intelligent surfaces (RIS) technology solves challenging problems in radio localization and tracking. For example, the multiple paths, due to the RIS, make the estimation of AoD, AoA and time of arrival achievable [31]. Moreover, the RIS technique enables the joint localization-synchronization process, more so in single-input single-output (SISO) systems [32]. RIS can also provide significant benefits to the estimation performance, and thus in localization and tracking. In this context, the localization process in the presence of RIS was addressed in [33–36]. In [33], the PEB and the OEB were derived for a 2D RIS-aided mmwave localization process. Additionally, the work in [34] addressed the impact of the number of RIS elements and the value of phase shifters on the position estimation accuracy. This paper also presented the role of the RIS in improving localization accuracy by comparing it with the conventional system involving one LoS and one NLoS. Moreover, the works in [35, 36] executed the joint localization-synchronization process and compared the achieved accuracy with the CRB benchmark for evaluation purposes.

In the context of tracking, tracking the position and velocity of the MS is necessary for efficient network control, as well as for offering useful services in cellular networks [37–42]. As such, the work in [37] tracked the MS by measuring the field strength data of surrounding BS and implementing the Kalman filter (KF). Next, the work in [38] measured the time difference of arrival and applied the KF to track the MS in NLoS cellular networks. In [39], the extended Kalman filter (EKF) was utilized to track the MS in a single BS cellular network, relying on measuring the AoA and the changing rate of the AoA. Furthermore, the work in [40] investigated tracking the MS based on Aulin's wave scattering channel model, where it performed the tracking process via two approaches: the EKF approach and the particle filter approach. Different trackers were proposed in [41, 42]. In particular, both a particle filter (PF) and a Rao-Blackwellised particle filter (RBPF) were proposed for the tracking process, and they are based on observing the strength of the received signal.

The works cited in [42–46] took a unique perspective on the tracking domain. Their objective

was to assess the effectiveness of the proposed tracking methods by establishing a benchmark for evaluation purposes. The [42] evaluated the performance of proposed trackers, derived a benchmark in terms of Bayesian Cramer Rao bound (BCRB) and used it as another assessment tool besides calculating the root mean square error (RMSE) in the simulation environment. Besides, the authors of [43] developed a general approach to calculate the BCRB for tracking a maneuvering target. They based this process on approximating the prior target probability density function (PDF) using a best-fitting Gaussian distribution. Besides, in [44], the BCRB was derived for the target tracking in a wireless sensor network comprising randomly distributed range-only sensors with quantized measurements. Furthermore, the work done in [45] computed the BCRB in tracking applications. The process depended on noisy measurements from distributions existing in radio propagation, and these were in the context of both line and NLoS environments. Additionally, the work in [46] presented the BCRB of the tracking process for the bearings of a manoeuvring target when the measurement equation was non-linear.

Tracking the MS in the 5G cellular networks and beyond is highly relevant because the 5G networks adopt mmwave and massive array technologies to support multiple gigabits per second for users and to efficiently offer additional services. However, a slight misalignment in the directives toward the MS significantly degrades the link quality, capacity, and service quality [25, 27, 47, 48]. In response, there has been a notable growth in radio-based high-precision tracking requirements for the 5G applications, making their use no longer limited to emergencies. Consequently, extensive studies and investigations for the estimation and tracking processes with mmwave technologies are found in and within [49–54]. In detail, the work in [49] discussed tracking the slow variations of the AoD and the AoA. Then, it investigated the detection of abrupt changes or blockages in the MS link. Besides, low-complexity tracking algorithms of the channel state information, AoA and AoD in mmwave systems were investigated in [50]. Moreover, the work in [51] designed sounding beamformers estimation and implemented an unscented KF for tracking the mmwave channels. This design followed the modeling of the underlying time dynamic state space as a linear Gauss-Markov process. Furthermore, the work in [52] suggested decomposing the antenna array into two different sub-arrays to track the variations in AoD/AoA based on the phase difference between them in the received signals. In [53], the authors reduced the computational overhead in tracking AoD and AoA in a mmwave channel by proposing an efficient adaptive channel estimation. They did so based on a small-angle assumption and by employing an autoregressive process to update the AoD and AoA. The authors of [54] studied a beam-tracking problem in distributed mmwave massive multiple-input multiple-output (MIMO) systems. Specifically, the authors utilized the mono-pulse beam direction estimation method first and suggested the implementation of the unscented KF for tracking and correcting the direction variations.

On the other hand, within the works [55–58], the tracking process was investigated in systems implementing RIS and MIMO technology, besides proposing algorithms for tracking the

time-varying channels and the MS. The work cited in [55] introduced a method for accurately tracking the three-dimensional beam in wireless communication scenarios, particularly in complex environments and remote villages. The method relies on utilizing a RIS to address blocking channel issues and optimize wireless parameters. Besides, the authors of [56] addressed the crucial challenge of estimating channel state information in Single-Input Multiple-Output (SIMO) communication systems enhanced by RIS. Specifically, it presented a low-complexity channel tracking framework for the uplink of RIS-enabled multi-user SIMO communication systems. This was particularly important because RIS operate passively and introduce complexities into channel estimation due to signal coupling. Additionally, the time-varying nature of wireless channels adds to the computational challenges of real-time channel tracking, especially when deploying RIS containing a substantial number of unit elements. In [57], the authors proposed an efficient beam-tracking for RIS. They suggested a practical codebook-based RIS passive configuration that relies on updating channel parameters, specifically the AoD from the RIS to users. This approach avoids the need for complex channel estimation procedures. In the same context, in [58], the tracking process was investigated in systems implementing RIS and MIMO technologies. Besides, the authors derived the BCRB to serve as a theoretical benchmark for the evaluation of the tracking process. In the aforementioned articles in this section, promising solutions were described for localization and tracking in 5G. However, some researchers have expressed concern about practical scenarios, in which some fundamental issues still need to be addressed before possible real-world applications can be assessed. They justify that it's self-evident that the impractical assumptions blur the true accuracy of the localization. For example, the HWIs, where needless to say always jeopardizes the performance of the systems as shown in [11, 59, 60].

With regard to the estimation and localization processes considering the HWIs, it was shown in [61] that the I/Q imbalance can reduce the accuracy of position and orientation estimation up to 12% in 5G mmwave systems. In [62], the authors derived position and orientation error bounds based on the HWIs. This was done to study the effect of HWIs on the localization and orientation bounds in 2D 5G mmwave systems. The authors of [31] went on to derive the CRB benchmark of the localization process in mmwave MIMO and RIS-aided mmwave SISO systems, demonstrating the harmful impacts of the HWIs on the localization process in these systems. Regarding the influence of HWIs on tracking, the work in [63] proposed custom designs for the auxiliary beams and for pilots with the purpose of angle tracking in mmwave systems taking into account errors in array calibration. For practical implementation purposes, the work proposed offline calibration in advance to mitigate the impact of the array calibration errors on the tracking process. Besides, the work in [64] proposed a robust Bayesian tracker for the AoA in mmwave-MIMO systems. During the tracking process, this work counted the uncertainty that resulted from the limited resolution of the phase shifters. Specifically, the uncertainty was modeled as a discrete Gaussian random variable with variance depending on the level of uncertainty. Furthermore, the phase noise error and channel gains parameters in the mmwave MIMO system were tracked in [65].

Nonetheless, these works in [31, 62] assumed another ideal condition, namely the perfect synchronization of the MS and BS prior to localization. In that regard, the works in [66] analyzed the localization process theoretically in the CRB term without actually executing the localization process, considering both the HWIs and the imperfect synchronization. Specifically, the work in [66] considered the localization process in the *mm*wave MIMO system when the synchronization process was performed as a preliminary step before the localization process. Regrettably, the works confirmed that the perfect synchronization assumption covers up an unseen part of the degradation in the localization process accuracy. In the same context, the work cited in [62] did not take advantage of the LoS link during localization, nor in synchronization. This work also failed to consider the synchronization process entirely, opting instead to assume that the system was perfectly synchronized before localization started. Moreover, although the LoS provides the most useful information for localization, the process in [31] depended only on the estimated parameters of the NLOS link made via the RIS, and not on those stemming from the LoS.

Regarding the studies conducted in references [63–65], they limited their investigation to a specific HWIs source and reflected its impact on the transition model of the estimated parameters. Moreover, they neglected the impacts of this specific HWIs source, as well as the other HWIs sources, on the transmitted and received pilots, where in reality, severe distortions could affect the pilots and then the estimation process and measurements.

Continuing within the influence of HWIs, the works cited in [67–70] approached the challenges posed by HWIs from a distinct standpoint. They utilized the machine learning technique (MLT) in reducing the HWIs impact of the transmitter on the communication systems performance. Specifically, these works implemented the *extreme learning machine* (ELM) algorithm to refine the synchronization in [67, 68], and to enhance the channel gain estimation in [69, 70]. The refinement process was done in two steps. Firstly, these works utilized ordinarily known processing to capture the initial coarse features of synchronization or channel estimation. Then, these works implemented the ELM for the refinement of the previous stage results. Despite this practical step, these works consider the HWIs only exist on the transmitter side while the receiver has perfect hardware. This assumption is not practical and hides the real complexity generated by the HWIs at the receiver side, where the HWIs at the receiver side depend on the received power and on the channel gain. Moreover, these works implemented the normal processes and appended the ELM to enhance the results in the price of increasing the complexity.

1.5 Scope and Contributions

As a result of the valuable gains obtained by deploying localization and tracking in wireless systems, the capabilities provided by *mm*wave technologies in this field, and with the goal of contributing to the realization of the goals practically, this thesis investigates the localization and tracking processes, their performance analysis, and the challenges they face in *mm*wave

multiple-input single-output (MISO) OFDM systems, taking into account the impact of HWIs on both the BS and MS and synchronization errors. *Thus, the main contributions in this thesis are as follows:*

- This thesis integrates the general HWIs model in the MISO-OFDM *mm*wave system, building a more realistic *mm*wave system. Doing so reveals that the resulting noise in the system is no longer the familiar AWGN. It is still statistically distributed as Gaussian noise, but its power depends on the transmitted power and the channel gain. Therefore, the received SNR has saturated to a certain level regardless of the transmitters' transmission power or antenna number.

- This thesis estimates the ToF and AoD from the BS by observing a well-known pilot broadcasted in the downlink from the multiple antennas BS, where that pilot is distorted by the HWIs noise described in the previous point. The maximum likelihood (ML) estimator is proposed for this estimation process as it can be implemented in such complex situations and provide an optimal estimation. For the purpose of estimation, the ML estimator's cost function is derived considering the HWIs. Needless to say, the HWIs complicate the estimation process since they decouple the channel magnitude from the channel phase in some terms of the cost function and couple them in others. After that, this thesis optimizes the cost function for purposes of the optimal estimated ToA and AoD. These obtained ToA and AoD are subsequently utilized for localization or can be processed for tracking purposes.

- This thesis commences by performing localization processes in perfectly synchronized MISO-OFDM *mm*wave systems. Initially, it investigates localization under the influence of HWIs alone. It then proceeds to examine localization challenges arising from both HWIs and NLoS conditions caused by scatterers with unknown positions. Subsequently, it explores the impact of synchronization errors, in addition to HWIs, through the implementation of a joint localization-synchronization process in an asynchronous RIS-aided *mm*wave MISO-OFDM system.

- This thesis derives the CRB of the localization process as follows: it starts with the derivations of the Fisher information matrix (FIM) of the estimated downlink channel parameters. Then, the channel parameters FIM is transformed to the localization FIM, which is the input to the inverse to obtain the CRB of the localization process. It's worth mentioning that because of HWIs, the CRB is different from that of ideal transceivers as the statistical quantities of the received pilots, the mean and the variance become dependent on some of the estimated downlink's parameters.

- This thesis investigates a comprehensive tracking process across various scenarios. Firstly, it tracks the range, direction, and location of the MS relative to the reference BS within the context of a perfectly synchronized MISO-OFDM *mm*wave system, taking into account

HWIs. Subsequently, the thesis proceeds to track the MS's position within an asynchronous RIS-aided *mm*wave MISO-OFDM system, also considering the influence of HWIs. These tracking procedures rely on estimated ToF and AoD, incorporating the MS's maneuvering and transition model, and employ KF and EKF techniques. Lastly, the thesis introduces a position-velocity tracking approach that accounts for HWIs, utilizing MLT, and compares its performance with the EKF-based method. In this context, it is crucial to highlight that this thesis suggests utilizing the Monte Carlo (MC) approach and MLT to mitigate the adverse effects of HWIs on accuracy.

- This thesis establishes the tracking performance benchmark, quantified by the BCRB, for each tracking scenario. More precisely, the BCRB is computed as the inverse of the Bayesian Information Matrix (BIM). The BIM is formed by combining the FIM derived from the received pilot measurements with the FIM corresponding to the MS's transition model.

Motivated by the details aforementioned in the previous section, the following points are considered during this thesis:

- This thesis assumes the MS operates in an environment with at least one LoS path to a non-obstructed BS, in other words, the existence of LoS during the localization and tracking processes. Mainly, because of implementing the multi-connectivity concept in the *mm*wave systems. It's worth noting the multi-connectivity concept for the *mm*wave research community is considered a promising solution to overcome the highly susceptible blockage issue of *mm*wave links. Thus, this feature allows an MS to maintain multiple possible LoS paths to different BSs, so dropping a link can be overcome by switching data paths [28, 30, 71, 72]. Furthermore, akin to the work presented in [58], in this thesis, it is assumed that an adequate number of RIS are deployed to ensure the continuous establishment of at least one NLoS link between the BS and the MS through the RIS.

- This thesis aims at investigating the localization and tracking processes, considering that both the BS and MS suffer from HWIs. Therefore, this thesis adopts a model that captures the hardware impairment characteristics that affect the localization and tracking processes without restricting to a specific impairment noise model. This model is utilized multiple times for the purpose of evaluating the localization performance as in [61, 66] or as in [11] for spectrum efficiency. It's worth declaring here that the HWIs are the *residual* part remaining and can not be removed when implementing the compensation algorithms. With regard to the RIS, as discussed in [73], these surfaces are nearly passive and ideal. They do not need any dedicated energy source, and they are not affected by receiver noise because they do not involve analog-to-digital/digital-to-analog converters (ADCs and DACs) or power amplifiers. As a result, these surfaces do not amplify nor introduce noise when reflecting the signals. Consequently, this thesis considers the RIS ideal following to [31, 74, 75],

or incorporates the impact of the HWIs on the RIS in the receiver side as it ended with degrading the received SNR, as outlined in [76–79].

- This thesis adopts the MISO mmwave scenario instead of the MIMO mmwave scenario, even though the MIMO mmwave scenario offers more efficient channel estimation. Mainly, because the MISO mmwave system is the most likely applicable scenario, as in [28, 30, 71], the massive arrays will be initially implemented only at the BS side while the MS will have one antenna.

- This thesis focuses on mobile-based estimation, localization, and tracking as the MS performs the process from the downlink measurements instead of at the BS side. It's predicted that mmwave communication should serve a massive number of terminals connected to the BS. Thus, mobile-based processing allows multiple terminals to be localized and tracked by exploiting the common transmission of the known pilot from the BS. Also, this relieves the burden on the BS as it distributes the processing task over the MSs [30, 71].

- This thesis employs the hybrid lateration and angulation technique, and it is a mobile-based processing category where the MS is equipped with a single antenna. This enforces the single-antenna MS to estimate ToF and the AoD from the BS rather than the AoA to the MS [71]. According to [71], when transmitting a single beam, the received amplitude depends on the beam pattern and the unknown channel amplitude, and thus it is not possible to estimate the AoD. However, in the case of transmitting more than one beam, the ratios between the received beams are independent of the channel gain and are only dependent on the beam patterns and hence on the direction in which they reach the MS, i.e. AoD. Thus, estimating AoD by single-antenna receiver depends on transmitting multiple beams which results in different received phases and magnitudes that do not depend on the channel gain but rather on the direction in which the receiver is seen relative to the transmitter. Here, it is worth noting that the multiple beams can be transmitted sequentially (i.e., time division), or at different sub-carriers (i.e., frequency division).

- This thesis considers the narrow-band system, that is when the system operates at f_c carrier frequency with bandwidth B, the typical narrow-band condition achieves, i.e., $\lambda_n = c/(\frac{n}{NT} + f_c) \approx \lambda_c = c/f_c$ for $\forall n \in \{1,2,\cdots,N\}$, where n is the sub-carrier index, N is the total number of sub-carriers, and $T = 1/B$ is the sampling period, while λ_c denotes the wavelength, and c is the speed of light.

This thesis has been organized as follows:

- *Chapter 2:*
  This chapter presents the required theoretical concepts and key points of this thesis. Firstly,

it shows the HWIs model and its integration in the wireless system. Then, it depicts the channel model of the LoS MISO channel, as well as the channel gain of the *mm*wave channel. Next, it addresses the estimation theory and discusses the basics of the CRB, the ML estimator, BCRB, and the tracking problems, including KF and EKF. Finally, it introduces the MLT and the ELM algorithm.

- *Chapter 3:*
  This chapter discusses the localization process when the BS and MS are equipped with non-ideal transceivers. Specifically, the localization process is performed in a perfectly synchronized 2D *mm*wave MISO-OFDM wireless communication system with the LoS connection only between the BS and the MS, i.e. no NLoS paths exist. Then, it is executed in a perfectly synchronized 3D *mm*wave MISO-OFDM wireless communication system with the LoS connection between the BS and the MS, additionally NLoS connections from unknown position reflectors. Later on, it undergoes execution of the localization process, considering the HWIs and synchronization errors. In essence, it is a joint localization-synchronization process in an asynchronous RIS-aided *mm*wave MISO-OFDM system. Here in this chapter, the ML estimator performs accurate estimation as the localization accuracy attains the lower bound of the theoretical accuracy presented by the CRB for perfect transceivers. Afterwards, this chapter demonstrates the theoretical accuracy by deriving the FIM of the estimated channel's parameters that is transformed into the FIM of the estimated position. The resulting position FIM represents the inverse operation of the CRB. Finally, extensive computer simulations are presented to depict the localization process accuracy in the existence of the HWIs.

- *Chapter 4:*
  This chapter introduces four distinct tracking scenarios. Initially, it conducts tracking processes to determine the range and direction of the MS relative to the reference BS within the context of a perfectly synchronized MISO-OFDM *mm*wave system, taking into account HWIs. These tracking operations rely on the KF. Subsequently, the chapter tracks the MS's position within the same perfectly synchronized system, employing the EKF methodology. Moving forward, the chapter extends its tracking efforts to encompass the MS's position within an asynchronous RIS-aided *mm*wave MISO-OFDM system. In this scenario, KF is implemented to accomplish the tracking process influenced by the HWIs and synchronization errors. Both KF and EKF tracking processes utilize estimated ToF and AoD data as discussed in Chapter 3. These methods incorporate the MS's movement and transition model. Finally, the chapter executes a position-velocity tracking approach that accounts for HWIs, utilizing MLT in comparison to the performance of the EKF. Following each tracking process, this chapter establishes the tracking performance benchmark, quantified by the BCRB, for each tracking scenario. The BCRB is computed as the inverse of the BIM. The BIM is formed by combining the FIM derived from the received pilot measurements with

the FIM corresponding to the MS's transition model. At the conclusion of each tracking scenario, comprehensive computer simulations are presented to illustrate tracking accuracy in the presence of HWIs and in the presence of the synchronization error in the case of the asynchronous system.

- *Chapter 5:*
  This chapter unveils the conclusive discoveries within this thesis and delves into significant limitations and avenues for further exploration in both the near and distant future.

1.6 List of Publications

1. **D. A. Tubail** and S. Ikki, "Range-Direction Tracking and Bayesian Cramer-Rao Bound Analysis in mmwave Systems Equipped with Imperfect Transceivers," *IEEE Wireless Communications Letters*, Accepted, 2023.

2. **D. A. Tubail**, B. Ceniklioglu, A. E. Canbilen, I. Develi and S. Ikki, "Error Bounds for 3D Localization and Maximum Likelihood Estimation of mm-Wave MISO OFDM Systems in the Presence of Hardware Impairments," *IEEE Communications Letters*, vol. 26, no. 9, pp. 2042-2046, Sept. 2022..

3. **D. Tubail**, B. Ceniklioglu, A. E. Canbilen, I. Develi and S. S. Ikki, "The Effect of Hardware Impairments on the Error Bounds of Localization and Maximum Likelihood Estimation of mm-Wave MISO-OFDM Systems," *IEEE Transactions on Vehicular Technology*, vol. 72, no. 3, pp. 4063-4067, March 2023.

4. B. Ceniklioglu, **D. A. Tubail**, A. E. Canbilen, I. Develi and S. S. Ikki, "Error Analysis of the Joint Localization and Synchronization of RIS-Assisted mm-Wave MISO-OFDM Under the Effect of Hardware Impairments," *IEEE Open Journal of the Communications* Society, vol. 3, pp. 2151-2161, 2022.

Submitted Works

1. **Deeb Tubail** and Salama Ikki, "Machine Learning and Extended Kalman Filter for Joint Position-Velocity Tracking in Imperfect mmwave Systems with Lower Bound Benchmark", *IEEE Journal on Selected Areas in Communications* , 2023.

2. **Deeb Tubail** and Salama Ikki, "Bayesian Cramer-Rao Bound and Extended Kalman Filter Based Tracking Through Non-Ideal Transceivers in 5G and Beyond", *IEEE Transactions on Vehicular Technology*, 2023.

3. **Deeb Tubail**, Mohammed El-Absi, Salama Ikki, Thomas Kaiser, "Hardware-Aware Joint Localization-Synchronization and Tracking in 5G and Beyond", *IEEE Open Journal of the Communications Society*, 2023.

Non-Included List of publications

1. **D. A. Tubail**, M. Alsmadi and S. Ikki, "Physical Layer Security in Downlink of Cell-Free Massive MIMO With Imperfect CSI," *IEEE Transactions on Information Forensics and Security*, vol. 18, pp. 2945-2960, 2023.

2. **D. Tubail**, M. El-Absi, S. Ikki and T. Kaiser, "Accuracy Limits of Chipless RFID Based Indoor Localization System at THz band," *Fifth International Workshop on Mobile Terahertz Systems* (IWMTS), Duisburg, Germany, 2022.

3. F. Ghaseminajm, M. Alsmadi, **D. Tubail** and S. S. Ikki, "RIS-Aided Mobile Localization Error Bounds Under Hardware Impairments," *IEEE Transactions on Communications*, vol. 70, no. 12, pp. 8331-8341, Dec. 2022.

4. Mohammed El-Absi, Ali Alhaj Abbas, **Deeb Tubail**, Furkan Ilgac, Ashraf Abuelhaija, Yamen Zantah, Aydin Sezgin, Thomas Kaiser, "Path Loss Modeling of RFID Backscatter Channels With Reconfigurable Intelligent Surface: Experimental Validation", *IEEE Access*, 2023.

CHAPTER 2

BACKGROUND CONCEPTS

This chapter lays the essential theoretical foundation necessary for comprehending the subsequent chapters within this work. In the sections that follow, this chapter delves into several pivotal aspects of this study, encompassing the model for HWIs, the channels model, key elements of basic estimation theory, and an introductory exploration of ML along with the ELM algorithm. Regarding the HWIs model, we introduce an analytically manageable framework for characterizing HWIs. This model allows us to investigate how the quality of these impairments affects the localization and tracking processes. Moving forward, we detail the model for LoS within the MISO channel, especially when one of its terminals employs either a Uniform Linear Array (ULA) or a Uniform Rectangular Array (URA). Additionally, we cover the path gain associated with mmWave channel communication, shedding light on how the AoD influences the received signal, while also addressing the impact of the distance separating the BS and MS on the received signal. Concluding this chapter, we provide overviews of estimation theory, delve into the characteristics and advantages of ML estimation, and explore the tracking process. We discuss the KF and EKF, elucidate the derivation of the CRB and BCRB, and offer a glimpse into the realm of MLT.

2.1 Hardware Impairments Model.

Commonly, wireless communication channels are modelled as linear filters. The received signals over the wireless channel are distorted because of their reception by a noisy receiver, as seen in Fig. 2.1. This noise that is created in the receiver and added to the output of the receiver hardware gives the total thermal noise generated by the different receiver components. This is conditional to the assumption of the ideal behaviour of the hardware components, which is not applicable practically. The practical hardware components have non-ideal behavior and cause

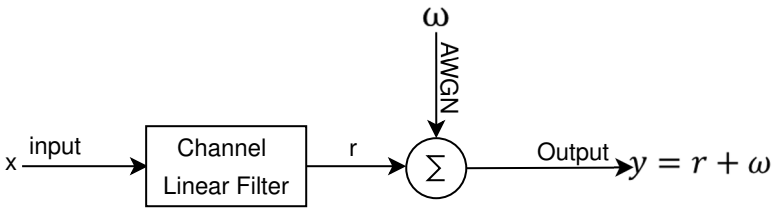

Figure 2.1: Wireless communication channel without HWIs.

non-linear distortion. For example, the amplification of the power amplifier in the transmitter is generally not linear. It acts linearly with a small input signal but saturates with stronger input signals. Similarly, the finite-resolution quantization component in the receiver performs a non-linear operation that is destructive and cannot be undone. More detailed descriptions of the non-linear behaviours of hardware components, which are termed "HWIs", including power amplifier non-linearity, amplitude/phase imbalance in I/Q mixers, phase noise in LoS, sampling jitter, and finite-resolution quantization in analog-to-digital converters, were covered in [11–14] and referenced therein.

As mentioned previously, a residual portion of the impairments still exists due to modelling inaccuracies and the destructive nature of some impairments. Since investigating the impact of those residual HWIs on the estimation and thus localization performance regardless of the source of the HWIs is the main goal of this work, this work adopts "the general residual HWIs model" described in [11, 80], as it reflects the nonlinear behaviours of the residual HWIs. According to the references, the residual HWIs are modelled as nonlinear memoryless filters at the transmitter and the receiver. Consequently, the wireless communication system with the existence of the HWIs becomes as Fig. 2.2 presents.

2.1.1 The General Residual HWIs Model

We can model the behaviour of residual HWIs as a nonlinear memoryless function as follows. Consider $x \sim CN(0,P)$ to be the input signal for a non-linear memoryless function $g(.)$, where this function produces the output $y = g(x)$, which is also a random variable with non-Gaussian distribution. The output y is correlated with the input x, and the output signal can be expressed

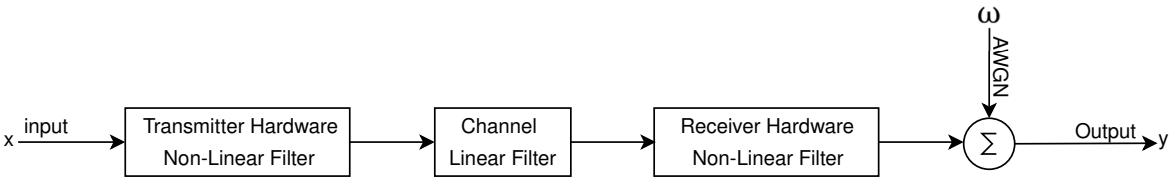

Figure 2.2: Hardware-impaired wireless system block diagram.

as

$$y = \frac{\mathbb{E}\{yx^*\}}{P}x + \eta,$$

where $\mathbb{E}\{|x|^2\} = P$, and the distortion term is

$$\eta = y - \frac{\mathbb{E}\{yx^*\}}{P}x.$$

It is evident that η is uncorrelated with x since

$$\mathbb{E}\{\eta x^*\} = \mathbb{E}\{yx^*\} - \frac{\mathbb{E}\{yx^*\}}{P}\mathbb{E}\{|x|^2\} = 0.$$

However, [11] provided examples showing that the input and the distortion term are generally not independent and that the distortion term η can also carry useful information. However, in the worst case, it is an independent complex Gaussian variable as follows:

$$\eta \sim CN\left(0\,,\ \mathbb{E}\{|y|^2\} - \frac{|\mathbb{E}\{yx^*\}|^2}{P}\right).$$

By knowing that the compensation algorithms used, the HWIs can be calibrated to make the average power of the input and output equal and thus

$$\mathbb{E}\{|y|^2\} = \mathbb{E}\{|x|^2\} = P,$$

and by defining

$$\sqrt{\kappa} = \frac{\mathbb{E}\{yx^*\}}{P},$$

the output of the non-linear function is given by

$$y = \sqrt{\kappa}x + \eta, \tag{2.1}$$

and the distortion power equals

$$P_\eta = \mathbb{E}\{|y|^2\} - \frac{|\mathbb{E}\{yx^*\}|^2}{P} = P - \frac{|\mathbb{E}\{yx^*\}|^2}{P} = P\left(1 - \frac{|\mathbb{E}\{yx^*\}|^2}{P^2}\right) = P(1-\kappa), \tag{2.2}$$

which is proportional to the input power P, with the proportionality constant $(1-\kappa)$. In other words, a fixed portion of the signal is turned into distortion, which is clear when we calculate the output power as

$$\mathbb{E}\{|y|^2\} = \kappa P + (1-\kappa)P = P, \quad \forall\kappa.$$

Fig. 2.3 illustrates the modelling of the behaviour of the residual HWIs as a non-linear memoryless function, where, as noted above, the key modelling characteristics are that the input signal $x \sim CN(0,P)$ is scaled by a deterministic factor κ. Then it is added to an uncorrelated

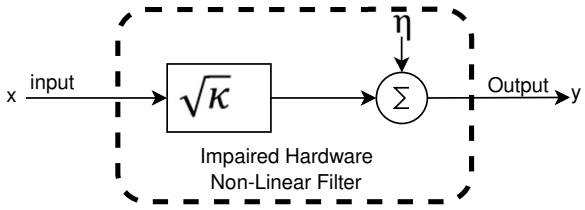

Figure 2.3: HWIs modelling

memoryless distortion term η which is, in the worst case, Gaussian distributed with zero mean and variance as in (2.2). Moreover, the term $\kappa \in (0,1]$ is the hardware quality factor in the case of ideal hardware $\kappa = 1$, which results in $y = x$.

Practically, κ is measured from the error vector magnitude (EVM) specified on the data sheets of the RF transceivers, which is a common metric for the distortion level in practical transceiver hardware [11]. The EVM is defined as the ratio between the average distortion magnitude and the signal magnitude after basic equalization. According to [80], the 3GPP LTE standard outlines the total EVM requirements within the interval [0.08, 0.175]. In this range, greater spectral efficiencies (modulations) are achievable with smaller EVM values. Conversely, there is an interest in larger EVMs when deploying a massive number of antennas, as these relaxed hardware constraints facilitate the use of cost-effective equipment. Based on the model represented by (2.1), and the equalized output that minimizes the mean squared error (MSE) which is $\sqrt{\kappa}y$, the EVM is defined as

$$\text{EVM} = \sqrt{\frac{\mathbb{E}\{|\sqrt{\kappa}y - x|^2\}}{\mathbb{E}\{|x|^2\}}} = \sqrt{\frac{(1-\kappa)P}{P}} = \sqrt{1-\kappa},$$

which leads to

$$\kappa = 1 - \text{EVM}^2. \tag{2.3}$$

Regarding multi-transceivers, Fig. 2.4 shows the HWIs of the multi-transceivers, where the input signal at i^{th} transceiver is P_i power, and the total input power is $P = \sum_{i=1}^{M} P_i$. In vector form, the transmitted signal is given according to

$$\begin{bmatrix} y_1 \\ y_2 \\ \vdots \\ y_M \end{bmatrix} = \begin{bmatrix} \sqrt{\kappa_1}x_1 \\ \sqrt{\kappa_2}x_2 \\ \vdots \\ \sqrt{\kappa_M}x_M \end{bmatrix} + \begin{bmatrix} \eta_1 \\ \eta_2 \\ \vdots \\ \eta_M \end{bmatrix}, \tag{2.4}$$

where

$$\eta_t \sim CN\left(\mathbf{0}, \text{diag}\Big(\big[P_1(1-\kappa_1), P_2(1-\kappa_2), \cdots, P_M(1-\kappa_M)\big]\Big)\right). \tag{2.5}$$

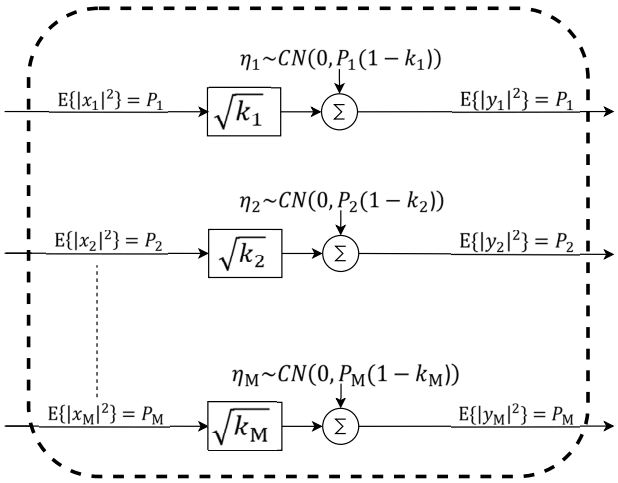

Figure 2.4: Multi-transceivers HWIs.

When assuming the case of identical transceivers, $\kappa_1 = \kappa_2 = \cdots = \kappa_M = \kappa_t$, and input power for all transceivers equal, $P_1 = P_2 = \cdots = P_M = \frac{P}{M}$, the output signal from the M transceivers is

$$\mathbf{y} = \sqrt{\kappa_t}\mathbf{x} + \eta_t, \tag{2.6}$$

where $\mathbf{y} = [y_1, y_2, \cdots, y_M]^{\mathrm{T}}$, $\mathbf{x} = [x_1, x_2, \cdots, x_M]^{\mathrm{T}}$, and $\eta_t \sim CN\left(\mathbf{0}, \frac{P}{M}(1-\kappa_t)\mathbf{I}_M\right)$. It is straightforward to check that

$$\mathbb{E}\{\|\mathbf{y}\|^2\} = \mathbb{E}\{\|\sqrt{\kappa_t}\mathbf{x}\|^2\} + \mathbb{E}\{\|\eta_t\|^2\} = \kappa_t \mathrm{P} + (1-\kappa_t)\mathrm{P} = \mathrm{P}, \quad \forall \kappa_t. \tag{2.7}$$

2.2 Channel Modelling

The goal of this section is to provide an overview of the relevant channel modelling techniques frequently used in the literature. Specifically, this section introduces the deterministic model of the LoS link, where such a model counts the array geometry, the correlation between the channel responses of different antennas, and the physical location and orientation of BS and MS. Then we introduce the loss of the mm wave path to provide a visual representation of the parameters that affect the loss of the path in this range of mm wave frequencies.

2.2.1 The ULA LoS Model

Fig. 2.8 illustrates the horizontal ULA LoS model, which is a very simple deterministic LoS channel model. Consider a horizontal ULA with adjacent antennas having an inter-spacing $d \in (0, 0.5]$, which is measured as the number of wavelengths between adjacent antennas. If a λ denotes the wavelength at the carrier frequency f_c, then the antenna spacing is λd meters. Furthermore, assume that the MS is located at fixed locations in the far field of the BS array, and

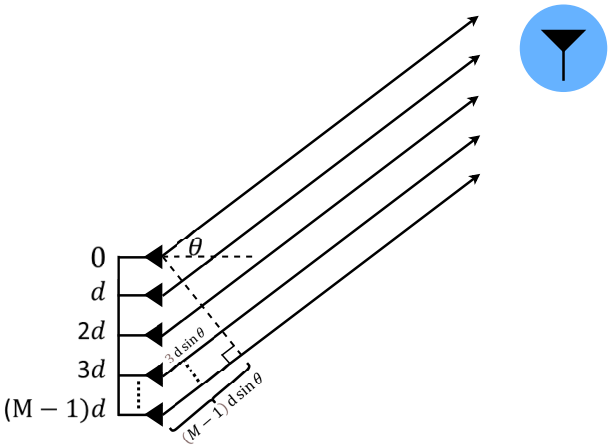

Figure 2.5: ULA to single-antenna LoS Model.

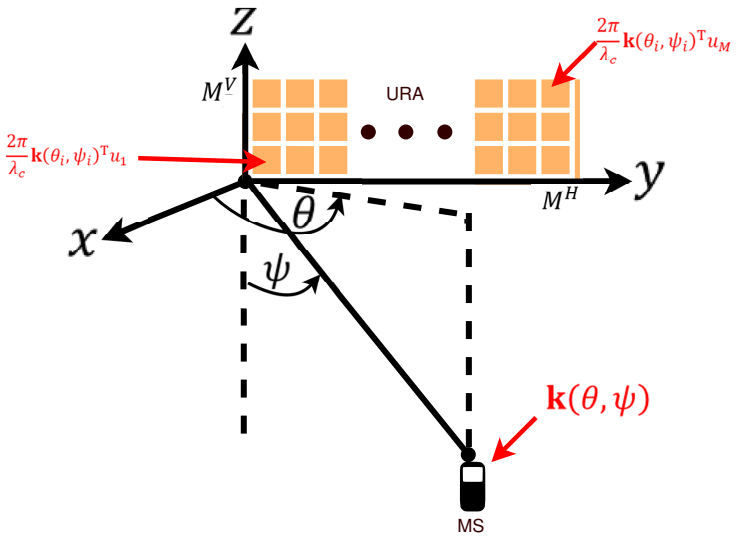

Figure 2.6: URA to single-antenna LoS Model.

the MS deviates by θ angle from the bore-sight direction of the ULA. Consequently, the phase difference between two adjacent antennas results from sending the signal to an antenna $d\sin(\theta)$ distance longer than the travel distance to the adjacent one. This leads to the array response with phase rotations that are multiples of $d\sin(\theta)$ as

$$\boldsymbol{\alpha}(\theta) = \left[1,\ e^{j\frac{2\pi}{\lambda_c}d\sin\theta},\cdots,e^{j(M-1)\frac{2\pi}{\lambda_c}d\sin\theta}\right]^{\mathrm{T}}, \tag{2.8}$$

where the azimuth angle to the MS $\theta \in [0, 2\pi)$.

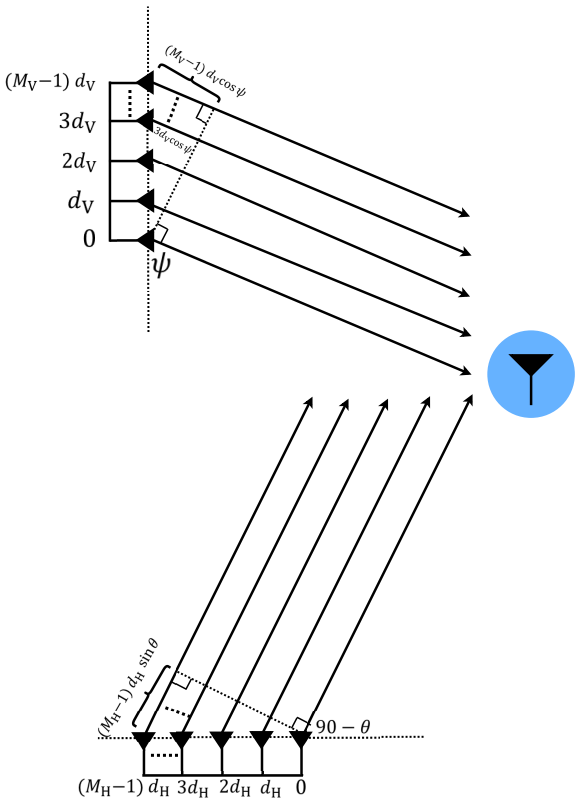

Figure 2.7: URA to single-antenna LoS Model.

2.2.2 The URA LoS Model

Fig.2.6 and Fig.2.7 illustrate the URA LoS MISO channel. In this channel, the location of each element is specified by

$$\mathbf{u}_m = \left[\text{ mod } \left(m-1, M^{\text{H}}\right) \times d_{\text{H}}\lambda_c,\, 0,\, \left\lfloor \frac{m-1}{M^{\text{H}}} \right\rfloor \times d_{\text{V}}\lambda_c \right]^{\text{T}}, \tag{2.9}$$

is the location vector of the m^{th} antenna element in the M-URA, and $d_{\text{H}}\lambda_c$ and $d_{\text{V}}\lambda_c$ refer to the horizontal and vertical inter-element spacing, respectively. The normalized position of the receiver is specified by the wave vector that is a function of the azimuth and elevation AOD, θ and ψ respectively, as

$$\mathbf{k} = [\sin\psi\cos\theta,\, \sin\psi\sin\theta,\, \cos\psi]^{\text{T}}. \tag{2.10}$$

Consequently, the phases shift resulting from the shift in the URA elements positions are represented by the BS array steering vector, α, is given by:

$$\alpha \in \mathbb{C}^{M\times 1} = \left[e^{j\frac{2\pi}{\lambda_c}\mathbf{k}^{\text{T}}u_1}, \cdots, e^{j\frac{2\pi}{\lambda_c}\mathbf{k}^{\text{T}}u_M} \right]^{\text{T}}, \tag{2.11}$$

2.2.3 *mm*wave Path Loss.

It is well known that the *mm*wave frequency range suffers from high atmospheric absorption, rain and foliage attenuation, strong penetration and reflection losses, and little diffraction, which essentially restrict their use to LoS outdoor-to-outdoor or indoor-to-indoor communications over relatively short distances [11]. The *mm*wave channel is modelled, for example, in [81, 82], and this model is frequently used in the networks that deal with the *mm* wave channel, i.e. [30, 35, 83].

According to [81, 82], the *mm*wave channel is affected by the operating frequency and the geometric distribution. More specifically, the path loss of the *mm*wave signal, when travelling a d-distance NLoS path between the transmitter and the receiver, can be described as

$$\mathrm{PL}(d) = \rho^2(d) = \epsilon^2(d)\zeta^2(d)\left(\frac{4\pi d}{\lambda}\right)^2, \tag{2.12}$$

where $\epsilon^2(d)$ is the reflection loss over distance d, $\zeta^2(d)$ is the additional propagation atmosphere attenuation above free space over distance d, and the last factor in the product is the free-space path loss over distance d. The propagation attenuation parameter $\zeta^2(d)$ can be predicted based on operating frequency as in [84], or obtained from channel measurements and can be generally applied for all scenarios with the same frequency and atmosphere condition. The free-space path loss can be calculated directly. The reflection loss $\epsilon^2(d)$ should be specifically calculated based on the input reflector geometry statistics and the reflection loss statistics.

The path loss of the LoS *mm*wave channel is similar to (2.12) except without reflection loss. i.e. $\epsilon^2(d) = 1$, and thus

$$\mathrm{PL}(d) = \rho^2(d_{\mathrm{LOS}}) = \zeta^2(d_{\mathrm{LOS}})\left(\frac{4\pi d_{\mathrm{LOS}}}{\lambda}\right)^2. \tag{2.13}$$

2.3 Introduction to Estimation Theory

This section presents some relevant technical and theoretical foundations of this work. Specifically, we introduce concepts used for estimating the values of unknown deterministic parameters from noisy measurements, as they are described in classical estimation theory. We provide an overview of the characteristics, advantages, and utilization of the ML estimator. We then present a benchmark that is used for evaluating the accuracy of the estimation process in the CRB term.

2.3.1 The Mathematical Estimation Problem

Consider $\mathbf{x}$ to be an observation vector of size L. Estimating the unknown value β is possible if the data $\mathbf{x}$ depends on the value β. If we aim to obtain a good estimation of β, the first step is to mathematically model the data that are inherently random and described by its PDF. It should be intuitively clear that because of this dependency, the PDF of the data is a function of β and thus changes corresponding to different values of β.

Since all information is embodied in the observed data $\mathbf{x}$ and its PDF, the more the PDF is influenced by the unknown parameter β, the better the estimation should be. Otherwise, if the PDF depends weakly upon β, or in the extreme case, if the PDF does not depend on it at all, then it is not expected to estimate a parameter with any degree of accuracy.

When β is deterministic but unknown, then the estimation process is called classical estimation. On the other hand, Bayesian estimation refers to when β is viewed as a random variable. The estimators are described as random variables, and their performance can only be completely characterized statistically or by their PDF.

Since the objective of the classical estimation theory is to search for optimal or at least acceptable estimators of unknown deterministic parameters, some optimality criteria are adopted for doing so. For example, the MSE, which is the most natural criterion, measures the average mean squared deviation of the estimator from the actual value. However, this natural criterion leads to unrealizable estimators as it cannot be written solely as a function of the data. Specifically, the examples in [85] demonstrate that this criterion depends on the bias, where a general rule is that that any criterion depends on the bias will lead to an unrealizable estimator. Consequently, an alternative criterion should be introduced instead of the MSE. Intuitively, the new approaches tend the bias to zero and find the estimator that minimizes the variance, where this estimator is termed the minimum variance unbiased (MVU) estimator. It has the average of the estimations that will yield the actual value of the unknown parameter $\mathbb{E}\{\hat{\beta}\} = \beta$, where $\hat{\beta}$ is the estimated values of the unknown deterministic parameter β.

The least squares (LS) is another approach that considers minimizing the variance as it measures the accuracy. Mainly, the LS approach targets minimizing the discrepancy, on average, between the estimation and the actual parameter value. In other words, it attempts to minimize the squared difference between the observation and the assumed signal or noiseless data. Here, the noiseless data is purely deterministic and is generated by some model that, in turn, depends upon the unknown parameter β while the observation is the distorted version of the signal.

The LS estimators class, in general, are non-optimal estimators, and worse, their statistical performance cannot be assessed. Despite this, they are implemented broadly in many possible applications and problems of interest. This refers to their ease of implementation and relaxed use (LS estimators are not restricted to any probabilistic assumptions about the data, since they require only the model of the signal).

2.3.2 Cramer-Rao bound

CRB places the lower bound on the variance of any unbiased estimator and is one of the easiest to determine among many other variance bounds. It essentially provides a benchmark to compare the performance of any unbiased estimator. It is also quite an indispensable tool because it clarifies the physical impossibility of finding any unbiased estimator whose variance is less than the CRB. It allows us to assert that an estimator that meets the CRB is the MVU estimator,

which happens when the estimator attains the bound for all values of the unknown parameter.

The CRB for a scalar parameter is given by

$$\text{var}(\hat{\beta}) \geq \text{CRB}(\beta) = \frac{1}{J(\beta)}, \tag{2.14}$$

which exists if the regularity condition is achieved as follows

$$\mathbb{E}\left\{\frac{\partial \ln p(\mathbf{x},\beta)}{\partial \beta}\right\} = 0, \quad \forall \beta, \tag{2.15}$$

where the derivative is evaluated at the actual value of β and the expectation is taken with respect to $p(\mathbf{x},\beta)$. The term $J(\beta)$ is the Fisher information of β, which is defined as

$$J(\beta) = -\mathbb{E}\left\{\frac{\partial^2 \ln p(\mathbf{x},\beta)}{\partial \beta^2}\right\}. \tag{2.16}$$

Transformation of Parameters: An important feature of the CRB is that it can be obtained for one parameter using the CRB of another parameter, given a known relationship between them. This frequently occurs in practice, as the desired parameter is often in some way related to some fundamental parameter. For instance, estimating $\beta = g(\mu)$ with $J(\beta)$ known yields

$$J(\mu) = \left(\frac{\partial \beta}{\partial \mu}\right)^2 J(\beta).$$

Extension to vector parameters: The CRB analysis can be extended to a vector parameter. For a vector parameter $\boldsymbol{\beta} = [\beta_1, \cdots, \beta_p]^{\mathrm{T}}$, the FIM of $\boldsymbol{\beta}$, $\mathbf{J}(\boldsymbol{\beta})$, becomes of $p \times p$ dimension, and its entity in the i^{th} raw and the j^{th} column is given by

$$\left[\mathbf{J}(\boldsymbol{\beta})\right]_{ij} = -\mathbb{E}\left\{\frac{\partial^2 \ln p(\mathbf{x};\boldsymbol{\beta})}{\partial \boldsymbol{\beta}_i \partial \boldsymbol{\beta}_j}\right\}, \tag{2.17}$$

and the CRB is of $\boldsymbol{\beta}$ is $\text{CRB}(\boldsymbol{\beta}) = \left[\mathbf{J}(\boldsymbol{\beta})\right]^{-1}$. Moreover, when $\boldsymbol{\beta} = \mathbf{g}(\boldsymbol{\mu})$, where $\boldsymbol{\mu}$ is an r dimension function, then

$$\mathbf{J}(\boldsymbol{\mu}) = \mathbf{T}\mathbf{J}(\boldsymbol{\beta})\mathbf{T}^{\mathrm{T}}, \tag{2.18}$$

where the transformation matrix $\mathbf{T} \in \mathbb{R}^{r \times p}$ is the Jacobian matrix defined as

$$\mathbf{T} \overset{(\text{def})}{=} \frac{\partial \boldsymbol{\beta}^{\mathrm{T}}}{\partial \boldsymbol{\mu}} = \begin{bmatrix} \frac{\partial \boldsymbol{\beta}_1}{\partial \mu_1} & \frac{\partial \boldsymbol{\beta}_2}{\partial \mu_1} & \cdots & \frac{\partial \boldsymbol{\beta}_p}{\partial \mu_1} \\ \frac{\partial \boldsymbol{\beta}_1}{\partial \mu_2} & \frac{\partial \boldsymbol{\beta}_2}{\partial \mu_2} & \cdots & \frac{\partial \boldsymbol{\beta}_p}{\partial \mu_2} \\ \vdots & \vdots & \ddots & \vdots \\ \frac{\partial \boldsymbol{\beta}_1}{\partial \mu_r} & \frac{\partial \boldsymbol{\beta}_2}{\partial \mu_r} & \cdots & \frac{\partial \boldsymbol{\beta}_p}{\partial \mu_r} \end{bmatrix}. \tag{2.19}$$

Generally, in the case of Gaussian observations, $\mathbf{x} \sim CN\left(\varphi(\boldsymbol{\beta}), \mathbf{C}(\boldsymbol{\beta})\right)$, so that both the mean and covariance may depend on $\boldsymbol{\beta}$, then [85]

$$[\mathbf{J}(\boldsymbol{\beta})]_{(i,j)} = 2\Re\left\{\left[\frac{\partial \varphi(\boldsymbol{\beta})}{\partial \beta_i}\right]^{\mathrm{H}} C^{-1}(\boldsymbol{\beta})\left[\frac{\partial \varphi(\boldsymbol{\beta})}{\partial \beta_j}\right]\right\} + \text{tr}\left[C^{-1}(\boldsymbol{\beta})\frac{\partial C(\boldsymbol{\beta})}{\partial \beta_i}C^{-1}(\boldsymbol{\beta})\frac{\partial C(\boldsymbol{\beta})}{\partial \beta_j}\right], \tag{2.20}$$

where

$$\frac{\partial \varphi(\boldsymbol{\beta})}{\partial \beta_i} = \left[\frac{\left[\partial \varphi(\boldsymbol{\beta})\right]_1}{\partial \beta_i}, \frac{\left[\partial \varphi(\boldsymbol{\beta})\right]_2}{\partial \beta_i}, \cdots, \frac{\left[\partial \varphi(\boldsymbol{\beta})\right]_L}{\partial \beta_i} \right]^{\mathrm{T}}, \tag{2.21}$$

$$\frac{\partial \mathbf{C}(\boldsymbol{\beta})}{\partial \beta_i} = \begin{bmatrix} \frac{[\partial \mathbf{C}(\boldsymbol{\beta})]_{11}}{\partial \beta_i} & \frac{[\partial \mathbf{C}(\boldsymbol{\beta})]_{12}}{\partial \beta_i} & \cdots & \frac{[\partial \mathbf{C}(\boldsymbol{\beta})]_{1L}}{\partial \beta_i} \\ \frac{[\partial \mathbf{C}(\boldsymbol{\beta})]_{21}}{\partial \beta_i} & \frac{[\partial \mathbf{C}(\boldsymbol{\beta})]_{22}}{\partial \beta_i} & \cdots & \frac{[\partial \mathbf{C}(\boldsymbol{\beta})]_{2L}}{\partial \beta_i} \\ \vdots & \vdots & \ddots & \vdots \\ \frac{[\partial \mathbf{C}(\boldsymbol{\beta})]_{L1}}{\partial \beta_i} & \frac{[\partial \mathbf{C}(\boldsymbol{\beta})]_{L2}}{\partial \beta_i} & \cdots & \frac{[\partial \mathbf{C}(\boldsymbol{\beta})]_{LL}}{\partial \beta_i} \end{bmatrix}, \tag{2.22}$$

and L is the total number of observations, i.e. size of $\mathbf{x}$.

Equivalent FIM: Assuming that

$$\mathbf{J}_\beta \in \mathbb{R}^{N\times N} = \begin{bmatrix} \mathbf{A} \in \mathbb{R}^{n\times n} & \mathbf{B} \in \mathbb{R}^{n\times(N-n)} \\ \mathbf{B}^{\mathrm{T}} \in \mathbb{R}^{(N-n)\times n} & \mathbf{C} \in \mathbb{R}^{(N-n)\times(N-n)} \end{bmatrix} \tag{2.23}$$

is the the FIM of $\beta = \left[\Theta \in \mathbb{R}^{1\times n}, \phi \in \mathbb{R}^{1\times(N-n)}\right]^{\mathrm{T}}$, then according to [86], the FIM of Θ is obtained by the formula as

$$\mathbf{J}_\Theta = \mathbf{A} - \mathbf{B}\mathbf{C}^{-1}\mathbf{B}^{\mathrm{T}}, \tag{2.24}$$

2.3.3 Maximum Likelihood Estimator.

The MVU estimator is not always available, which necessitates finding alternatives. The ML technique is the most popular when investigating possible estimators, and is desirable in situations where the MVU estimator does not exist or cannot be found. In fact, the ML estimator is quite an advantageous strategy for complicated estimation problems. For many practical cases of the interests, the ML performance is optimal for large enough data records, as it virtually equates to the MVU estimator in efficiency. For, the reasons mentioned above, almost all practical estimators are based on the ML approach.

Consider an unknown deterministic scalar β. The estimated value $\hat{\beta}$ is the value from the allowable range of β that maximizes the PDF $\mathrm{P}(\mathbf{x};\boldsymbol{\beta})$. One approach that we can use to determine the maximum value is to compute the derivative of the ML function as

$$\frac{\partial \ln p(\mathbf{x};\boldsymbol{\beta})}{\partial \boldsymbol{\beta}} = 0, \tag{2.25}$$

which may lead to a closed-form solution. However, when a closed-form expression cannot be found for the ML estimator, a numerical approach employs either a grid search or an iterative maximization of the ML function [85].

The ML Estimator optimality: For large data records (or asymptotically), the ML estimators are unbiased, achieve the CRB, and have a Gaussian PDF, i.e. $\hat{\beta} \overset{a}{\sim} N(\beta, I^{-1}(\beta))$, where $I(\beta)$ is the

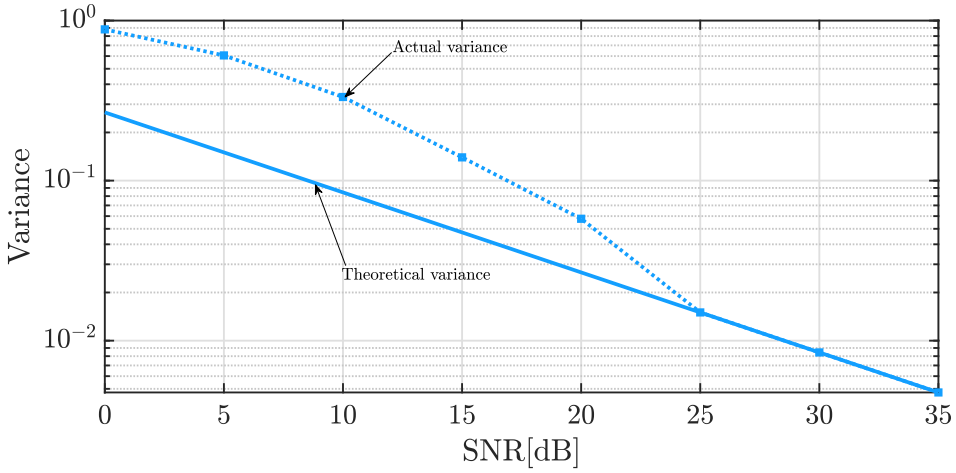

Figure 2.8: The ML variance versus the theoretical variance w.r.t SNR.

Fisher information evaluated at the true value of β. It is therefore asymptotically efficient, and hence asymptotically optimal [85]. In addition, according to [85], with the small data records case, the asymptotic optimality is achieved with a high enough SNR. For example, in the case of small data records, the ML estimator can attain the CRB when the SNR is high enough, as seen in Fig. 2.8 that illustrates the accuracy of an ML estimator with the SNR plotted against the theoretical variance for a signal-in-noise problem.

2.3.4 Bayesian Cramer-Rao bound

Regarding this, we compute the BFIM that counts for the information obtained from measurements, in addition to information gained from the priori knowledge. Afterward, the incorporation of the useful information from the observations and the priori information together results in the BFIM.

The BFIM, $\mathbf{J}_{\mathbf{s}}^{(\mathrm{B})}$, is given by [87]:

$$\mathbf{J}_{\mathbf{s}}^{(\mathrm{B})} = \underbrace{\mathbf{J}_{\mathbf{s}}^{(\mathrm{M})}}_{\text{Measurements}} + \underbrace{\mathbf{J}_{\mathbf{s}}^{(\mathrm{I})}}_{\text{Priori Information}}, \tag{2.26}$$

where the superscript (B), (O), and (I) refer to Bayesian, the measurements, the priori information, respectively. Mathematically, we can express the FIM of the measurements and the priori information as:

$$\mathbf{J}_{\mathbf{s}}^{(\mathrm{M})} = \mathbb{E}\left\{-\frac{\partial^2 \log p(y|\mathbf{s})}{\partial \mathbf{s}(\partial \mathbf{s})^{\mathrm{T}}}\right\} \tag{2.27}$$

$$\mathbf{J}_{\mathbf{s}}^{(\mathrm{I})} = \mathbb{E}\left\{-\frac{\partial^2 \log p(\mathbf{s})}{\partial \mathbf{s}(\partial \mathbf{s})^{\mathrm{T}}}\right\}, \tag{2.28}$$

where $p(y|\mathbf{s})$ is the PDF of the measurements y given to the vector $\mathbf{s}$, while $p(\mathbf{s})$ is the PDF of the $\mathbf{s}$. Consequently, (2.26) can mathematically be reformulated to [58, 87]:

$$\mathbf{J}_{\mathbf{s}}^{(\mathrm{B})}[t] = \underbrace{\mathbf{J}_{\mathbf{s}}^{(\mathrm{M})}[t]}_{\text{Measurements}} + \underbrace{\mathbf{G}_{22}[t] - \mathbf{G}_{21}[t]\Big[\mathbf{J}_{\mathbf{s}}^{(\mathrm{B})}[t-1] + \mathbf{G}_{11}[t]\Big]^{-1}\mathbf{G}_{12}[t]}_{\text{Priori Information}}, \tag{2.29}$$

where $\mathbf{J}_{\mathbf{s}}^{(\mathrm{B})}[t]$ is the BFIM at the t^{th} sample, and $\mathbf{J}_{\mathbf{s}}^{(\mathrm{B})}[t-1]$ is the BFIM at the previous sample, while the $\mathbf{G}_{ij}$ matrices are discussed later on.

Regarding the measurements FIM, it is calculated at each t sample according to the definition in (2.27), which is the same definition in subsection 2.3.2 and (2.20) and (2.17) within. For example, considering that the measurements, $\mathbf{Y}$, have the following distribution

$$p\Big(\mathbf{Y}|\mathbf{s}\Big) \sim N\Big(\mathbf{f}(\mathbf{s}), \mathbf{C}\Big), \tag{2.30}$$

where $\mathbf{C}$ is the covariance matrix, then

$$\log p\Big(\mathbf{Y}|\mathbf{s}\Big) = A - \frac{1}{2}\log|\mathbf{C}| - \frac{1}{2}\Big[\Big(\mathbf{Y}-\mathbf{f}(\mathbf{s})\Big)^{\mathrm{T}}\mathbf{C}^{-1}\Big(\mathbf{Y}-\mathbf{f}(\mathbf{s})\Big)\Big], \tag{2.31}$$

where A is a constant. Following that, and considering the definition in (2.27)

$$\mathbf{J}_{\mathbf{s}}^{(\mathrm{M})} = \mathbb{E}\left\{\left(\frac{\partial \mathbf{f}(\mathbf{s})}{\partial \mathbf{s}}\right)^{\mathrm{T}}\mathbf{C}^{-1}\frac{\partial \mathbf{f}(\mathbf{s})}{\partial \mathbf{s}}\right\} \tag{2.32}$$

In the context of the $\mathbf{G}_{ij}$ matrices involved in the FIM of the priori information are defined as:

$$\mathbf{G}_{ij}[t] = \mathbb{E}\left\{-\frac{\partial^2 \log p\big(\mathbf{s}[t]\big|\mathbf{s}[t-1]\big)}{\partial \mathbf{s}[t+i-2]\big(\partial \mathbf{s}[t+j-2]\big)^{\mathrm{T}}}\right\}, \tag{2.33}$$

where $p\big(\mathbf{s}[t]\big|\mathbf{s}[t-1]\big)$ is the conditional probability of $\mathbf{s}[t]$ given $\mathbf{s}[t-1]$. Assuming that this conditional probability is given by:

$$p\big(\mathbf{s}[t]\big|\mathbf{s}[t-1]\big) \sim N\big(\mathbf{A}\mathbf{s}[t-1], \mathbf{B}\mathbf{Q}\mathbf{B}^{\mathrm{T}}\big), \tag{2.34}$$

then, the log(.) function of the Gaussian PDF described in (2.34) is

$$\log p\big(\mathbf{s}[t]\big|\mathbf{s}[t-1]\big) = C - \frac{1}{2}\log\Big|\mathbf{B}\mathbf{Q}\mathbf{B}^{\mathrm{T}}\Big| - \frac{1}{2}\Big[\Big(\mathbf{s}[t]-\mathbf{A}\mathbf{s}(t-1)\Big)^{\mathrm{T}}\big(\mathbf{B}\mathbf{Q}\mathbf{B}^{\mathrm{T}}\big)^{-1}\Big(\mathbf{s}[t]-\mathbf{A}\mathbf{s}[t-1]\Big)\Big], \tag{2.35}$$

where C is a constant. Consequently, the first and second derivatives of (2.35) with respect to $\mathbf{s}[t]$

and $\mathbf{s}[t-1]$, are:

$$\begin{aligned}
&\frac{\partial \log p\Big(\mathbf{s}[t]|\mathbf{s}[t-1]\Big)}{\partial \mathbf{s}[t]} = -\big(\mathbf{B}\mathbf{Q}\mathbf{B}^{\mathrm{T}}\big)^{-1}\Big(\mathbf{s}[t]-\mathbf{A}\mathbf{s}[t-1]\Big)\\
&\frac{\partial \log p\Big(\mathbf{s}[t]|\mathbf{s}[t-1]\Big)}{\partial \mathbf{s}[t-1]} = \mathbf{A}^{\mathrm{T}}\big(\mathbf{B}\mathbf{Q}\mathbf{B}^{\mathrm{T}}\big)^{-1}\Big(\mathbf{s}[t]-\mathbf{A}\mathbf{s}[t-1]\Big)\\
&\frac{\partial\Big(-\big(\mathbf{B}\mathbf{Q}\mathbf{B}^{\mathrm{T}}\big)^{-1}\Big(\mathbf{s}[t]-\mathbf{A}\mathbf{s}[t-1]\Big)\Big)}{\partial\big(\mathbf{s}[t]\big)^{\mathrm{T}}} = -\big(\mathbf{B}\mathbf{Q}\mathbf{B}^{\mathrm{T}}\big)^{-1},\\
&\frac{\partial\Big(-\big(\mathbf{B}\mathbf{Q}\mathbf{B}^{\mathrm{T}}\big)^{-1}\Big(\mathbf{s}[t]-\mathbf{A}\mathbf{s}[t-1]\Big)\Big)}{\partial\big(\mathbf{s}[t-1]\big)^{\mathrm{T}}} = \big(\mathbf{B}\mathbf{Q}\mathbf{B}^{\mathrm{T}}\big)^{-1}\mathbf{A},\\
&\frac{\partial\Big(\mathbf{A}^{\mathrm{T}}\big(\mathbf{B}\mathbf{Q}\mathbf{B}^{\mathrm{T}}\big)^{-1}\Big(\mathbf{s}[t]-\mathbf{A}\mathbf{s}[t-1]\Big)\Big)}{\partial\big(\mathbf{s}[t]\big)^{\mathrm{T}}} = \mathbf{A}^{\mathrm{T}}\big(\mathbf{B}\mathbf{Q}\mathbf{B}^{\mathrm{T}}\big)^{-1},\\
&\frac{\partial\Big(\mathbf{A}^{\mathrm{T}}\big(\mathbf{B}\mathbf{Q}\mathbf{B}^{\mathrm{T}}\big)^{-1}\Big(\mathbf{s}[t]-\mathbf{A}\mathbf{s}[t-1]\Big)\Big)}{\partial\big(\mathbf{s}[t-1]\big)^{\mathrm{T}}} = -\mathbf{A}^{\mathrm{T}}\big(\mathbf{B}\mathbf{Q}\mathbf{B}^{\mathrm{T}}\big)^{-1}\mathbf{A},
\end{aligned}$$

where $\mathbf{Q}$ is a symmetric matrix. Accordingly, the $\mathbf{G}$ matrices of the priori information in (2.29) definitions and evaluation are:

$$\begin{aligned}
\mathbf{G}_{11}[t] &= \mathbb{E}\left\{-\frac{\partial^2 \log p\Big(\mathbf{s}[t]|\mathbf{s}[t-1]\Big)}{\partial \mathbf{s}[t-1]\Big(\partial \mathbf{s}[t-1]\Big)^{\mathrm{T}}}\right\} = \mathbf{A}^{\mathrm{T}}\big(\mathbf{B}\mathbf{Q}\mathbf{B}^{\mathrm{T}}\big)^{-1}\mathbf{A},\\
\mathbf{G}_{12}[t] &= \mathbb{E}\left\{-\frac{\partial^2 \log p\Big(\mathbf{s}[t]|\mathbf{s}[t-1]\Big)}{\partial \mathbf{s}[t-1]\Big(\partial \mathbf{s}[t]\Big)^{\mathrm{T}}}\right\} = -\mathbf{A}^{\mathrm{T}}\big(\mathbf{B}\mathbf{Q}\mathbf{B}^{\mathrm{T}}\big)^{-1},\\
\mathbf{G}_{21}[t] &= \mathbb{E}\left\{-\frac{\partial^2 \log p\Big(\mathbf{s}[t]|\mathbf{s}[t-1]\Big)}{\partial \mathbf{s}[t]\Big(\partial \mathbf{s}[t-1]\Big)^{\mathrm{T}}}\right\} = -\big(\mathbf{B}\mathbf{Q}\mathbf{B}^{\mathrm{T}}\big)^{-1}\mathbf{A},\\
\mathbf{G}_{22}[t] &= \mathbb{E}\left\{-\frac{\partial^2 \log p\Big(\mathbf{s}[t]|\mathbf{s}[t-1]\Big)}{\partial \mathbf{s}[t]\Big(\partial \mathbf{s}[t]\Big)^{\mathrm{T}}}\right\} = \big(\mathbf{B}\mathbf{Q}\mathbf{B}^{\mathrm{T}}\big)^{-1}.
\end{aligned}$$

Moreover, it is easy to note that the initial BFIM is

$$\mathbf{J}_{\mathbf{s}}^{(\mathrm{B})}(0) = \mathbb{E}\left\{-\frac{\partial^2 \log p\Big(\mathbf{s}(0)\Big)}{\partial \mathbf{s}(0)(\partial \mathbf{s}(0))^{\mathrm{T}}}\right\}. \tag{2.36}$$

Finally, the BCRB at the t^{th} sample is given by computing the inverse of the BFIM $\mathbf{J}_{\mathbf{s}}^{(\mathrm{B})}[t]$ in (2.29) at that sample, where the recursive evaluation of (2.29) start with the initial value $\mathbf{J}_{\mathbf{s}}^{(\mathrm{B})}(0)$ defined in (2.36).

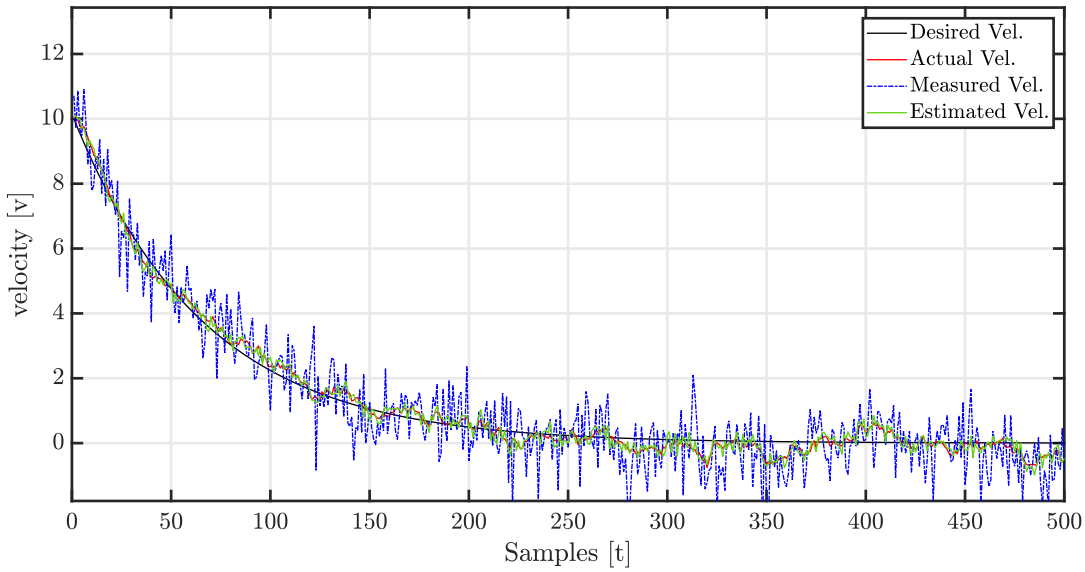

Figure 2.9: Tracking concept.

2.3.5 Tracking Process and Kalman Filters

The tracking process is considered an estimation process of a time-varying random unknown. Specifically, it is a generalization of the Bayesian estimation process that the unknown is not only a random variable but also changes with time. Consequently, the solution of these Bayesian estimation processes as well as the tracking process is performed based on prior knowledge about the unknown and based on the measurements performed to obtain information about the unknown.

For example, assume that the is a moving object trying to stop by controlling/reducing its velocity to have a velocity at each sample A percent of its previous one. However, due to control errors or external factors, the actual velocity is a noisy version of the desired one and is modeled as

$$v[t] = Av[t-1] + w[t], \tag{2.37}$$

where $v[t]$ and $v[t-1]$ are the current and previous samples, respectively, while $w[t]$ is the noise. Besides, assume that there is a sensor that provides measurements that have a relationship with the velocity as

$$x[t] = Bv[t] + u[t], \tag{2.38}$$

where $x[t]$ and $u[t]$ are the measurement and the measurement error samples, while B is the relationship between the measurement and the velocity. For instance, in the case of the sensor of the Doppler frequency f_D that has $f_D = \frac{v}{\lambda}$, the constant $B = \frac{1}{\lambda}$ in this case where λ is the wavelength of the transmitted signal,

Here (2.37) presents prior knowledge and the transition model of the unknown velocity, and (2.38) presents the measurements required to estimate the unknown velocity. An illustration of this example: the desired velocity, the actual velocity, the measured velocity, and the estimated velocity are in Fig. 2.9. Moreover, the velocity is estimated considering the transition model in (2.37) and the measurements in (2.38). One of the solutions to these kinds of problems is the KF, which is described in the next subsection.

2.3.5.1 Vector Kalman Filter

The KF is the generalized version of the Wiener filter. Unlike the Wiener filter, which is restricted to stationary scalar signals and noises, KF accommodates vector signals and noises, which may additionally be non-stationary and vary in time. Specifically, these non-stationary signals that are embedded in noise, evolve in time and their change is characterized by a dynamical or state model, where KF generalizes the sequential MMSE estimator to track the signals in time considering the dynamical model. When the signal and noise are jointly Gaussian, then the KF is an optimal MMSE estimator, and when not, it is the optimal LMMSE estimator.

Consider the signal vector at the t^{th} samples, $\mathbf{s}[t] \in \mathbb{R}^{p\times 1}$, is according to the *Gauss-Markov* model as:

$$\mathbf{s}[t] = \mathbf{A}\mathbf{s}[t-1] + \mathbf{B}\mathbf{u}[t] \quad t > 0, \tag{2.39}$$

where $\mathbf{A}$ and $\mathbf{B}$ are known with dimension $p \times p$ and $p \times r$, respectively. The driven noise vector $\mathbf{u}[t]$ is of $r \times 1$ dimension and modelled as a zero-mean Gaussian random, i.e. $\mathbf{u}[t] \sim N(\mathbf{0}, \mathbf{Q})$. Consequently, the conditional probability of $\mathbf{s}[t]$ given $\mathbf{s}[t-1]$ is

$$p\big(\mathbf{s}[t]\big|\mathbf{s}[t-1]\big) \sim N\big(\mathbf{s}[t-1], \mathbf{Q}\big). \tag{2.40}$$

Besides, for any two samples $t \neq t'$, $\mathbf{u}[t]$ and $\mathbf{u}[t']$ are independent and achieve $\mathbb{E}\{\mathbf{u}[t]\mathbf{u}^{\mathrm{T}}[t']\} = \mathbf{0}\ \forall\, t \neq t'$, which achieves being $\mathbf{u}[t]$ a vector (WGN). Moreover, the signal vector $\mathbf{s}[t]$ satisfies

$$p\big(\mathbf{s}[t]\big|\mathbf{s}[0:t-1]\big) = p\big(\mathbf{s}[t]\big|\mathbf{s}[t-1]\big), \tag{2.41}$$

where $\mathbf{s}[0:t-1]$ is the collection of the signals from the first sample to the $t-1$ samples.

In the same context, the initial state $\mathbf{s}[-1]$ has $p \times 1$ dimension, independent of $\mathbf{u}[t]\ \forall t$, and also has the model of a Gaussian random variable, i.e. $\mathbf{s}[-1] \sim N\Big(\mathbf{s}_0, \mathbf{Q}_0\Big)$. It's worth mentioning here that $\mathbf{s}_0$ and $\mathbf{Q}_0$ are determined arbitrarily or based on some previous information, and their impact shortly becomes negligible as the number of samples increases.

Besides, when the measurements/observations vector $\mathbf{x}[t]$ with $M \times 1$ dimension, is according to the *Bayesian linear* model as:

$$\mathbf{x}[t] = \mathbf{H}[t]\mathbf{s}[t] + \mathbf{w}[t] \quad t > 0, \tag{2.42}$$

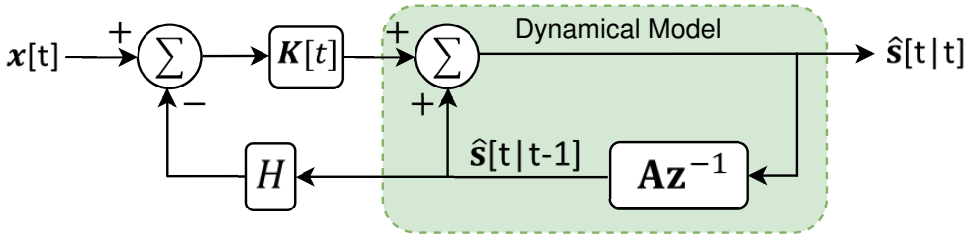

Figure 2.10: Observations and the dynamical model relationship in KF.

where the observations matrix $\mathbf{H}$ is known with dimension $M \times p$ and may vary with time. The measurements noise vector $\mathbf{w}[t]$ is of $M \times 1$ dimension and with random distribution as i.e. $\mathbf{w}[t] \sim N(\mathbf{0}, \mathbf{C}[t])$, where for any two samples $t \neq t'$, $\mathbf{w}[t]$ and $\mathbf{w}[t']$ are independent, which achieves being $\mathbf{w}[t]$ a vector (WGN).

Now, tracking the signaling vector $\mathbf{s}[t]$ can be implemented sequentially based on $\mathbf{x}[0:t]$, the observations from the first sample to the t^{th} sample. Specifically, (2.43) represents the recursive steps required for implementing the KF, where they are:

$$\hat{\mathbf{s}}[t|t-1] = \mathbf{A}\hat{\mathbf{s}}[t-1|t-1], \tag{2.43a}$$

$$\mathbf{N}[t|t-1] = \mathbf{A}\mathbf{N}[t-1|t-1]\mathbf{A}^{\mathrm{T}} + \mathbf{B}\mathbf{Q}\mathbf{B}^{\mathrm{T}}, \tag{2.43b}$$

$$\mathbf{K}[t] = \mathbf{N}[t|t-1]\mathbf{H}^{\mathrm{T}}[t]\Big(\mathbf{C}[t] + \mathbf{H}[t]\mathbf{N}[t|t-1]\mathbf{H}^{\mathrm{T}}[t]\Big)^{-1}, \tag{2.43c}$$

$$\hat{\mathbf{s}}[t|t] = \hat{\mathbf{s}}[t|t-1] + \mathbf{K}[t]\big(\mathbf{x}[t] - \mathbf{H}[t]\hat{\mathbf{s}}[t|t-1]\big), \tag{2.43d}$$

$$\mathbf{N}[t|t] = \Big(\mathbf{I} - \mathbf{K}[t]\mathbf{H}[t]\Big)\mathbf{N}[t|t-1]. \tag{2.43e}$$

In this context, the tracking process starts with initializing (2.43a) and (2.43b) by $\hat{\mathbf{s}}[-1|-1] = \mathbf{s}_0$ and $\mathbf{N}[-1|-1] = \mathbf{B}\mathbf{Q}_0\mathbf{B}^{\mathrm{T}}$, where (2.43a) represents the prediction step formulated based on the transition model in (2.39), while (2.43b) calculates the minimum prediction MSE matrix $\mathbf{N} \in \mathbb{R}^{p \times p}$.

Moreover, (2.43c) determines the Kalman gain matrix $\mathbf{K} \in \mathbb{R}^{p \times M}$ based on matrix $\mathbf{C}$. Specifically, the matrix $\mathbf{C}$ specifies the errors in the measurements process, defined in (2.42). Regarding this, the entities of $\mathbf{C}$ can be determined according to the CRB of the estimated values, or any other methods providing a more accurate description for $\mathbf{C}$, specifically when the measurements process accuracy can not achieve the CRB.

Afterward, the step in (2.43d) corrects the prediction benefiting from the current measurements $\mathbf{x}[t]$ in correcting the prediction $\hat{\mathbf{s}}[t|t-1]$ in (2.43a) aiming to obtain more accurate signal $\hat{\mathbf{s}}[t|t]$ vector. Regarding the $\hat{\mathbf{s}}[t|t]$, it is the output from the tracker for the t^{th} sample, where the current t^{th} tracker output depends on the information from the initial sample to the $(t')^{\text{th}}$ sample. Finally, the minimum MSE matrix is given according to (2.43e), and then, $\hat{\mathbf{s}}[t|t]$ and $\mathbf{N}[t|t]$ are re-fed again as the previous value in (2.43a) and (2.43b).

2.3.5.2 Extended Kalman Filter

In practice, the dynamic model and/or the measurement equations can be nonlinear, and then, the previous approach is no longer valid. Mathematically, instead of the linear signal vector and measurements vector in (2.39) and (2.42), respectively, we have one/two nonlinear relationships as:

$$\mathbf{s}[t] = \mathbf{a}\big(\mathbf{s}[t-1]\big) + \mathbf{B}\mathbf{u}[t] \quad t > 0, \tag{2.44}$$

$$\mathbf{x}[t] = \mathbf{h}\big(\mathbf{s}[t]\big) + \mathbf{w}[t] \qquad t > 0, \tag{2.45}$$

where $\mathbf{a}$ is a p-dimensional non-linear function and $\mathbf{h}$ is an M-dimensional function, while all other matrices have the same dimensions as in the previous filter. Moreover, $\mathbf{a}\big(\mathbf{s}[t-1]\big)$ describes the true physical model for the evolution of the state, while $\mathbf{h}\big(\mathbf{s}[t]\big)$ transforms the state variables to the noiseless measurements.

Fortunately, an approximate solution based on linearizing $\mathbf{a}$ and/or $\mathbf{h}$, and then implementing the linear KF in (2.43), where the resulting filter is the EKF. However, no optimality properties about the extended filter and its performance depend on the accuracy of the linearization.

By linearizing $\mathbf{a}\big(\mathbf{s}[t-1]\big)$ around $\hat{\mathbf{s}}[t-1|t-1]$ and $\mathbf{h}\big(\mathbf{s}[t]\big)$ around $\hat{\mathbf{s}}[t|t-1]$ using Taylor expansion, the first-order Taylor expansion are given as:

$$\mathbf{a}\big(\mathbf{s}[t-1]\big) \approx \mathbf{a}\big(\hat{\mathbf{s}}[t-1|t-1]\big) + \left.\frac{\partial \mathbf{a}}{\partial \mathbf{s}[t-1]}\right|_{\mathbf{s}[t-1]=\hat{\mathbf{s}}[t-1|t-1]} \big(\mathbf{s}[t-1] - \hat{\mathbf{s}}[t-1|t-1]\big), \tag{2.46}$$

$$\mathbf{h}\big(\mathbf{s}[t]\big) \approx \mathbf{h}\big(\hat{\mathbf{s}}[t|t-1]\big) + \left.\frac{\partial \mathbf{h}}{\partial \mathbf{s}[t]}\right|_{\mathbf{s}[t]=\hat{\mathbf{s}}[t|t-1]} \big(\mathbf{s}[t] - \hat{\mathbf{s}}[t|t-1]\big). \tag{2.47}$$

By defining the following Jacobian matrices as:

$$\mathbf{A}[t-1] = \left.\frac{\partial \mathbf{a}}{\partial \mathbf{s}[t-1]}\right|_{\mathbf{s}[t-1]=\hat{\mathbf{s}}[t-1|t-1]}, \tag{2.48}$$

$$\mathbf{H}[t] = \left.\frac{\partial \mathbf{h}}{\partial \mathbf{s}[t]}\right|_{\mathbf{s}[t]=\hat{\mathbf{s}}[t|t-1]}, \tag{2.49}$$

the linearized version of the non-linear equations (2.44) and (2.45), respectively, are:

$$\mathbf{s}[t] = \mathbf{A}[t-1]\mathbf{s}[t-1] + \mathbf{B}\mathbf{u}[t] + \Big(\mathbf{a}\big(\hat{\mathbf{s}}[t-1|t-1]\big) - \mathbf{A}[t-1]\hat{\mathbf{s}}[t-1|t-1]\Big), \tag{2.50}$$

$$\mathbf{x}[t] = \mathbf{H}[t]\mathbf{s}[t] + \mathbf{w}[t] + \Big(\mathbf{h}\big(\hat{\mathbf{s}}[t|t-1]\big) - \mathbf{H}[t]\hat{\mathbf{s}}[t|t-1]\Big), \tag{2.51}$$

Now, the sequential tracking procedures of the signalling vector $\mathbf{s}[t]$ according to the EKF become:

$$\hat{\mathbf{s}}[t|t-1] = \mathbf{a}\big(\hat{\mathbf{s}}[t-1|t-1]\big), \tag{2.52a}$$

$$\mathbf{N}[t|t-1] = \mathbf{A}[t-1]\mathbf{N}[t-1|t-1]\mathbf{A}^{\mathrm{T}}[t-1] + \mathbf{B}\mathbf{Q}\mathbf{B}^{\mathrm{T}}, \tag{2.52b}$$

$$\mathbf{K}[t] = \mathbf{N}[t|t-1]\mathbf{H}^{\mathrm{T}}[t]\Big(\mathbf{C}[t] + \mathbf{H}[t]\mathbf{N}[t|t-1]\mathbf{H}^{\mathrm{T}}[t]\Big)^{-1}, \tag{2.52c}$$

$$\hat{\mathbf{s}}[t|t] = \hat{\mathbf{s}}[t|t-1] + \mathbf{K}[t]\Big(\mathbf{x}[t] - \mathbf{h}\big(\hat{\mathbf{s}}[t|t-1]\big)\Big), \tag{2.52d}$$

$$\mathbf{N}[t|t] = \Big(\mathbf{I} - \mathbf{K}[t]\mathbf{H}[t]\Big)\mathbf{N}[t|t-1]. \tag{2.52e}$$

In the case of perfect measurements, i.e. the matrix $\mathbf{C}[t] = \mathbf{0}$, $\hat{\Theta}[t] = \Theta[t]$, and when the linearization process is very close to the non-linear relationship, i.e. $\mathbf{f}\big(\hat{\mathbf{p}}[t|t-1]\big) = F[t]\hat{\mathbf{p}}[t|t-1]$, then (2.43c) devolves to be $\mathbf{K}[t] = \big(F[t]\big)^{-1}$, and (2.43d) becomes: $\hat{\mathbf{p}}[t|t] = \big(F[t]\big)^{-1}\Theta[t]$. The final relationship implies that the tracked values can be obtained only based on their relationship with the measurements that are considered the actual/real values.

2.4 Introduction to Machine Learning

2.4.1 Machine Learning Methodology and Problems

The conventional engineering design flow starts with a deep analysis of the problem carried out by a number of experts, culminating with the mathematical model that captures the key features of the problem aiming to derive hand-crafted solutions to the problem. This standard flow requires a precise model of the set-up under study and relies on domain knowledge and on design optimized for the problem at hand.

In comparison with the conventional engineering design flow, the MLT is to collect large data sets, e.g., of labelled speech, images or videos, and to use this information to train general-purpose learning machines to carry out the desired task. In more detail, MLT requires the specification of an objective, of a model to be trained, and of an optimization technique, and then, it lets large amounts of data dictate algorithms and solutions[88].

MLT outperforms the conventional engineering flow in development cost and time terms, or with complex problems to be studied and analyzed in its full generality. However, MLT has a key disadvantage as it produces suboptimal performance in general, hinders the interpretability of the solution, and applies only to a limited set of problems. In conclusion, MLT may be useful for [88]:

1. mapping well-defined inputs to well-defined outputs;
2. large data sets of input-output pairs;
3. the existence of clear feedback with clearly definable goals and metrics;
4. no need for optimal solutions, or for detailed explanations for how the decision was made;
5. and the function being learned should not change rapidly over time.

Regarding the learning tasks, mainly, three different types of MLT problems as follows[88]:

- Supervised learning:
  Supposing, there are N training data set, $D = \big\{(x_1, t_1), \cdots, (x_N, t_N)\big\}$, where x_n is the input, and t_n is the corresponding response or label. The "supervised learning" aims at generalizing the observations in the data set D to new inputs $x_n \notin D$. For example, x_n is the text of

an email, $t_n \in$ {Spam, Not spam}, the goal of supervised learning is to predict the value of the label t_n for an input $x_n \notin D$ based on the learning/observation from D set. Now, when the response t is discrete and a limited set of values as in the example, the problem is called *Classification*, while it is called *Regression* problems in case of a continuous or unbounded response set t. An example of a regression problem is to predict the temperature t based on current meteorological observations x. It's worth noting here that knowing the conditional distribution of $p(t|x)$ that defines a profile of beliefs over all possible of the response t given the input x, is very effective for the prediction process.

- Unsupervised learning:
  Supposing, there are N unlabelled training data set, $D = \{x_1, \cdots, x_N\}$, the "unsupervised learning" generally targets learning properties of the mechanism that generates this data set. For example, clustering applications aim at grouping similar x_n, or generative modelling applications which is the problem of learning a generating mechanism to produce artificial examples that are similar to available data in the data set D.

  It's good to mention that there is a path between "supervised" and "unsupervised" learning, called " semi-supervised learning" when not all x are labelled, where the unlabelled x data provides information about the distribution of x.

- Reinforcement learning:
  Reinforcement learning tries to infer the optimal sequential decisions based on feedback from previous actions. For any t response corresponding to a state x, the learner provides feedback about the made decision, and the environment moves on to a different state. An example of this is navigation in a given environment in the presence of obstacles by penalizing decisions that result in collisions.

  Considering supervised and unsupervised learning, reinforcement learning is different from both of them. Specifically, it is unlike "supervised" as the learner is not provided with the optimal actions t to select in a given state x. Besides, given the availability of feedback, it is not fully unsupervised. Moreover, unlike supervised and unsupervised learning, it is influenced by previous actions on future states and feedback.

More classifications can be presented for MLT problems from different angles, however, we restrict this paper to the aforementioned classification.

2.4.2 Extreme learning machines

It's clear as discussed in the previous subsection that the success of MLT relies on the coexistence of large data and efficient learning techniques (algorithms). Neural networks, as a kind of MLT, consist of neurons, connections, and weights. In this context, the neuron receives input signals from former neurons and sends out output signals to later neurons. The relation between neurons

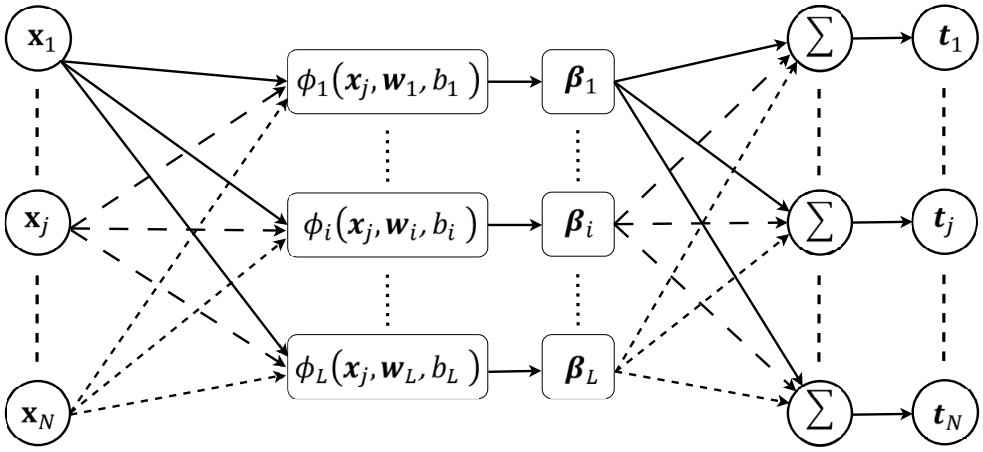

Figure 2.11: Extreme learning machines block diagram.

in the different layers, called connection, delivers an important parameter called weight, which affects the processing of the input signals to produce the output signals.

Regarding the weights, training the network optimizes the weights to obtain the best approximate data. Different approaches are used to obtain the weights. Many current training algorithms are gradient-based algorithms that, unfortunately, always converge at local extrema and do not achieve the global solution, depending on the parameter initialization and the complexity of the feature space.

On the other hand, ELM is a promising learning technique that provides efficient unified solutions to generalized feed-forward networks including but not limited to (both single- and multi-hidden-layer) neural networks, radial basis function (RBF) networks, and kernel learning[89]. It can offer significant advantages such as fast learning speed, ease of implementation, and minimal human intervention, so the ELM approach is a strong potential alternative technique for conventional MLT [89].

According to the ELM approach, the hidden neurons are important but can be randomly generated and independent of applications. Fig. 2.11 demonstrates the idea and implementation of single hidden layer feed-forward networks and the ELM approach. In detail, assuming N training data set $D = \{(\mathbf{x}_1, \mathbf{t}_1), (\mathbf{x}_2, \mathbf{t}_2), \cdots, (\mathbf{x}_N, \mathbf{t}_N)\}$, where $\mathbf{x}_i = [x_{i1}, x_{i2}, \cdots, x_{in}]^{\mathrm{T}} \in \mathbb{R}^n$ and $\mathbf{t}_i = [t_{i1}, t_{i2}, \cdots, t_{im}]^{\mathrm{T}} \in \mathbb{R}^m$. Moreover, the single hidden layer feed-forward network has L hidden neurons and activation functions $\phi_i(\mathbf{x}_j, \mathbf{w}_i, b_i)$, and then,

$$\sum_{i=1}^{L} \beta_i \phi_i(\mathbf{x}_j, \mathbf{w}_i, b_i) = \mathbf{t}_j \quad j = 1, \cdots, N, \tag{2.53}$$

where $\mathbf{w}_i = [w_{i1}, w_{i2}, \cdots, w_{in}]^{\mathrm{T}} \in \mathbb{R}^n$ is the weight vector connecting the i^{th} hidden node and the input nodes, b_i is the bias in the i^{th} hidden node, while the weight vector connecting the i^{th} hidden node and the output nodes is $\beta_i = [\beta_{i1}, \beta_{i2}, \cdots, \beta_{im}]^{\mathrm{T}} \in \mathbb{R}^m$. It's worth noting in this ELM that the input weight vectors and the bias $\mathbf{w}_i$, b_i for each i^{th}. Examples of the non-linear activation function are in table 2.1.

Function	Formula
Sigmoid function	$\phi(\mathbf{x},\mathbf{w},b) = \frac{1}{1+\exp\left(-(\mathbf{w}^{\mathrm{T}}.\mathbf{x}+b)\right)}$
Fourier function	$\phi(\mathbf{x},\mathbf{w},b) = \sin\left(\mathbf{w}^{\mathrm{T}}.\mathbf{x}+b\right)$
Gaussian function	$\phi(\mathbf{x},\mathbf{w},b) = \exp\left(-b\|\mathbf{x}-\mathbf{w}\|^2\right)$
Multi-quadrics function	$\phi(\mathbf{x},\mathbf{w},b) = \left(\|\mathbf{x}-\mathbf{w}\|^2+b^2\right)^{1/2}$
Hard-limit function	$\phi(\mathbf{x},\mathbf{w},b) = \begin{cases}1, & \mathbf{w}^{\mathrm{T}}.\mathbf{x}-b\geq 0\\ 0. & \text{otherwise}\end{cases}$

Table 2.1: Activation functions

The N equations presented in (2.53) can be written in vector form as:

$$\mathbf{H}\beta = \mathbf{T}, \tag{2.54}$$

where

$$\mathbf{H}(\mathbf{w}_1,\cdots,\mathbf{w}_L,b_1,\cdots,b_L,\mathbf{x}_1,\cdots,\mathbf{x}_N) = \begin{bmatrix}\phi_1(\mathbf{x}_1,\mathbf{w}_1,b_1) & \cdots & \phi_L(\mathbf{x}_1,\mathbf{w}_L,b_L)\\ \vdots & \cdots & \vdots\\ \phi_1(\mathbf{x}_N,\mathbf{w}_1,b_1) & \cdots & \phi_L(\mathbf{x}_N,\mathbf{w}_L,b_L)\end{bmatrix}_{N\times L}, \tag{2.55}$$

$$\mathbf{T} = \begin{bmatrix}\mathbf{t}_1^{\mathrm{T}}\\ \vdots\\ \mathbf{t}_N^{\mathrm{T}}\end{bmatrix}_{N\times m}, \tag{2.56}$$

and

$$\beta = \begin{bmatrix}\beta_1^{\mathrm{T}}\\ \vdots\\ \beta_L^{\mathrm{T}}\end{bmatrix}_{L\times m}. \tag{2.57}$$

Consequently, the matrix β is obtained by the pseudo-inverse operation as:

$$\beta = \left(\mathbf{H}^{\mathrm{T}}\mathbf{H}\right)^{-1}\mathbf{H}^{\mathrm{T}}\mathbf{T}. \tag{2.58}$$

Later for any new data set $\hat{D} = \{\hat{\mathbf{x}}_j\}$, $j = 1,\cdots,\hat{N}$, the estimated outputs from the single hidden layer are obtained from:

$$\mathbf{o}_{\hat{N}\times m} = \mathbf{H}(\mathbf{w}_1,\cdots,\mathbf{w}_L,b_1,\cdots,b_L,\mathbf{x}_1,\cdots,\mathbf{x}_{\hat{N}})_{\hat{N}\times L}\times\beta_{L\times m}. \tag{2.59}$$

2.5 Summary

This chapter establishes the foundational theoretical framework essential for understanding subsequent chapters. The key topics covered include the model for HWIs, the channels model,

fundamental aspects of estimation theory, and an introductory exploration of MLT with a focus on the ELM algorithm. The HWIs model introduces a manageable framework for characterizing impairments, allowing an investigation into how these affect the localization and tracking processes. The chapter also details the LoS model within the MISO channel, mainly when the BS uses either a ULA or a URA. Additionally, the discussion covers the path gain in mmwave channel communication, emphasizing the influence of AoD on the received signal and considering the impact of the distance between the BS and the MS on the received signal. The chapter concludes with overviews of estimation theory, exploring the characteristics and advantages of ML estimation and delving into the tracking process. The KF and EKF are discussed, along with the derivation of the CRB and BCRB. Finally, a glimpse into the realm of MLT is provided.

CHAPTER 3

LOCALIZATION PROCESS AND CRAMER-RAO BOUND

This chapter investigates the localization process and the relevant CRB in *mm*wave MISO system. Specifically, it presents the downlink channel parameters estimation process, the localization process, and the CRB benchmark for three practical scenarios. Mainly in these scenarios, the BS called the reference BS, broadcasts well-known pilots to the MS that targets measuring and estimating its direction and distance referring to the reference BS. However, these scenarios raise different practical challenges. Specifically, the first scenario is the simplest, and it is a 2D *mm*wave MISO system involving a single LoS link between the BS and the MS, and both BS and MS are equipped with imperfect transceivers. The second scenario is a more complicated and real scenario as it is not only an imperfect system similar to the first scenario but also a multipath 3D system. Here, in these two scenarios, it is assumed that the BS and the MS are perfectly synchronized to the same clock by performing a preliminary synchronization step through the uplink channel, e.g. using a two-way synchronization protocol. Unlike the previous scenarios, the third scenario involves the synchronization challenges to the localization in a hardware-impaired system. Doing so is by considering the reflected link, the NLoS link, from the known-position RIS. The precision of the localization process in these situations is assessed by computing the RMSE of positions and comparing them to benchmarks set by the CRB. The acceptable RMSE values or localization errors depend on the specific application and scenarios. For instance, prior research in [90] outlines diverse upper bounds for localization errors in different applications and scenarios within the context of 5G and 6G.

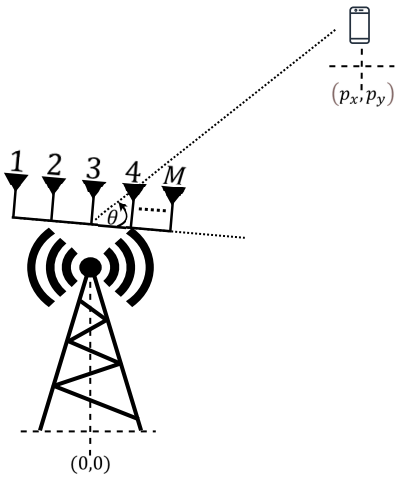

Figure 3.1: Geometry of the considered 2D mmwave MISO-OFDM scenario.

3.1 2D perfect synchronous mmwave MISO system

This section aims to investigate a localization process distorted by HWIs. We consider the localization process in a perfectly synchronized 2D mmwave MISO-OFDM wireless communication system that only has a LoS connection between the BS and the MS. In this context, the communication system description and the channel between the BS and MS are presented. Next, the HWIs model is integrated into the transceivers at the entities in this system, where the impaired transmitted and received signals/pilots are derived and statistically modelled. Then, the channel parameters including the AoD and the ToF, are estimated by observing the received pilots. These parameters lead to the MS position coordinates depending on the geometric relationships that connect the ToF and AoD with the MS position. Afterward, this section derives the FIM of the estimated channel's parameters and transforms it into the FIM of the estimated position. Then, the inverse operation of the position FIM results in the CRB that evaluates the accuracy of the localization process. Finally, extensive computer simulations were conducted to illustrate the performance of the localization process in the presence of the HWIs.[1]

3.1.1 System and Channel Models

In this section, the localization process is carried out in a mmwave MISO-OFDM wireless communication system consisting of a single BS and a single MS, as shown in Fig. 3.1. Specifically, it is a perfectly synchronous 2D system and the BS is located at the origin, without losing generality. Besides, the BS is equipped with a ULA of M elements, while the MS is as single-antenna entity. Moreover, the MS occupies the unknown position $\boldsymbol{p} = [p_x \; p_y]^{\mathrm{T}}$ and establishes communication with the BS only over a LoS mmwave path.

[1]This work was accepted in *IEEE Transactions on Vehicular Technology* as "The Effect of Hardware Impairments on the Error Bounds of Localization and Maximum Likelihood Estimation of mmwave MISO-OFDM Systems"

It should be noted here that two ideal conditions are assumed, with the aim of decoupling the degradation in the localization performance due to HWIs from other sources. The first assumption is that only the LoS link between BS and MS exists (i.e., no unknown NLoS links). This is a common assumption since the LoS path provides the most useful information for positioning and can be easily isolated based on the received power due to path orthogonality [30, 61]. However, the degradation due to the unknown NLoS paths will be considered in section 3.2.

Perfect synchronization is the second commonly used assumption. For example, in [20, 23, 71], the authors isolated the effects of HWIs by removing the possibility of localization performance deterioration due to synchronization errors. According to this assumption, the BS and the MS are perfectly synchronized to the same clock by performing a preliminary synchronization step through the uplink channel, e.g. using a two-way synchronization protocol [20, 91]. Since it is well recognized that, in practice, synchronization errors must be taken into account, we present the synchronization process jointly with the localization process in section 3.3.

By considering that the MS is located within the far field of the BS antenna arrays, we achieve the plane-wave assumption. Consequently, the LoS mmwave channel between the MS and the BS in this 2D setting is modelled according to the deterministic LoS channel model. Accordingly, the LoS channel between the MS and the BS can be presented as an $M \times 1$ sized complex channel vector, as it can be defined by

$$\boldsymbol{h}[n] = \gamma \boldsymbol{\alpha}(\theta) \exp\left(-j2\pi n \tfrac{\tau}{NT}\right), \tag{3.1}$$

where n is the subcarrier index, while N is the total number of subcarriers, and $T = 1/B$ is the sampling period with B denoting the bandwidth. Moreover, $\gamma = \rho e^{j\phi}$ with ρ and ϕ are the modulus and the phase of the complex amplitude γ, where ρ is given according to (2.13). Besides, $\boldsymbol{\alpha}(\theta)$ denotes the BS array steering vector as a function of the AoD, θ, and can be defined as

$$\boldsymbol{\alpha}(\theta) = \left[1,\ e^{j\frac{2\pi}{\lambda_c} d \sin\theta}, \cdots, e^{j(M-1)\frac{2\pi}{\lambda_c} d \sin\theta}\right]^{\mathrm{T}}, \tag{3.2}$$

where $\lambda_c = c/f_c$ denotes the wavelength, c and f_c are the speed of light and the carrier frequency, respectively, and $d = \lambda_c/2$ defines the ULA inter-element spacing.

Furthermore, as seen in Fig. 3.1, the AoD, θ, presents the orientation of the MS relative to the BS, and is thus given by

$$\theta = \mathrm{atan2}(p_y, p_x). \tag{3.3}$$

From the same figure, the propagation delay τ, which specifies a circle centered on the BS with radius $r = c\tau$ and where $r^2 = p_x^2 + p_y^2$, is given by

$$\tau = \frac{1}{c}\sqrt{p_x^2 + p_y^2}. \tag{3.4}$$

3.1.2 Signaling with HWIs

Here, we present the residual HWIs model and demonstrate how it is mathematically incorporated into the system mathematically. We present the impaired pilots and signals and illustrate their statistical distributions at both the transmitter and the receiver.

The transmitter is modeled by considering k simultaneously transmitted OFDM symbols for each n subcarrier, where these symbols are sequentially transmitted G times, and the g^{th} transmission has $\boldsymbol{z}^g[n] = \left[z_1^g[n], \cdots, z_k^g[n]\right]^{\mathrm{T}}$ with power $P = \mathbb{E}\{\|\boldsymbol{z}^g[n]\|^2\}$.

The BS performs the hybrid analog/digital beamforming to precode these symbols, then transforms them to the time-domain by utilizing an inverse fast Fourier transform (IFFT). Later, the symbols are combined with a cyclic prefix (CP) of length $T_c = DT$, where D is the length of CP in symbols. Next, the RF precoding is applied by using the hybrid beamforming matrix $\boldsymbol{F}^g[n] \in \mathbb{C}^{M \times k}$, which imposes a power constraint $\|\boldsymbol{F}^g[n]\|_{\mathrm{F}} = 1$.

Considering these as well as the HWIs at the BS, the transmitted signal over the n^{th} subcarrier at time g^{th} can be expressed as follows [11, 92]

$$\boldsymbol{s}^g[n] = \sqrt{\kappa_t}\boldsymbol{F}^g[n]\boldsymbol{z}^g[n] + \boldsymbol{\eta}_t^g[n], \tag{3.5}$$

where $\kappa_t \in (0,1]$ refers to the BS hardware quality factor while $\boldsymbol{\eta}_t^g[n] \in \mathbb{C}^{M \times 1}$ denotes the distortion noise at the transmitter that is independent of $\boldsymbol{z}^g[n]$, and that can be modeled as $CN(\boldsymbol{0}, \frac{P}{M}(1-\kappa_t)\mathbf{I}_M)$. This demonstrates that $\mathbb{E}\{\|\mathbf{s}^g[n]\|^2\} = P \ \forall n$. Note that $\kappa_t = 1$ in the case of ideal transmitter hardware, which yields $\boldsymbol{s}^g[n] = \boldsymbol{F}^g[n]\boldsymbol{z}^g[n]$.

On the other side, the receiver removes the CP and applies the fast Fourier transform (FFT) on the OFDM symbols to recover the original data bits. After that, the signal conveyed from the BS to the MS through the n^{th} subcarrier at time g^{th}, which is exposed to the HWIs at the receiver, can be written as follows [11]

$$y^g[n] = \sqrt{\kappa_r}\sqrt{\kappa_t}(\boldsymbol{h}[n])^{\mathrm{T}}\boldsymbol{F}^g[n]\boldsymbol{z}^g[n] + \sqrt{\kappa_r}(\boldsymbol{h}[n])^{\mathrm{T}}\boldsymbol{\eta}_t^g[n] + \eta_r^g[n] + w^g[n], \tag{3.6}$$

where $\kappa_r \in (0,1]$ is the receiver hardware quality factor while $\eta_r^g[n] \sim CN(0, PM\rho^2(1-\kappa_r))$ refers to the distortion noise at the receiver side, and $w^g[n] \sim CN(0,\sigma^2)$ denotes the additive white Gaussian noise (AWGN). Considering (3.6), it is clear that $y^g[n] \sim CN(\mu_y, \sigma_y^2)$, where

$$\mu_y^g = \sqrt{\kappa_t\kappa_r}(\boldsymbol{h}[n])^{\mathrm{T}}\boldsymbol{F}^g[n]\boldsymbol{z}^g[n], \tag{3.7}$$

and

$$\sigma_y^2 = PM\rho^2(1-\kappa_t\kappa_r) + \sigma^2. \tag{3.8}$$

Hence, the SNR is defined by

$$\text{SNR} = \frac{\kappa_t\kappa_r}{(1-\kappa_t\kappa_r) + \frac{\sigma^2}{PM\rho^2}}. \tag{3.9}$$

Assuming high OFDM signal power, i.e., $P >> 1$, an asymptotic SNR value can be obtained by using (5) as follows

$$\lim_{P\to\infty} \text{SNR} = \frac{\kappa_t \kappa_r}{(1-\kappa_t\kappa_r)}. \tag{3.10}$$

This expression proves that the SNR only depends on the transmitter and receiver hardware quality factors for the high power values of the OFDM signals. Furthermore, in the case of the ideal hardware assumption, i.e., $\kappa_t = \kappa_r = 1$, the SNR value approaches infinity.

3.1.3 Channel Parameters Estimation and Localization

Equations (3.3) and (3.4) indicate the relationships between the geometric position and the channel parameters. This illustrates that estimating the channel parameters leads to guessing the unknown position of the MS, $\boldsymbol{p}$. Here. we focus on estimating the channel parameter vector $\boldsymbol{\beta} = [\tau, \theta, \rho, \phi]^{\mathrm{T}}$ by using the ML estimator and considering $\boldsymbol{\beta}$, we can estimate τ and θ by taking the nuisance parameters ρ and ϕ into account.

Assuming that the transmitted symbols, the beamforming matrix, the AWGN variance and the HWIs coefficients are known to the receiver, while the other parameters are deterministic unknowns, the ML estimator of τ and θ is given by

$$(\hat{\tau}, \hat{\theta}) = \arg\max_{\tau,\theta} \left[\max_{\rho,\phi} L(\tau, \theta, \rho, \phi) \right], \tag{3.11}$$

where $L(\tau, \theta, \rho, \phi) = \log(f(\boldsymbol{Y}|\tau, \theta, \rho, \phi))$ represents the log-likelihood function of $\boldsymbol{Y}$, which is the set of all observations for given τ, θ, ρ and ϕ values, while $f(\cdot)$ is the PDF of $\boldsymbol{Y}$. Now, defining $K = M(1-\kappa_t\kappa_r)$, the log-likelihood function can be written as

$$L(\tau, \theta, \rho, \phi) = -\frac{NG}{2} \ln(2\pi(KP\rho^2 + \sigma^2)) - \frac{\sum_{g=1}^{G} ||\boldsymbol{y}^g - \sqrt{\kappa_t}\sqrt{\kappa_r}\rho e^{j\phi}\mathbf{w}^g||^2}{2(KP\rho^2 + \sigma^2)}, \tag{3.12}$$

where $\boldsymbol{y}^g = \left[y^g[0], \ldots, y^g[N-1]\right]^{\mathrm{T}}$ and $\mathbf{w}^g$ is defined by

$$\mathbf{w}^g = \begin{bmatrix} \boldsymbol{\alpha}(\theta)\boldsymbol{F}^g[0]\boldsymbol{z}^g[0] \\ \vdots \\ e^{-j2\pi[N-1]\frac{\tau}{NT}}\boldsymbol{\alpha}(\theta)\boldsymbol{F}^g[N-1]\boldsymbol{z}^g[N-1] \end{bmatrix}. \tag{3.13}$$

Noting that the sole parameters of interest are τ and θ, the ML estimation problem first requires finding the estimated values of ρ and ϕ, which maximize (3.12) according to (3.11). To this end, the estimation of ϕ, i.e., $\hat{\phi}$, is calculated from

$$\frac{\partial L(\tau, \theta, \rho, \phi)}{\partial \phi} = \frac{j\sqrt{\kappa_t\kappa_r}\rho e^{j\phi}\sum_{g=1}^{G}(\mathbf{w}^g)^{\mathrm{H}}(\mathbf{y}^g - \sqrt{\kappa_t\kappa_r}\rho e^{j\phi}\mathbf{w}^g)}{KP\rho^2 + \sigma^2}, \tag{3.14}$$

where $\partial L(\tau,\theta,\rho,\phi)/\partial\phi = 0$. Hereby, the estimated value of $e^{j\phi}$ is solved by

$$e^{j\hat{\phi}} = \frac{\sum_{g=1}^{G}(\mathbf{w}^g)^{\mathrm{H}}\mathbf{y}^g}{\sqrt{\kappa_t}\sqrt{\kappa_r}\rho\sum_{g=1}^{G}\|\mathbf{w}^g\|^2}. \tag{3.15}$$

Next, after substituting (3.15) into (3.12), the estimated value of ρ is calculated from

$$\frac{\partial L(\tau,\theta,\rho,\phi)}{\partial\rho} = -\frac{NGKP\rho}{KP\rho^2+\sigma^2} + \frac{KP\rho\sum_{g=1}^{G}||\mathbf{y}^g - \frac{\sum_{i=1}^{G}(\mathbf{w}^i)^{\mathrm{H}}\mathbf{y}^i}{\sum_{i=1}^{G}||\mathbf{w}^i||^2}\mathbf{w}^g||^2}{(KP\rho^2+\sigma^2)^2}, \tag{3.16}$$

where $\partial L(\tau,\theta,\rho,\phi)/\partial\rho = 0$, which leads to

$$\hat{\rho} = \sqrt{\frac{\sum_{g=1}^{G}||\mathbf{y}^g - \frac{\sum_{i=1}^{G}(\mathbf{w}^i)^{\mathrm{H}}\mathbf{y}^i}{\sum_{i=1}^{G}||\mathbf{w}^i||^2}\mathbf{w}^g||^2}{NGKP} - \frac{NG\sigma^2}{NGKP}}. \tag{3.17}$$

Now, utilizing (3.12), (3.15) and (3.17), the log-likelihood function of $\boldsymbol{Y}$ can be obtained as only depending on τ and θ values by

$$\hat{L}(\tau,\theta) = -\frac{NG}{2}\ln(2\pi(KP\hat{\rho}^2+\sigma^2)) - \frac{\sum_{g=1}^{G}||\mathbf{y}^g - \sqrt{\kappa_t}\sqrt{\kappa_r}\hat{\rho}e^{j\hat{\phi}}\mathbf{w}^g||^2}{2(KP\hat{\rho}^2+\sigma^2)}. \tag{3.18}$$

Unfortunately, (3.18) cannot be expressed in any projection matrix, and does not have a cLoSed-form solution, either. Thus, a numerical search algorithm can be utilized to solve $\hat{L}(\tau,\theta)$. Here, an estimation of the MS position can be made by solving (3.3) and (3.4) and replacing the actual values with the estimated ones. Consequently, the estimated position is given as: $\hat{\boldsymbol{p}} = c\hat{\tau}[\cos\hat{\theta}\ \sin\hat{\theta}]^{\mathrm{T}}$.

3.1.4 Fisher Information Matrices and Cramer-Rao lower bound.

In this subsection, we derive the FIM and the CRB for the position estimation problem of the mmwave MISO-OFDM systems in the presence of transceiver HWIs. In this context, by defining $\varphi^g[n] = \mu_y^g$ in (3.7) and $C_y = \sigma_y^2$ in (3.8), the elements of the symmetric FIM matrix, $\mathbf{J}_{\boldsymbol{\beta}} \in \mathbb{R}^{4\times4}$, are calculated according (2.20) that is:

$$[\mathbf{J}_{\boldsymbol{\beta}}]_{(i,j)} = 2\sum_{g=1}^{G}\sum_{n=0}^{N-1}\Re\left\{\left(\frac{\partial\varphi^g[n]}{\partial\beta_i}\right)^{\mathrm{H}}C_y^{-1}\left(\frac{\partial\varphi^g[n]}{\partial\beta_j}\right)\right\} + \mathrm{tr}\left[C_y^{-1}\frac{\partial C_y}{\partial\beta_i}C_y^{-1}\frac{\partial C_y}{\partial\beta_j}\right], \tag{3.19}$$

where β_i represents the i^{th} parameter of $\boldsymbol{\beta}$. In order to compute the elements of $\mathbf{J}_{\boldsymbol{\beta}}$, the following statements are defined:

$$\bar{\mathbf{F}} = \sqrt{\kappa_t}\sqrt{\kappa_r}\mathbf{F}^g[n]\boldsymbol{z}^g[n],$$
$$\mathbf{B} = \mathrm{diag}[0,1,\ldots,M-1] \in \mathbb{R}^{M\times M},$$

and then the required derivations in (3.19) are obtained as follows:

$$\begin{aligned}
\frac{\partial \varphi^g[n]}{\partial \tau} &= (\frac{-j2\pi n}{NT})\rho \exp(j(\phi - 2\pi n \frac{\tau}{NT}))\boldsymbol{\alpha}(\theta)^{\mathrm{T}}\bar{\mathbf{F}},\\
\frac{\partial \varphi^g[n]}{\partial \theta} &= j\frac{2\pi}{\lambda_c} d\cos\theta\rho \exp(j(\phi - 2\pi n \tfrac{\tau}{NT}))\boldsymbol{\alpha}(\theta)^{\mathrm{T}}\mathbf{B}\bar{\mathbf{F}},\\
\frac{\partial \varphi^g[n]}{\partial \rho} &= e^{j\phi}e^{-j2\pi n\frac{\tau}{NT}}\boldsymbol{\alpha}(\theta)^{\mathrm{T}}\bar{\mathbf{F}},\\
\frac{\partial \varphi^g[n]}{\partial \phi} &= j\rho e^{j\phi}e^{-j2\pi n\frac{\tau}{NT}}\boldsymbol{\alpha}(\theta)^{\mathrm{T}}\bar{\mathbf{F}}.
\end{aligned}$$

Additionally, the derivatives of the noise variance C_y with respect to the unknown channel parameters vector can be calculated as

$$\begin{aligned}
\frac{\partial C_y}{\partial \rho} &= 2PM\rho(1-\kappa_t\kappa_r),\\
\frac{\partial C_y}{\partial \tau} &= \frac{\partial C_y}{\partial \theta} = \frac{\partial C_y}{\partial \phi} = 0.
\end{aligned}$$

Then, the FIM can be obtained in the position domain by transforming the channel parameter vector $\boldsymbol{\beta}$ to the location parameters vector $\boldsymbol{\mu} = [p_x, p_y, \rho, \phi]^{\mathrm{T}}$. For this purpose, $\mathbf{J}_{\boldsymbol{\mu}} \in \mathbb{R}^{4\times 4}$, which is the FIM of $\boldsymbol{\mu}$, can be computed according to the following relationship

$$\mathbf{J}_{\boldsymbol{\mu}} = \mathbf{T}\mathbf{J}_{\boldsymbol{\beta}}\mathbf{T}^{\mathrm{T}}, \tag{3.20}$$

where $\mathbf{T}$ is the transformation matrix defined by

$$\mathbf{T} \overset{(\mathrm{def})}{=} \frac{\partial \boldsymbol{\beta}^{\mathrm{T}}}{\partial \boldsymbol{\mu}} = \begin{bmatrix} \frac{\partial \tau}{\partial p_x} & \frac{\partial \theta}{\partial p_x} & \frac{\partial \rho}{\partial p_x} & \frac{\partial \phi}{\partial p_x} \\ \frac{\partial \tau}{\partial p_y} & \frac{\partial \theta}{\partial p_y} & \frac{\partial \rho}{\partial p_y} & \frac{\partial \phi}{\partial p_y} \\ \frac{\partial \tau}{\partial \rho} & \frac{\partial \theta}{\partial \rho} & \frac{\partial \rho}{\partial \rho} & \frac{\partial \phi}{\partial \rho} \\ \frac{\partial \tau}{\partial \phi} & \frac{\partial \theta}{\partial \phi} & \frac{\partial \rho}{\partial \phi} & \frac{\partial \phi}{\partial \phi} \end{bmatrix}, \tag{3.21}$$

in which all the entries are equal to zero, except:

$$\begin{aligned}
&\frac{\partial \rho}{\partial \rho} = \frac{\partial \phi}{\partial \phi} = 1,\\
&\frac{\partial \tau}{\partial p_x} = \frac{p_x}{c\sqrt{p_x^2+p_y^2}}, \quad \frac{\partial \tau}{\partial p_y} = \frac{p_y}{c\sqrt{p_x^2+p_y^2}},\\
&\frac{\partial \theta}{\partial p_x} = \frac{-p_y/p_x^2}{1+(p_y/p_x)^2}, \quad \text{and} \quad \frac{\partial \theta}{\partial p_y} = \frac{1/p_x}{1+(p_y/p_x)^2}.
\end{aligned}$$

Here, the PEB can also be derived by utilizing the FIM $\mathbf{J}_{\boldsymbol{\mu}}$ given in (3.20) as

$$\mathrm{PEB} = \sqrt{[(\mathbf{J}_{\boldsymbol{\mu}})^{-1}]_{(1,1)} + [(\mathbf{J}_{\boldsymbol{\mu}})^{-1}]_{(2,2)}}. \tag{3.22}$$

The values of $\sqrt{\mathrm{CRB}(\cdot)}$ can be obtained in a similar way to the PEB values, i.e., by inverting the FIM $\mathbf{J}_{\boldsymbol{\beta}}$ in (16), using the corresponding diagonal entries and taking the square root [71].

3.1.5 Simulation Results

This subsection presents the computer simulation results obtained for the aforementioned position estimation process. We investigated the effects of transceiver HWIs on the accuracy of the localization in the mmwave MISO-OFDM system. For simplicity, it is assumed that the system is equipped with a BS operating at $f_c = 60$ GHz, with bandwidth $B = 40$ MHz and the number of simultaneously transmitted beams $K = 1$. Unless otherwise stated, it is also assumed that the BS transmits a known signal from $M = 10$ antennas by using $N = 20$ subcarriers at $G = 12$ transmission times with power P. Furthermore, without loss of generality, we assume that both the transmitter and receiver have the same distortion coefficient, κ, which can be practically measured from the EVM that is specified on the data sheets of the RF transceivers i.e., $\kappa = 1 - \text{EVM}^2$ [11]. The localization process is repeated for ten different locations distributed over no more than ten meters for $\theta \in [0°, 90°]$, wherein each location, the transmitted power P varies to ensure $\frac{P|\rho|^2}{\sigma^2}$ is the same for the ten locations.

First, RMSE is calculated to assess the performance of the ML estimator based on 1000 MC trials per position. Accordingly, Fig. 3.2 presents the RMSE values for the position estimation process using an ML estimator for different HWIs distortion values. This figure also presents the localization process when the channel is perfectly known i.e., when the first two parameters of the channel vector β, ρ and ϕ, are known. As the quality of the received signal increases, the estimation process accuracy increases, and the RMSE values asymptotically approach zero in the case of ideal hardware, i.e., $\kappa_t = \kappa_r = 1$. However, in the case of non-ideal hardware, the RMSE values saturate to a certain limit since the quality of the received signal is bounded by (3.10). Additionally, when the HWIs distortion level increases with decreasing values of $\kappa = \kappa_t = \kappa_r$, the

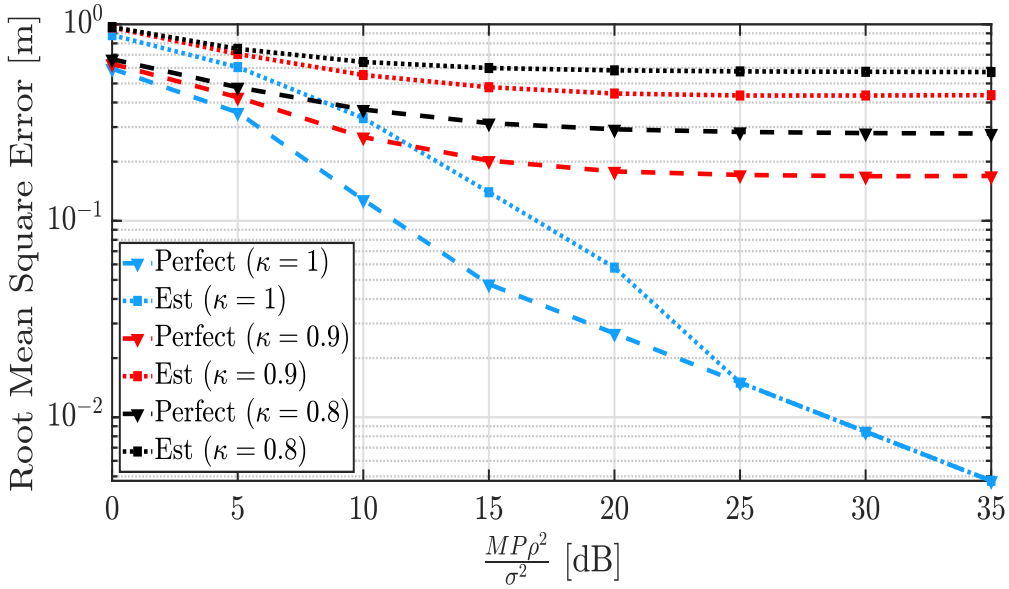

Figure 3.2: RMSE versus transmission power.

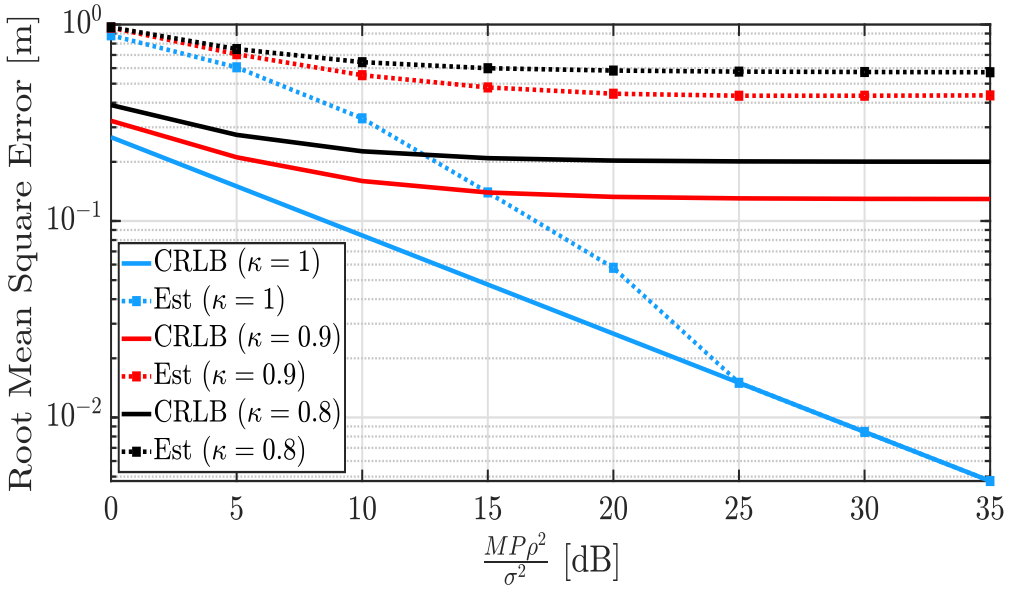

Figure 3.3: PEB/RMSE versus transmission power with different HWIs distortion levels.

amount of estimation error increases.

Fig. 3.3 presents the effect of transceiver HWIs on the position estimation accuracy, and this is done in terms of PEB with respect to the different $\frac{P\rho^2}{\sigma^2}$ values. It can be observed that with increasing transmission power (and thus $\frac{P\rho^2}{\sigma^2}$ values), we can approximate the estimation error to zero in the ideal case ($\kappa_t = \kappa_r = 1$), while the HWIs limits this decrease. This occurs because increasing the transmission power boosts both the non-noisy signal $\varphi^g[n]$ and the HWIs distortion term $PM\rho^2(1-\kappa_t\kappa_r)$, simultaneously. In the same context, RMSE achieves the PEB when $\frac{MP\rho^2}{\sigma^2} \geq 25$ dB, which we understand from (3.9), where the SNR is also greater than 25 dB. In the case of non-ideal hardware, from (3.10), the SNR saturates at 6.3 dB and 2.5 dB when $\kappa = 0.9$ and $\kappa = 0.8$, respectively, that are lower than the SNR that makes the RMSE achieving the PEB. Besides, the Fig. 3.3 shows that the estimation accuracy worsens as the effect of the HWIs increases depending on κ_t and κ_r.

Fig.3.4 depicts the effect of the number of BS antennas on the estimation accuracy when $\frac{P|\rho|^2}{\sigma^2} =$ 0 dB. It is clear that increasing the number of antennas enhances the accuracy of localization with ideal and non-ideal equipment since increasing M also increases the numerator of the SNR statement, $PM\rho^2\kappa_t\kappa_r$, more so than its denominator $PM\rho^2(1-\kappa_t\kappa_r)$, when $\kappa_t\kappa_r \geq 0.5$. However, it is difficult to enhance the localization accuracy in this way since the accelerating number of transmitter antennas increases the hardware complexity. Therefore, in the case of non-ideal transceivers, it is essential to consider the maximum number of antennas that leads to significant accuracy enhancement. For example, in the current simulation scenario, equipping the BS with more than 30 antennas only for localization accuracy enhancement purposes is not worth it. We can also note that localization accuracy decreases with the declining equipment quality.

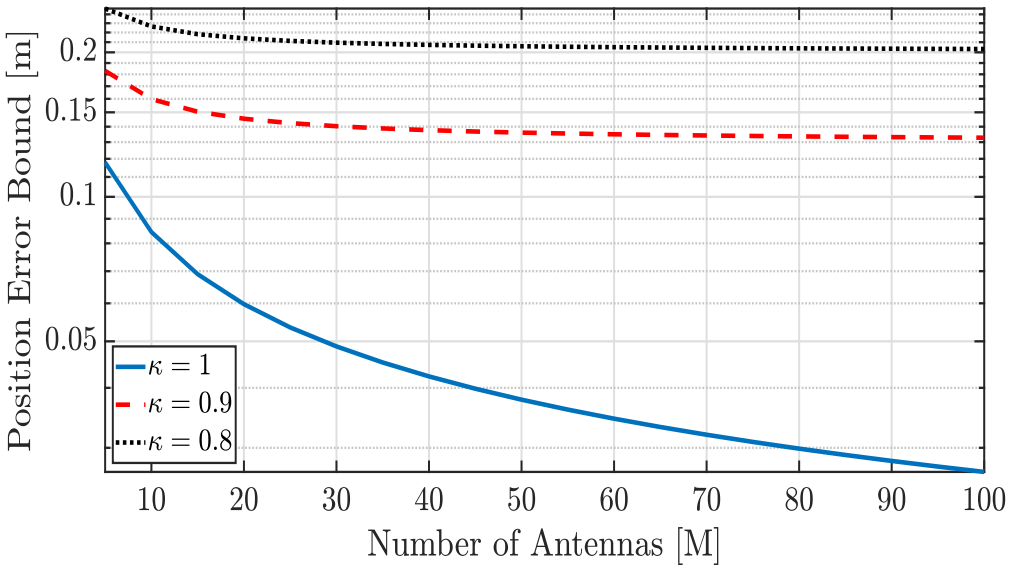

Figure 3.4: PEB versus the number of antennas at BS with different HWIs levels.

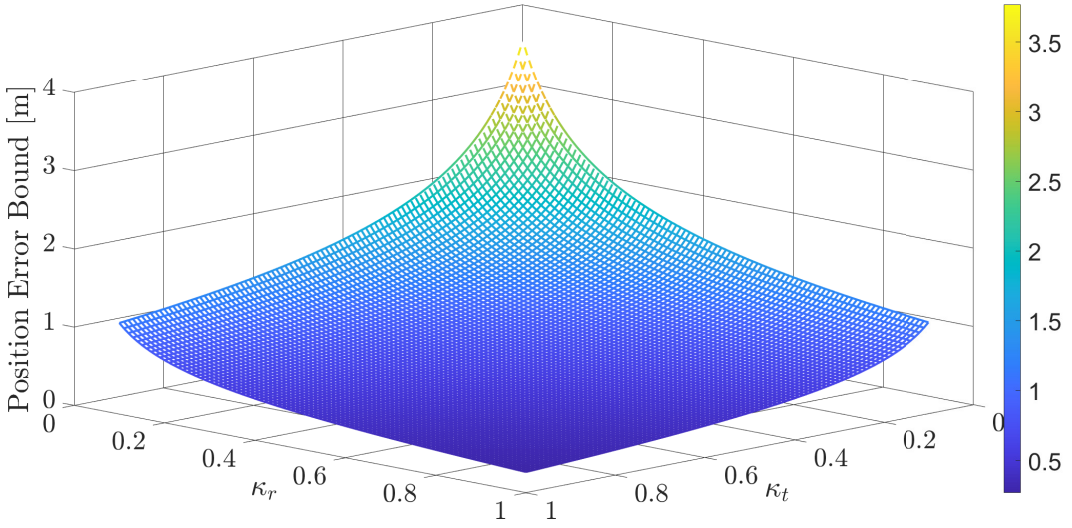

Figure 3.5: PEB versus the HWIs coefficient κ.

Finally, Fig. 3.5 illustrates the localization accuracy with respect to the HWIs coefficients κ_t and κ_r. This figure illustrates that each transceiver has a similar effect on the accuracy of the localization process, which can also be noted from (3.9).

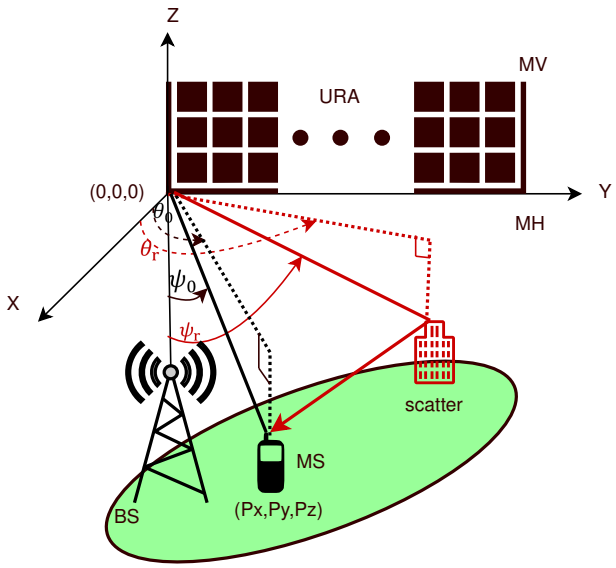

Figure 3.6: Geometry of the considered 3D mmwave MISO-OFDM scenario.

3.2 3D perfect synchronous mmwave MISO system in the existence of NLoS

This section investigates a more realistic and complex localization process than that in section 3.1. Specifically, the 3D localization accuracy of mmwave MISO-OFDM systems is investigated when there are HWIs at both the BS and the MS, and in the existence of NLoS paths from unknown scatterers. Regarding this, the 3D system model and the relevant mmwave channel are presented. Besides, the localization is performed by estimating the downlink channel parameters of the LoS path using the ML estimator at the MS side. Then, we transform these channel parameters into ones for localization. The FIM is employed to assess the accuracy of the estimation processes, considering the NLoS paths. After that, the limit of localization is calculated in terms of the PEB. Finally, Computer simulations are conducted to demonstrate the impacts of HWIs and the NLoS paths from unknown scatterers on the localization process. [2].

3.2.1 System and Channel Models

Consider an mmwave MISO-OFDM wireless communication system consisting of a single BS with M antennas and a single-antenna MS as shown in Fig.3.6. A 3D scenario with a URA, which has M_{H} horizontal antennas, M_{V} vertical antennas and $M = M_{\mathrm{H}} \times M_{\mathrm{V}}$ antennas in total, is addressed for the BS, which is assumed to be located at the origin [0, 0, 0]. The MS, on the other hand, is surrounded by R unknown scatters and is placed at an unknown position $\mathbf{p} = [p_x \; p_y \; p_z]^{\mathrm{T}}$.

[2]This work was accepted in IEEE Communications Letters as "Error Bounds for 3D Localization and Maximum Likelihood Estimation of mmwave MISO-OFDM Systems in the Presence of Hardware Impairments"

The azimuth and elevation angles between the BS and MS are represented by θ and ψ, respectively, where the subscript "0" refers to a direct link between the BS and MS and the subscript "r" refers to an r^{th} NLoS link between them. It is also assumed that the BS and MS are synchronized to the same clock offset through the use of a preliminary synchronization algorithm in the uplink channel. The destructive effects of HWIs are considered at both the BS and MS sides. The channel and the transceiver models are detailed as follows.

The complex channel vector of the i^{th} path between the BS and MS associated with the n^{th} subcarrier is given by

$$\mathbf{h}_i[n] = \gamma_i \alpha(\theta_i, \psi_i) \exp\left(-j2\pi n \tfrac{\tau_i}{NT}\right), \tag{3.23}$$

where $\mathbf{h}_i[n] \in \mathbb{C}^{M\times 1}$, τ_i is the propagation delay, and $T = 1/B$ is the sampling period, with B denoting the bandwidth that achieves the typical narrowband condition, i.e., the wavelength $\lambda_n = c/(\frac{n}{NT} + f_c) \approx \lambda_c = c/f_c \ \ \forall n \in \{1, 2, \cdots, N\}$, where N is the total number of subcarriers, and c and f_c are the speed of light and the carrier frequency, respectively. ρ_i and ϕ_i are, respectively, the modulus and phase of the complex amplitude $\gamma_i = \rho_i e^{j\phi_i}$. Finally, $\alpha(\theta_i, \psi_i)$ denotes the BS array steering vector associated with the i^{th} path and is a function of the azimuth and elevation AOD, θ_i and ψ_i, respectively, as

$$\alpha(\theta_i, \psi_i) = \left[e^{j\frac{2\pi}{\lambda_c}\mathbf{k}(\theta_i,\psi_i)^{\mathrm{T}}u_1}, \cdots, e^{j\frac{2\pi}{\lambda_c}\mathbf{k}(\theta_i,\psi_i)^{\mathrm{T}}u_M} \right]^{\mathrm{T}}. \tag{3.24}$$

Additionally, the wave vector $\mathbf{k}(\theta_i, \psi_i)$ is defined as follows

$$\mathbf{k}(\theta_i, \psi_i) = [\sin\psi_i \cos\theta_i,\ \sin\psi_i \sin\theta_i,\ \cos\psi_i]^{\mathrm{T}}. \tag{3.25}$$

In (3.24), $\mathbf{u}_m$ represents the location of the m^{th} antenna of the BS, which can be given by

$$\mathbf{u}_m = \left[0,\ \bmod(m-1, M_{\mathrm{H}}) \times d_{\mathrm{H}}\lambda_c,\ \left\lfloor \frac{m-1}{M_{\mathrm{H}}} \right\rfloor \times d_{\mathrm{V}}\lambda_c \right]^{\mathrm{T}}, \tag{3.26}$$

where $d_{\mathrm{H}}\lambda_c$ and $d_{\mathrm{V}}\lambda_c$ stand for the horizontal and vertical inter-element spacing, respectively.

3.2.2 Signaling with HWIs

Similar to section 3.1, it is assumed that the BS transmits G signals sequentially, while the g^{th} transmission has k simultaneously transmitted OFDM symbols, i.e., $\mathbf{z}^g[n] = \left[z_1^g[n], \cdots, z_k^g[n]\right]^{\mathrm{T}}$ for each subcarrier, a power value of $P = \mathbb{E}\{\|\mathbf{z}^g[n]\|^2\}$. The precoding process and the transmitter hybrid beamforming matrix $\mathbf{F}^g[n] \in \mathbb{C}^{M\times k} = \mathbf{F}_{\mathrm{RF}}\mathbf{F}_{\mathrm{BB}}^g[n]$ also are described section 3.1. Considering these and taking into account the HWIs at the BS, the transmitted signal over the n^{th} subcarrier at the g^{th} transmission instant can be written as

$$\mathbf{s}^g[n] = \sqrt{\kappa_t}\mathbf{F}^g[n]\mathbf{z}^g[n] + \eta_t^g[n], \tag{3.27}$$

where $\kappa_t \in (0,1]$ denotes the hardware quality factor for the BS and $\eta_t^g[n] \in \mathbb{C}^{M\times 1}$ represents the distortion noise at the transmitter that is independent of $\mathbf{z}^g[n]$, and follows $CN(\mathbf{0}, \frac{P}{M}(1-\kappa_t)\mathbf{I}_M)$. This guarantees equal power to all transmitted signals, i.e., $\mathbb{E}\{\|\mathbf{s}^g[n]\|^2\} = P\ \forall n$.

At the receiver side, the received signal of the n^{th} subcarrier at the g^{th} transmission time, which is under the effect of receiver HWIs, can be expressed as follows

$$y^g[n] = \sqrt{\kappa_r}\sqrt{\kappa_t}(\mathbf{h}_0[n])^{\mathrm{T}}\mathbf{F}^g[n]\mathbf{z}^g[n] + \sum_{i=1}^{R}\sqrt{\kappa_r}\sqrt{\kappa_t}(\mathbf{h}_i[n])^{\mathrm{T}}\mathbf{F}^g[n]\mathbf{z}^g[n] + \sqrt{\kappa_r}\sum_{i=0}^{R}(\mathbf{h}_i[n])^{\mathrm{T}}\eta_t^g[n] + \eta_r^g[n] + w^g[n], \tag{3.28}$$

where $\kappa_r \in (0,1]$ is the receiver hardware quality factor, $\eta_r^g[n] \sim CN\big(0, PM(1-\kappa_r)\sum_{i=0}^{R}\rho_i^2\big)$ represents the distortion noise at the receiver side and $w^g[n] \sim CN(0,\sigma^2)$ is the additive white Gaussian noise (AWGN).

3.2.3 Channel Parameters Estimation and Localization

The unknown position of the MS, $\mathbf{p}$, can be expressed by noting that τ_0 indicates a circle centered on the BS with radius $r = c\tau_0$ from MS according to $r^2 = p_x^2 + p_y^2 + p_z^2$, and the geometric relationships between the BS, scatterers and the MS, can be given by

$$\tau_0 = \frac{1}{c}\sqrt{p_x^2+p_y^2+p_z^2}, \quad \psi_0 = \sin^{-1}\frac{\sqrt{p_x^2+p_y^2}}{\sqrt{p_x^2+p_y^2+p_z^2}}, \quad \text{and} \quad \theta_0 = \operatorname{atan2}(p_y, p_x), \tag{3.29}$$

where $\operatorname{atan2}(\cdot,\cdot)$ defines the four-quadrant inverse tangent function. Hence, $\mathbf{p}$ can be predicted by using the estimation of the LoS channel parameters vector, β. Accordingly, by replacing the actual values with the estimated ones, i.e., $\hat{\mathbf{p}} = [\hat{r}\sin\hat{\psi}_0\cos\hat{\theta}_0,\ \hat{r}\sin\hat{\psi}_0\sin\hat{\theta}_0,\ -\hat{r}\cos\hat{\psi}_0]^{\mathrm{T}}$, and then solving (3.29), an estimation on the MS position can be made by taking also the parameters ρ_0 and ϕ_0 into account.

Noting that the LoS path, $\mathbf{h}_0$, provides the most useful information for positioning, and that it can be easily isolated based on the received power due to path orthogonality [61], the estimation is performed through the LoS path while neglecting the NLoS paths. Thus, the ML estimator considers the received signal in (3.28) as $y^g[n] \sim CN(\mu_y, \sigma_y^2)$ with $\mu_y = \sqrt{\kappa_t\kappa_r}(\mathbf{h}_0[n])^{\mathrm{T}}\mathbf{F}^g[n]\mathbf{z}^g[n]$ and $\sigma_y^2 = PM(1-\kappa_t\kappa_r)\rho_0^2 + \sigma^2$.

During the estimation process, all parameters are deterministic unknowns except the transmitted symbols, the beamforming matrix, and the AWGN variance that is estimated in the initial access in mmwave systems [35, 71, 93]. Moreover, the HWIs coefficients are calculated from the EVM, which is specified in the data sheets of RF components [11]. Considering that, the parameters τ_0, θ_0 and ψ_0 can be estimated by using the following ML estimation rule

$$(\hat{\tau_0}, \hat{\theta_0}, \hat{\psi_0}) = \underset{\tau_0,\theta_0,\psi_0}{\arg\max}\big[\max_{\rho_0,\phi_0} L(\tau_0,\theta_0,\psi_0,\rho_0,\phi_0)\big], \tag{3.30}$$

where $L(\tau_0,\theta_0,\psi_0,\rho_0,\phi_0)=\log(f(\mathbf{y}|\tau_0,\theta_0,\psi_0,\rho_0,\phi_0))$ represents the log-likelihood function of $\mathbf{y}$, which is the set of all observations for given τ_0, θ_0, ψ_0, ρ_0 and ϕ_0 values, while $f(\cdot)$ is the PDF of $\mathbf{y}$. After some simple manipulations, the log-likelihood function can be written as

$$L(\tau_0,\theta_0,\psi_0,\rho_0,\phi_0)=-\frac{NG}{2}\ln(2\pi(PM(1-\kappa_t\kappa_r)\rho_0^2+\sigma^2))-\frac{\sum_{g=1}^{G}||\mathbf{y}^g-\sqrt{\kappa_t}\sqrt{\kappa_r}\rho_0 e^{j\phi_0}\mathbf{w}^g||^2}{2(PM(1-\kappa_t\kappa_r)\rho_0^2+\sigma^2)}, \quad (3.31)$$

where $\mathbf{y}^g=\left[y^g[0],\ldots,y^g[N-1]\right]^{\mathrm{T}}$ as given in (3.28), and $\mathbf{w}^g$ is

$$\mathbf{w}^g=\begin{bmatrix}\alpha^{\mathrm{T}}(\theta_0,\psi_0)\mathbf{F}^g[0]\mathbf{z}^g[0]\\ \vdots \\ e^{-j2\pi[N-1]\frac{\tau_0}{NT}}\alpha^{\mathrm{T}}(\theta_0,\psi_0)\mathbf{F}^g[N-1]\mathbf{z}^g[N-1]\end{bmatrix}. \quad (3.32)$$

It is worth noting here that the estimated values of ϕ_0 and ρ_0, which maximize (3.31) according to (3.30), should be obtained first, since the sole parameters of interest are τ_0, θ_0 and ψ_0. Therefore, $\hat{\phi}_0$, is calculated from

$$\frac{\partial L(\tau_0,\theta_0,\psi_0,\rho_0,\phi_0)}{\partial\phi_0}=\frac{j\sqrt{\kappa_t\kappa_r}\rho_0 e^{j\phi_0}\sum_{g=1}^{G}(\mathbf{w}^g)^{\mathrm{H}}(\mathbf{y}^g-\sqrt{\kappa_t\kappa_r}\rho_0 e^{j\phi_0}\mathbf{w}^g)}{PM(1-\kappa_t\kappa_r)\rho_0^2+\sigma^2}=0. \quad (3.33)$$

Following that, the estimated value of $e^{j\phi_0}$ is obtained as

$$e^{j\hat{\phi}_0}=\frac{\sum_{g=1}^{G}(\mathbf{w}^g)^{\mathrm{H}}\mathbf{y}^g}{\sqrt{\kappa_t}\sqrt{\kappa_r}\rho_0\sum_{g=1}^{G}\|\mathbf{w}^g\|^2}. \quad (3.34)$$

Next, after substituting (3.34) into (3.31), the estimated value of ρ_0 is calculated from

$$\frac{\partial L(\tau_0,\theta_0,\psi_0,\rho_0)}{\partial\rho_0}=\frac{-NGPM(1-\kappa_t\kappa_r)\rho_0}{PM(1-\kappa_t\kappa_r)\rho_0^2+\sigma^2}+\frac{PM(1-\kappa_t\kappa_r)\rho_0\sum_{g=1}^{G}||\mathbf{y}^g-\frac{\sum_{i=1}^{G}(\mathbf{w}^i)^{\mathrm{H}}\mathbf{y}^i}{\sum_{i=1}^{G}||\mathbf{w}^i||^2}\mathbf{w}^g||^2}{(PM(1-\kappa_t\kappa_r)\rho_0^2+\sigma^2)^2}, \quad (3.35)$$

where $\partial L(\tau_0,\theta_0,\psi_0,\rho_0)/\partial\rho_0=0$, which leads to

$$\hat{\rho}_0=\sqrt{\frac{(\sum_{g=1}^{G}||\mathbf{y}^g-\frac{\sum_{i=1}^{G}(\mathbf{w}^i)^{\mathrm{H}}\mathbf{y}^i}{\sum_{i=1}^{G}||\mathbf{w}^i||^2}\mathbf{w}^g||^2)-NG\sigma^2}{NGPM(1-\kappa_t\kappa_r)}}. \quad (3.36)$$

Now, utilizing (3.31), (3.34) and (3.36), the log-likelihood function of $\mathbf{y}$ can be rewritten in terms of τ_0, θ_0 and ψ_0 as follows

$$\hat{L}(\tau_0,\theta_0,\psi_0)=-\frac{NG}{2}\ln(2\pi(PM(1-\kappa_t\kappa_r)\hat{\rho}_0^2+\sigma^2))-\frac{\sum_{g=1}^{G}||\mathbf{y}^g-\sqrt{\kappa_t}\sqrt{\kappa_r}\hat{\rho}_0 e^{j\hat{\phi}_0}\mathbf{w}^g||^2}{2(PM(1-\kappa_t\kappa_r)\hat{\rho}_0^2+\sigma^2)}. \quad (3.37)$$

Unfortunately, (3.37) cannot be defined in any projection matrix, and does not have a closed-form solution, either. Thus, it can be solved by using a numerical search algorithm. Moreover, (3.37) indicates that the estimation error depends on the value of $\sum_{i=1}^{R}(\frac{\rho_i}{\rho_0})^2$ in (3.39), since $\mathbf{y}^g$ involves both the LoS and the ignored NLoS parameters as seen from (3.28), while $\sqrt{\kappa_t}\sqrt{\kappa_r}\hat{\rho}_0 e^{j\hat{\phi}_0}\mathbf{w}^g$ in (3.37) only contains the LoS parameters.

3.2.4 Fisher Information Matrices and Cramer-Rao lower bound

Here, we derive the FIM for the position estimation problem in the 3D mmwave MISO-OFDM systems in the presence of transceiver HWIs, and the NLoS paths.

As was stated in the previous section, the first term in (3.28), which is the noiseless part of the received signal that conveys meaningful information, is defined as $\varphi^g[n] = \sqrt{\kappa_r \kappa_t}(\mathbf{h}_0[n])^{\mathrm{T}}\mathbf{F}^g[n]\mathbf{z}^g[n]$, while the other terms represent the noise in the received signal with a variance value of

$$C_y = PM(1-\kappa_t\kappa_r)(\rho_0^2 + \sum_{i=1}^{R}\rho_i^2) + PM\kappa_t\kappa_r\sum_{i=1}^{R}\rho_i^2 + \sigma^2. \tag{3.38}$$

Now, the SNR value can be defined by using (3.28) and (3.38). After some simple mathematical operations, we obtain

$$\mathrm{SNR} = \frac{\kappa_t\kappa_r}{(1-\kappa_t\kappa_r) + \sum_{i=1}^{R}(\frac{\rho_i}{\rho_0})^2 + \frac{\sigma^2}{PM\rho_0^2}}. \tag{3.39}$$

Assuming that the OFDM signals have high power or the transmitter is equipped with a high number of antennas, an asymptotic value of the SNR can also be calculated by utilizing (3.39) as follows

$$\lim_{P \text{ or } M\to\infty} \mathrm{SNR} = \frac{\kappa_t\kappa_r}{(1-\kappa_t\kappa_r) + \sum_{i=1}^{R}(\frac{\rho_i}{\rho_0})^2}. \tag{3.40}$$

This expression proves that the SNR depends on the transmitter and receiver hardware quality factors, κ_t and κ_r, as well as on the LoS to NLoS path gain ratio.

Following that, and according to [85], the elements of the symmetric FIM matrix ,$\mathbf{J}_\beta \in \mathbb{R}^{5\times5}$, of the LoS channel parameters vector $\beta = [\tau_0, \theta_0, \psi_0, \rho_0, \phi_0]^{\mathrm{T}}$ can be calculated from (2.20) or from (3.19). However, in order to compute the elements of $\mathbf{J}_\beta$, the following statements should be defined

$$\begin{aligned}
&\bar{\mathbf{F}} = \sqrt{\kappa_t}\sqrt{\kappa_r}\mathbf{F}^g[n]\mathbf{z}^g[n]\\
&\mathbf{B}_{\theta_0} = \mathrm{diag}[\frac{\partial \mathbf{k}(\theta_0,\psi_0)^{\mathrm{T}}}{\partial\theta_0}u_1, \ldots, \frac{\partial \mathbf{k}(\theta_0,\psi_0)^{\mathrm{T}}}{\partial\theta_0}u_M] \in \mathbb{R}^{M\times M},\\
&\mathbf{B}_{\psi_0} = \mathrm{diag}[\frac{\partial \mathbf{k}(\theta_0,\psi_0)^{\mathrm{T}}}{\partial\psi_0}u_1, \ldots, \frac{\partial \mathbf{k}(\theta_0,\psi_0)^{\mathrm{T}}}{\partial\psi_0}u_M] \in \mathbb{R}^{M\times M},\\
&\frac{\partial \mathbf{k}(\theta_0,\psi_0)}{\partial\theta_0} = [-\cos\psi_0\sin\theta_0, \cos\psi_0\cos\theta_0, 0]^{\mathrm{T}},\\
&\frac{\partial \mathbf{k}(\theta_0,\psi_0)}{\partial\psi_0} = [-\sin\psi_0\cos\theta_0, -\sin\psi_0\sin\theta_0, \cos\psi_0]^{\mathrm{T}}.
\end{aligned}$$

Then, the required derivations are as follows

$$\frac{\partial \varphi^g[n]}{\partial \tau_0} = \frac{-j2\pi n}{NT}\rho_0 \exp(j(\phi_0 - 2\pi n\frac{\tau_0}{NT}))\alpha(\theta_0,\psi_0)^{\mathrm{T}}\bar{\mathbf{F}},$$
$$\frac{\partial \varphi^g[n]}{\partial \theta_0} = j\frac{2\pi}{\lambda_c}\rho_0 \exp(j(\phi_0 - 2\pi n\frac{\tau_0}{NT}))\alpha(\theta_0,\psi_0)^{\mathrm{T}}\mathbf{B}_{\theta_0}\bar{\mathbf{F}},$$
$$\frac{\partial \varphi^g[n]}{\partial \psi_0} = j\frac{2\pi}{\lambda_c}\rho_0 \exp(j(\phi_0 - 2\pi n\frac{\tau_0}{NT}))\alpha(\theta_0,\psi_0)^{\mathrm{T}}\mathbf{B}_{\psi_0}\bar{\mathbf{F}},$$
$$\frac{\partial \varphi^g[n]}{\partial \rho_0} = e^{j\phi_0}e^{-j2\pi n\frac{\tau_0}{NT}}\alpha(\theta_0,\psi_0)^{\mathrm{T}}\bar{\mathbf{F}}.$$
$$\frac{\partial \varphi^g[n]}{\partial \phi_0} = j\rho_0 e^{j\phi_0}e^{-j2\pi n\frac{\tau_0}{NT}}\alpha(\theta_0,\psi_0)^{\mathrm{T}}\bar{\mathbf{F}},$$
$$\frac{\partial C_y}{\partial \rho_0} = 2PM\rho_0(1-\kappa_t\kappa_r), \frac{\partial C_y}{\partial \tau_0} = \frac{\partial C_y}{\partial \theta_0} = \frac{\partial C_y}{\partial \psi_0} = \frac{\partial C_y}{\partial \phi_0} = 0.$$

The FIM can be obtained in the position domain by transforming the LoS channel parameters vector β into the location parameters vector $\mu = [p_x, p_y, p_z, \rho_0, \phi_0]^T$. For this purpose, $\mathbf{J}_\mu \in \mathbb{R}^{5\times 5}$, which is the FIM of μ, can be computed according to the transformation formula (2.19), similar to (3.20) in section 3.1, where the transformation matrix $\mathbf{T}$ here is defined by

$$\mathbf{T} \overset{(\text{def})}{=} \frac{\partial \beta^{\mathrm{T}}}{\partial \mu} = \begin{bmatrix} \frac{\partial \tau_0}{\partial p_x} & \frac{\partial \theta_0}{\partial p_x} & \frac{\partial \psi_0}{\partial p_x} & \frac{\partial \rho_0}{\partial p_x} & \frac{\partial \phi_0}{\partial p_x} \\ \frac{\partial \tau_0}{\partial p_y} & \frac{\partial \theta_0}{\partial p_y} & \frac{\partial \psi_0}{\partial p_y} & \frac{\partial \rho_0}{\partial p_y} & \frac{\partial \phi_0}{\partial p_y} \\ \frac{\partial \tau_0}{\partial p_z} & \frac{\partial \theta_0}{\partial p_z} & \frac{\partial \psi_0}{\partial p_z} & \frac{\partial \rho_0}{\partial p_z} & \frac{\partial \phi_0}{\partial p_z} \\ \frac{\partial \tau_0}{\partial \rho_0} & \frac{\partial \theta_0}{\partial \rho_0} & \frac{\partial \psi_0}{\partial \rho_0} & \frac{\partial \rho_0}{\partial \rho_0} & \frac{\partial \phi_0}{\partial \rho_0} \\ \frac{\partial \tau_0}{\partial \phi_0} & \frac{\partial \theta_0}{\partial \phi_0} & \frac{\partial \psi_0}{\partial \phi_0} & \frac{\partial \rho_0}{\partial \phi_0} & \frac{\partial \phi_0}{\partial \phi_0} \end{bmatrix}, \tag{3.41}$$

in which, based on (3.29), all the entries are equal to zero, except:

$$\frac{\partial \rho_0}{\partial \rho_0} = \frac{\partial \phi_0}{\partial \phi_0} = 1,$$
$$\frac{\partial \tau_0}{\partial p_x} = \frac{p_x}{c\sqrt{p_x^2+p_y^2+p_z^2}}, \quad \frac{\partial \tau_0}{\partial p_y} = \frac{p_y}{c\sqrt{p_x^2+p_y^2+p_z^2}}, \quad \frac{\partial \tau_0}{\partial p_z} = \frac{p_z}{c\sqrt{p_x^2+p_y^2+p_z^2}},$$
$$\frac{\partial \theta_0}{\partial p_x} = \frac{-p_y/p_x^2}{1+(p_y/p_x)^2}, \quad \frac{\partial \theta_0}{\partial p_y} = \frac{1/p_x}{1+(p_y/p_x)^2},$$
$$\frac{\partial \psi_0}{\partial p_x} = \frac{p_x p_z}{(p_x^2+p_y^2+p_z^2)\sqrt{p_x^2+p_y^2}}, \quad \frac{\partial \psi_0}{\partial p_y} = \frac{p_y p_z}{(p_x^2+p_y^2+p_z^2)\sqrt{p_x^2+p_y^2}}, \quad \frac{\partial \psi_0}{\partial p_z} = \frac{-\sqrt{p_x^2+p_y^2}}{p_x^2+p_y^2+p_z^2}.$$

Here, the PEB can be derived by:

$$\text{PEB} = \sqrt{[(\mathbf{J}_\mu)^{-1}]_{(1,1)} + [(\mathbf{J}_\mu)^{-1}]_{(2,2)} + [(\mathbf{J}_\mu)^{-1}]_{(3,3)}}. \tag{3.42}$$

3.2.5 Simulation Results

In this section, the PEB results are provided for *mm*wave MISO-OFDM systems under the effect of transceiver HWIs and the NLoS from unknown scatterers. We consider a scenario where the

system is equipped by a BS operating at $f_c = 60$ GHz with a bandwidth value of $B = 40$ MHz and $N = 20$ sub-carriers, where $\lambda_1 = \lambda_2 = \cdots \lambda_{20} \approx 5$ mm, i.e., typical narrowband conditions. For simplicity, only one beam is conveyed at each transmission time. It is also assumed that the BS transmits a known signal from $M = 25$ URA antennas $G = 12$ transmission times with power P, unless otherwise stated. Moreover, the antenna array elements are arranged in a square for $M_H = M_V = \sqrt{M}$, spaced by length $d_{\mathrm{H}} = d_{\mathrm{V}} = \frac{\lambda_c}{2}$. The single antenna MS is surrounded by R local scatters.

The localization process is repeated for 10 different locations by varying the transmitted power P to ensure that $\frac{P\rho_0^2}{\sigma^2}$ is the same at each position. Lastly, the severity of the HWIs is represented by $\kappa = \kappa_t = \kappa_r$, which are measured from the EVM that is specified in the data sheets of RF transceivers, where $\kappa = 1 - \mathrm{EVM}^2$ [11].

In Fig. 3.7, the effect of transceiver HWIs on the position estimation accuracy is presented in terms of PEB with respect to the different values of $\frac{P\rho_0^2}{\sigma^2}$. Here, a single LoS link exists between the BS and MS. It is observed that the estimation error tends to zero in the ideal case ($\kappa_t = \kappa_r = 1$) when we increase the transmission power. On the other hand, the HWIs inhibit the enhancing effect that increased transmission power has on the accuracy of localization. The reason for this is that increasing the transmission power boosts both the non-noisy signal $\varphi^g[n]$ and the HWIs distortion term $PM(1-\kappa_t\kappa_r)(\rho_0^2 + \sum_{i=1}^{R}\rho_i^2)$ in (3.38), simultaneously. Besides, Fig. 3.7 shows that the increasing severity of the HWIs results in a low estimation accuracy.

Furthermore, Fig. 3.7 compares the case where only the LoS path exists with the case where both LoS and the NLoS paths exist. In the second case, the ratio between the gain of the LoS path to the sum of the gains of the NLoS paths "LoS-to-multipath ratio" (LMR) is ${\rho_0}^2/\sum_{i=1}^{R}\rho_i^2$. It can

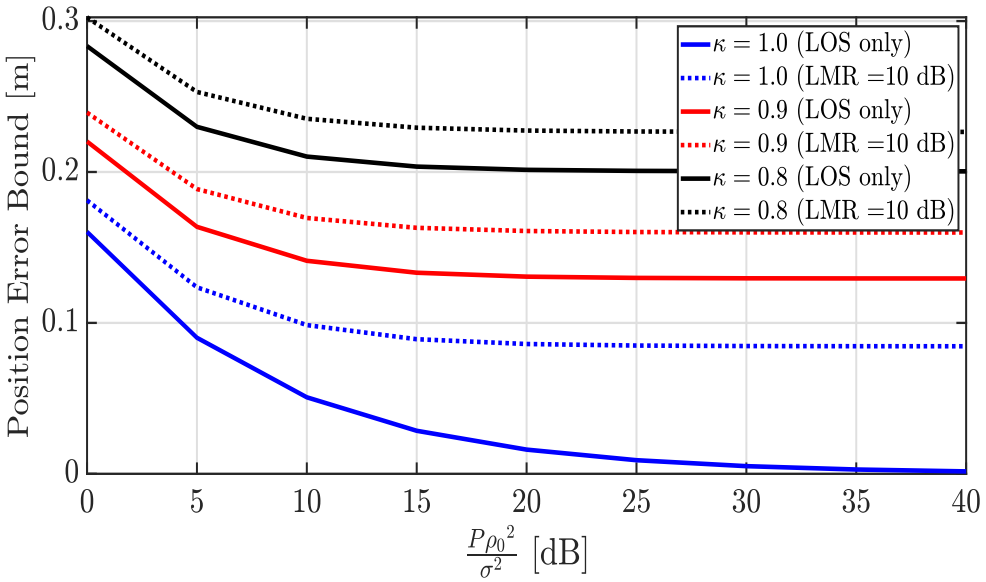

Figure 3.7: PEB versus transmission power with different HWIs distortion levels.

be seen clearly from this figure that the reflected links from unknown scatters have a harmful effect on the PEB value. Furthermore, increasing the power, by increasing $\frac{P\rho_0^2}{\sigma^2}$, increases the NLoS distortion term $PM\kappa_t\kappa_r\sum_{i=1}^{R}\rho_i^2$ even when $\kappa_t = \kappa_r = 1$.

Next, the performance of the ML estimator is investigated in Fig. 3.8 in terms of the RMSE. This is based on 1000 MC trials for each position at varying HWIs distortion levels, where RMSE is the metric of the remoteness between the predicted values from the real. This figure is clearly consistent with Fig. 3.7, in which the estimation process accuracy enhances as the quality of the received signal increases. For instance, in the case of perfect hardware, the RMSE values asymptotically approximate to zero, while the RMSE values saturate to a certain limit in the case of non-ideal hardware since the quality of the received signal is bounded by (3.40). Additionally, when the HWIs distortion level increases with decreasing values of κ, the amount of estimation error rises.

Lastly, Fig.3.9 depicts the effect of the NLoS path strength on the estimation accuracy when $\frac{P\rho_0^2}{\sigma^2} = 10$ dB. Evidently, the greater the LoS gain, the more accurate the localization process will be regardless of the state of the equipment, since increasing the ratio of $\rho_0^2/\sum_{i=1}^{R}\rho_i^2$ enhances the quality of the received pilot as seen in (3.39). Moreover, it is clear that when this ratio increases, the PEB value saturates to the PEB value of the LoS-only case seen in Fig. 3.7.

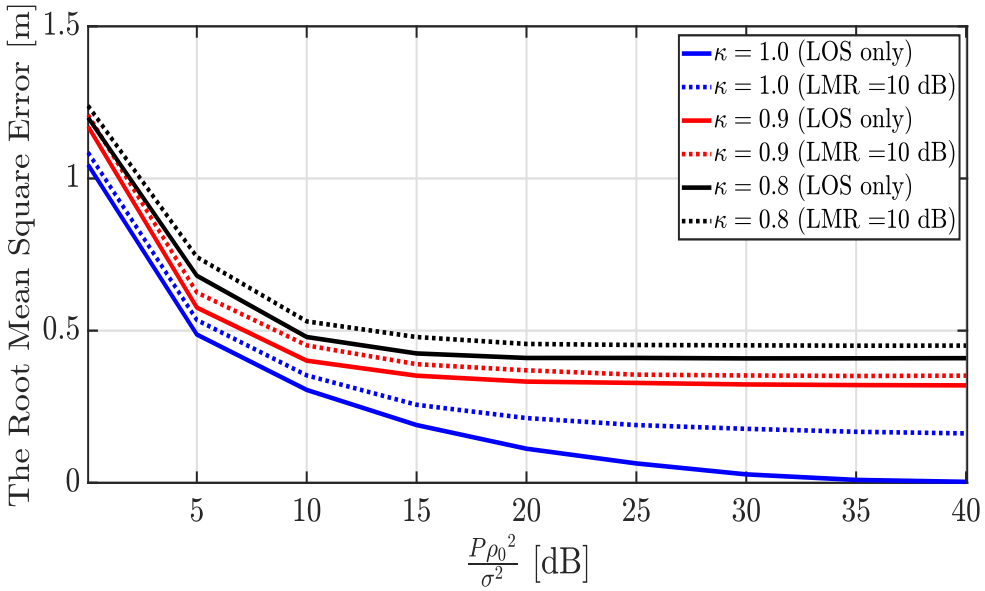

Figure 3.8: RMSE versus transmission power with different HWIs distortion levels.

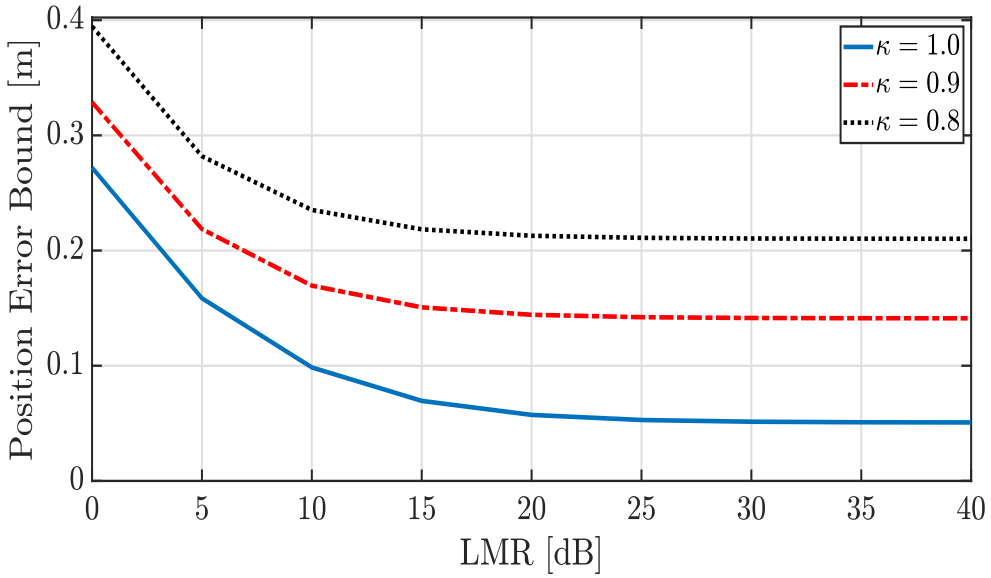

Figure 3.9: PEB versus LMR with different HWIs distortion levels.

3.3 Joint Localization-Synchronization Process in RIS-aided *mm*wave MISO system

This section investigates the joint localization-synchronization process in RIS-aided *mm*wave MISO-OFDM system. In particular, we target realistic circumstances where the theoretical assumptions of a perfect synchronous system and ideal transceivers no longer exist. We take a close look at the MISO-*mm*wave system implementing OFDM, with the existence of the RIS. Since the positions of the RIS and BS are known, the single antenna MS can estimate its position, and jointly synchronize itself with the reference BS. This can be accomplished using the ML estimator, whose cost function is derived considering the transceivers' HWIs. Next, we present the theoretical bounds of the joint localization-synchronization process in the CRB term. Lastly, we conduct computer simulations to demonstrate the impact of the HWIs on the joint localization-synchronization process accuracy.

3.3.1 System and Channel Models

This subsection describes the 3D RIS-aided *mm*wave MISO-OFDM system and the *mm*wave channel, where the joint localization-synchronization process is executed. Since this work focuses on the HWIs in the RIS-aided *mm*wave MISO-OFDM system, while performing the joint localization-synchronization process, we are restricted with the same system and the channel model assumed in the literature as in [35, 36] when the HWIs weren't considered or in[94] when considering the HWIs. Consider a single antenna MS, in an arbitrary time sample, occupying an unknown 3D position in the RIS-aided *mm*wave MISO-OFDM wireless communication sys-

tem, as Fig.3.10 illustrates. The MS receives directly from the BS equipped with M_{B} uniform rectangular arrays (URA), which have $M_{\mathrm{B}}^{\mathrm{H}}$ horizontal antennas, $M_{\mathrm{B}}^{\mathrm{V}}$ vertical antennas and thus $M_{\mathrm{B}} = M_{\mathrm{B}}^{\mathrm{H}} \times M_{\mathrm{B}}^{\mathrm{V}}$ antennas in total. Simultaneously, the MS has an indirect link with the BS through an RIS equipped with M_{R} URA elements, which similarly has $M_{\mathrm{R}}^{\mathrm{H}}$ horizontal elements, $M_{\mathrm{R}}^{\mathrm{V}}$ vertical elements and thus $M_{\mathrm{R}} = M_{\mathrm{R}}^{\mathrm{H}} \times M_{\mathrm{R}}^{\mathrm{V}}$ elements in total. Moreover, the system operates at f_c carrier frequency with bandwidth B that achieves the typical narrow-band condition, i.e., $\lambda_n = c/(\frac{n}{NT} + f_c) \approx \lambda_c = c/f_c$ for $\forall n \in \{1,2,\cdots,N\}$, where n is the sub-carrier index, N is the sub-carriers number, and $T = 1/B$ is the sampling period, while λ_c denotes the wavelength, and c is the speed of light.

The complex channel vector of the direct link of the n^{th} sub-carrier, $\mathbf{h}_0[n] \in \mathbb{C}^{M_{\mathrm{B}} \times 1}$, can be defined as

$$\mathbf{h}_0[n] = \gamma_0 \alpha(\theta_0, \psi_0, M_{\mathrm{B}}) \exp\left(-j2\pi n \tfrac{\tau_0}{NT}\right), \tag{3.43}$$

where the subscript “0" refers to the direct link between the MS and the BS, τ_0 is the signal propagation delay over the LoS link from the BS to the MS, which includes the clocks offset Δ, and $\gamma_0 = \rho_0 e^{j\phi_0}$ with ρ_0 and ϕ_0 are the magnitude and the phase of γ_0.

Following that, $\alpha(\theta_0, \psi_0, M_{\mathrm{B}}) \in \mathbb{C}^{M_{\mathrm{B}} \times 1}$ denotes the BS array steering vector associated with the LoS path. Generally, the steering vector α is a function of the number of antennas, the azimuth AoD, and the elevation AoD, M, θ, and ψ, respectively, where α is given by

$$\alpha(\theta, \psi, M) \in \mathbb{C}^{M \times 1} = \left[e^{j\frac{2\pi}{\lambda_c}\mathbf{k}(\theta,\psi)^{\mathrm{T}} u_1}, \cdots, e^{j\frac{2\pi}{\lambda_c}\mathbf{k}(\theta,\psi)^{\mathrm{T}} u_M}\right]^{\mathrm{T}}, \tag{3.44}$$

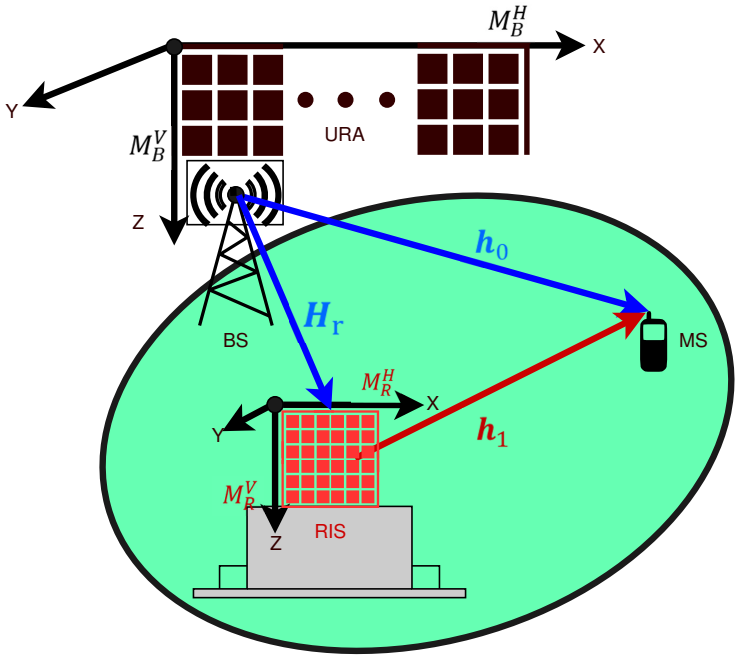

Figure 3.10: The RIS-aided mmwave MISO-OFDM system.

with $\mathbf{k}(\theta,\psi)$ as the wave vector and defined as

$$\mathbf{k}(\theta,\psi)=[\sin\psi\cos\theta,\ \sin\psi\sin\theta,\ \cos\psi]^{\mathrm{T}}, \tag{3.45}$$

$\mathbf{u}_m$ is the location vector of the m^{th} antenna of the M URA, which can be given by

$$\mathbf{u}_m=\left[\bmod(m-1,M^{\mathrm{H}})\times d_{\mathrm{H}}\lambda_c, 0, \left\lfloor\frac{m-1}{M^{\mathrm{H}}}\right\rfloor\times d_{\mathrm{V}}\lambda_c\right]^{\mathrm{T}}, \tag{3.46}$$

where $d_{\mathrm{H}}\lambda_c$ and $d_{\mathrm{V}}\lambda_c$ stand for the horizontal and vertical inter-element spacing, respectively.

Next, as shown in Fig.3.10, the RIS creates an NLoS path between the BS and MS, in which the incident signal on the RIS from the transmitter over $\mathbf{H}_{\mathrm{r}}[n]\in\mathbb{C}^{M_{\mathrm{B}}\times M_{\mathrm{R}}}$ link is beamed to the MS over $\mathbf{h}_1[n]\in\mathbb{C}^{M_{\mathrm{R}}\times 1}$ path. Here, the BS-RIS path over the n^{th} sub-carrier is

$$\mathbf{H}_{\mathrm{r}}[n]=\gamma_{\mathrm{r}}\alpha(\theta_{\mathrm{r}},\psi_{\mathrm{r}},M_{\mathrm{B}})(\alpha(\bar{\theta}_{\mathrm{r}},\bar{\psi}_{\mathrm{r}},M_{\mathrm{R}}))^{\mathrm{T}}\mathrm{e}^{\left(-j2\pi n\frac{\tau_{\mathrm{r}}}{NT}\right)}, \tag{3.47}$$

where the subscript "r" refers to the link between the BS and the RIS, $\gamma_{\mathrm{r}}=\rho_{\mathrm{r}}e^{j\phi_{\mathrm{r}}}$ is the complex amplitude of the BS-RIS link, and τ_{r} is the propagation time for the same link. By defining θ_{r} and ψ_{r} as the AoD from the BS, while $\bar{\theta}_{\mathrm{r}}$ and $\bar{\psi}_{\mathrm{r}}$ as AoA to the RIS, the steering vectors $\alpha(\theta_{\mathrm{r}},\psi_{\mathrm{r}},M_{\mathrm{B}})\in\mathbb{C}^{M_{\mathrm{B}}\times 1}$ and $\alpha(\bar{\theta}_{\mathrm{r}},\bar{\psi}_{\mathrm{r}},M_{\mathrm{R}})\in\mathbb{C}^{M_{\mathrm{R}}\times 1}$ are given according to (3.44), while the wave vectors $\mathbf{k}(\theta_{\mathrm{r}},\psi_{\mathrm{r}})$ and $\mathbf{k}(\bar{\theta}_{\mathrm{r}},\bar{\psi}_{\mathrm{r}})$ are defined according to (3.45), where the RIS's elements interspace is d_{r}.

Coming to the RIS-MS link associated with the n^{th} sub-carrier, $\mathbf{h}_1[n]\in\mathbb{C}^{M_{\mathrm{R}}\times 1}$, it can be given as

$$\mathbf{h}_1[n]=\gamma_1\alpha(\theta_1,\psi_1,M_{\mathrm{R}})\exp\left(-j2\pi n\frac{\tau_1}{NT}\right), \tag{3.48}$$

where the subscript "1" refers to the link between them RIS and MS, τ_1 is the RIS-MS link propagation delay including Δ, $\gamma_1=\rho_1e^{j\phi_1}$ is the complex gain over the RIS-MS link, and $\alpha(\theta_1,\psi_1,M_{\mathrm{R}})\in\mathbb{C}^{M_{\mathrm{R}}\times 1}$ is the array steering vector.

Accordingly, the BS-MS NLoS link through the RIS, $\mathbf{h}^g_{\mathrm{NLOS}}[n]\in\mathbb{C}^{M_{\mathrm{B}}\times 1}$, is given by

$$\mathbf{h}^g_{\mathrm{NLOS}}[n]=\mathbf{H}_{\mathrm{r}}[n]\Omega^g\mathbf{h}_1[n], \tag{3.49}$$

where Ω^g is the phase control matrix of the RIS at transmission g, which is a diagonal matrix with unit-modulus entries, i.e., $\Omega^g=\mathrm{diag}([\mathrm{e}^{j\omega^g_1},\ldots,\mathrm{e}^{j\omega^g_{M_{\mathrm{R}}}}])$, for $\Omega^g\in\mathbb{C}^{M_{\mathrm{R}}\times M_{\mathrm{R}}}$.

Consequently, the BS-MS channel including the LoS and the NLoS paths considering the n^{th} sub-carrier and the g^{th} transmission is

$$\mathbf{h}^g[n]\in\mathbb{C}^{M_{\mathrm{B}}\times 1}=\mathbf{h}_0[n]+\mathbf{H}_{\mathrm{r}}[n]\Omega^g\mathbf{h}_1[n]. \tag{3.50}$$

3.3.2 Signaling with HWIs

Considering the residual HWIs at the transceivers in the BS and the MS, we model both the impaired transmitter and the impaired receiver in this subsection. Seeking to perform the joint localization-synchronization process of MS, the BS broadcasts a well-known sequence as K OFDM symbols with power P utilizing N orthogonal sub-carriers, G sequenced times as in 3.1 and 3.2 sections. Accordingly, the BS that suffers from HWIs broadcasts in the g^{th} transmission through the n^{th} sub-carrier the following signal

$$\mathbf{s}^g[n] = \sqrt{\kappa_t}\mathbf{F}^g[n]\mathbf{z}^g[n] + \eta_t^g[n], \tag{3.51}$$

where $\kappa_t \in (0,1]$ is the transmitter hardware quality factor coefficient, and $\eta_t^g[n] \in \mathbb{C}^{M_{\text{B}}\times 1}$ is the transmitter distortion term that is independent of $\mathbf{z}^g[n]$. The covariance matrix is denoted by $\Upsilon[n] = \mathbb{E}\{(\mathbf{F}^g[n]\mathbf{z}^g[n])(\mathbf{F}^g[n]\mathbf{z}^g[n])^{\text{H}}\}$, where the average power $P = \text{tr}(\Upsilon[n])$. Referring to the HWIs model, the distortion noise is given as $\eta_t^g[n] \sim CN(\mathbf{0}, \Lambda[n])$, where $\Lambda[n] = (1-\kappa_t)\text{diag}(\Upsilon_{11}[n], \cdots, \Upsilon_{M_{\text{B}}M_{\text{B}}}[n])$, and $\text{tr}(\Lambda[n]) = P(1-\kappa_t)\ \forall n$. Accordingly,

$$\mathbb{E}\{(\mathbf{s}^g[n])^{\text{H}}(\mathbf{s}^g[n])\} = \kappa_t P + (1-\kappa_t)P = P\ \forall n.$$

Following, the received signal through the LoS link over the n^{th} subcarrier at the g^{th} transmission time is

$$r_{\text{LOS}}^g[n] = \sqrt{\kappa_t}(\mathbf{h}_0[n])^{\text{T}}\mathbf{F}^g[n]\mathbf{z}^g[n] + (\mathbf{h}_0[n])^{\text{T}}\eta_t^g[n], \tag{3.52}$$

whereas the received copy through the NLoS link over the n^{th} subcarrier at the g^{th} transmission time is given by

$$r_{\text{NLOS}}^g[n] = \sqrt{\kappa_t}(\mathbf{h}_1[n])^{\text{T}}\Omega^g(\mathbf{H}_{\text{r}}[n])^{\text{T}}\mathbf{F}^g[n]\mathbf{z}^g[n] + (\mathbf{h}_1[n])^{\text{T}}\Omega^g(\mathbf{H}_{\text{r}}[n])^{\text{T}}\eta_t^g[n]. \tag{3.53}$$

The output of the imperfect transceiver of the MS is given according to the model in (2.1). Therefore, the MS's distorted signal by the HWIs and the additive white Gaussian noise (AWGN), $w^g[n] \sim CN(0,\sigma^2)$, can be expressed as:

$$\begin{aligned} y^g[n] = {} & \sqrt{\kappa_t\kappa_r}(\mathbf{h}_0[n])^{\text{T}}\mathbf{F}^g[n]\mathbf{z}^g[n] + \sqrt{\kappa_t\kappa_r}(\mathbf{h}_1[n])^{\text{T}}\Omega^g(\mathbf{H}_{\text{r}}[n])^{\text{T}}\mathbf{F}^g[n]\mathbf{z}^g[n] \\ & + \sqrt{\kappa_r}(\mathbf{h}_1[n])^{\text{T}}\Omega^g(\mathbf{H}_{\text{r}}[n])^{\text{T}}\eta_t^g[n] + \sqrt{\kappa_r}(\mathbf{h}_0[n])^{\text{T}}\eta_t^g[n] + \eta_r^g[n] + w^g[n], \end{aligned} \tag{3.54}$$

where $\kappa_r \in (0,1]$ presents the quality factor of the receiver hardware, and $\eta_r^g[n] \sim CN(0, C_{\eta_r})$ represents the receiver HWIs distortion. Here, $C_{\eta_r} = P_{\text{r}}(1-\kappa_r)$ presents the power of the receiver noise attributed to HWIs, and P_{r} is the input power to the MS, which equals

$$P_{\text{r}} = P_{\text{LOS}} + P_{\text{NLOS}} = PM_{\text{B}}(\rho_0^2 + M_{\text{R}}^2\rho_{\text{r}}^2\rho_1^2). \tag{3.55}$$

Specifically, $P_{\text{LOS}} = PM_{\text{B}}\rho_0^2$ is the power reaching the receiver over the LoS path, while $P_{\text{NLOS}} = PM_{\text{B}}M_{\text{R}}^2\rho_{\text{r}}^2\rho_1^2$ is the part of power passing to the receiver through the NLoS path. Besides, the BS

causes $C_{\eta_t} = P\kappa_r(1-\kappa_t)M_{\mathrm{B}}(\rho_0^2 + M_{\mathrm{R}}^2\rho_{\mathrm{r}}^2\rho_1^2)$ distortion power at the MS side, and thus the distortion power accumulative at the receiver based on (3.54) is given by

$$\begin{aligned} C_y &= C_{\eta_t} + C_{\eta_r} + \sigma^2 \\ &= P(1-\kappa_t\kappa_r)M_{\mathrm{B}}(\rho_0^2 + M_{\mathrm{R}}^2\rho_{\mathrm{r}}^2\rho_1^2) + \sigma^2. \end{aligned} \tag{3.56}$$

Here, it is clear that C_y in (3.56) represents the power of the noisy signals in (3.54), while the noiseless part of (3.54) is

$$\varphi^g[n] = \sqrt{\kappa_t\kappa_r} \times \left[(\mathbf{h}_0[n])^{\mathrm{T}} + (\mathbf{h}_1[n])^{\mathrm{T}}\Omega^g(\mathbf{H}_{\mathrm{r}}[n])^{\mathrm{T}}\right]\mathbf{F}^g[n]\mathbf{z}^g[n]. \tag{3.57}$$

Accordingly, the SNR of the signal in (3.54) is

$$\mathrm{SNR} = \frac{\kappa_t\kappa_r M_{\mathrm{B}}(\rho_0^2 + M_{\mathrm{R}}^2\rho_{\mathrm{r}}^2\rho_1^2)}{(1-\kappa_t\kappa_r)M_{\mathrm{B}}(\rho_0^2 + M_{\mathrm{R}}^2\rho_{\mathrm{r}}^2\rho_1^2) + (\sigma^2/P)}, \tag{3.58}$$

and its asymptotic value when $P \to \infty$, i.e. the OFDM symbols power is high enough, is

$$\lim_{P\to\infty} \mathrm{SNR} = \frac{\kappa_t\kappa_r}{1-\kappa_t\kappa_r}. \tag{3.59}$$

It is also worth mentioning here that when $\kappa_t = \kappa_r = 1$, i.e. the case of ideal hardware transceivers, the received signal in (3.54) becomes

$$y^g[n] = \left[(\mathbf{h}_0[n])^{\mathrm{T}} + (\mathbf{h}_1[n])^{\mathrm{T}}\Omega^g(\mathbf{H}_{\mathrm{r}}[n])^{\mathrm{T}}\right]\mathbf{F}^g[n]\mathbf{z}^g[n] + w^g[n],$$

which consists only of the noiseless signal plus the white noise, where the variance of the received signal becomes $C_y = \sigma^2$, the variance of the AWGN. As such, the quality of the received signal is expressed by

$$\mathrm{SNR} = \frac{M_{\mathrm{B}}(\rho_0^2 + M_{\mathrm{R}}^2\rho_{\mathrm{r}}^2\rho_1^2)}{(\sigma^2/P)}, \tag{3.60}$$

and thus

$$\lim_{P\to\infty} \mathrm{SNR} \to \infty, \tag{3.61}$$

which practically implies that, unlike the perfect systems with AWGN only, improving the quality of the received pilots by boosting the transmission power is bounded due to the existence of the HWIs.

3.3.3 Channel Parameters Estimation and Joint Localization-Synchronization Process

This section addresses the joint localization-synchronization processes along with the tracking performed by the single antenna MS. In specific, these processes are executed by observing how

the pilot is distorted by the imperfect transceivers at both the MS and BS, as seen in the received signal from (3.54).

Accordingly, we first present the relationships between the parameters in (3.54) and the 3D coordinates of the RIS-aided mmwave MISO-OFDM system in Fig.3.10. Then, we execute the joint localization-synchronization process based on these relationships and on the MLE, where its log-likelihood function is reformulated to consider the HWIs. Finally, tracking a MS process is presented, as it is carried out by the KFT implemented behind the MLE stage. Regarding this, the KFT is designed based on the errors in estimating the positions and according to the MS transition model.

Fig.3.11 depicts the relationships between the channel parameters in (3.54) and the 3D coordinates of the unknown position MS at $\mathbf{p}_{\mathrm{m}} = [\mathrm{p}_x, \mathrm{p}_y, \mathrm{p}_z]^{\mathrm{T}}$, the known position BS at $[\mathrm{b}_x, \mathrm{b}_y, \mathrm{b}_z]^{\mathrm{T}}$, and the known position RIS at $[\mathrm{r}_x, \mathrm{r}_y, \mathrm{r}_z]^{\mathrm{T}}$. According to Fig.3.11, when the BS positions at the original point, without loss of generality, the geometric relationships can be expressed as follows

$$\tau_0 = \frac{\sqrt{\mathrm{p}_x^2 + \mathrm{p}_y^2 + \mathrm{p}_z^2}}{c} + \Delta, \qquad \psi_0 = \sin^{-1}\left(\frac{\sqrt{\mathrm{p}_x^2 + \mathrm{p}_y^2}}{\sqrt{\mathrm{p}_x^2 + \mathrm{p}_y^2 + \mathrm{p}_z^2}}\right),$$

$$\theta_0 = \mathrm{atan2}(\mathrm{p}_y, \mathrm{p}_x), \qquad \tau_1 = \frac{\sqrt{(\mathrm{p}_x - \mathrm{r}_x)^2 + (\mathrm{p}_y - \mathrm{r}_y)^2 + (\mathrm{p}_z - \mathrm{r}_z)^2}}{c} + \Delta,$$

$$\psi_1 = \sin^{-1}\left(\frac{\sqrt{(\mathrm{p}_x - \mathrm{r}_x)^2 + (\mathrm{p}_y - \mathrm{r}_y)^2}}{\sqrt{(\mathrm{p}_x - \mathrm{r}_x)^2 + (\mathrm{p}_y - \mathrm{r}_y)^2 + (\mathrm{p}_z - \mathrm{r}_z)^2}}\right),$$

$$\theta_1 = \mathrm{atan2}((\mathrm{p}_y - \mathrm{r}_y), (\mathrm{p}_x - \mathrm{r}_x)). \tag{3.62}$$

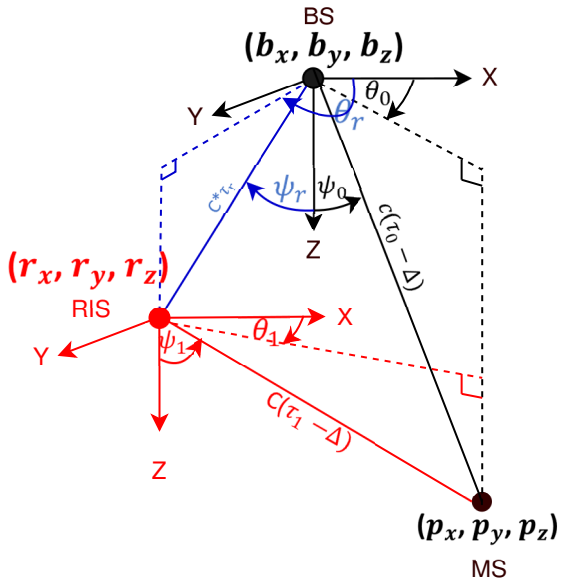

Figure 3.11: The RIS-aided mmwave MISO-OFDM system 3D coordinates.

It is clear that by having the BS and RIS placed at known and fixed positions, the $\mathbf{H}_r$ link's parameters are known constants, and can be given as

$$\tau_{\mathrm{r}} = \frac{\sqrt{\mathrm{r}_x^2+\mathrm{r}_y^2+\mathrm{r}_z^2}}{c},\ \psi_{\mathrm{r}} = \sin^{-1}\left(\frac{\sqrt{\mathrm{r}_x^2+\mathrm{r}_y^2}}{\sqrt{\mathrm{r}_x^2+\mathrm{r}_y^2+\mathrm{r}_z^2}}\right),$$
$$\theta_{\mathrm{r}} = \mathrm{atan2}(\mathrm{r}_y,\mathrm{r}_x),\ \bar{\psi}_{\mathrm{r}} = -\pi+\psi_{\mathrm{r}},\ \bar{\theta}_{\mathrm{r}} = -\pi+\theta_{\mathrm{r}}. \tag{3.63}$$

Due to the Gaussian white noise and the HWIs noises, the distorted pilot in (3.54) is Gaussian with mean $\varphi^g[n]$ and variance C_y defined in (3.56) and (3.57), respectively. As such, the channel parameters in the mean $\varphi^g[n]$ are unknowns, deterministic, and achieve the geometric relationships in (3.62) for any position of the MS. Moreover, the transmitted symbols and the beamforming matrix are known, and estimating the AWGN variance is possible for the initial access of mmWave systems [36, 71, 93].

For this purpose, the ML estimator is chosen to estimate the MS's position and the clock drift, $[\mathbf{p}_{\mathrm{m}}\ ,\ \Delta]$. Referring to the ML rule, these parameters can be estimated through

$$\left(\hat{\mathbf{p}}_{\mathrm{m}}\ ,\ \hat{\Delta}\right) = \underset{\tau_0,\theta_0,\psi_0,\tau_1,\theta_1,\psi_1}{\arg\max}\left[\max_{\rho_0,\phi_0,\rho_1,\phi_1} L\left(\tau_0,\theta_0,\psi_0,\rho_0,\phi_0,\tau_1,\theta_1,\psi_1,\rho_1,\phi_1\right)\right],$$

where

$$L\left(\tau_0,\theta_0,\psi_0,\rho_0,\phi_0,\tau_1,\theta_1,\psi_1,\rho_1,\phi_1\right) = \log\left(f\left(\mathbf{y}\middle|\tau_0,\theta_0,\psi_0,\rho_0,\phi_0,\tau_1,\theta_1,\psi_1,\rho_1,\phi_1\right)\right)$$

represents the log-likelihood function of $\mathbf{y}$, which is the set of all observations for given τ_0, θ_0, ψ_0, ρ_0, ϕ_0, τ_1, θ_1, ψ_1, ρ_1 and ϕ_1 values, while $f(\cdot)$ is the PDF of $\mathbf{y}$. After some simple manipulations, the log-likelihood function of $\mathbf{y}$ can be written as

$$\begin{aligned} L\left(\tau_0,\theta_0,\psi_0,\rho_0,\phi_0,\tau_1,\theta_1,\psi_1,\rho_1,\phi_1\right) = &-\frac{NG}{2}\ln\left(2\pi\left(KP(\rho_0^2+M_{\mathrm{R}}^2\rho_{\mathrm{r}}^2\rho_1^2)+\sigma^2\right)\right) \\ &-\frac{\sum_{g=1}^{G}||\mathbf{y}^g-\sqrt{\kappa_t\kappa_r}\rho_0 e^{j\phi_0}\mathbf{w}_0^g-\sqrt{\kappa_t\kappa_r}\rho_1 e^{j\phi_1}\mathbf{w}_1^g||^2}{2\left(KP(\rho_0^2+M_{\mathrm{R}}^2\rho_{\mathrm{r}}^2\rho_1^2)+\sigma^2\right)}, \end{aligned} \tag{3.64}$$

where $K=(1-\kappa_{\mathrm{t}}\kappa_{\mathrm{r}})M_{\mathrm{B}}$, and $\mathbf{y}^g = \left[y^g[0],\ldots,y^g[N-1]\right]^{\mathrm{T}}$ as given in (3.54), while $\mathbf{w}_0^g$ and $\mathbf{w}_1^g$ are

$$\mathbf{w}_0^g = \begin{bmatrix} \alpha^{\mathrm{T}}(\theta_0,\psi_0,M_{\mathrm{B}})\mathbf{F}^g[0]\mathbf{z}^g[0] \\ \vdots \\ e^{-j2\pi[N-1]\frac{\tau_0}{NT}}\alpha^{\mathrm{T}}(\theta_0,\psi_0,M_{\mathrm{B}})\mathbf{F}^g[N-1]\mathbf{z}^g[N-1] \end{bmatrix},$$

$$\mathbf{w}_1^g = \begin{bmatrix} \alpha^{\mathrm{T}}(\theta_1,\psi_1,M_{\mathrm{R}})\Omega^g\mathbf{H}_{\mathrm{r}}^{\mathrm{T}}[0]\mathbf{F}^g[0]\mathbf{z}^g[0] \\ \vdots \\ e^{j2\pi[N-1]\frac{\tau_1}{NT}}\alpha^{\mathrm{T}}(\theta_1,\psi_1,M_{\mathrm{R}})\Omega^g\mathbf{H}_{\mathrm{r}}^{\mathrm{T}}[N-1]\mathbf{F}^g[N-1]\mathbf{z}^g[N-1] \end{bmatrix}.$$

It is evident that the estimated values of ϕ_0 and ϕ_1 that maximize (3.64) can be given as

$$\frac{\partial L(\tau_0,\theta_0,\psi_0,\rho_0,\phi_0,\tau_1,\theta_1,\psi_1,\rho_1,\phi_1)}{\partial \phi_0} = \frac{\sum_{g=1}^{G}(\mathbf{w}_0^g)^{\mathrm{H}}(\mathbf{y}^g - \sqrt{\kappa_t\kappa_r}\rho_0 e^{j\phi_0}\mathbf{w}_0^g - \sqrt{\kappa_t\kappa_r}\rho_1 e^{j\phi_1}\mathbf{w}_1^g)}{\frac{KP(\rho_0^2+M_{\mathrm{R}}^2\rho_{\mathrm{r}}^2\rho_1^2)+\sigma^2}{1/j\sqrt{\kappa_t\kappa_r}\rho_0 e^{j\phi_0}}} = 0,$$

$$\frac{\partial L(\tau_0,\theta_0,\psi_0,\rho_0,\phi_0,\tau_1,\theta_1,\psi_1,\rho_1,\phi_1)}{\partial \phi_1} = \frac{\sum_{g=1}^{G}(\mathbf{w}_1^g)^{\mathrm{H}}(\mathbf{y}^g - \sqrt{\kappa_t\kappa_r}\rho_0 e^{j\phi_0}\mathbf{w}_0^g - \sqrt{\kappa_t\kappa_r}\rho_1 e^{j\phi_1}\mathbf{w}_1^g)}{\frac{KP(\rho_0^2+M_{\mathrm{R}}^2\rho_{\mathrm{r}}^2\rho_1^2)+\sigma^2}{1/j\sqrt{\kappa_t\kappa_r}\rho_1 e^{j\phi_1}}} = 0,$$

where after mathematical manipulation, the above equations become

$$\left(\rho_0\sum_{g=1}^{G}(\mathbf{w}_0^g)^{\mathrm{H}}\mathbf{w}_0^g\right)e^{j\phi_0} + \left(\rho_1\sum_{g=1}^{G}(\mathbf{w}_0^g)^{\mathrm{H}}\mathbf{w}_1^g\right)e^{j\phi_1} = \frac{\sum_{g=1}^{G}(\mathbf{w}_0^g)^{\mathrm{H}}\mathbf{y}^g}{\sqrt{\kappa_t\kappa_r}},$$

$$\left(\rho_0\sum_{g=1}^{G}(\mathbf{w}_1^g)^{\mathrm{H}}\mathbf{w}_0^g\right)e^{j\phi_0} + \left(\rho_1\sum_{g=1}^{G}(\mathbf{w}_1^g)^{\mathrm{H}}\mathbf{w}_1^g\right)e^{j\phi_1} = \frac{\sum_{g=1}^{G}(\mathbf{w}_1^g)^{\mathrm{H}}\mathbf{y}^g}{\sqrt{\kappa_t\kappa_r}}.$$

Following that, the estimated values of $e^{j\phi_0}$ and $e^{j\phi_1}$ are obtained as

$$e^{j\hat{\phi}_0} = \frac{c_{11}\sum_{g=1}^{G}(\mathbf{w}_0^g)^{\mathrm{H}}\mathbf{y}^g - c_{01}\sum_{g=1}^{G}(\mathbf{w}_1^g)^{\mathrm{H}}\mathbf{y}^g}{\sqrt{\kappa_t\kappa_r}\rho_0[c_{00}c_{11}-c_{01}c_{10}]} = \frac{C^{(0)}}{\sqrt{\kappa_t\kappa_r}\rho_0}, \tag{3.65}$$

$$e^{j\hat{\phi}_1} = \frac{c_{00}\sum_{g=1}^{G}(\mathbf{w}_1^g)^{\mathrm{H}}\mathbf{y}^g - c_{10}\sum_{g=1}^{G}(\mathbf{w}_0^g)^{\mathrm{H}}\mathbf{y}^g}{\sqrt{\kappa_t\kappa_r}\rho_1[c_{00}c_{11}-c_{01}c_{10}]} = \frac{C^{(1)}}{\sqrt{\kappa_t\kappa_r}\rho_1}, \tag{3.66}$$

where $c_{ij} = \sum_{g=1}^{G}(\mathbf{w}_i^g)^{\mathrm{H}}\mathbf{w}_j^g$. Next, after substituting the values of $e^{j\hat{\phi}_0}$ and $e^{j\hat{\phi}_1}$ into (3.64), the log-likelihood function of $\mathbf{y}$ can be given as

$$\begin{aligned} L(\tau_0,\theta_0,\psi_0,\rho_0,\tau_1,\theta_1,\psi_1,\rho_1) = &-\frac{NG}{2}\ln\left(2\pi\left(KP(\rho_0^2+M_{\mathrm{R}}^2\rho_{\mathrm{r}}^2\rho_1^2)+\sigma^2\right)\right) \\ &-\frac{\sum_{g=1}^{G}||\mathbf{y}^g - C^{(0)}\mathbf{w}_0^g - C^{(1)}\mathbf{w}_1^g||^2}{2\left(KP(\rho_0^2+M_{\mathrm{R}}^2\rho_{\mathrm{r}}^2\rho_1^2)+\sigma^2\right)}, \end{aligned} \tag{3.67}$$

and then the estimated values of ρ_0 and ρ_1 are calculated from

$$\frac{\partial L(\tau_0,\theta_0,\psi_0,\rho_0,\tau_1,\theta_1,\psi_1,\rho_1)}{\partial \rho_0} = \frac{-NGKP\rho_0}{\left(KP(\rho_0^2+M_{\mathrm{R}}^2\rho_{\mathrm{r}}^2\rho_1^2)+\sigma^2\right)} + \frac{KP\rho_0\sum_{g=1}^{G}||\mathbf{y}^g - C^{(0)}\mathbf{w}_0^g - C^{(1)}\mathbf{w}_1^g||^2}{\left(KP(\rho_0^2+M_{\mathrm{R}}^2\rho_{\mathrm{r}}^2\rho_1^2)+\sigma^2\right)^2} = 0,$$

$$\frac{\partial L(\tau_0,\theta_0,\psi_0,\rho_0,\tau_1,\theta_1,\psi_1,\rho_1)}{\partial \rho_1} = \frac{-NGKPM_{\mathrm{R}}^2\rho_{\mathrm{r}}^2\rho_1}{\left(KP(\rho_0^2+M_{\mathrm{R}}^2\rho_{\mathrm{r}}^2\rho_1^2)+\sigma^2\right)} + \frac{KPM_{\mathrm{R}}^2\rho_{\mathrm{r}}^2\rho_1\sum_{g=1}^{G}||\mathbf{y}^g - C^{(0)}\mathbf{w}_0^g - C^{(1)}\mathbf{w}_1^g||^2}{\left(KP(\rho_0^2+M_{\mathrm{R}}^2\rho_{\mathrm{r}}^2\rho_1^2)+\sigma^2\right)^2} = 0,$$

which leads to

$$\hat{\rho}_0^2 + M_{\mathrm{R}}^2\rho_{\mathrm{r}}^2\hat{\rho}_1^2 = \frac{\left(\sum_{g=1}^{G}||\mathbf{y}^g - C^{(0)}\mathbf{w}_0^g - C^{(1)}\mathbf{w}_1^g||^2\right) - NG\sigma^2}{NGKP}. \tag{3.68}$$

Now, with the substitution of $C^{(0)}$ from (3.65), $C^{(1)}$ from (3.66) and (3.68) into (3.67), the log-likelihood function of $\mathbf{y}$ can be rewritten in terms of τ_0, θ_0, ψ_0,τ_1, θ_1 and ψ_1 as

$$L\left(\tau_0,\theta_0,\psi_0\tau_1,\theta_1,\psi_1\right) = -\frac{NG}{2} - \frac{NG}{2}\ln\left(\frac{2\pi}{NG}\sum_{g=1}^{G}\left\|\mathbf{y}^g - \frac{c_{11}\sum_{i=1}^{G}(\mathbf{w}_0^i)^{\mathrm{H}}\mathbf{y}^i - c_{01}\sum_{i=1}^{G}(\mathbf{w}_1^i)^{\mathrm{H}}\mathbf{y}^i}{c_{00}c_{11}-c_{01}c_{10}}\mathbf{w}_0^g - \frac{c_{00}\sum_{i=1}^{G}(\mathbf{w}_1^i)^{\mathrm{H}}\mathbf{y}^i - c_{10}\sum_{i=1}^{G}(\mathbf{w}_0^i)^{\mathrm{H}}\mathbf{y}^i}{c_{00}c_{11}-c_{01}c_{10}}\mathbf{w}_1^g\right\|^2\right). \tag{3.69}$$

Following that, a numerical search algorithm is used to maximize this cost function. Specifically, a 4D grid search algorithm over the space of $[\mathbf{p}_{\mathrm{m}}, \Delta] = [\mathrm{p}_x, \mathrm{p}_y, \mathrm{p}_z, \Delta]$ is used to find the optimal point. In particular, each point over the 4D search grid is converted to the channel parameters $[\tau_0,\theta_0,\psi_0,\tau_1,\theta_1,\psi_1]$ according to (3.62). Then the channel parameters are fed into the cost function, where the optimal point presenting the estimated position and clock offset $[\hat{\mathbf{p}}_{\mathrm{m}}, \hat{\Delta}]$, is the point that maximizes the cost function. It is important to mention here that works as in [35, 36, 71] presented adequate initialization and low complex approaches to overcome the burden of multidimensional optimization.

3.3.4 Fisher Information Matrices and Cramer-Rao lower bound

This subsection presents the achievable accuracy of the joint localization-synchronization process in the 3D RIS-assisted mmWave MISO-OFDM system, in a system suffering from the HWIs at the transceivers at both the MS and BS. It presents the FIM that measures the amount of information obtained from the observations in (3.54). It is worth mentioning here that the pseudo-inverse of the observation FIM is the CRB that assesses the 3D joint localization-synchronization process in an RIS-assisted mmWave MISO-OFDM system suffering from HWIs.

Let us start by defining the vector of downlink channel parameters, given as $\beta = [\tau_0, \theta_0, \psi_0, \rho_0, \phi_0, \tau_1, \theta_1, \psi_1, \rho_1, \phi_1]^{\mathrm{T}}$, and the vector of localization parameter as $\mu = [\mathrm{p}_x, \mathrm{p}_y, \mathrm{p}_z, \Delta]^{\mathrm{T}}$, where the elements of the FIM $\mathbf{J}_\beta \in \mathbb{R}^{10\times10}$, which measures the amount of information about β obtained from observing $y^g[n]$ in (3.54). These are given according to (2.20) similar to (3.19) in section 3.1, where the noiseless signal is $\varphi^g[n]$ in (3.57), while the noise variance is C_y in (3.56).

In order to compute the elements of $\mathbf{J}_\beta$, the following statements should be defined:

$$
\begin{aligned}
&\overline{\mathbf{F}^g}[n] = \sqrt{\kappa_t}\sqrt{\kappa_r}\mathbf{F}^g[n]\mathbf{z}^g[n],\\
&\frac{\partial \mathbf{k}(\theta_i,\psi_i)}{\partial \theta_i} = [-\cos\psi_i \sin\theta_i, \cos\psi_i\cos\theta_i, 0]^{\mathrm{T}},\\
&\frac{\partial \mathbf{k}(\theta_i,\psi_i)}{\partial \psi_i} = [-\sin\psi_i \cos\theta_i, -\sin\psi_i\sin\theta_i, \cos\psi_i]^{\mathrm{T}},\\
&\mathbf{B}_{\theta_0} = \mathrm{diag}\left[\left[\frac{\partial \mathbf{k}(\theta_0,\psi_0)}{\partial \theta_0}\right]^{\mathrm{T}} u_1, \ldots, \left[\frac{\partial \mathbf{k}(\theta_0,\psi_0)}{\partial \theta_0}\right]^{\mathrm{T}} u_{M_{\mathrm{B}}}\right] \in \mathbb{R}^{M_{\mathrm{B}}\times M_{\mathrm{B}}},\\
&\mathbf{B}_{\psi_0} = \mathrm{diag}\left[\left[\frac{\partial \mathbf{k}(\theta_0,\psi_0)}{\partial \psi_0}\right]^{\mathrm{T}} u_1, \ldots, \left[\frac{\partial \mathbf{k}(\theta_0,\psi_0)}{\partial \psi_0}\right]^{\mathrm{T}} u_{M_{\mathrm{B}}}\right] \in \mathbb{R}^{M_{\mathrm{B}}\times M_{\mathrm{B}}}.\\
&\mathbf{B}_{\theta_1} = \mathrm{diag}\left[\left[\frac{\partial \mathbf{k}(\theta_1,\psi_1)}{\partial \theta_1}\right]^{\mathrm{T}} u_1, \ldots, \left[\frac{\partial \mathbf{k}(\theta_1,\psi_1)}{\partial \theta_1}\right]^{\mathrm{T}} u_{M_{\mathrm{R}}}\right] \in \mathbb{R}^{M_{\mathrm{R}}\times M_{\mathrm{R}}},\\
&\mathbf{B}_{\psi_1} = \mathrm{diag}\left[\left[\frac{\partial \mathbf{k}(\theta_1,\psi_1)}{\partial \psi_1}\right]^{\mathrm{T}} u_1, \ldots, \left[\frac{\partial \mathbf{k}(\theta_1,\psi_1)}{\partial \psi_1}\right]^{\mathrm{T}} u_{M_{\mathrm{R}}}\right] \in \mathbb{R}^{M_{\mathrm{R}}\times M_{\mathrm{R}}}.
\end{aligned}
$$

and then compute the derivations of $\varphi^g[n]$ with respect to vector β are

$$
\begin{aligned}
&\frac{\partial \varphi^g[n]}{\partial \tau_0} = \frac{-j2\pi n}{NT}\rho_0 \exp(j(\phi_0 - 2\pi n\frac{\tau_0}{NT}))\alpha(\theta_0,\psi_0,M_{\mathrm{B}})^{\mathrm{T}}\,\overline{\mathbf{F}^g}[n],\\
&\frac{\partial \varphi^g[n]}{\partial \theta_0} = j\frac{2\pi}{\lambda_c}\rho_0 \exp(j(\phi_0 - 2\pi n\tfrac{\tau_0}{NT}))\alpha(\theta_0,\psi_0,M_{\mathrm{B}})^{\mathrm{T}}\mathbf{B}_{\theta_0}\overline{\mathbf{F}^g}[n],\\
&\frac{\partial \varphi^g[n]}{\partial \psi_0} = j\frac{2\pi}{\lambda_c}\rho_0 \exp(j(\phi_0 - 2\pi n\tfrac{\tau_0}{NT}))\alpha(\theta_0,\psi_0,M_{\mathrm{B}})^{\mathrm{T}}\mathbf{B}_{\psi_0}\overline{\mathbf{F}^g}[n],\\
&\frac{\partial \varphi^g[n]}{\partial \rho_0} = e^{j\phi_0}e^{-j2\pi n\frac{\tau_0}{NT}}\,\alpha(\theta_0,\psi_0,M_{\mathrm{B}})^{\mathrm{T}}\,\overline{\mathbf{F}^g}[n].\\
&\frac{\partial \varphi^g[n]}{\partial \phi_0} = j\rho_0 e^{j\phi_0}e^{-j2\pi n\frac{\tau_0}{NT}}\,\alpha(\theta_0,\psi_0,M_{\mathrm{B}})^{\mathrm{T}}\,\overline{\mathbf{F}^g}[n],\\
&\frac{\partial \varphi^g[n]}{\partial \tau_1} = \frac{-j2\pi n}{NT}\rho_1 e^{j\phi_1}e^{-j2\pi n\frac{\tau_1}{NT}}\,\alpha(\theta_1,\psi_1,M_{\mathrm{R}})^{\mathrm{T}}\Omega^g(\mathbf{H}_{\mathrm{r}}[n])^{\mathrm{T}}\,\overline{\mathbf{F}^g}[n],\\
&\frac{\partial \varphi^g[n]}{\partial \theta_1} = j\frac{2\pi}{\lambda_c}\rho_1 \exp(j(\phi_1 - 2\pi n\tfrac{\tau_1}{NT}))\alpha(\theta_1,\psi_1,M_{\mathrm{R}})^{\mathrm{T}}\mathbf{B}_{\theta_1}\Omega^g(\mathbf{H}_{\mathrm{r}}[n])^{\mathrm{T}}\,\overline{\mathbf{F}^g}[n],\\
&\frac{\partial \varphi^g[n]}{\partial \psi_1} = j\frac{2\pi}{\lambda_c}\rho_1 \exp(j(\phi_1 - 2\pi n\tfrac{\tau_1}{NT}))\alpha(\theta_1,\psi_1,M_{\mathrm{R}})^{\mathrm{T}}\mathbf{B}_{\psi_1}\Omega^g(\mathbf{H}_{\mathrm{r}}[n])^{\mathrm{T}}\,\overline{\mathbf{F}^g}[n],
\end{aligned}
$$

$$
\begin{aligned}
&\frac{\partial \varphi^g[n]}{\partial \rho_1} = \exp(j(\phi_1 - 2\pi n\tfrac{\tau_1}{NT}))\alpha(\theta_1,\psi_1,M_{\mathrm{R}})^{\mathrm{T}}\Omega^g(\mathbf{H}_{\mathrm{r}}[n])^{\mathrm{T}}\,\overline{\mathbf{F}^g}[n],\\
&\frac{\partial \varphi^g[n]}{\partial \phi_1} = j\rho_1 \exp(j(\phi_1 - 2\pi n\tfrac{\tau_1}{NT}))\alpha(\theta_1,\psi_1,M_{\mathrm{R}})^{\mathrm{T}}\Omega^g(\mathbf{H}_{\mathrm{r}}[n])^{\mathrm{T}}\,\overline{\mathbf{F}^g}[n],
\end{aligned}
$$

and calculate the derivatives of the noise variance C_y with respect to the same vector

$$\begin{aligned}
&\frac{\partial C_y}{\partial \rho_0} = 2P(1-\kappa_t\kappa_r)M_{\mathrm{B}}\rho_0,\\
&\frac{\partial C_y}{\partial \rho_1} = 2P(1-\kappa_t\kappa_r)M_{\mathrm{B}}M_{\mathrm{R}}^2\rho_{\mathrm{r}}^2\rho_1.\\
&\frac{\partial C_y}{\partial \tau_0}=\frac{\partial C_y}{\partial \theta_0}=\frac{\partial C_y}{\partial \psi_0}=\frac{\partial C_y}{\partial \phi_0}=\frac{\partial C_y}{\partial \tau_1}=\frac{\partial C_y}{\partial \theta_1}=\frac{\partial C_y}{\partial \psi_1}=\frac{\partial C_y}{\partial \phi_1}=0.
\end{aligned}$$

Following that, the FIM of the position parameters vector $\mathbf{J}_\mu \in \mathbb{R}^{4\times 4}$ is according to the following transformation formula (2.19), similar to (3.20) in section 3.1, where the transformation matrix $\mathbf{T}$ here is defined by

$$\mathbf{T} \in \mathbb{R}^{10\times 8} \overset{(\mathrm{def})}{=} \frac{\partial \beta^{\mathrm{T}}}{\partial \mu} =$$

$$\begin{bmatrix}
\frac{\partial\tau_0}{\partial M_x} & \frac{\partial\theta_0}{\partial M_x} & \frac{\partial\psi_0}{\partial M_x} & \frac{\partial\rho_0}{\partial M_x} & \frac{\partial\phi_0}{\partial M_x} & \frac{\partial\tau_1}{\partial M_x} & \frac{\partial\theta_1}{\partial M_x} & \frac{\partial\psi_1}{\partial M_x} & \frac{\partial\rho_{\mathrm{R}}}{\partial M_x} & \frac{\partial\phi_{\mathrm{R}}}{\partial M_x}\\
\frac{\partial\tau_0}{\partial M_y} & \frac{\partial\theta_0}{\partial M_y} & \frac{\partial\psi_0}{\partial M_y} & \frac{\partial\rho_0}{\partial M_y} & \frac{\partial\phi_0}{\partial M_y} & \frac{\partial\tau_1}{\partial M_y} & \frac{\partial\theta_1}{\partial M_y} & \frac{\partial\psi_1}{\partial M_y} & \frac{\partial\rho_{\mathrm{R}}}{\partial M_y} & \frac{\partial\phi_{\mathrm{R}}}{\partial M_y}\\
\frac{\partial\tau_0}{\partial M_z} & \frac{\partial\theta_0}{\partial M_z} & \frac{\partial\psi_0}{\partial M_z} & \frac{\partial\rho_0}{\partial M_z} & \frac{\partial\phi_0}{\partial M_z} & \frac{\partial\tau_1}{\partial M_z} & \frac{\partial\theta_1}{\partial M_z} & \frac{\partial\psi_1}{\partial M_z} & \frac{\partial\rho_{\mathrm{R}}}{\partial M_z} & \frac{\partial\phi_{\mathrm{R}}}{\partial M_z}\\
\frac{\partial\tau_0}{\partial \rho_0} & \frac{\partial\theta_0}{\partial \rho_0} & \frac{\partial\psi_0}{\partial \rho_0} & \frac{\partial\rho_0}{\partial \rho_0} & \frac{\partial\phi_0}{\partial \rho_0} & \frac{\partial\tau_1}{\partial \rho_0} & \frac{\partial\theta_1}{\partial \rho_0} & \frac{\partial\psi_1}{\partial \rho_0} & \frac{\partial\rho_{\mathrm{R}}}{\partial \rho_0} & \frac{\partial\phi_{\mathrm{R}}}{\partial \rho_0}\\
\frac{\partial\tau_0}{\partial \phi_0} & \frac{\partial\theta_0}{\partial \phi_0} & \frac{\partial\psi_0}{\partial \phi_0} & \frac{\partial\rho_0}{\partial \phi_0} & \frac{\partial\phi_0}{\partial \phi_0} & \frac{\partial\tau_1}{\partial \phi_0} & \frac{\partial\theta_1}{\partial \phi_0} & \frac{\partial\psi_1}{\partial \phi_0} & \frac{\partial\rho_{\mathrm{R}}}{\partial \phi_0} & \frac{\partial\phi_{\mathrm{R}}}{\partial \phi_0}\\
\frac{\partial\tau_0}{\partial \rho_{\mathrm{R}}} & \frac{\partial\theta_0}{\partial \rho_{\mathrm{R}}} & \frac{\partial\psi_0}{\partial \rho_{\mathrm{R}}} & \frac{\partial\rho_0}{\partial \rho_{\mathrm{R}}} & \frac{\partial\phi_0}{\partial \rho_{\mathrm{R}}} & \frac{\partial\tau_1}{\partial \rho_{\mathrm{R}}} & \frac{\partial\theta_1}{\partial \rho_{\mathrm{R}}} & \frac{\partial\psi_1}{\partial \rho_{\mathrm{R}}} & \frac{\partial\rho_{\mathrm{R}}}{\partial \rho_{\mathrm{R}}} & \frac{\partial\phi_{\mathrm{R}}}{\partial \rho_{\mathrm{R}}}\\
\frac{\partial\tau_0}{\partial \phi_{\mathrm{R}}} & \frac{\partial\theta_0}{\partial \phi_{\mathrm{R}}} & \frac{\partial\psi_0}{\partial \phi_{\mathrm{R}}} & \frac{\partial\rho_0}{\partial \phi_{\mathrm{R}}} & \frac{\partial\phi_0}{\partial \phi_{\mathrm{R}}} & \frac{\partial\tau_1}{\partial \phi_{\mathrm{R}}} & \frac{\partial\theta_1}{\partial \phi_{\mathrm{R}}} & \frac{\partial\psi_1}{\partial \phi_{\mathrm{R}}} & \frac{\partial\rho_{\mathrm{R}}}{\partial \phi_{\mathrm{R}}} & \frac{\partial\phi_{\mathrm{R}}}{\partial \phi_{\mathrm{R}}}\\
\frac{\partial\tau_0}{\partial \Delta} & \frac{\partial\theta_0}{\partial \Delta} & \frac{\partial\psi_0}{\partial \Delta} & \frac{\partial\rho_0}{\partial \Delta} & \frac{\partial\phi_0}{\partial \Delta} & \frac{\partial\tau_1}{\partial \Delta} & \frac{\partial\theta_1}{\partial \Delta} & \frac{\partial\psi_1}{\partial \Delta} & \frac{\partial\rho_{\mathrm{R}}}{\partial \Delta} & \frac{\partial\phi_{\mathrm{R}}}{\partial \Delta}
\end{bmatrix}.$$

and the elements of the transformation matrix $\mathbf{T}$ depend on the geometric relationships between the parameters of the β vector and those of the μ vector described in (3.62). Consequently, the elements of the transformation matrix $\mathbf{T}$ are zero except:

$$\begin{aligned}
&\frac{\partial\tau_0}{\partial\Delta}=\frac{\partial\tau_1}{\partial\Delta}=1,\quad \frac{\partial\tau_0}{\partial \mathrm{p}_x}=\frac{\mathrm{p}_x}{c\sqrt{\mathrm{p}_x^2+\mathrm{p}_y^2+\mathrm{p}_z^2}},\quad \frac{\partial\tau_0}{\partial \mathrm{p}_y}=\frac{\mathrm{p}_y}{c\sqrt{\mathrm{p}_x^2+\mathrm{p}_y^2+\mathrm{p}_z^2}},\quad \frac{\partial\tau_0}{\partial \mathrm{p}_z}=\frac{\mathrm{p}_z}{c\sqrt{\mathrm{p}_x^2+\mathrm{p}_y^2+\mathrm{p}_z^2}},\\
&\frac{\partial\theta_0}{\partial \mathrm{p}_x}=\frac{-\mathrm{p}_y}{\mathrm{p}_x^2+\mathrm{p}_y^2},\quad \frac{\partial\theta_0}{\partial \mathrm{p}_y}=\frac{\mathrm{p}_x}{\mathrm{p}_x^2+\mathrm{p}_y^2},\quad \frac{\partial\psi_0}{\partial \mathrm{p}_x}=\frac{|\mathrm{p}_z|\,\mathrm{p}_x}{(\mathrm{p}_x^2+\mathrm{p}_y^2+\mathrm{p}_z^2)\sqrt{\mathrm{p}_x^2+\mathrm{p}_y^2}},\quad \frac{\partial\psi_0}{\partial \mathrm{p}_y}=\frac{|\mathrm{p}_z|\,\mathrm{p}_y}{(\mathrm{p}_x^2+\mathrm{p}_y^2+\mathrm{p}_z^2)\sqrt{\mathrm{p}_x^2+\mathrm{p}_y^2}},\\
&\frac{\partial\psi_0}{\partial \mathrm{p}_z}=\frac{-\mathrm{p}_z\sqrt{\mathrm{p}_x^2+\mathrm{p}_y^2}}{|\mathrm{p}_z|(\mathrm{p}_x^2+\mathrm{p}_y^2+\mathrm{p}_z^2)},\quad \frac{\partial\tau_1}{\partial \mathrm{p}_x}=\frac{(\mathrm{p}_x-\mathrm{r}_x)}{c\sqrt{(\mathrm{p}_x-\mathrm{r}_x)^2+(\mathrm{p}_y-\mathrm{r}_y)^2+(\mathrm{p}_z-\mathrm{r}_z)^2}},
\end{aligned}$$

$$\frac{\partial \tau_1}{\partial \mathrm{p}_y}=\frac{(\mathrm{p}_y-\mathrm{r}_y)}{c\sqrt{(\mathrm{p}_x-\mathrm{r}_x)^2+(\mathrm{p}_y-\mathrm{r}_y)^2+(\mathrm{p}_z-\mathrm{r}_z)^2}},\quad \frac{\partial \tau_1}{\partial \mathrm{p}_z}=\frac{(\mathrm{p}_z-\mathrm{r}_z)}{c\sqrt{(\mathrm{p}_x-\mathrm{r}_x)^2+(\mathrm{p}_y-\mathrm{r}_y)^2+(\mathrm{p}_z-\mathrm{r}_z)^2}},$$

$$\frac{\partial \theta_1}{\partial \mathrm{p}_x}=\frac{-\frac{\mathrm{p}_y-\mathrm{r}_y}{(\mathrm{p}_x-\mathrm{r}_x)^2}}{1+(\frac{\mathrm{p}_y-\mathrm{r}_y}{\mathrm{p}_x-\mathrm{r}_x})^2},\quad \frac{\partial \theta_1}{\partial \mathrm{p}_y}=\frac{1/(\mathrm{p}_x-\mathrm{r}_x)}{1+(\frac{\mathrm{p}_y-\mathrm{r}_y}{\mathrm{p}_x-\mathrm{r}_x})^2},\quad \frac{\partial \psi_1}{\partial \mathrm{p}_x}=\frac{|\mathrm{p}_z-\mathrm{r}_z|(\mathrm{p}_x-\mathrm{r}_x)/\sqrt{(\mathrm{p}_x-\mathrm{r}_x)^2+(\mathrm{p}_y-\mathrm{r}_y)^2}}{(\mathrm{p}_x-\mathrm{r}_x)^2+(\mathrm{p}_y-\mathrm{r}_y)^2+(\mathrm{p}_z-\mathrm{r}_z)^2},$$

$$\frac{\partial \psi_1}{\partial \mathrm{p}_y}=\frac{|\mathrm{p}_z-\mathrm{r}_z|(\mathrm{p}_y-\mathrm{r}_y)/\sqrt{(\mathrm{p}_x-\mathrm{r}_x)^2+(\mathrm{p}_y-\mathrm{r}_y)^2}}{(\mathrm{p}_x-\mathrm{r}_x)^2+(\mathrm{p}_y-\mathrm{r}_y)^2+(\mathrm{p}_z-\mathrm{r}_z)^2},\quad \frac{\partial \psi_1}{\partial \mathrm{p}_z}=\frac{-(\mathrm{p}_z-\mathrm{r}_z)\sqrt{(\mathrm{p}_x-\mathrm{r}_x)^2+(\mathrm{p}_y-\mathrm{r}_y)^2}/|\mathrm{p}_z-\mathrm{r}_z|}{(\mathrm{p}_x-\mathrm{r}_x)^2+(\mathrm{p}_y-\mathrm{r}_y)^2+(\mathrm{p}_z-\mathrm{r}_z)^2}.$$

Finally, the CRB of the joint localization-synchronization process is from the pseudo-inverse of the later FIM, $\left(\mathbf{J}_\mu\right)^{-1}$, and thus, the PEB and the SEB are known as

$$\mathrm{PEB}=\sqrt{[(\mathbf{J}_\mu)^{-1}]_{(1,1)}+[(\mathbf{J}_\mu)^{-1}]_{(2,2)}+[(\mathbf{J}_\mu)^{-1}]_{(3,3)}}, \tag{3.70}$$

$$\mathrm{SEB}=\sqrt{[(\mathbf{J}_\mu)^{-1}]_{(4,4)}}, \tag{3.71}$$

where (SEB) refers to the synchronization error bound.

3.3.5 Simulation Results

This subsection conducts numerical experiments to discuss the joint localization-synchronization process in the 3D RIS-assisted mm-wave MISO-OFDM system under the harmful effects of the HWIs. We consider the same settings and scenarios of simulation assumed in section 3.2. In these experiments, the single antenna MS at any unknown position receives two copies of the known signal. The first copy reaches directly from the known position BS, where the BS is in the original point $[0,0,0]$ and is equipped with $M_{\mathrm{B}}=16$ antennas. The second copy is through the $M_{\mathrm{R}}=36$ elements RIS which is located in a known position in $[0.2,8,0.5]$ and generates the phase control matrix (Ω^g) by assuming equiprobable binary random variables. Moreover, it is important to note that the two copies of the pilot are distorted by the transceivers of the BS and MS, as the transceivers are non-ideal and suffer from HWIs with distortion coefficients $\kappa_t=\kappa_r=\kappa$ for simplicity, and their clocks drift with $\Delta=NT/8=62.5$ ns.

This subsection discusses performing the joint localization-synchronization process depending on receiving two copies of the pilot distorted by the HWIs noises, where the destructive impact of the HWIs is presented in Fig.3.12 and Fig.3.13. Specifically, the figures show the accuracy and the theoretical accuracy of the joint localization-synchronization process in terms of the RMSE and CRB at different values of κ and $\frac{P\rho_0^2}{\sigma^2}$. It is worth mentioning that the RMSE to assess the performance of the joint localization-synchronization process is calculated based on the MC computer simulation.

According to these figures, increasing the HWIs of the transceivers deteriorates the quality of the received signal, which leads to performing a less accurate joint localization-synchronization process, as the figures depict clearly. Moreover, the figures show that generally boosting the transmission power to improve the quality of the received signal enhances the accuracy of the joint

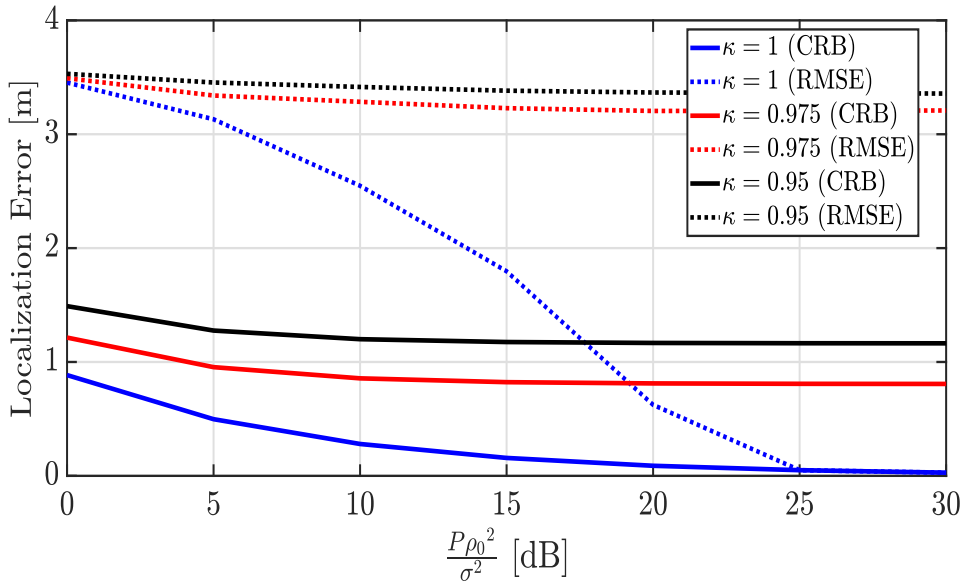

Figure 3.12: PEB and CRB versus the transmission power with different κ.

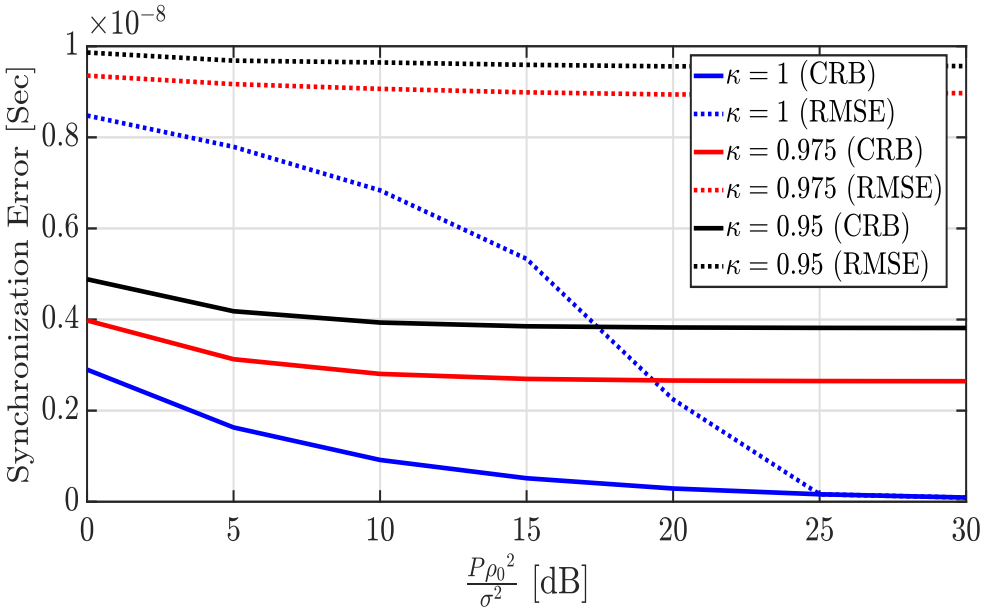

Figure 3.13: SEB and CRB versus the transmission power with different κ.

localization-synchronization process. Unfortunately, these accuracy enhancements are limited to a certain level when the hardware qualities of the transceivers are imperfect.

When the transceivers are ideal (i.e., $\kappa = 1$), it is clear that increasing the transmission power eliminates the AWGN impact and causes the errors to approximate zero, as shown by (3.61), while the existence of the HWIs bounds the position and synchronization errors to a non-zero level. This is because increasing the transmission power boosts both the non-noisy signal $\varphi^g[n]$ and the HWIs distortion term in C_y simultaneously, as seen from (3.56) and (3.57) in the case of

hardware-impaired transceivers. Besides, as apparent in the figures, in the low power range, the HWIs distortion is low, so the differences between the accuracy of the processes associated with the different κ values are negligible, while the differences in their accuracy become notable in the range of high power.

Moreover, it is observed that the RMSE achieves the CRB when $\frac{P\rho_0^2}{\sigma^2} \geq 25$ dB in the ideal transceiver scenario, and thus the SNR in (3.60) is also greater than 25 dB. In the case of non-ideal hardware, according to (4.12), the SNR saturates at 12.85 dB and 9.66 dB when $\kappa = 0.975$ and 0.95, respectively, which are lower than the SNR, making the RMSE achieve the PEB and SEB.

3.4 Summary

This chapter addresses the localization process and CRB in hardware-impaired mmwave-MISO-OFDM systems, where the BS transmits well-known pilots, and the MS determines its location by estimating the channel parameters using an ML estimator. Then, the FIM and the CRB of the channel and the localization processes are computed. In this context, the localization process and CRB are investigated in three hardware-impaired systems. The first scenario, which is the simplest, is a 2D mmwave MISO system involving a single LoS link between the BS and the MS. In the second scenario, the 3D localization accuracy degrades due to the HWIs and the multipath from unknown positions scatterers. Regarding the third scenario, it is an asynchronous RIS-aided mmwave MISO system. Accordingly, we perform the synchronization processes jointly with the localization process depending on the LoS link from the reference BS and the NLoS link reflected from the known-position RIS. Finally, numerical experiments are conducted for a detailed explanation and investigation of the processes executed in the three scenarios.

CHAPTER 4

TRACKING PROCESS AND BAYESIAN CRAMER-RAO BOUND

This chapter discusses the tracking process under HWIs and the synchronization errors. In the first section of this chapter, we present two tracking processes restricted to the HWIs only in a 3D perfectly synchronous mmwave MISO system. Furthermore, in the second section, we consider the synchronization errors and the HWIs. Precisely, in the second section, the tracking process is executed in an asynchronous RIS-assisted mmwave MISO-OFDM system suffering from the HWIs. The third part of this chapter presents the implementation of MLT to accomplish the tracking process. For each tracking process, this chapter derives the BCRB benchmark for tracking process assessment and conducts numerical experiments to discuss the tracking process and the BCRB.

4.1 3D Perfectly Synchronous mmwave MISO System

This section addresses the tracking process in a perfectly synchronous mmwave MISO system. Firstly, it presents the BCRB and the tracking process of the range and direction of a MS regarding the reference BS. Next, it explains tracking the position of the MS and the relevant BCRB. It's worth remembering here that the tracking process is considered an estimation process of time-varying random unknowns, where the tracking process is performed depending on obtaining measurements about the unknowns and considering the prior information about their transition or changing as seen in section 2.3.5. For this purpose, this chapter presents the system model where the tracking processes are executed. Then, it presents the measurement process where the tracking processes are performed depending on measuring the range and the direction of the MS relevant to the reference BS. After that, this section presents the transition model and the tracking solutions based on the measurements' nature, the transition model, and the relationship between them.

4.1.1 System Model and signalling

Fig.4.1 presents the time-varying channel in the mmwave MISO-OFDM system where the tracking processes are executed. This system runs the same setting described in section 3.2, except neglecting the NLoS paths from unknown scatterers as their impact is similar to the HWIs impact and studied in the same section 3.2.

At any arbitrary t^{th} time sample, the BS maintains a direct connection with the MS, $\mathbf{h}_n[t] \in \mathbb{C}^{M\times 1}$, that over the n^{th} sub-carrier is defined as

$$\mathbf{h}_n[t] = \gamma[t]\alpha[t]\exp\left(-j2\pi n\frac{\tau[t]}{NT}\right), \tag{4.1}$$

where N is the sub-carriers number, T is the sampling period, the term $\tau[t]$ is the ToF between the BS and MS, and $\gamma[t] = \rho[t]e^{j\phi[t]}$ with $\rho[t]$ and $\phi[t]$ are the modulus and the phase of the complex amplitude $\gamma[t]$. Besides, the BS array steering vector, $\alpha[t]$, is

$$\alpha[t] \in \mathbb{C}^{M\times 1} = \left[e^{j\frac{2\pi}{\lambda_c}\mathbf{k}^{\mathrm{T}}[t]u_1}, \cdots, e^{j\frac{2\pi}{\lambda_c}\mathbf{k}^{\mathrm{T}}[t]u_M}\right]^{\mathrm{T}}, \tag{4.2}$$

where

$$\mathbf{k}[t] = [\sin\psi[t]\cos\theta[t],\ \sin\psi[t]\sin\theta[t],\ \cos\psi[t]]^{\mathrm{T}}. \tag{4.3}$$

is the wave vector, and $\theta[t]$ and $\psi[t]$ are the azimuth and elevation AoD at the t^{th} sample, respectively. The location vector of the m^{th} antenna of the M URA, $\mathbf{u}_m$ is fixed as defined in (3.26).

In this system, the BS encodes the well-known pilot, pre-agreed between the BS and the MS, in K OFDM symbols that are dispatched over N different sub-carriers G times in sequential transmissions with power P. Consequently, the transmitted signal from the BS is

$$\mathbf{s}_n^g[t] = \sqrt{\kappa_t}\mathbf{F}_n^g[t]\mathbf{z}_n^g + \boldsymbol{\eta}_n^g[t], \tag{4.4}$$

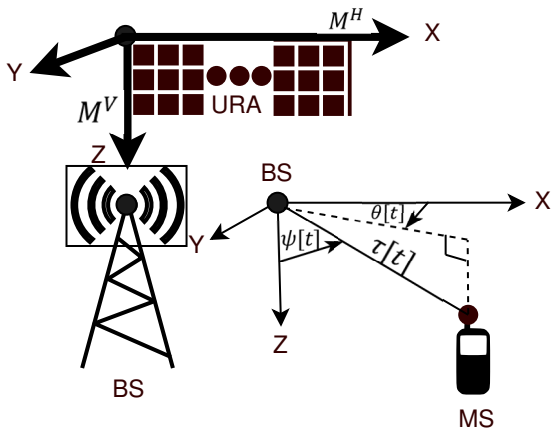

Figure 4.1: The 3D mmwave MISO-OFDM system.

where $\mathbf{z}_n^g \in \mathbb{C}^{K\times 1} = \left[z_n^{g^{(1)}}, \cdots, z_n^{g^{(K)}}\right]^{\mathrm{T}}$ is the OFDM symbols presenting the pilot during the g^{th} transmission with P power over the n^{th} sub-carrier, and $\mathbf{F}_n^g[t] \in \mathbb{C}^{M\times k}$ is the transmitter hybrid beamforming matrix. Besides, the transmitter quality is measured by $\kappa_t \in (0,1]$, and the HWIs term generated by the non-ideal transmitter, $\boldsymbol{\eta}_n^g[t] \in \mathbb{C}^{M\times 1}$, is independent of $\mathbf{z}_n^g$ and modeled as

$$\boldsymbol{\eta}_n^g[t] \sim CN(\mathbf{0}, \Lambda_n^g[t]), \tag{4.5}$$

where $\Lambda_n^g[t]$ is calculated as

$$\Lambda_n^g[t] = (1-\kappa_t)\mathrm{diag}\big(\Upsilon^g_{n_{(1,1)}}[t], \cdots, \Upsilon^g_{n_{(M,M)}}[t]\big), \tag{4.6}$$

accomplishing

$$\mathrm{tr}\left(\Lambda_n^g[t]\right) = P(1-\kappa_t)\ \forall n. \tag{4.7}$$

Regarding, $\Upsilon_n^g[t]$, it represents the covariance matrix that is defined as

$$\Upsilon_n^g[t] = \mathbb{E}\{(\mathbf{F}_n^g[t]\mathbf{z}_n^g)(\mathbf{F}_n^g[t]\mathbf{z}_n^g)^{\mathrm{H}}\},$$

and achieves $\mathrm{tr}(\Upsilon_n^g[t]) = P$. Consequently, the total transmitted power from the BS is

$$\mathbb{E}\left\{(\mathbf{s}_n^g[t])^{\mathrm{H}}(\mathbf{s}_n^g[t])\right\} = \kappa_t P + (1-\kappa_t)P = P\ \forall n.$$

Moreover, when the OFDM symbols of $\mathbf{z}_n^g$ have equal power, $\frac{P}{M}$, for simplicity, then the HWIs at the transmitter are $CN(\mathbf{0}, \frac{P}{M}(1-\kappa_t)\mathbf{I}_M)$ and achieve $\mathbb{E}\{\|\mathbf{s}_n^g[t]\|^2\} = P\ \forall n$.

The received signal by the non-ideal MS over the n^{th} subcarrier at the g^{th} transmission time is

$$y_n^g[t] = \sqrt{\kappa_t\kappa_r}\big(\mathbf{h}_n[t]\big)^{\mathrm{T}}\mathbf{F}_n^g[t]\mathbf{z}_n^g + \sqrt{\kappa_r}\big(\mathbf{h}_n[t]\big)^{\mathrm{T}}\boldsymbol{\eta}_n^g[t] + \eta_n^g[t] + w_n^g[t], \tag{4.8}$$

where $w_n^g[t] \sim CN(0,\sigma^2)$ denotes the additive white Gaussian noise (AWGN) at the t^{th} samples, and $\kappa_r \in (0,1]$ is the MS hardware quality factor, while $\eta_n^g[t] \sim CN(0,(1-\kappa_r)PM\rho^2[t])$ represents the MS HWIs distortion at the t^{th} sample. Besides, $y_n^g[t] \sim CN(\varphi_n^g[t], \sigma_y^2[t])$, where the mean

$$\varphi_n^g[t] = \sqrt{\kappa_t\kappa_r}(\mathbf{h}_n[t])^{\mathrm{T}}\mathbf{F}_n^g[t]\mathbf{z}_n^g, \tag{4.9}$$

while the variance is

$$\sigma_y^2[t] = PM(1-\kappa_t\kappa_r)\rho^2[t] + \sigma^2. \tag{4.10}$$

Moreover, the SNR of the signal in (4.8) is

$$\mathrm{SNR} = \frac{\kappa_t\kappa_r\rho^2[t]}{(1-\kappa_t\kappa_r)\rho^2[t] + (\sigma^2/MP)}, \tag{4.11}$$

and its asymptotic value when $P \to \infty$ or $M \to \infty$ is

$$\lim_{P \text{ or } M \to \infty} \text{SNR} = \frac{\kappa_t \kappa_r}{1 - \kappa_t \kappa_r}, \tag{4.12}$$

while it is

$$\lim_{P \text{ or } M \to \infty} \text{SNR} \to \infty, \tag{4.13}$$

in the case of ideal transceivers, i.e. $\kappa_t = \kappa_r = 1$. The asymptotic values practically imply that systems with only AWGN are different from non-ideal systems. In other words, improving the quality of the received pilots by boosting the transmission power or increasing the number of antennas is bounded in non-ideal systems due to the existence of the HWIs.

4.1.2 Measurements

The tracking solutions depend on the measurement. Specifically, the single-antenna MS with a non-ideal transceiver executes the tracking process by observing the pilots dispatched from the imperfect transceiver of the BS. Consequently, it estimates its range and direction relevant to the reference BS. In this context, estimating the range $\tau[t]$, and the direction $\theta[t]$ and $\psi[t]$, for any arbitrary t^{th} sample, these parameters are approximated using the following ML technique, specifically by maximizing the log-likelihood function that is:

$$\begin{aligned} \hat{L}(\tau[t], \theta[t], \psi[t]) = &-\frac{NG}{2} \ln(2\pi(PM(1-\kappa_{tx}\kappa_{rx})\hat{\rho}^2[t] + \sigma^2)) \\ &- \frac{\sum_{g=1}^{G} ||\mathbf{y}^g[t] - \sqrt{\kappa_{tx}\kappa_{rx}}\hat{\rho}[t] e^{j\hat{\phi}[t]} \mathbf{w}^g[t]||^2}{2(PM(1-\kappa_{tx}\kappa_{rx})\hat{\rho}^2[t] + \sigma^2)}. \end{aligned} \tag{4.14}$$

where $\mathbf{y}^g[t] = \left[y_0^g[t], \ldots, y_{N-1}^g[t]\right]^{\mathrm{T}}$ as given in (4.8),

$$\mathbf{w}^g[t] = \begin{bmatrix} \alpha^{\mathrm{T}}[t] \mathbf{F}_0^g[t] \mathbf{z}_0^g \\ \vdots \\ e^{-j2\pi[N-1]\frac{\tau[t]}{NT}} \alpha^{\mathrm{T}}[t] \mathbf{F}_{N-1}^g[t] \mathbf{z}_{N-1}^g \end{bmatrix},$$

$$\hat{\rho}[t] = \sqrt{\frac{\left(\sum_{g=1}^{G} \left\| \mathbf{y}^g[t] - \frac{\sum_{i=1}^{G} (\mathbf{w}^i[t])^{\mathrm{H}} \mathbf{y}^i[t]}{\sum_{i=1}^{G} ||\mathbf{w}^i[t]||^2} \mathbf{w}^g[t] \right\|^2\right) - NG\sigma^2}{NGPM(1-\kappa_t\kappa_r)}}, \tag{4.15}$$

and

$$e^{j\hat{\phi}[t]} = \frac{\sum_{g=1}^{G} \left(\mathbf{w}^g[t]\right)^{\mathrm{H}} \mathbf{y}^g[t]}{\sqrt{\kappa_t \kappa_r}\, \rho[t] \sum_{g=1}^{G} \left\| \mathbf{w}^g[t] \right\|^2}.$$

The numerical search is used in finding the optimal values of $\hat{\Theta} = \left[\hat{\tau}[t], \hat{\theta}[t], \hat{\psi}[t]\right]^{\mathrm{T}}$, which maximize the log-likelihood function in (4.14) since it does not have a closed-form solution.

It is intuitive that the estimated values of $\hat{\Theta}$ are a noisy version of the real values of Θ, represented as follows

$$\hat{\Theta}[t] = \Theta[t] + \mathbf{w}[t], \tag{4.16}$$

where the vector $\mathbf{w}[t] \in \mathbb{R}^{3\times 1}$ presents the estimation process error at the t^{th} position sample with the covariance matrix $\mathbf{C}[t] \in \mathbb{R}^{3\times 3}$. It is known that the ML estimator is an unbiased estimator and its outputs are Gaussian random variables, and thus $\hat{\Theta}[t] \sim CN\Big(\Theta[t], \mathbf{C}[t]\Big)$.

4.1.3 Range-Direction Tracking and Bayesian Cramer-Rao bound

This subsection investigates the range and direction tracking of an MS considering the practical scenario of hardware-impaired BS and MS. In this regard, we propose estimating the range and direction values by optimizing (4.14). Then, we treat these estimated values based on KF sequences, considering the range and the direction transition model. This section adopts KF as it can achieve an optimal tracking process since the range and direction have a Gaussian transition model and the estimated range and direction values, output from the ML estimator are also Gaussian. [1]

4.1.3.1 Kalman Filter Based Tracker

Coming to the transition model of Θ, the difference between two successive samples is modeled as independent Gaussian noise [49, 58, 64]. Consequently, the transition model of Θ from sample to sample is

$$\Theta[t] = \Theta[t-1] + \mathbf{u}[t], \tag{4.17}$$

where $\mathbf{u}[t] \sim N(\mathbf{0}, \mathbf{Q})$, $\mathbf{Q} = \text{diag}\Big([\sigma_\tau^2, \sigma_\theta^2, \sigma_\psi^2]\Big)$, and the values of $\sigma_\tau^2, \sigma_\theta^2$ and σ_ψ^2 should depend on the possible change in these components from sample to sample. Moreover, the conditional probability of $\Theta[t]$ given $\Theta[t-1]$ is

$$p\Big(\Theta[t]\Big|\Theta[t-1]\Big) \sim N\Big(\Theta[t-1], \mathbf{Q}\Big). \tag{4.18}$$

Besides, due to independence between any two samples of $\mathbf{u}[t]$, then

$$p\Big(\Theta[t]\Big|\Theta[0:t-1]\Big) = p\Big(\Theta[t]\Big|\Theta[t-1]\Big),$$

where $\Theta[0:t-1]$ is the collection of tracked values from the first sample to the $t-1$ sample.

Then, since the signal vector in (4.17) is according to the Gauss-Markov model, and considering that the signal vector $\Theta[t]$ and the ML estimation error $\mathbf{w}[t]$ are jointly Gaussian, then the

[1] This work was accepted as "Range-Direction Tracking and Bayesian Cramer-Rao Bound Analysis in mmwave Systems Equipped with Imperfect Transceivers," in IEEE Wireless Communications Letters, doi: 10.1109/LWC.2023.3295727.

KF has an optimal performance regarding the $\Theta[t]$ tracking process, where the tracking process is performed based on the estimated values from the beginning to the t^{th} sample, $\hat{\Theta}[0:t]$, and using the sequential equations in (2.43) in section 2.3.5.1

It is important to note in these equations that the Kalman gain matrix $\mathbf{K}$ determines the degree of measurement tracking based on the uncertainty level of the measurements matrix $\mathbf{C}$ in comparison to the uncertainty level of the model $\mathbf{Q}$. Concerning the $\mathbf{C}$ matrix, it can be concluded that the accuracy of describing the level of uncertainty in the estimation process leads to accurate tracking. Therefore, this work selects $\mathbf{C}$ according to the CRB of the estimation process. However, when the ML estimation cannot achieve the CRB (i.e., in the case of HWIs), this work suggests determining $\mathbf{C}$ as the average of the estimation errors based on the MC technique. Specifically, in this method, we generate a sufficient number of uniformly and randomly distributed $\Theta[t]$ in the area of the range and direction change, where these points are different from those that will be used later in the tracking scenario. Next, the estimation process and the measurements are performed for each $\Theta[t]$ in a sufficient number of realizations. We assumed a sufficient number of these random values for the AWGN and HWIs noises. Later, the measurement error matrices are averaged over the realizations for each $\hat{\Theta}[t]$. After that, the resulting averaged matrices for all $\hat{\Theta}[t]$ are averaged again to obtain the covariance matrix that is used to represent the measurement error during the tracking process.

4.1.3.2 Bayesian Cramer-Rao bound

Here we derive the BCRB that presents the most achievable accuracy when tracking Θ of MS moving in mmwave MISO-OFDM system. Initially, we present the observation FIM that measures the amount of information obtained from the observations in (4.8) distorted by the HWIs. The inverse of the observation FIM represents the estimation uncertainty matrix used for tracking gain in (2.43c). Next, we derive the BIM by combining the information obtained from the observations with the a priori information in (4.18). After that, calculating the BCRB benchmark is through the inverse of the BIM.

The elements of the observation FIM $\mathbf{J}_{\Theta}[t] \in \mathbb{R}^{3\times3}$, are given according to the EFIM formula in (2.24) in section 2.3.2, as $\Theta[t]$ is a part of $\beta[t] = \left[\Theta[t], \rho[t], \phi[t]\right]$. In this context, $\mathbf{J}_{\beta}[t] \in \mathbb{R}^{5\times5}$, representing the FIM of $\beta[t]$ at the t^{th} sample, is calculated according to (3.19) in section 3.1, where $\varphi_n^g[t]$ and $\sigma_y^2[t]$ are the mean and the noise variance of the received signal in (4.8) at the t^{th}, respectively. Besides, these elements of $\mathbf{J}_{\beta}[t]$ at each sample are calculated as shown in subsection 3.2.4.

At the t^{th} sample, the BIM of $\Theta[t]$, $\mathbf{J}_{\Theta}^{(\text{B})}[t] \in \mathbb{R}^{3\times3}$, counting the information obtained from the observations in (4.8) and the a priori information in (4.18), is calculated according to (2.29) as

$$\mathbf{J}_{\Theta}^{(\text{B})}[t] = \underbrace{\mathbf{J}_{\Theta}[t]}_{\text{Observations}} + \underbrace{\mathbf{G}_{22}[t] - \mathbf{G}_{21}[t]\left[\mathbf{J}_{\Theta}^{(\text{B})}[t-1] + \mathbf{G}_{11}[t]\right]^{-1}\mathbf{G}_{12}[t]}_{\text{A priori Information}}, \tag{4.19}$$

where the superscript (B) refers to Bayesian, and $\mathbf{G}_{11}[t] = \mathbf{G}_{22}[t] = -\mathbf{G}_{12}[t] = -\mathbf{G}_{21}[t] = \mathbf{Q}^{-1}$, according to the definition in (2.33) and the derivation in section 2.3.4.

4.1.3.3 Simulation Results

In this subsection, we conduct numerical experiments to investigate the range and direction tracking process of the single-antenna MS in the system described in section 3.2. In these experiments, we assume that the initial state of the MS is $\Theta[0] = [10^{-8}, \pi/4, \pi/4]$, and the dynamic transition between 300 samples is according to (4.18) with $\mathbf{Q} = \text{diag}([10^{-18}, 10^{-4}, 10^{-4}])$.

The tracking process is executed based on two pillars. Firstly, $\hat{\Theta}$ is obtained by optimizing (4.14), and it is then processed by the KF sequence in (2.43) in subsection 2.3.5.1, and this is done in combination with the transition model in (4.17). These procedures are repeated every t^{th} sample. Accordingly, Fig.4.2 presents the range τ and direction angles θ, ψ tracking errors concerning different values of κ. Firstly, the figure depicts the tracking process accuracy without processing the estimated data by *KFT* sequence, which is called *Data-Only*. Next, the figure conducts a comparison with *KFT-MC* illustrating the tracking accuracy gained by *KFT* measurement processing, where *KFT-MC* describes the measurement errors of $\hat{\Theta}$, i.e. the $\mathbf{C}$ matrix, based on the MC computer simulation method. After that, presenting the proposed *KFT-MC* advantages, the figure shows a comparison with *KFT-CRB* that determines the $\mathbf{C}$ matrix based on the CRB analysis of $\hat{\Theta}$. Lastly, it compares all the achievable accuracy with the minimum possible errors illustrated by the BCRB.

Moreover, the figure illustrates that the tracking accuracy in terms of RMSE and the BCRB deteriorates as the quality of the transceivers, κ, is reduced. However, increasing pilot transmission power P enhances the accuracy that is unfortunately bounded by the HWIs, which is not the case with the ideal hardware. Regarding the ideal case, increasing P continuously enhances the tracking accuracy that matches the BCRB when the received pilot's quality, $\frac{P\rho^2}{\sigma^2}$, is high enough. On the other hand, the non-ideal hardware saturates the pilot's quality at a value that is not high enough to make the tracking accuracy match the BCRB. In the same context, when the pilot

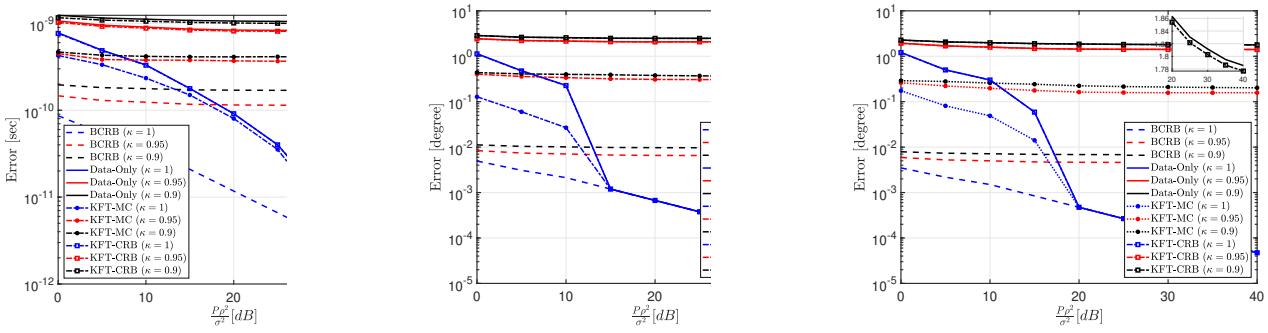

(a) Range(τ) (b) Azimuth (θ) (c) Elevation (ψ)

Figure 4.2: Tracking error and BCRB versus the transmission power with different κ.

transmission power P is small i.e., small $\frac{P\rho^2}{\sigma^2}$, then the HWIs noise is low and the reduction of the tracking accuracy becomes approximately independent of the κ values.

Fortunately, *KFT-MC* presents significant enhancements in the tracking accuracy for both impaired and ideal transceivers. Regarding the impaired transceivers, the proposed *KFT-MC* overcomes the HWIs limits and improves the tracking accuracy over the $\frac{P\rho^2}{\sigma^2}$ range. However, with perfect transceivers, the impact of the *KFT-MC* becomes more significant at the range of small $\frac{P\rho^2}{\sigma^2}$ values, but has negligible enhancements at the range of high $\frac{P\rho^2}{\sigma^2}$ values.

Furthermore, it can be concluded from Fig.4.2 that an accurate description of the measurement errors, the $\mathbf{C}$ matrix, improves the tracking accuracy. In detail, the figure presents that the tracking accuracy of the *KFT-MC* scenario is better than that of the *KFT-CRB* scenario. The reason for this is that the *KFT-MC* approach formulates a more realistic covariance matrix $\mathbf{C}$ than the *KFT-CRB*, which considers the accuracy that is never achieved due to the HWIs or due to not a high enough value of $\frac{P\rho^2}{\sigma^2}$ in the ideal case. On a side note, when the estimation accuracy is close to the CRB (as in range $\hat{\tau}$), the *KFT-CRB* enhances the tracking accuracy, while when the estimation accuracy is far from the CRB (as in $\hat{\theta}$ and $\hat{\psi}$), the *KFT-CRB* slightly enhances the tracking accuracy.

4.1.4 Position Tracking and Bayesian Cramer-Rao bound

This subsection investigates the tracking process of a maneuvering MS that exists in the mmwave MISO-OFDM system. More specifically, the MS moves in a maneuvering style and tries to track its position that evolves with time relying on the broadcast pilots from the reference BS. For tracking purposes, the MS estimates the channel parameters, i.e. the AoD $\theta[t], \psi[t]$ and the ToF $\tau[t]$, periodically at every t^{th} position/time sample. Then, it accomplishes the tracking process by implementing the EKF for each t^{th} sample, working with all previously estimated values until the t^{th} current sample. To achieve an accurate tracking process, this work designs the EKF considering the estimation errors due to HWIs and the MS maneuvering behavior.

4.1.4.1 Extended Kalman Filter Based Tracker

As Fig.4.3 depicts, at any arbitrary t^{th} position/time sample, when the MS occupies the unknown position $\mathbf{P}[t] = \left[x[t],\, y[t],\, z[t]\right]^{\text{T}}$, the channel parameters $\tau[t]$, $\theta[t]$, and $\psi[t]$ are directly connected with the system coordinates through the following geometric relationships:

$$\begin{aligned}
\tau[t] &= \sqrt{x^2[t] + y^2[t] + z^2[t]}/c, \\
\theta[t] &= \text{atan2}\left(y[t], x[t]\right) \\
\psi[t] &= \sin^{-1}\left(\frac{\sqrt{x^2[t] + y^2[t]}}{\sqrt{x^2[t] + y^2[t] + z^2[t]}}\right),
\end{aligned} \tag{4.20}$$

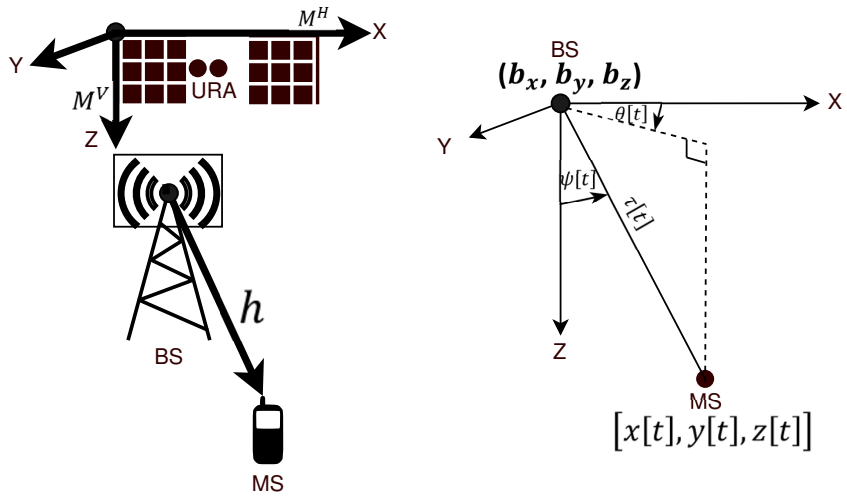

Figure 4.3: The 3D mmwave MISO-OFDM system.

and without loss of generality, this occurs when the BS position is at the origin.

In regard to the dynamics of MS mobility, the MS is considered to have a maneuvering behavior since it changes its position between any two successive samples as independent Gaussian noise [58]. Considering that the MS position at the t^{th} sample is $\mathbf{P}[t]$, then the Markov probability transition model introduced for the successive MS tracking problem is given as

$$\mathbf{P}[t] = \mathbf{P}[t-1] + \mathbf{u}[t], \tag{4.21}$$

where the random MS motion vector $\mathbf{u}[t]$ is modeled as a zero-mean Gaussian random vector with the covariance matrix $\mathbf{Q}$, i.e. and $\mathbf{u}[t] \sim N(\mathbf{0}, \mathbf{Q})$. It should be noted that $\mathbf{Q} = \text{diag}\big([\sigma_x^2, \sigma_y^2, \sigma_z^2]\big)$, and the values σ_x^2, σ_y^2, and σ_z^2 are the variances of the random motion in x, y, and z axes. Moreover, $\mathbf{Q}$ is time-invariant, independent of the t, and its diagonal elements only depend on the possible change in the 3D position components from sample to sample. Moreover, according to [58], for any two samples $t \neq t'$, $\mathbf{u}[t]$ and $\mathbf{u}[t']$ are independent and achieve $\mathbb{E}\{\mathbf{u}[t]\mathbf{u}^{\text{T}}[t']\} = \mathbf{0}\ \forall\ t \neq t'$, which implies that $\mathbf{u}[t]$ is a vector (WGN).

Besides, the initial state of the position vector $\mathbf{P}[-1]$ is modelled as a Gaussian random variable: $\mathbf{P}[-1] \sim N\Big(\mathbf{P}_0, \mathbf{Q}_0\Big)$, which is also independent of $\mathbf{u}[t]$. It's important to note here that $\mathbf{P}_0$ and $\mathbf{Q}_0$ are the initial values of the tracker in subsection 2.3.5.2. Moreover, these initials can be determined arbitrarily or based on some previous information, and their impact shortly becomes negligible as the number of samples increases [85]. Coming to the prior information of the MS movement, based on (4.21), the conditional probability of $\mathbf{P}[t]$ given $\mathbf{P}[t-1]$ is

$$p\Big(\mathbf{P}[t]|\mathbf{P}[t-1]\Big) \sim N\Big(\mathbf{P}[t-1], \mathbf{Q}\Big). \tag{4.22}$$

Accordingly, since for any two samples $t \neq t'$, $\mathbf{u}[t]$ and $\mathbf{u}[t']$ in (4.21) are independent, thus the MS positions $\mathbf{P}[t]$ form a Markov chain satisfying

$$p\Big(\mathbf{P}[t]|\mathbf{P}[0:t-1]\Big) = p\Big(\mathbf{P}[t]|\mathbf{P}[t-1]\Big), \tag{4.23}$$

where $\mathbf{P}[0:t-1]$ is the collection of user positions from the first sample to the $t-1$ sample.

In arriving at the observation vector, it is obvious that the estimated values of $\hat{\Theta}[t]$ rely on the real values of $\mathbf{P}[t]$ as follows

$$\hat{\Theta}[t] = \mathbf{f}\big(\mathbf{P}[t]\big) + \mathbf{w}[t], \tag{4.24}$$

since the real $\Theta[t]$ is a function of the signal vector, as can be seen below

$$\Theta[t] = \mathbf{f}\big(\mathbf{P}[t]\big) = \begin{bmatrix} \frac{\sqrt{x^2[t]+y^2[t]+z^2[t]}}{c} \\ \text{atan2}(y[t], x[t]) \\ \sin^{-1}\left(\frac{\sqrt{x^2[t]+y^2[t]}}{\sqrt{x^2[t]+y^2[t]+z^2[t]}}\right) \end{bmatrix}. \tag{4.25}$$

Naturally, the signal vector $\mathbf{P}[t]$ and the noises are jointly Gaussian, and thus the KF is an optimal sequential MMSE estimator for $\mathbf{P}[t]$. Unfortunately, the KF is inapplicable since the observation vector $\Theta[t]$ and the signal vector $\mathbf{P}[t]$ have a non-linear relationship [85]. However, by the linearization of $\mathbf{f}\big(\mathbf{P}[t]\big)$, it is possible to implement a suboptimal tracking process depending on EKF [85]. Consequently, using Taylor's expansion, the linearized relationship of $\mathbf{f}\big(\mathbf{P}[t]\big)$ is given as

$$F[t] \in \mathbb{R}^{3\times 3} = \frac{\partial \mathbf{f}\big(\mathbf{P}[t]\big)}{\partial \mathbf{P}[t]}\Big|_{\mathbf{P}[t]=\hat{\mathbf{P}}[t|t-1]}, \tag{4.26}$$

where the elements of the linearized relationship matrix, the Jacobian matrix $F[t]$, are zeros except the following:

$$\big[F[t]\big]_{(1,1)} = \frac{\partial \tau[t]}{\partial x[t]} = \frac{x[t]}{c\sqrt{x^2[t]+y^2[t]+z^2[t]}},$$

$$\big[F[t]\big]_{(1,2)} = \frac{\partial \tau[t]}{\partial y[t]} = \frac{y[t]}{c\sqrt{x^2[t]+y^2[t]+z^2[t]}},$$

$$\big[F[t]\big]_{(1,3)} = \frac{\partial \tau[t]}{\partial z[t]} = \frac{z[t]}{c\sqrt{x^2[t]+y^2[t]+z^2[t]}},$$

$$\big[F[t]\big]_{(2,1)} = \frac{\partial \theta[t]}{\partial x[t]} = \frac{-y[t]}{x^2[t]+y^2[t]},$$
$$\big[F[t]\big]_{(2,2)} = \frac{\partial \theta[t]}{\partial y[t]} = \frac{x[t]}{x^2[t]+y^2[t]},$$

$$\big[F[t]\big]_{(3,1)} = \frac{\partial \psi[t]}{\partial x[t]} = \frac{|z[t]|\,x[t]}{(x^2[t]+y^2[t]+z^2[t])\sqrt{x^2[t]+y^2[t]}},$$
$$\big[F[t]\big]_{(3,2)} = \frac{\partial \psi[t]}{\partial y[t]} = \frac{|z[t]|\,y[t]}{(x^2[t]+y^2[t]+z^2[t])\sqrt{x^2[t]+y^2[t]}},$$
$$\big[F[t]\big]_{(3,3)} = \frac{\partial \psi[t]}{\partial z[t]} = \frac{-z[t]\sqrt{x^2[t]+y^2[t]}}{|z[t]|\,(x^2[t]+y^2[t]+z^2[t])}. \tag{4.27}$$

Now this tracking process can be solved using the EKF sequence in section 2.3.5.2. Additionally, in this tracking process, we use the MC technique in determining the measurement uncertainty level represented by matrix $\mathbf{C}$. Specifically, since the ML estimation cannot achieve the CRB (i.e., in the case of HWIs), this work suggests determining $\mathbf{C}$ as the average of the estimation errors based on the MC technique, the same technique used in subsection 4.1.3.

4.1.4.2 Bayesian Cramer-Rao bound

This subsection derives the benchmark of the position tracking process running in a 3D mmwave MISO-OFDM system suffering from HWIs. To do so, we start by computing the BIM that heavily depends on two types of information, the first being that around the tracked positions obtained from the observations in (4.8), and the second being that which is a priori known in (4.22). Regarding the first type, it is represented by the observation FIM that is computed for each position sample, assuming the MS is fixed at each sample and taking into account the harmful impact of the HWIs. As well, in the same context, it is significantly useful to obtain the observation FIM of $\hat{\Theta}[t]$ and then its CRB as they are exploited in the design of $\mathbf{C}[t]$ matrix in (2.52c).

We then look at the a priori information in (4.22), which describes the uncertainty in MS motion. Next, the useful information from the observations and the priori information is incorporated together with the purpose of calculating the BIM. This way, we can obtain the BCRB from the pseudo-inverse operation of the BIM.

Let's define $\mathbf{J}_{\mathbf{P}}^{(\mathrm{B})}[t] \in \mathbb{R}^{3\times 3}$ as the BIM of the position at the arbitrary t sampleis, and $\mathbf{J}_{\mathbf{P}}^{(\mathrm{M})}[t] \in \mathbb{R}^{3\times 3}$ as the observation FIM, then BIM is given by (2.29), where according to section 2.3.4 and the a priori information in (4.22), the $\mathbf{G}[t]$ matrices are:

$$\mathbf{G}_{11}[t] = \mathbf{G}_{22}[t] = -\mathbf{G}_{12}[t] = -\mathbf{G}_{21}[t] = \mathbf{Q}^{-1} \in \mathbb{R}^{3\times 3}. \tag{4.28}$$

Coming to the useful information gained from the observations, it is clear that the pilot in (4.8) is not directly dependent on the MS coordinates $\mathbf{P}$. Instead of, it is a function of the channel parameters that are connected with coordinates by the geometric relationships in (4.20). Therefore, we find the FIM that measures the amount of information from the pilots around the channel parameters first, and then we transform it into the FIM of the position according to the formula in (2.19). Accordingly, we define the vector of the downlink channel parameters at the t^{th} position as follows

$$\boldsymbol{\beta}[t] = [\tau[t],\, \theta[t],\, \psi[t],\, \rho[t],\, \phi[t]]^{\mathrm{T}},$$

and find the FIM of $\boldsymbol{\beta}[t]$, $\mathbf{J}_{\boldsymbol{\beta}}^{(\mathrm{M})}[t] \in \mathbb{R}^{5\times 5}$, from (2.20).

Following that, we transform the $\mathbf{J}_{\boldsymbol{\beta}}^{(\mathrm{M})}[t]$ matrix to FIM of the position vector $\mathbf{J}_{\mathbf{P}}^{(\mathrm{M})}[t] \in \mathbb{R}^{3\times 3}$ as

$$\mathbf{J}_{\mathbf{P}}^{(\mathrm{M})}[t] = \mathbf{T}^{\mathrm{T}}[t]\mathbf{J}_{\boldsymbol{\beta}}^{(\mathrm{M})}[t]\mathbf{T}[t], \tag{4.29}$$

where $\mathbf{T}[t]$ is the transformation matrix at the t^{th} sample that is defined in (2.19). It is worth noting the following transformation matrix

$$\left[\mathbf{T}[t]\right]_{(1:3,1:3)} = F^{\mathrm{T}}[t], \tag{4.30}$$

where $F[t]$ is defined in (4.26), and the remaining elements of the transformation matrix $\mathbf{T}$ are zeros. It is also important to note that the following vectors and matrices $\boldsymbol{\beta}, \mathbf{J}_{\boldsymbol{\beta}}^{(\mathrm{M})}, \mathbf{T}$, and $\mathbf{J}_{\mathbf{P}}^{(\mathrm{M})}$ depend on MS location and are updated from one position to another.

By initializing the BIM as $\mathbf{J}_{\mathbf{P}}^{(\mathrm{B})}(0)$, according to (2.36), the BIM at the t^{th} position can be evaluated recursively as in (2.29), and consequently the BCRB of tracking $\mathbf{P}[t]$ at the t^{th} sample is given by computing the inverse of $\mathbf{J}_{\mathbf{P}}^{(\mathrm{B})}[t]$. In this way, the dynamic PEB is given by

$$\mathrm{PEB}[t] = \sqrt{\left[\mathbf{J}_{\mathbf{P}}^{(\mathrm{B})}[t]\right]_{(1,1)}^{-1} + \left[\mathbf{J}_{\mathbf{P}}^{(\mathrm{B})}[t]\right]_{(2,2)}^{-1} + \left[\mathbf{J}_{\mathbf{P}}^{(\mathrm{B})}[t]\right]_{(3,3)}^{-1}}. \tag{4.31}$$

4.1.4.3 Simulation Results

In this subsection, we conduct numerical experiments to investigate tracking the position of a maneuvering MS, considering a realistic scenario where the MS and the BS are non-ideal transceivers in the perfectly synchronized 3D mmwave MISO-OFDM system. The configurations of the numerical experiments are described in the simulation subsection 3.2.5. For tracking purposes, the MS initializes its journey from the position [5, 5, 5] and moves between $S = 300$ sample positions according to the (4.22). Moreover, it is assumed that the average movement distance of the MS between adjacent samples is determined by $\mathbf{Q} = \mathrm{diag}\big([0.1,\, 0.1,\, 0.1]\big)$ accomplishing $\mathbb{E}\{\|\mathbf{P}[t] - \mathbf{P}[t-1]\|_2\} = \sqrt{0.3}$ m. To evaluate the tracking process, we present the theoretical accuracy in terms of PEB defined in (4.31) when discussing BCRB. Besides, the performance of EKF is presented in the RMSE that is defined as

$$\mathrm{RMSE} = \sqrt{\mathbb{E}\left\{\frac{\|\mathbf{P}[t] - \hat{\mathbf{P}}[t]\|_2^2}{S}\right\}}.$$

Figs.4.4 and 4.5 present the achieved accuracy of the tracking process based on the mobile motion uncertainty and the noisy measurements, $\hat{\Theta}$. Regarding the latter, Fig.4.4 depicts the tracking process accuracy considering two causes of noise affecting the measurements. As expected, the quality of the measurements is highly related to the perfectness of the transceivers, as well as to the accuracy of the optimization algorithm of (4.14). It is worth remembering here that the accuracy of the search algorithm for optimizing (4.14) is affected by the number of searching points in the 3D grid over $\Theta = \left[\tau,\, \theta,\, \psi\right]^{\mathrm{T}}$.

This figure considers two levels of HWIs distortion $\kappa = 0.95, 0.9$, and two levels of estimation accuracy, A and L for accurate and low accuracy, respectively. Moreover, the figure presents the accuracy of the tracking process that only depends on the measurement accuracy without

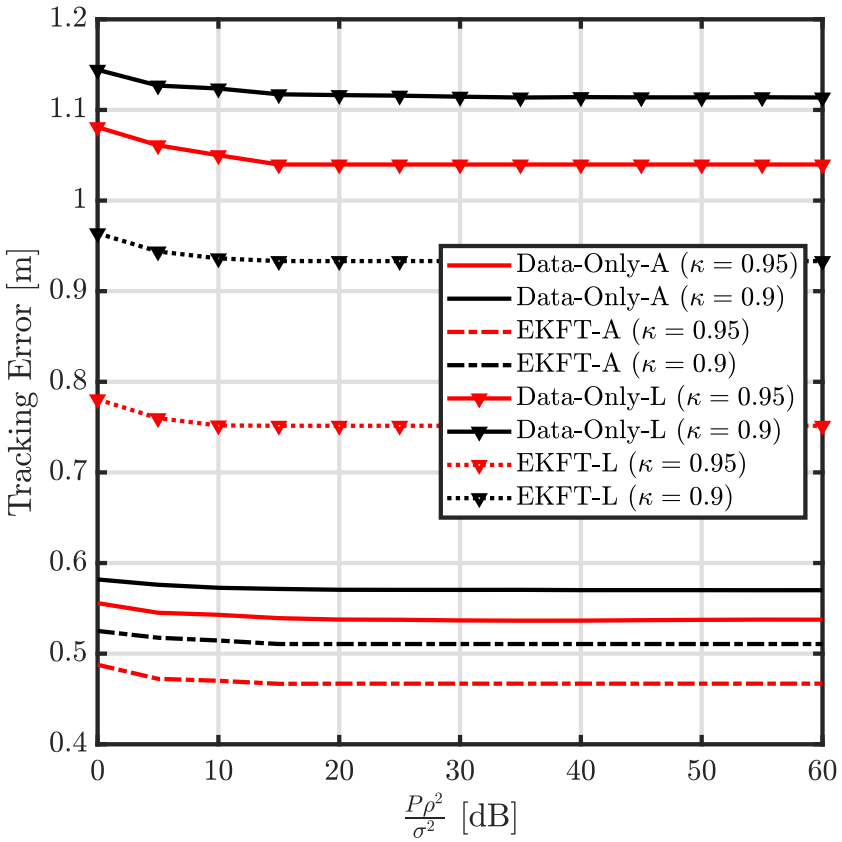

Figure 4.4: Tracking error versus transmission power with different $\hat{\Theta}[t]$ estimation accuracy.

processing by EKFT, which is titled as "*Data-Only*" tracking process. Then, the figure compares the *Data-Only* tracking process with the tracking process that takes into account both the measurement accuracy and the mobility model, "*EKFT*". It is clear from the figure that as the quality of the measurements increases, i.e. enhancing the estimator accuracy and/or the transceiver quality, the tracking accuracy improves. Additionally, it is noted that the tracking with *EKFT* is more accurate than *Data-Only* tracking as it benefits from prior information around the MS motion.

Fig.4.5 illustrates in greater detail the tracking process, where the figure compares *EKFT* and *Data-Only* in the case of ideal transceivers, $\kappa = 1$. As in the previous figure, *EKFT* outperforms the *Data-Only* method in accuracy. However, unlike the *Data-Only* model, the accuracy of *EKFT* is bounded when $\frac{P\rho}{\sigma^2} \geq 30$[dB]. We consider the case of high-quality observations, where $\frac{P\rho}{\sigma^2} \geq 30$[dB] simultaneously with an accurate optimizer, and which leads to perfect and noiseless measurements. In the case of perfect measurements, the *EKFT* accuracy is limited due to the linearization inaccuracy, and thus, it is worth depending on the noiseless measurements that however are not easy to achieve.

Fig.4.6 presents the accuracy of the tracking process in terms of RMSE and the BCRB at different values of κ. The figure clarifies that the tracking accuracy deteriorates as the HWIs noise

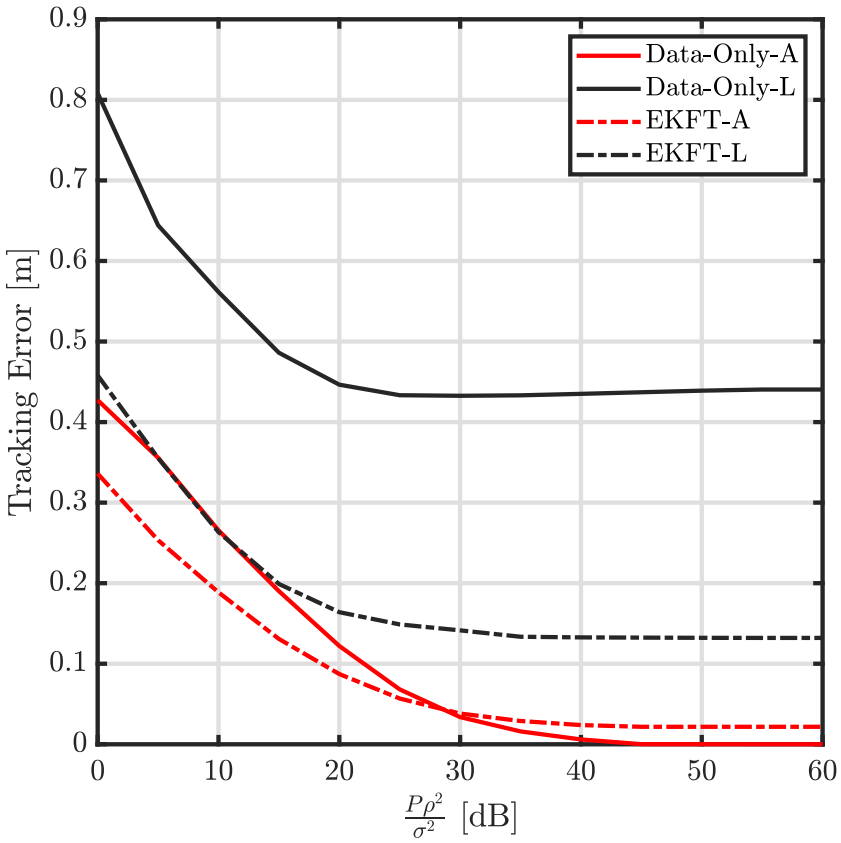

Figure 4.5: Tracking error versus transmission power with different $\hat{\Theta}$ estimation accuracy given to no HWIs $\kappa = 1$.

becomes more significant (represented by κ). Besides, it is clear that increasing the transmission power improves the tracking accuracy, as the BCRB and RMSE of EKFT indicate. However, the accuracy enhancements due to increasing the transmission power are limited since increasing the transmission also magnifies the HWIs noise as seen in (4.10). On the other hand, in the case of ideal transceivers, boosting the transmission power improves the tracking accuracy constantly, and with no limit in the case of the theoretical assumption *Data-Only*, or reaching the linearization bound in the *EKFT* case. Importantly, the linearization bound prevents the *EKFT* method from matching the BCRB, while the *Data-Only* approach achieves the BCRB when the $\frac{P\rho}{\sigma^2}$ values are high enough.

Fig. 4.7 demonstrates that a more appropriate selection of the $\mathbf{C}$ matrix helps the *EKFT* compensate for the lack of measurement accuracy, where the figure presents the accuracy of the tracking process in terms of RMSE, with different κ and $\mathbf{C}$ matrix values. Specifically, the figure presents two scenarios with the *EKFT*, where the first scenario, referred to as the *CRB*, occurs when the $\mathbf{C}$ matrix is the average of the CRBs of the Θ estimation processes. The second scenario occurs when the $\mathbf{C}$ matrix is the average of the RMSE for the estimation processes of Θ based on the MC computer simulation.

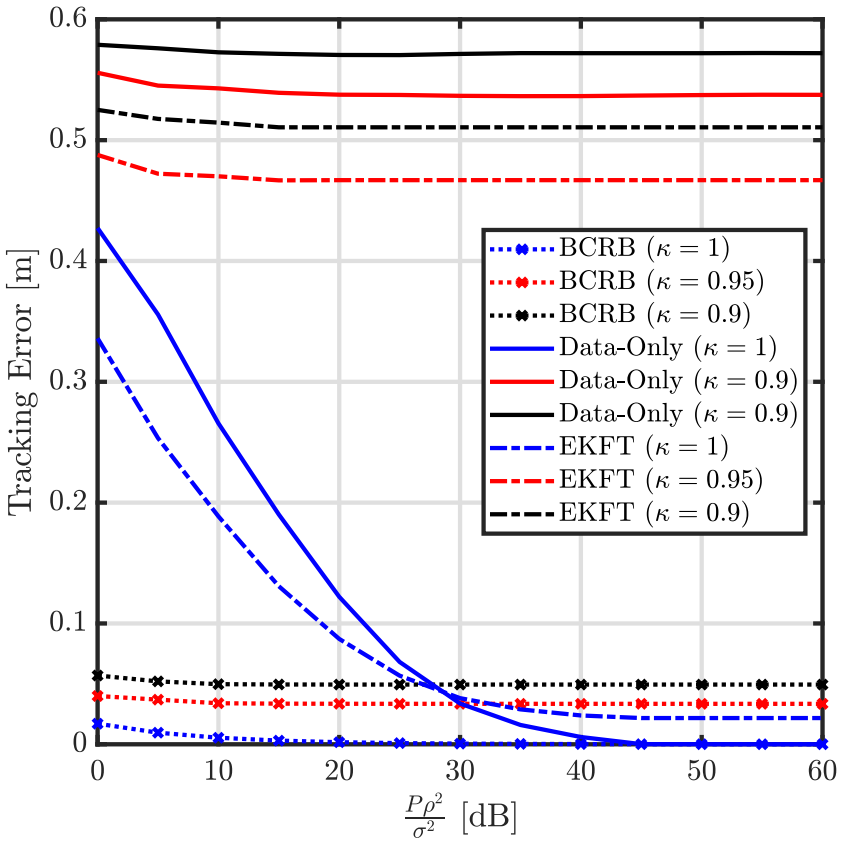

Figure 4.6: Tracking error and BCRB versus transmission power with different HWIs levels κ.

In Fig.4.7, we can note improvements to the tracking accuracy of the *MC* scenario, leading it to outperform the *CRB* scenario for both impaired and ideal transceivers. Regarding the perfect transceivers, the impact of the *MC* becomes more significant at low-quality received pilots, i.e. the range of small $\frac{P\rho^2}{\sigma^2}$ values, but no difference in the tracking accuracy at the range of high $\frac{P\rho^2}{\sigma^2}$ values. The reason is that the *MC* approach formulates a more realistic covariance matrix $\mathbf{C}$ than that from the *CRB* case. The matrix $\mathbf{C}$ in the *CRBcase* represents the accuracy of the estimation process, which never achieves the bound due to the HWIs or due to the low values of $\frac{P\rho^2}{\sigma^2}$ in the ideal case. However, when the $\frac{P\rho^2}{\sigma^2}$ value is high enough, there are no differences between the accuracy associated with the case of *CRB* and that of the *MC* case.

Fig.4.8 investigates the impact of the number of antennas at the BS on the tracking accuracy, as indicated by the BCRB. Evidently, adding more antennas to the BS improves the tracking accuracy at the cost of hardware complexity. However, these improvements in accuracy are bounded because of the HWIs, which is not the case when the transceivers are ideal. It is clear from (4.9) and (4.10) that the addition of more antennas enhances the power of the received pilot and the distortion of HWIs, at least in the case of imperfect transceivers. On the other side, the harmful noise distorting the received pilot in the case of ideal transceivers is independent of the number of antennas, which means that adding more antennas is equivalent to achieving more

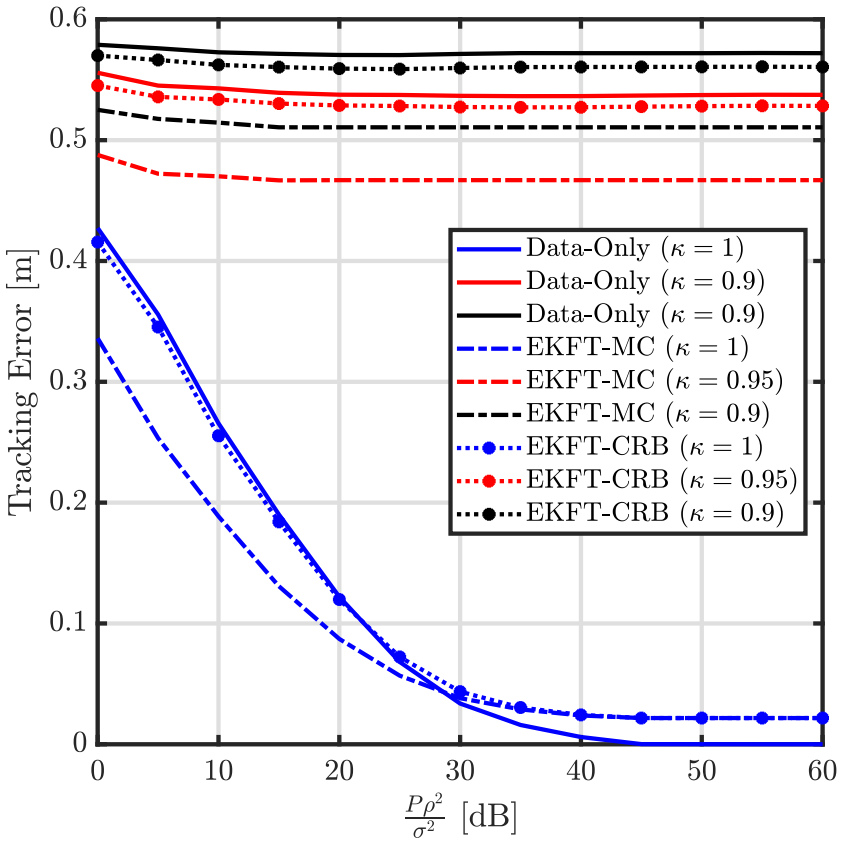

Figure 4.7: Tracking error versus transmission power with different $\mathbf{C}$ design and HWIs levels κ.

accuracy.

4.2 Tracking in asynchronous RIS-assisted mmwave MISO-OFDM system

This section investigates the tracking in a RIS-assisted mmwave MISO-OFDM system, targeting realistic circumstances where the theoretical assumptions of a perfectly synchronous system and ideal transceivers no longer exist. We implement KF for tracking purposes paying attention to synchronization errors and HWIs-driven accuracy degradation. Specifically, the tracking process depends on the estimated positions obtained from the 4D grid search algorithm and the cost function in (3.69) in section 3.3, additionally to the transition model of the MS described in (4.34). Next, we present the theoretical bounds of the accuracy of the tracking process in the BCRB term. Lastly, we conduct computer simulations to discuss the tracking process and the BCRB considering the mentioned circumstances.

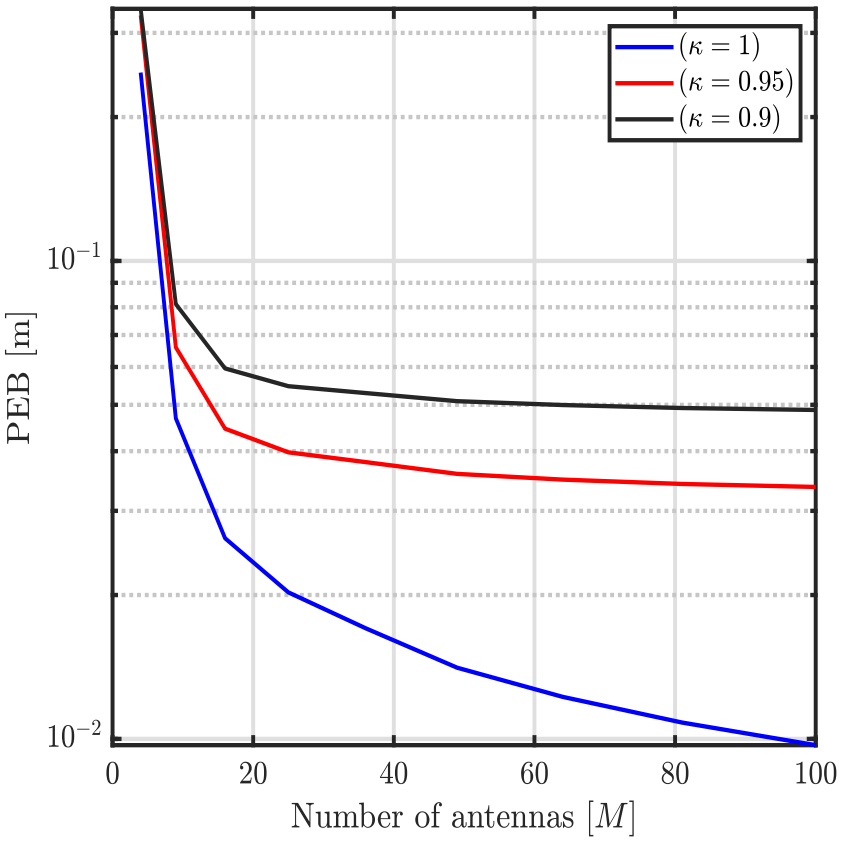

Figure 4.8: BCRB versus the number of BS's antennas M.

4.2.1 Position Tracking and Bayesian Cramer-Rao bound

In this section, the tracking process is executed in the same system described previously in section 3.3. Therefore, the channel's parameters and the MS's position are dependent on time and involve from one position/sample to another. Here with the mobile terminal scenario, we append the independent variable $[t]$ to the equations to refer to the values at the t^{th} position sample. For example, the position of the MS in the t^{th} sample is $\mathbf{p}[t]$ and the estimated position becomes $\hat{\mathbf{p}}[t]$.

4.2.1.1 Kalman Filter Based Tracking Process

This subsection introduces tracking a MS that moves between two consecutive positions, $\mathbf{p}[t-1]$ and $\mathbf{p}[t]$, according to the Gaussian transition model. The ML localizes the MS by optimizing (3.69) at each sample, and then each estimated position is fed into the KF. Concerning the KF, its matrices are determined depending on the transition model of the MS and the localization accuracy harmed by the HWIs and synchronization errors.

Initially, it is self-evident that the estimated position $\hat{\mathbf{p}}$ in the previous subsection is a noisy version of the real $\mathbf{p}$. Therefore,

$$\hat{\mathbf{p}}[t] = \mathbf{p}[t] + \mathbf{w}[t], \tag{4.32}$$

where the vector $\mathbf{w}[t] \in \mathbb{R}^{3\times 1}$ presents the localization process error at the t^{th} position sample with the covariance matrix $\mathbf{C}[t] \in \mathbb{R}^{3\times 3}$. According to [95], the estimated positions can be approximated to Gaussian random variables, and thus $\hat{\mathbf{P}}[t] \sim CN\Big(\mathbf{P}[t], \mathbf{C}[t]\Big)$.

In arriving at a model for the dynamics of the MS mobility when the MS is maneuvering as it changes its position and moves with uncertain rates and steps perturbed by slight undesired position corrections, street fraction, wind gusts, etc. Regarding this, the change in the position of the MS can be modeled as a zero-mean Gaussian random variable with variance depending on the physical capabilities in the change in the velocity components from sample to sample [58, 85, 95]. Accordingly, the difference between two successive positions at any two adjacent samples is modeled as independent Gaussian noise. Thus, the Markov state transition model introduced for the successive MS tracking problem is given as

$$\mathbf{p}[t] = \mathbf{p}[t-1] + \mathbf{u}[t], \tag{4.33}$$

where $\mathbf{u}[t] \sim N(\mathbf{0}, \mathbf{Q})$, $\mathbf{Q} = \text{diag}([\sigma_x^2, \sigma_y^2, \sigma_z^2])$, and the values of σ_x^2, σ_y^2, and σ_z^2 should depend on the possible change in the position components from sample to sample. Thus, based on (4.33), the conditional probability of $\mathbf{p}[t]$ given $\mathbf{p}[t-1]$ is

$$p\left(\mathbf{p}[t] | \mathbf{p}[t-1]\right) \sim N(\mathbf{p}[t-1], \mathbf{Q}). \tag{4.34}$$

Moreover, according to [58], for any two samples $t \neq t'$, $\mathbf{u}[t]$ and $\mathbf{u}(t')$ are independent, and thus the user positions $\mathbf{p}_{\text{m}}[t]$ form a Markov chain satisfying

$$p\left(\mathbf{p}[t] | \mathbf{p}(0:t-1)\right) = p\left(\mathbf{p}[t] | \mathbf{p}[t-1]\right), \tag{4.35}$$

where $\mathbf{p}(0:t-1)$ is the collection of user positions from the first sample to the $t-1$ samples.

Now, it is clear that (4.33) evolves according to the Gauss-Markov model, while (4.32) represents the observation vector that is modelled by the Bayesian linear model. Accordingly, the tracking of $\mathbf{p}[t]$ can be implemented sequentially based on $\hat{\mathbf{p}}(0:t)$ observations and using the KF described in subsection 2.3.5.1, where in (2.43), $\mathbf{A} = \mathbf{I}_3$, $\mathbf{B} = \mathbf{I}_3$ and $\mathbf{H} = \mathbf{I}_3$.

4.2.1.2 Bayesian Cramer-Rao bound

This section presents the best achievable accuracy of the tracking process in the 3D RIS-aided *mm*wave MISO-OFDM system. Precisely, the tracking process in this system suffers from synchronization errors and the HWIs at the transceivers at both the MS and BS. Initially, it presents the FIM that measures the amount of information obtained from the observations in (3.54). Next, it formulates the BIM by considering the priori information in (4.34) simultaneously with the information obtained from the observations. Now, the BCRB benchmark that evaluates tracking a non-stationary MS in the RIS-aided *mm*wave MISO-OFDM system suffering from HWIs is the inverse of the BIM.

By defining $\mu = [\mathrm{p}_x,\ \mathrm{p}_y,\ \mathrm{p}_z,\ \Delta]^{\mathrm{T}}$, for an arbitrary t sample, the BIM of $\mu[t]$ vector, $\mathbf{J}_{\mu}^{(\mathrm{B})}[t] \in \mathbb{R}^{4\times 4}$, can be computed according to (2.29). Considering the priori information represented in (4.34), then

$$p\Big(\mu[t]|\mu[t-1]\Big) = p\Big(\mathbf{P}[t]|\mathbf{P}[t-1]\Big).$$

Consequently, according to the definition in (2.33), and taking into account that Δ is constant over the different samples, then the $\mathbf{G}$ matrices are expressed as: $\mathbf{G}_{11}[t] = \mathbf{G}_{22}[t] = -\mathbf{G}_{12}[t] = -\mathbf{G}_{21}[t] \in \mathbb{R}^{4\times 4}$, where

$$\mathbf{G}_{11}[t] = \begin{bmatrix} \mathbb{E}\left\{ -\frac{\partial^2 \log p\left(\mathbf{P}[t]|\mathbf{P}[t-1]\right)}{\partial \mathbf{P}[t-1](\partial \mathbf{P}[t-1])^{\mathrm{T}}} \right\} & 0 \\ 0 & 0 \end{bmatrix}, \tag{4.36}$$

and

$$\mathbb{E}\left\{ -\frac{\partial^2 \log p\Big(\mathbf{P}[t]|\mathbf{P}[t-1]\Big)}{\partial \mathbf{P}[t-1](\partial \mathbf{P}[t-1])^{\mathrm{T}}} \right\} = \mathbf{Q}^{-1}.$$

The remain term in (2.29), $\mathbf{J}_{\mu}^{(\mathrm{M})}[t]$, that represents the information obtained from the observations in (3.54), is updated as follows

$$\mathbf{J}_{\mu}^{(\mathrm{M})}[t] = \mathbf{T}[t]\mathbf{J}_{\beta}[t]\mathbf{T}^{\mathrm{T}}[t]\ \forall t, \tag{4.37}$$

where $\mathbf{T}[t]$ and $\mathbf{J}_{\beta}[t]$ are presented in subsection 3.3.4. It should be noted that when the MS transits to a new location in a given sample t^{th}, the following vectors and matrices $\beta, \mathbf{J}_{\beta}, \mathbf{T}, \mu$ and $\mathbf{J}_{\mu}$ that depend on the location of the MS change from their previous state to a new one. Consequently, at each sample, $\beta[t]$, $\mathbf{J}_{\beta}[t]$, and $\mathbf{T}[t]$ are updated according to (3.62) and Subsection 3.3.4.

Now, by initializing $\mathbf{J}_{\mu}^{(\mathrm{B})}(0) = \mathbb{E}\left\{ -\frac{\partial^2 \log p\Big(\mathbf{P}(0)\Big)}{\partial \mathbf{P}(0)(\partial \mathbf{P}(0))^{\mathrm{T}}} \right\}$, the BCRB of the estimation of $\mu[t]$ at the t^{th} sample is given by computing the inverse of $\mathbf{J}_{\mu}^{(\mathrm{B})}[t]$.

4.2.1.3 Simulation Results

In this section, we conduct numerical experiments to discuss tracking in the 3D RIS-aided mmwave MISO-OFDM system under the harmful effects of HWIs. We consider the same settings and scenarios of simulation assumed in section 3.3.5. In these simulations, it is assumed that the MS starts from the initial position in [7, 7, 2] mobility between 300 sample positions according to the $p\left(\mathbf{p}_{\mathrm{m}}(t)|\mathbf{p}_{\mathrm{m}}(t-1)\right) \sim N(\mathbf{p}_{\mathrm{m}}(t-1), \mathbf{Q})$ transition model. Moreover, it is assumed that the average

movement distance of MS between adjacent samples is determined by $\mathbf{Q} = \text{diag}([0.03,\ 0.07,\ 0.01])$ that achieves $\mathbb{E}\{\|\mathbf{p}_\text{m}(t) - \mathbf{p}_\text{m}(t-1)\|_2\} = \sqrt{0.11}$ m.

Fig.4.9 presents the accuracy of the tracking process at varying values of κ when the $\mathbf{C}$ matrix, the matrix that describes the errors in the estimated position, is determined based on the MC approach. This approach suggests determining $\mathbf{C}$ as the average of the estimation errors. Specifically, in this method, we generate 300 uniformly and randomly distributed $\theta[t]$ in the area of the range and direction change, where these points are different from those that will be used later in the tracking scenario. Next, the estimation process and the measurements are performed for each $\theta[t]$ in 500 of realizations. Later, the measurement error matrices are averaged over the realizations for each $\hat{\theta}[t]$. After that, the resulting averaged matrices for all $\hat{\theta}[t]$ are averaged again to obtain the covariance matrix that is used to represent the measurement error during the tracking process. Notably, the tracking accuracy in the BCRB and RMSE terms deteriorates when we boost the HWIs noise represented by κ. On the other hand, when the HWIs noise attenuates as a consequence of reducing the transmission data power P, and thus the $\frac{P\rho_0^2}{\sigma^2}$ value is small, the precision of the tracking process remains virtually the same regardless of the different values κ.

Moreover, it is clear that in the case of ideal hardware, the accuracy of the tracking process, the RMSE term, can match the theoretical BCRB when the quality of the received signal is high enough. On the other hand, the nonideal hardware saturates the accuracy of the tracking process, as it saturates the accuracy of the localization process that is the base for the tracking process. Fortunately, the more appropriate selection of the matrix $\mathbf{C}$ helps the KF compensate for the lack of accuracy, as shown in Fig. 4.10.

Fig. 4.10 presents the accuracy of the tracking process in terms of RMSE, with different κ and $\mathbf{C}$ matrix values. Firstly, the figure plots the accuracy of the tracking process without

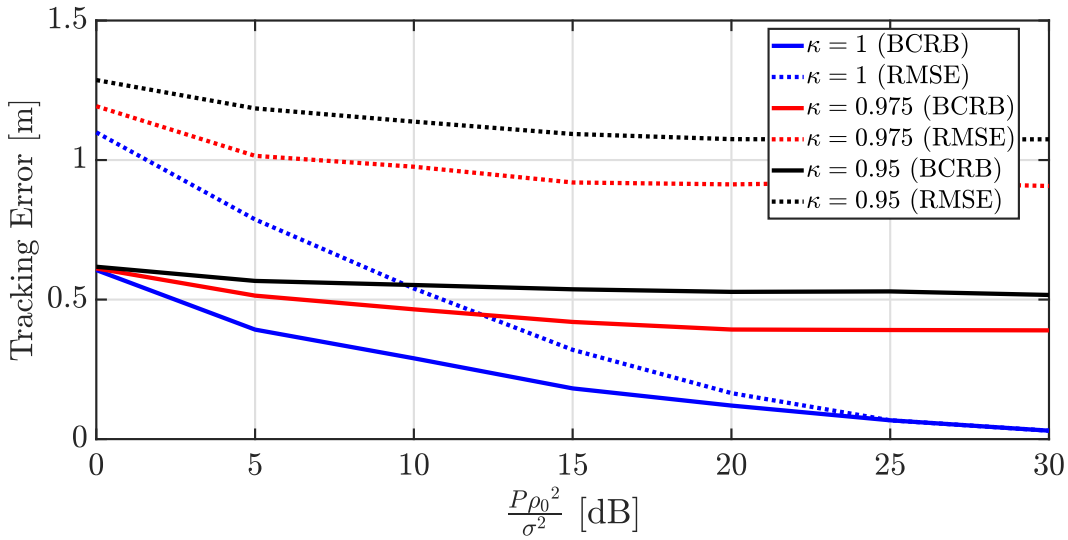

Figure 4.9: Tracking error and BCRB versus the transmission power with different κ.

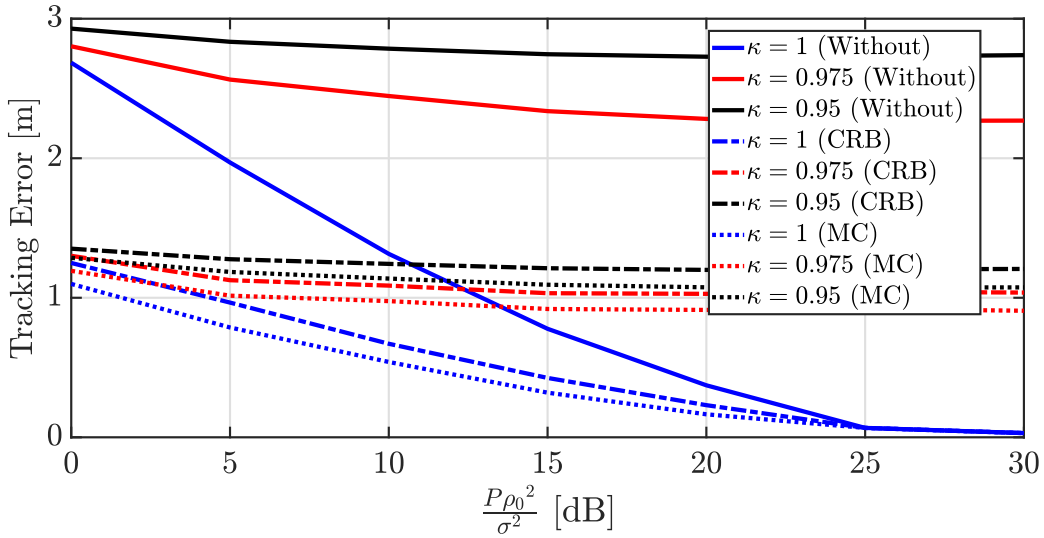

Figure 4.10: Tracking error and BCRB versus the transmission power with different **C** matrix and κ.

implementing the KF, the raw output of the localization process, which we referred to as *Without*. At the same time, the figure presents two scenarios with the KF, where the first scenario, referred to as the *CRB*, is when the **C** matrix is the average of the CRBs of the localization processes, while the second scenario is when the **C** matrix is the average of the RMSE of the localization processes based on the MC approach, the *MC* scenario.

In Fig.4.10, a significant improvement in tracking accuracy due to KF for both impaired and ideal transceivers. Regarding the perfect transceivers, the impact of the KF becomes more significant in low-quality received pilots, that is, the range of small $\frac{P\rho_0^2}{\sigma^2}$ values, but no difference in tracking accuracy in the range of high $\frac{P\rho_0^2}{\sigma^2}$ values. More interestingly, in the case of non-ideal transceivers, where the KF improves the tracking accuracy over the $\frac{P\rho_0^2}{\sigma^2}$ range.

Moreover, Fig.4.10 declares that selecting the **C** matrix that represents the accuracy of the estimator, or the accuracy of the localization process as here, affects the accuracy of the tracking process. In other words, this figure shows that the precision of the tracking process of the *CRB* scenario is less than that seen in the *MC* scenario. The reason is that the MC technique formulates a more realistic covariance matrix **C** than the one from the *CRB* case, where the matrix **C** in the *CRB* case represents the localization process accuracy never achieved due to the HWIs or due to a not high enough value of $\frac{P\rho_0^2}{\sigma^2}$ in the ideal case. However, when the $\frac{P\rho_0^2}{\sigma^2}$ value is high enough, there are no differences between the accuracy associated with the *CRB* case and that of the *MC* case. Even more, their accuracy equals that of the *Without* case.

4.3 Machine Learning Solution

The process of tracking the position of an MS jointly with its velocity, known as *joint position-velocity tracking*, is executed in the 3D mmwave MISO-OFDM system illustrated in Fig.4.11. Specifically, this section discusses the joint position-velocity tracking process of a moving MS in the hardware-impaired mmwave MISO-OFDM system. where the system is perfectly synchronized, and its configurations and signalling are described in section 4.1. Subsequently, we introduce the joint position-velocity tracking problem, including the MS transition model and its relation with the measurements. Later on, the BCRB benchmark of the joint position-velocity tracking is derived. Finally, two tracking solutions are proposed: a solution using EKF, and based on MLT.

4.3.1 The Joint Position-Velocity Tracking Problem

The joint position-velocity tracking depends on the same measurements described in subsection 4.1.2, where these measurements, ToF and AoDs relevant to reference BS, are related to the MS position at the t^{th} sample, according to

$$\tau[t] = \frac{\sqrt{x^2[t] + y^2[t] + z^2[t]}}{c}, \tag{4.38a}$$

$$\theta[t] = \operatorname{atan2}\big(y[t], x[t]\big), \tag{4.38b}$$

$$\psi[t] = \sin^{-1}\left(\frac{\sqrt{x^2[t] + y^2[t]}}{\sqrt{x^2[t] + y^2[t] + z^2[t]}}\right), \tag{4.38c}$$

where the BS, without loss of generality, is located at the origin. Moreover, the 3D velocities can be obtained by counting how fast the position changes between two samples in time as

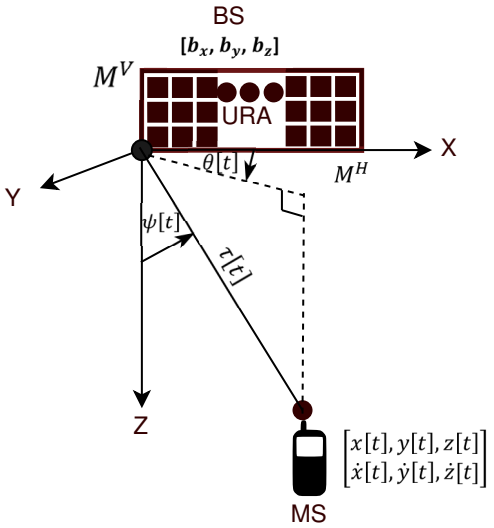

Figure 4.11: The joint position-velocity tracking process in mmwave MISO-OFDM system.

$$\dot{x}[t] = \frac{x[t] - x[t-1]}{\Delta}, \tag{4.39a}$$

$$\dot{y}[t] = \frac{y[t] - y[t-1]}{\Delta}, \tag{4.39b}$$

$$\dot{z}[t] = \frac{z[t] - z[t-1]}{\Delta}, \tag{4.39c}$$

where Δ is the time difference between any two consecutive samples. In this regard, the MS measures the ToF and the direction periodically every Δ time. In addition, the MS transition model is counted during the joint position-velocity tracking process.

Coming to the transition model of a moving MS, the MS is maneuvering as it changes its speed, or it moves at a constant velocity perturbed only by slight speed corrections due to street fraction, wind gusts, etc. Accordingly, changes in the velocity of the MS can be modelled as a zero-mean Gaussian random variable with variance depending on the physical capabilities in the change in the velocity components from sample to sample [85, 95].

For the 3D transition model, we define the 3D position-velocity vector at the t^{th} sample as

$$\mathbf{p}[t] = \big[x[t],\, y[t],\, z[t],\, \dot{x}[t],\, \dot{y}[t],\, \dot{z}[t]\big]^{\mathrm{T}}, \quad \in \mathbb{R}^{6\times 1} \tag{4.40}$$

where the $x[t]$, $y[t]$, and $z[t]$ represent the 3D components of the MS position at the t^{th} sample, while $\dot{x}[t]$, $\dot{y}[t]$ and $\dot{z}[t]$ are the velocity components in 3D coordinates for the same sample. Then, the transition model for the MS motion is

$$\mathbf{p}[t] = \mathbf{A}\mathbf{p}[t-1] + \mathbf{B}\mathbf{u}[t], \tag{4.41}$$

where the derivation of this model and the definitions of the constant matrices $\mathbf{A}$ and $\mathbf{B}$ are in appendix A. Besides, $\mathbf{u}[t]$ presents the random MS motion vector and is given by

$$\mathbf{u}[t] = \big[u_x[t],\, u_y[t],\, u_z[t]\big]^{\mathrm{T}}, \tag{4.42}$$

where it is modelled as a zero-mean Gaussian random variable, i.e. $\mathbf{u}[t] \sim N(\mathbf{0}, \mathbf{Q})$. Here, $\mathbf{Q} = \mathrm{diag}\big([\sigma_x^2, \sigma_y^2, \sigma_z^2]\big)$ is time-invariant, t-independent, and the variance values σ_x^2, σ_y^2, and σ_z^2 of the random motion in x, y, and z axis should depend on the possible change in the 3D velocity components from sample to sample. Furthermore, for any two samples $t \neq t'$, $\mathbf{u}[t]$ and $\mathbf{u}[t']$ are independent and achieve $\mathbb{E}\{\mathbf{u}[t]\mathbf{u}^{\mathrm{T}}[t']\} = \mathbf{0}\ \forall\ t \neq t'$, which results in $\mathbf{u}[t]$ being a vector (WGN) [58].

It is worth noting here that since for any two samples $t \neq t'$, $\mathbf{u}[t]$ and $\mathbf{u}[t']$ in (4.41) are independent, so the MS positions-velocity vector $\mathbf{P}[t]$ forms a Markov chain satisfying

$$p\big(\mathbf{P}[t]\big|\mathbf{P}[0:t-1]\big) = p\big(\mathbf{P}[t]\big|\mathbf{P}[t-1]\big), \tag{4.43}$$

where $p\big(\mathbf{P}[t]\big|\mathbf{P}[t-1]\big)$ is the conditional probability of $\mathbf{P}[t]$ given $\mathbf{P}[t-1]$, and $\mathbf{P}[0:t-1]$ is the collection of user position-velocity from the first sample to the $t-1$ sample. Following that and based on (4.41) and the probability distribution of $\mathbf{u}[t]$, it is easy to conclude that

$$p\big(\mathbf{P}[t]\big|\mathbf{P}[t-1]\big) \sim N\big(\mathbf{AP}[t-1], \mathbf{BQB}^{\mathrm{T}}\big). \tag{4.44}$$

Coming to the initial conditions, the initial state of the position-velocity vector $\mathbf{P}[-1]$ is independent of $\mathbf{u}[t]$ and follows the distribution of a Gaussian random variable, i.e. $\mathbf{P}[-1] \sim N\Big(\mathbf{P}_0, \mathbf{BQ}_0\mathbf{B}^{\mathrm{T}}\Big)$. It is noteworthy here that $\mathbf{P}_0$ and $\mathbf{Q}_0$ can be determined arbitrarily or based on some previous information. Next, they are fed as the initial values of the EKF in section 2.3.5.2, where their impact soon becomes negligible as the number of samples increases [85].

To accomplish the position-velocity tracking process, we measure $[\tau[t],\ \theta[t],\ \psi[t]]$ after Δ time by observing the distorted version of the pilots broadcast from the BS. Specifically, these measurements are obtained using the ML estimator described in Subsection 4.1.2 because it takes into account the HWIs during the measurement process. The measurement accuracy and the model play a crucial role in the performance of the tracking process, as they determine the filter gain and correct the estimation step in the filter, as explained when the MC technique is used to enhance the tracking performance in the chapter 4.

4.3.2 Bayesian Cramer-Rao bound

The assessment and performance analysis of the joint position-velocity tracking process in a 3D mmwave MISO-OFDM system suffering from HWIs are derived here. Specifically, we derive the BCRB considering the maneuvering of the MS and the HWIs in the system. With respect to this, we calculate the BIM, which accounts for the information obtained from the measurements by observing the pilots in (4.8), in addition to the information gained from the a priori knowledge described in (4.44). The BIM of the non-linear joint position-velocity tracking process at the t^{th} sample, $\mathbf{J}_{\mathbf{P}}^{(\mathrm{B})}[t] \in \mathbb{R}^{6\times 6}$, is performed based on (2.29) in section 2.3.4, similar to the tracking processes here in chapter 4.

The measurements FIM, $\mathbf{J}_{\mathbf{P}}^{(\mathrm{M})}$ that present useful information about $\mathbf{P}$ gained from the pilots received, cannot be calculated directly. The reason is that there is no direct relationship connecting $\mathbf{P}$ with the pilots received in (4.8), the mean in (4.9), and the variance in (4.10). Alternatively, $\mathbf{P}$ has a non-linear relationship, seen in (4.51), with the channel parameters vector $\beta[t] = \big[\Theta[t],\ \rho[t],\ \phi[t]\big]^{\mathrm{T}}$ that is directly related to the pilots and their mean and variance. In this context, firstly, we find the FIM of $\boldsymbol{\beta}[t]$, $\mathbf{J}_{\boldsymbol{\beta}}^{(\mathrm{M})}[t]$, and then, we extract the FIM of $\Theta[t]$, $\mathbf{J}_{\Theta}^{(\mathrm{M})}[t]$. Next, $\mathbf{J}_{\mathbf{P}}^{(\mathrm{M})}$ is obtained in terms of $\mathbf{J}_{\Theta}^{(\mathrm{M})}[t]$ based on the relationship between $\mathbf{P}[t]$ and $\Theta[t]$.

In this context, the matrix $\mathbf{J}_{\boldsymbol{\beta}}^{(\mathrm{M})}[t]$ is obtained based on the receive pilots $y_n^g[t]$ in (4.8) that have complex Gaussian distributions, with $\varphi_n^g[t]$ in (4.9) as the mean and $\sigma_y^2[t]$ in (4.10) as its variance, where the derivatives of these elements of $\mathbf{J}_{\boldsymbol{\beta}}^{(\mathrm{M})}[t]$ are in Subsection 3.2.4.

It is clear that not all of the elements of the $\mathbf{J}_{\boldsymbol{\beta}}^{(\mathrm{M})}[t]$ are associated with $\Theta[t]$; therefore, the FIM of $\Theta[t]$ is obtained using the Equivalent FIM formula as described in (2.3.2) in subsection 2.24. In the lower bound, the measurements $\hat{\Theta}[t]$ in (4.50) achieve the best accuracy and then $\mathbf{C}[t] = \left(\mathbf{J}_{\Theta}^{(\mathrm{M})}[t]\right)^{-1}$, where $\mathbf{J}_{\Theta}^{(\mathrm{M})}[t]$ is the FIM of $\hat{\Theta}[t]$. Consequently, the measurements have the following probability distribution

$$p\left(\hat{\Theta}[t]|\mathbf{P}[t]\right) \sim N\left(\mathbf{f}(\mathbf{p}[t]), \left(\mathbf{J}_{\Theta}^{(\mathrm{M})}[t]\right)^{-1}\right), \tag{4.45}$$

and thus

$$\mathbf{J}_{\mathbf{P}}^{(\mathrm{M})} = (F[t])^{\mathrm{T}} \mathbf{J}_{\Theta}^{(\mathrm{M})}[t] F[t]. \tag{4.46}$$

where $F[t]$ is the Jacobian matrix defined in (4.52). It is worth noting that the vectors and matrices $\boldsymbol{\beta}, \mathbf{J}_{\boldsymbol{\beta}}^{(\mathrm{M})}, \mathbf{J}_{\Theta}^{(\mathrm{M})}, \mathbf{J}_{\mathbf{P}}^{(\mathrm{M})}$, and $F[t]$ should be updated from one sample to another because they depend on the position of the MS.

Regarding the FIM of the priori information, $\mathbf{J}_{\mathbf{P}}^{(\mathrm{I})}$, it measures the amount of useful information for the tracking process from knowing the MS transition model described in (4.41). The $\mathbf{G}$ matrices related to $\mathbf{J}_{\mathbf{P}}^{(\mathrm{I})}$ and defined in (2.33) are

$$\begin{aligned}
\mathbf{G}_{11}[t] \in \mathbb{R}^{6\times 6} &= \mathbf{A}^{\mathrm{T}}\left(\mathbf{B}\mathbf{Q}\mathbf{B}^{\mathrm{T}}\right)^{-1}\mathbf{A}, \\
\mathbf{G}_{12}[t] \in \mathbb{R}^{6\times 6} &= -\mathbf{A}^{\mathrm{T}}\left(\mathbf{B}\mathbf{Q}\mathbf{B}^{\mathrm{T}}\right)^{-1}, \\
\mathbf{G}_{21}[t] \in \mathbb{R}^{6\times 6} &= -\left(\mathbf{B}\mathbf{Q}\mathbf{B}^{\mathrm{T}}\right)^{-1}\mathbf{A}, \\
\mathbf{G}_{22}[t] \in \mathbb{R}^{6\times 6} &= \left(\mathbf{B}\mathbf{Q}\mathbf{B}^{\mathrm{T}}\right)^{-1},
\end{aligned} \tag{4.47}$$

as shown in subsection 2.3.4.

Finally, the BCRB of the joint position-velocity tracking process in the t^{th} sample is given by computing the inverse of the BIM. Consequently, the PEB and the velocity error bound (VEB) in the t^{th} sample, respectively, are given by

$$\mathrm{PEB}[t] = \sqrt{\left[\mathbf{J}_{\mathbf{P}}^{(\mathrm{B})}[t]\right]_{(1,1)}^{-1} + \left[\mathbf{J}_{\mathbf{P}}^{(\mathrm{B})}[t]\right]_{(2,2)}^{-1} + \left[\mathbf{J}_{\mathbf{P}}^{(\mathrm{B})}[t]\right]_{(3,3)}^{-1}}, \tag{4.48}$$

$$\mathrm{VEB}[t] = \sqrt{\left[\mathbf{J}_{\mathbf{P}}^{(\mathrm{B})}[t]\right]_{(4,4)}^{-1} + \left[\mathbf{J}_{\mathbf{P}}^{(\mathrm{B})}[t]\right]_{(5,5)}^{-1} + \left[\mathbf{J}_{\mathbf{P}}^{(\mathrm{B})}[t]\right]_{(6,6)}^{-1}}. \tag{4.49}$$

4.3.3 The Proposed Solutions

This subsection seeks to present solutions for the tracking process explained in subsection 4.3.1. Taking into account the nature of the measurements and the transition model, the KF is the optimal solution for this process. However, due to the non-linear relationship in the tracking process, the KF is inapplicable, and so the EKF is proposed as a suboptimal alternative. In

conclusion, the solution to this tracking problem is performed by combining the measurements with the transition model and implementing the EKF sequence at each Δ time.

Next, based on scrutinizing the EKF solution, this section investigates the execution of an accurate tracking process while reducing the tracking complexity, and mitigating the prior knowledge about the transition model and the initial conditions. In response, we suggest and investigate the implementation of MLT as a solution for the joint position-velocity tracking process. In this solution, all we need to do is train the MLT on position-velocity values obtained from (4.38) and (4.39) based on the output from (4.14). Another important point in this context is to have fast, simple learning, since the learning and the tracking are executed on the MS board. Therefore, we use the ELM because it can offer significant advantages, such as fast learning speed, ease of implementation, and minimal human intervention [89].

4.3.3.1 Extended Kalman Filter Tracker

Based on (4.16), the estimated values and measurements of $\hat{\Theta}[t]$ are noisy versions of $\Theta[t]$, which are functions of the real values of position parameters in $\mathbf{P}[t]$ as follows

$$\begin{aligned}\hat{\Theta}[t] &= \Theta[t] + \mathbf{w}[t], \\ &= \mathbf{f}\big(\mathbf{p}[t]\big) + \mathbf{w}[t],\end{aligned} \tag{4.50}$$

where

$$\Theta[t] = \mathbf{f}\big(\mathbf{p}[t]\big) = \begin{bmatrix} \frac{\sqrt{x^2[t]+y^2[t]+z^2[t]}}{c} \\ \text{atan2}(y[t], x[t]) \\ \sin^{-1}\left(\frac{\sqrt{x^2[t]+y^2[t]}}{\sqrt{x^2[t]+y^2[t]+z^2[t]}}\right) \end{bmatrix}. \tag{4.51}$$

In addition, (4.41) and (4.16) show that the signal vector $\mathbf{p}[t]$ with the noises is jointly Gaussian, and thus the KF is an optimal sequential MMSE estimator for $\mathbf{p}[t]$. However, since the measurements vector $\Theta[t]$ is a non-linear relationship of the signal vector $\mathbf{p}[t]$, the KF is inapplicable in this case. Fortunately, a suboptimal tracking process can be achieved by linearizing the $\mathbf{f}\big(\mathbf{p}[t]\big)$ and then implementing the EKF [85]. By leveraging the Taylor expansion, the linearized relationship of $\mathbf{f}\big(\mathbf{p}[t]\big)$ can be given as

$$F[t] \in \mathbb{R}^{3\times 6} = \frac{\partial \mathbf{f}\big(\mathbf{p}[t]\big)}{\partial \big(\mathbf{p}[t]\big)}\Big|_{\mathbf{p}[t]=\hat{\mathbf{p}}[t|t-1]}, \tag{4.52}$$

and consequently, the linearized version of the measurements equation in (4.50) is

$$\hat{\Theta}[t] = F[t]\mathbf{p}[t] + \mathbf{w}[t] + \Big(\mathbf{f}\big(\hat{\mathbf{p}}[t|t-1]\big) - F[t]\hat{\mathbf{p}}[t|t-1]\Big), \tag{4.53}$$

where the Jacobian Matrix, $F[t]$, elements:

$$[F[t]]_{(1,1)},\ [F[t]]_{(1,2)},\ [F[t]]_{(1,3)},\ [F[t]]_{(2,1)},\ [F[t]]_{(2,2)},\ [F[t]]_{(3,1)},\ [F[t]]_{(3,2)},\ [F[t]]_{(3,3)},$$

are the same in (4.27) in section 4.1.4.1, while the following terms:

$$[F[t]]_{(1,4)} = \frac{\partial \tau[t]}{\partial \dot{x}[t]}, [F[t]]_{(1,5)} = \frac{\partial \tau[t]}{\partial \dot{y}[t]}, [F[t]]_{(1,6)} = \frac{\partial \tau[t]}{\partial \dot{z}[t]},$$
$$[F[t]]_{(2,4)} = \frac{\partial \theta[t]}{\partial \dot{x}[t]}, [F[t]]_{(2,5)} = \frac{\partial \theta[t]}{\partial \dot{y}[t]},$$
$$[F[t]]_{(3,4)} = \frac{\partial \psi[t]}{\partial \dot{x}[t]}, [F[t]]_{(3,5)} = \frac{\partial \psi[t]}{\partial \dot{y}[t]}, [F[t]]_{(3,6)} = \frac{\partial \psi[t]}{\partial \dot{z}[t]},$$

equal zero.

Now, tracking the signalling vector $\mathbf{p}[t]$ according to the EKF can be implemented sequentially based on $\hat{\Theta}[0:t]$ measurements and considering (4.41) and (4.53) as described in subsection 2.3.5.2. Regarding this solution, the tracking accuracy and the convergence of the solution depend on the Kalman gain matrix that is given based on matrix $\mathbf{C}$, as seen in (2.43c). Specifically, the matrix $\mathbf{C}$ specifies the errors in the measurements process, defined in (4.50). In this context, according to [85], the matrix $\mathbf{C}$ is determined from the CRB of the estimated values. Nonetheless, the estimation process cannot achieve the CRB due to HWIs [96, 97]. Therefore, we expect that the enhancements in the tracking accuracy are limited. Besides, it is notable that the EKF requires prior information and initial conditions about the MS transition besides the matrix $\mathbf{C}$. Furthermore, the tracking process using EKF proposes complexity as it consists of recursive procedures as seen in subsection 2.3.5.2.

4.3.3.2 Machine Learning Tracking Solution

This subsection targets performing a simple and accurate tracking process based on MLT instead of EKF, without the need for prior knowledge or initial conditions. Specifically, it is shown in Subsections 2.3.5.1 and 2.3.5.2 that as the accuracy of the measurements increases, the outputs of the KF and EKF tend to be the measurements themselves and do not take into account the transition model. In response, MLT is carried out to attain accurate and reliable tracking results. Furthermore, this simplifies the tracking process as it replaces the sequential equations in subsection 2.3.5.2, and the mathematical operations therein with simpler mathematical operations as shall be seen in this subsection. Moreover, this subsection demonstrates that this matrix is constructed without any information about the transition model or the initial conditions.

As illustrated in Fig.4.12, the output measurements from the estimator in (4.14) are converted to a noisy position-velocity vector, $\tilde{\mathbf{p}}[t] \in \mathbb{R}^{6\times 1}$, using the geometric relationship in (4.38) and (4.39). After that, the noisy position-velocity vector, $\tilde{\mathbf{p}}[t]$, is processed by an ELM block described in subsection 2.4.2. The definitions and the description of the entities of the ELM block in Fig.4.12 are as follows:

- In the training phase, we collect N records of the noisy position-velocity vectors as $\mathbf{X}_{N\times 6} = \{(\tilde{\mathbf{p}}_i[t])^{\mathrm{T}}, i = 1, \cdots, N\}$. We also record the target matrix of N real position-velocity vectors $\mathbf{p}[t]$ in (4.40), $\mathbf{T}_{N\times 6} = \{(\mathbf{p}_i[t])^{\mathrm{T}}, i = 1, \cdots, N\}$. After that, the output weight matrix β is

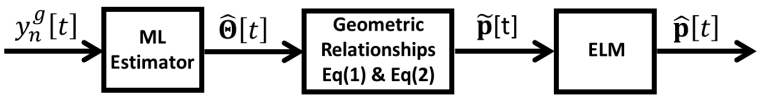

Figure 4.12: Based ELM tracker block diagram.

obtained based on equations from (2.55) to (2.58), and using the *Sigmoid function* as the non-linear activation function in this work, which is

$$\phi\big(\mathbf{x},\mathbf{w},b\big)=\frac{1}{1+\exp\big(-(\mathbf{w}^{\mathrm{T}}.\mathbf{x}+b)\big)}, \tag{4.54}$$

where $\mathbf{w}\in\mathbb{R}^{6\times1}$ is the input weight vector, b is the bias, and $\mathbf{x}\in\mathbb{R}^{6\times1}$ is the noisy position-velocity sample. In this phase, the output weight matrix β is obtained by the pseudo-inverse operation in (2.58) in subsection 2.4.2.

- In the implementation phase, for each noisy position-velocity vector, $\tilde{\mathbf{p}}_i[t]$, the tracked vector after the *ELM* block in Fig.4.12, is given according to (2.59) as

$$(\hat{\mathbf{p}}[t])^{\mathrm{T}}=\mathbf{H}\Big(\mathbf{w}_1,\cdots,\mathbf{w}_L,b_1,\cdots,b_L,(\tilde{\mathbf{p}}[t])^{\mathrm{T}}\Big)_{1\times L}\times\beta_{L\times6}, \tag{4.55}$$

where the definition of $\mathbf{H}$ is in (2.55) in subsection 2.4.2.

4.3.4 Simulation Results

This subsection discusses the numerical results of the joint position-velocity tracking process for a 3D mmwave MISO-OFDM system under the harmful effects of the HWIs, where the settings are described in subsection 3.2.5. Besides, we assume that the single-antenna MS starts its mobility between 1000 sample positions from the initial position-velocity in [5, 5, 5, 0, 0, 0], where the MS physical capabilities never exceed 0.5 m/s on any axis, and the samples are taken every $\Delta=0.1$ s.

Within the discussion of the results, we present the BCRB as a benchmark to assess the tracking process accuracy measured in the RMSE term. In fact, we present three methodologies for tracking purposes. In detail, the first method is called (*M-only*), where it calculates the MS position and velocities depending on the measurements only using the geometric relationship in (4.38) and (4.39). The second method, called (*EKFT*), is the EKF tracker specified in subsection 4.3.3.1. Lastly, the third method is called (*ELMT*) and is based on the ELM algorithm described in subsection 4.3.3.2. In this approach, the neural network is a single layer with $L=10$ neurons. We obtained our results using 5000 training samples, each of which is a raw vector of six elements in size.

The accuracy of the joint position-velocity tracking process with different levels of the transceivers' quality is presented in Fig.4.13 - Fig.4.15. Specifically, these figures depict the impact of the pilots' power, presented in the $\frac{P\rho_0^2}{\sigma^2}$ term, on the tracking accuracy considering different κ values. Next are the general conclusions that can be delineated from the figures.

It is clear that improving the transceiver hardware quality enhances tracking accuracy. Furthermore, by boosting the pilots' power, the tracking accuracy also improves. Besides, *EKFT* and *ELMT* trackers demonstrate an improvement to the tracking accuracy over *M-only*. Regarding the *EKFT* tracker, we see improvements because it considers the transition model of the MS besides the measurements, which is not the case in *M-only*. In the context of the *ELMT* tracker, accuracy improvement rises from the training phase of the ELM algorithm by minimizing the difference between the output of the geometric relationship in (4.38) and (4.39) and the real values. The following are the specific details and differences in the position and velocity results.

Fig.4.13 shows that the accuracy improvement with the non-ideal transceivers case is bounded to a certain level due to the bounded nature of the received pilot quality as seen in (4.12). On the other hand, in the case of ideal transceivers, the tracking accuracy more readily approcahes the PEB as the pilots' power increases. Besides, the figure shows that the performance of *EKFT* and *ELMT* trackers saturates at $\frac{P\rho_0^2}{\sigma^2} \geq 35$ dB. Considering the *EKFT* tracker, the saturation results from the difference between the real and the linearized values as seen in (4.53). Regarding the *ELMT* tracker, the output weight matrix from the training is not accurate enough to minimize the error and achieve the BCRB. However, the direct calculation in *M-only* achieves the BCRB at high-quality received pilots, i.e. the measurements are approximately real, and thus relying on the measurements only in the high-quality measurements case is preferable as it is more accurate and simpler.

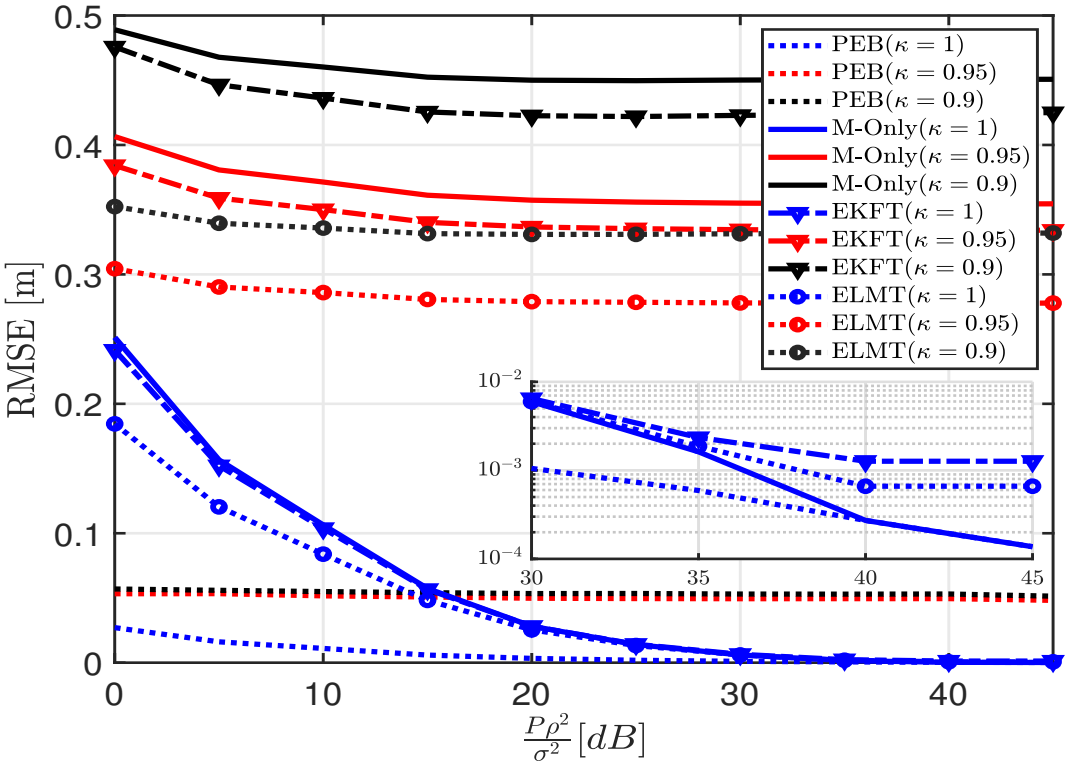

Figure 4.13: Position RMSE and PEB versus the transmission power and κ.

Regarding the velocity, Fig.4.14 and Fig.4.15 discuss the achieved accuracy associated with the velocity. It is clear that the *EKFT* and *ELMT* trackers have significant enhancements in velocity accuracy in comparison to the *M-only* solution. However, none of the solutions/trackers including *M-only* achieve the VEB, neither in the case of ideal transceivers nor in the case of imperfect transceivers. The reason for this is that the velocity calculations are independent of the received pilots and the measurements $\Theta[\hat{t}]$, which is different from the position. Instead of that, they are calculated only by relying on the estimated position and then using the geometric relationship in (4.39). Consequently, the achieved enhancement by the *EKFT* is gained from the useful information about the transition model, while the achieved accuracy by *ELMT* gained from the training phase on minimizing the difference between the output of the geometric relationship and the actual values.

4.4 Summary

In this chapter, we discuss the tracking process paying attention to HWIs and the synchronization errors. Subsequently, we started with a perfectly synchronized but hardware-impaired 3D perfectly synchronous mmwave MISO system. The second part counts for the synchronization error in addition to the HWIs, where the tracking is executed in an asynchronous RIS-assisted mmwave MISO-OFDM system. The third part investigates utilizing the MLT for the joint position-velocity

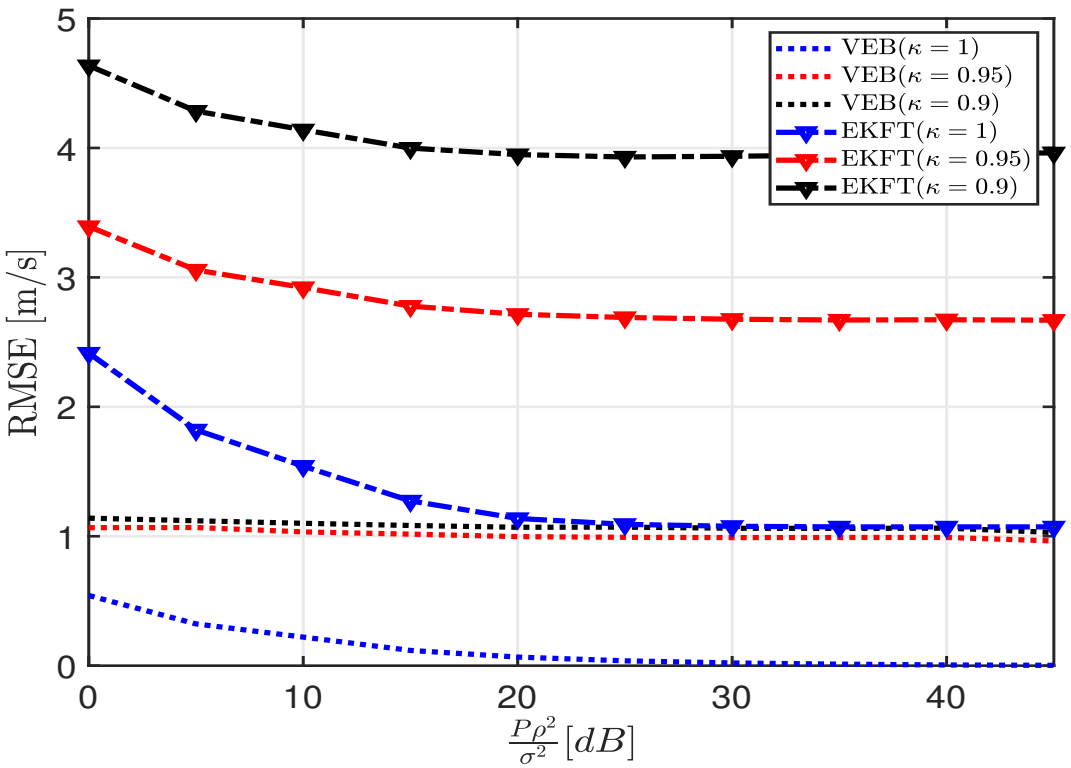

Figure 4.14: Velocity RMSE and VEB versus the transmission power and κ.

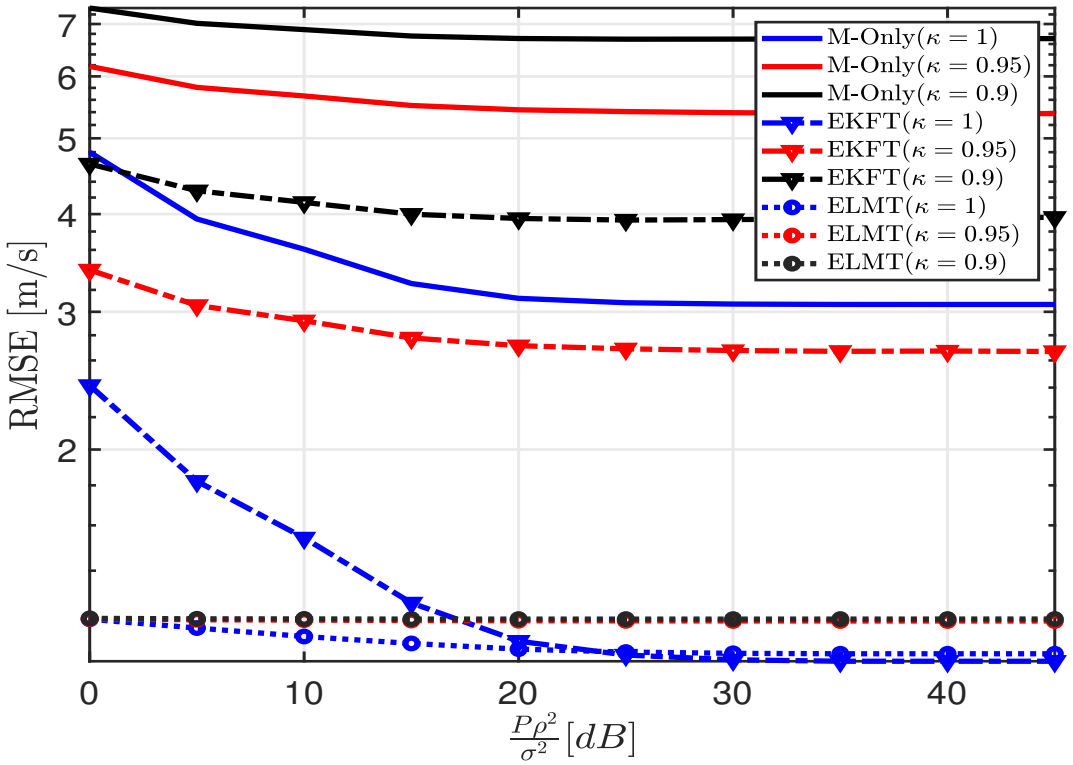

Figure 4.15: Velocity RMSE versus the transmission power and κ.

tracking process.

In the perfectly synchronized system, section 4.1, we investigated two tracking processes: the range-direction tracking process, and the position tracking process. The two tracking processes in this system rely on estimating the AoD and ToF relevant to the reference BS. For range-direction tracking, the measured AoD and ToF have a Gaussian statistical model and are connected with linear relationships to range and direction, the tracked parameters that also are modelled as a Gaussian random variable. Consequently, KF is the proposed tracking solution as it provides the optimal solution for this tracking problem. However, for position tracking, the ToF and AoD measurements have nonlinear relationships with position. Accordingly, KF is inapplicable and EKF is implemented to deal with the non-linear relationships, where it can achieve a suboptimal solution.

Regarding position tracking in the asynchronous RIS-assisted *mm*wave MISO-OFDM system, section 4.2, it depends on the estimated position resulting from the joint localization-synchronization described in subsection 3.3.3. The estimated positions are approximated to the Gaussian measurements, and clearly, they are linearly connected with the tracked positions. Consequently, KF is the optimal solution for this tracking operation. In the context of KF and EKF, this chapter suggests the MC approach to enhance the tracking accuracy distorted by the HWIs and synchronization errors when they exist.

Exploring the application of the MLT for tracking, we leverage its capabilities to offer a

streamlined and highly accurate tracking solution that doesn't rely on prior information for the joint position-velocity tracking process. In this section, we employ the ELM algorithm for this task and assess its performance in comparison to the EKF-based solution. ELM is chosen in this context due to its speed and simplicity in learning, making it a suitable choice for both learning and tracking operations on the MS board.

For evaluation, this chapter derives the BCRB benchmark for each tracking scenario. Following, this chapter presents simulations where the results reveal that the HWIs distortion prevents the tracking process from achieving the theoretical bound, presented by the BCRB which is only possible in the case of ideal transceivers. Finally, computer simulation results illustrate the ability of the MC techniques to improve tracking accuracy, since it involves more accurate information around measurement errors. Besides, the computer simulation experiments show the enhancement in the tracking accuracy when using the MLT for tracking purposes.

CHAPTER 5

CONCLUSIONS AND FUTURE RESEARCH

This chapter presents the ultimate findings within this thesis and explores pertinent limitations and areas of inquiry for both the immediate and distant future. In general, this thesis delves into the study of localization and tracking processes and derives the relevant benchmarks in terms of CRB and BCRB. Specifically, the investigation focuses on localization and tracking processes within mmWave systems, considering the impact of HWIs and synchronization errors whenever they are present. The following detailed conclusions are based on the contributions outlined in Section 1.5. Subsequently, this chapter underscores the limitations of the thesis and then proposes future research.

5.1 Conclusions

- In Chapter 3, we conducted localization procedures within a MISO-OFDM mmWave system under ideal synchronization conditions but with the presence of HWIs. In this context, a 2D localization process was executed, relying on estimating the LoS downlink parameters. The accuracy of this localization process was solely affected by the presence of HWIs.
- Continuing in Chapter 3, we extended our investigation to a 3D localization process, which encountered HWIs and the challenges posed by NLoS conditions caused by unknown scatterers. Additionally, we delved into the consequences of synchronization errors alongside HWIs by implementing a joint localization-synchronization process within an asynchronous RIS-aided mmWave MISO-OFDM system.
- Chapter 3 introduced a method for estimating the range and direction of a single-antenna MS in relation to a multiple-antenna BS. This estimation relied on observing the well-known pilot signals transmitted from the BS in the downlink. The utilization of the

ML estimator was chosen due to its suitability for handling complex scenarios and its capability to yield optimal estimates. Besides, for assessment, this chapter derived the CRB benchmark for the localization process in the existence of the HWIs. It started with the derivations of the FIM of the estimated downlink channel parameters. Then, it transformed the channel parameters FIM to the localization FIM, which is inverted to obtain the CRB of the localization processes.

- In Chapter 4, diverse tracking processes were explored. Initially, it monitored the range, direction, and location of the MS relative to the reference BS within the framework of a perfectly synchronized MISO-OFDM mmWave system while considering the presence of HWIs. Subsequently, the chapter investigated tracking the MS's position within an asynchronous RIS-aided mmWave MISO-OFDM system, accounting for the influence of HWIs and synchronization errors. These tracking processes relied on estimating Time of Flight (ToF) and AoD, incorporating MS maneuvering and transition models, and utilizing KF and EKF techniques.

- In the context of tracking range and direction, these parameters exhibited a linear relationship with the measurements. Consequently, the KF emerged as the ideal choice to deliver an optimal solution for this tracking task. Likewise, when considering the tracking process in the RIS-aided mmWave system, the tracked position depended on the outcomes of the joint localization-synchronization processes, making KF the optimal solution once again. However, when it came to position tracking and position-velocity tracking, the straightforward application of KF was not feasible. In these cases, the EKF served as a viable alternative, capable of providing a suboptimal yet effective solution.

- Furthermore, Chapter 4 introduced a position-velocity tracking approach that addresses HWIs, employing MLT, and compared its performance with the EKF-based method. It's worth mentioning here that Chapter 4 proposed MC techniques and MLT to significantly enhance tracking accuracy and mitigate the adverse effects of HWIs and synchronization errors whenever they exist.

- Finally, in Chapter 4, for the assessment of the tracking process, benchmarks for tracking performance were established in each scenario, and quantified through the BCRB. To be specific, the BCRB is calculated as the inverse of the BIM, where the BIM is constructed by merging the FIM obtained from the received pilot measurements with the FIM associated with the MS's transition model.

The primary achievement of this thesis lies in the acknowledgment that idealized assumptions, such as flawless transceivers and perfectly synchronized systems, obscure the true accuracy of localization and tracking processes. This assertion is substantiated both theoretically, through the examination of the CRB and BCRB benchmarks, and empirically, through the execution of

localization and tracking procedures. Additionally, this thesis endeavours to underscore that the adverse effects of HWIs and synchronization errors can be mitigated, offering two distinct approaches: MC techniques and MLT. In this context, the thesis introduces a robust mathematical framework for investigating localization and tracking processes across various systems and within realistic scenarios. Furthermore, it highlights the capability of mitigating the harmful impact of HWIs and synchronization errors during the execution of the localization and tracking processes.

Nevertheless, this work carries certain assumptions that may be regarded as constraints within the scope of this research. Furthermore, our study has the potential to inspire fellow researchers to delve into additional inquiries and explorations

5.2 Limitations and Future Directions

While exploring the keystone of this thesis, which is the influence of the practical aspects on the localization and tracking processes, we carry out our study on mmwave systems considering some assumptions that can be counted as limitations to this thesis.

- **Wide-band systems:** We assumed the mmwave system was a narrow-band system without discussing wide-band systems. Consequently, future research could explore localization and tracking processes in wide-band mmwave systems.
- **Doppler effect:** Given the assumptions for narrow-band and low-speed mobility, the impact of the Doppler effect and its variation over the subcarriers was negligible. Therefore, future research could focus on tracking considering high-speed mobility and the Doppler effect or explore systems that address the Doppler effect, such as those implementing the orthogonal time-frequency space (OTFS) concept.
- **Sources of individual HWIs:** This thesis addressed the impact of residual HWIs on the localization and tracking processes. However, future work could involve investigating localization and tracking processes under specific HWIs sources.
- **Comprehensive MLT:** This thesis provided the ELM technique as an example to highlight MLT as a promising candidate for mitigating the adverse impact of HWIs and synchronization errors on localization and tracking processes. Future research could delve deeper into utilizing MLT in the localization and tracking process.
- **Accuracy enhancement:** This thesis implemented ML estimator, KF, and EKF as trackers, and MLT and MC for accuracy enhancement. However, future research could explore different estimators and trackers and propose various approaches to overcome and mitigate the factors causing accuracy degradation.

APPENDIX A

THE MS POSITION-VELOCITY TRANSITION MODEL

The changes in velocity on one axis between any two adjacent samples are

$$\dot{d}[t] = \dot{d}[t-1] + u[t], \tag{A.1}$$

where $\dot{d}[t]$ is the velocity at the t^{th} sample, and $u[t]$ is the MS maneuvering and motion uncertainty that should be derivable from the physics of the motion of MS. Consequently, the change in the MS position can be approximately modelled as

$$\begin{aligned} d[t] &= d[t-1] + \frac{1}{2}\big(\dot{d}[t] + \dot{d}[t-1]\big)\Delta, \\ &= d[t-1] + \big(\dot{d}[t-1] + \frac{1}{2}u[t]\big)\Delta, \end{aligned} \tag{A.2}$$

while Δ is the time interval between two adjacent samples. We must note here that this approximation is perfect when the average velocity over Δ equals $\frac{1}{2}\big(\dot{d}[t] + \dot{d}[t-1]\big)$.

To guarantee the physical capabilities and that the MS movement is limited by the physical constraints, the term α is plugged into the velocity equation in (A.1) to be

$$\dot{d}[t] = \alpha\dot{d}[t-1] + u[t], \tag{A.3}$$

where $\alpha = \sqrt{\frac{v-\sigma^2}{v}}$, $\sigma^2 = \mathbb{E}\{u^2[t]\}$, and v present the MS motion capability that is the same for all samples, i.e., $v = \mathbb{E}\{\dot{d}^2[t]\}\ \forall t$.

In order to expand the 3D state space model for the MS motion, we define the 3D position-velocity vector at the t^{th} sample as

$$\mathbf{p}[t] = \big[x[t],\, y[t],\, z[t],\, \dot{x}[t],\, \dot{y}[t],\, \dot{z}[t]\big]^{\mathrm{T}}, \tag{A.4}$$

then, the transition model for the MS motion is

$$\mathbf{p}[t] = \mathbf{A}\mathbf{p}[t-1] + \mathbf{B}\mathbf{u}[t], \tag{A.5}$$

where the $x[t]$, $y[t]$, and $z[t]$ represent the 3D components of the MS position at the t^{th} sample, while $\dot{x}[t]$, $\dot{y}[t]$ and $\dot{z}[t]$ are the velocity components in 3D coordinates for the same sample. Moreover, the constant matrices $\mathbf{A}$ and $\mathbf{B}$, respectively, can be defined as

$$\mathbf{A} = \begin{bmatrix} 1 & 0 & 0 & \Delta & 0 & 0 \\ 0 & 1 & 0 & 0 & \Delta & 0 \\ 0 & 0 & 1 & 0 & 0 & \Delta \\ 0 & 0 & 0 & \alpha_x & 0 & 0 \\ 0 & 0 & 0 & 0 & \alpha_y & 0 \\ 0 & 0 & 0 & 0 & 0 & \alpha_z \end{bmatrix}, \tag{A.6}$$

and

$$\mathbf{B} = \begin{bmatrix} \frac{\Delta}{2} & 0 & 0 \\ 0 & \frac{\Delta}{2} & 0 \\ 0 & 0 & \frac{\Delta}{2} \\ 1 & 0 & 0 \\ 0 & 1 & 0 \\ 0 & 0 & 1 \end{bmatrix}. \tag{A.7}$$

APPENDIX B

PHYSICAL LAYER SECURITY IN DOWNLINK OF CELL-FREE MASSIVE MIMO WITH IMPERFECT CSI

Abstract

This paper[1] investigates the threat of passive eavesdropping on downlink cell-free massive MIMO (CF-MaMIMO) systems, examining in a particular system under the effects of imperfect channel estimation. Physical layer security (PLS) techniques and power allocation algorithms are typically adopted to deteriorate the quality of eavesdropped signals. In the downlink stream, artificial noise (AN) is broadcasted simultaneously with the users‚Äô data streams, with the aim of jamming the eavesdropper's signal without sacrificing the quality of service (QoS). However, imperfect channel estimation results in AN leakage to legitimate users. Our work considers this condition, and the power allocation algorithms we present determine the minimum power that is needed to maintain the user's Qos even in the presence of leaked AN. We first propose the cooperative PLS algorithm (**COP**), which facilitates AN broadcasting via access point (AP) cooperation. Unfortunately, this cooperation wastes some of the power used to send the AN and, in most cases, increases the computational complexity. We then present the independent PLS algorithm (**IND**), where the goal is to regain this power by allowing each AP to broadcast AN independently. However, to meet the feasibility criterion, this occurs at the cost of increasing the number of used antennas. This technique reduces the power allocation complexity but increases the computational complexities of the precoder design and the channel estimation process. Our results reveal that the proposed algorithms enhance the security performance of CF-MaMIMO. We evaluate such performance from numerous angles including the number of users, number of APs, QoS, beamforming, AN leakage, and channel estimation techniques.

Physical Layer Security, Cell-Free, Massive MIMO, Eavesdropper, Artificial Noise, Estimation.

[1]This project was conducted as part of the PhD program, but it has not been incorporated into the thesis. This work was published as: D. A. Tubail, M. Alsmadi and S. Ikki, "Physical Layer Security in Downlink of Cell-Free Massive MIMO With Imperfect CSI," in IEEE Transactions on Information Forensics and Security, vol. 18, pp. 2945-2960, 2023, doi: 10.1109/TIFS.2023.3272769.

B.1 Introduction

Massive multiple-input multiple-output (MaMIMO) technologies are pivotal towards the realization of 5G networks requirements (e.g., the ever-increasing demand for higher data rates, stronger connectivity and greater area coverage) [98]. An up-and-coming descendant of MaMIMO systems that has garnered significant attraction takes a cell-free form (CF-MaMIMO), where a large number of distributed access points (APs) serves a smaller number of distributed users over a certain coverage area using the same time-frequency resources as those in beamforming technology [99, 100].

The distributed APs are connected to an extremely powerful central processing unit (CPU) via a backhaul link. In this way, each AP is able to transmit the received uplink data to the CPU, which can then send the downlink data to the other APs using its power control coefficient. This cooperation between the APs and CPU can be easily implemented as a way to resist large-scale fading effects, minimize inter-user interference, enhance signal quality, increase capacity and reliability, improve energy efficiency, and mitigate the effects of hardware impairments [99–102].

That being said, CF-MaMIMO systems face many challenges. For example, the use of a massive number of APs causes significant energy consumption and leads to astronomical hardware costs[99]. Moreover, as security becomes more and more of a concern in wireless communication systems, witnessed the emergence of increasingly demanding security requirements, especially in cases where enormous amounts of data need to be safely transmitted [103].

Physical layer security (PLS) is considered an alternative solution to traditional, computationally expensive, technologies. It aims to reinforce secure communications by exploiting the physical properties of wireless channels in protecting the system against passive and active eavesdropping [104].

The concept of using PLS for degraded wire-tap channels was studied early on in [105]. Furthermore, the works in [106] and [107] discussed the PLS of wireless systems with quasi-static fading channels and Free-Space optical links, respectively. In these works, a single-antenna transmitter aims to send confidential messages over a half-duplex communication network without external helpers and in the presence of an eavesdropper. The receiver begins by broadcasting pseudo-random AN, which is then used by the transmitter to mask the confidential signal being sent. These works analyzed security performance by assessing the probability of exposure, and performed power allocation in an attempt to maximize system throughput under certain security and reliability constraints.

However, it is important to note that the receiver can only decode the confidential message if it has knowledge of the instantaneous channel state information (CSI), the power transmitted in each phase, the channel gain, the transceiver noise variance, and the power distribution among the signal and the AN. Unfortunately, these criteria are difficult to satisfy.

There are also similar difficulties in the PSL of MIMO systems. The work in [108], for instance, looked at securing communication over a fading wireless medium from a hidden eavesdropper.

Part of the available power was used to target-broadcast AN directly towards the eavesdropper. This work discussed two scenarios, the first of which assumed a multiple-antenna transmitter broadcasting AN into the null of the user. However, this scenario neglects the case where the eavesdropper's channel is highly correlated to that of a legitimate user i.e., the eavesdropper is also in the null space of the users. The second scenario was a two-phase securing approach similar to that in [106, 107], and it greatly capitalized on the use of relays. It should be noted that the two-phase securing approach performed by two transmissions over two time slots in [106–108] wastes bandwidth and necessitates greater power consumption for each transmission in a single-user communication system.

Furthermore, these scenarios neglected practicality upon the assumption of perfect CSI knowledge being shared between all nodes. Besides, these works only consider the case of one communicating pair, one transmitter and one receiver, not the multi-user communication case. Next, the work in [109] analyzed security degradation due to the use of imperfect CSI in the precoding design. The work then presented an optimal power allocation approach to simultaneously meet the security and QoS requirements of a single-user MIMO system. Moreover, the work in [110] optimized the regularization parameter in a regularized channel inversion precoder, and this was used to maximize the secrecy sum rate of a multi-user multi-eavesdropper MIMO system.

The authors in [111] also proposed a joint precoding algorithm to simultaneously send the legitimate streams and AN, with the hopes of maximizing the secrecy rate in multi-user MIMO systems in the presence of multiple multi-antenna eavesdroppers. Unfortunately, the proposed algorithm failed to consider QoS requirements and could lead to confusion when users have highly correlated channels with eavesdroppers.

PLS was also studied and implemented by those in [104, 112] in the context of relay-aided multi-user MIMO systems. The authors in [112] secured the system by broadcasting legitimate streams simultaneously with the AN in the null of the legitimate users/relay as users/relay were multiple-antenna entities. In [104], the terminals mixed the legitimate streams with fake streams and sent them together to a relay that amplified and forwarded them to their destinations.

The works in [113–117] investigated the PLS in MaMIMO. The work in [113] specifically derived the secrecy sum rate of the downlink given to passive eavesdropping and maximum ratio transmission precoding. The work in [114] analyzed the impact of imperfect CSI on the PLS in a multi-user MaMIMO system, all the while taking into account the channel estimation error due to white noise. They also considered the existence of outdated CSI errors during the time users are non-stationary. However, the error estimation due to non-orthogonal pilots (caused by the users' mobility and asynchronous pilots) was not incorporated into this assessment.

The authors of [115] proposed different legitimate data and AN precoders targeting the maximization of the secrecy rate lower-bound in multi-cell MaMIMO systems. They considered a hidden eavesdropper as well as the effects of non-orthogonal pilots. However, this work overlooked

The current work	The existing literature
Enables broadcasting the AN from distributed antennas	None of the existing literature broadcasted AN from distributed antennas
Secures the system by performing optimal power allocation and enabling the broadcasting of the AN	[109, 110, 114, 116–122] secured the system by performing optimal power allocation only without enabling the broadcasting of the AN
Addresses imperfect channels estimation and the leaked AN	[104, 106–108, 110, 112, 113] considered perfect channels estimation and no AN leakage
Addresses passive and hidden eavesdropping	[111, 117–123] addressed non-hidden and active eavesdropping

Table B.1: Summary of the comparison between the current work and the existing literature.

system requirements during precoder design, resulting in AN being leaked to legitimate users. This ultimately demonstrates the importance of proper power allocation between the users and AN streams. This work used its AN null-space precoder in conjunction with the known precoders in [116], where the downlink secrecy rate of a relay-assisted MaMIMO system was derived.

Here, the legitimate user employed the zero-forcing precoder for the data, and the null-space precoder for the AN. In this way, the secrecy rate was maximized against an active imposter by proposing optimal power allocation all the while considering the QoS of the system. Furthermore, joint power and time allocation were optimized to maximize the secrecy outage capacity of passive eavesdropping in a relay-assisted MaMIMO system considering imperfect instantaneous legitimate CSI in [117].

PLS in CF-MaMIMO systems was addressed in [118–122]. The work in [118] presented the secrecy performance of a downlink CF-MaMIMO system over spatially correlated Rayleigh fading channels in the presence of an active pilot spoofing attack. Next, the works in [119–122] presented power allocation as a solution to secure the downlink transmission against active eavesdropping.

The rest of this paper is organized as follows: Section II presents the comparison with the existing literature and the contributions, and Section III describes the system model including the channel estimation and beamforming techniques. Section IV and Section V discuss the **COP** and the **IND** algorithms, respectively. Section VI discusses the hardware and computational complexities of the proposed algorithms while section VII presents the simulation results. Finally, the paper is concluded in Section VIII.

B.2 Related-Works Comparison and Contributions

Considering the importance of this topic, and motivated by what has already been done in the literature, we present a CF-MaMIMO system with a hidden eavesdropper. We compare the contributions of this work with the existing literature, summarizing it all in Table I.

Firstly, to the best of our knowledge, this work is the first to broadcast AN in CF-MaMIMO systems with distributed antennas. Moreover, we transmit data streams and beamform AN into the null of legitimate users after optimizing power budget allocation. This strategy outperforms, in terms of security performance, the power allocation scheme without AN used in [109, 110, 114, 116–122].

Furthermore, our work differs from [111, 118–123] in that we address the problem of passive and hidden eavesdropping. We specifically take into account that the eavesdropper usually tries to remain hidden, passive and with unavailable CSI [117]. On the other hand, the active eavesdropper places itself physically close to the user in order to tap into its CSI, or to exploit the weakness of the channel estimation stage by capturing the predetermined pilot sequence and using it to pose as a legitimate user [124]. A myriad of different methods can be implemented to combat active eavesdropping. In this way, power allocation can minimize leaked data rates, as was done in [117–122]. Furthermore, knowing the CSI of the eavesdropper can be used to beamform the data streams to users and AN toward the eavesdropper, as in [123].

In our case, we target AN broadcasting towards the null space of the legitimate channel. This technique both confuses the passive eavesdropper and prevents any jamming that could be done to legitimate users. Moreover, in terms of the achievable secrecy rate gains, the performance of null space-based AN precoders is superior to that of all other AN precoders [116]. In addition, this precoder design is unrelated to that of the users. As such, the beamforming techniques employed for user data streams (e.g., zero-forcing, regular zero-forcing, minimum mean square error etc.) can also be implemented when sending the AN. Besides, the leaked AN amount to users is not at all related to the number of eavesdroppers or to their situation. Rather, it depends on the errors committed when estimating the legal users' channels, i.e., zero leakage in the perfect estimation case.

Regarding estimation errors and AN leakage, unlike the works in [104, 106–108, 110, 112, 113], we assume the practical case where the estimation of the channels between the APs and the users is imperfect. Using these estimated channels when precoding the AN consequently, and inevitably, results in AN power leakage to legitimate users. Fortunately, this leakage can be managed by 1) using more accurate channel estimators, as demonstrated by [114], 2) modifying the data and the AN precoders as in [115, 123], or 3) optimizing the power allocation between the data and the AN as in [116]. We consequently adopt a power allocation algorithm to treat the impact of the leaked AN and to guarantee the required SNR. Besides, the power control approach degrades the quality of the eavesdropped signal even in the case of a highly correlated eavesdropper channel.

To supplement the strategies currently present in the literature regarding PLS, this work proposes two algorithms that enhance the security performance of a CF-MaMIMO system with multiple antennas hidden and a passive eavesdropper, i.e., the wiretap CSI is unknown. Moreover, this work assumes the worst-case scenario, where the eavesdropper has perfect knowledge of its own channels and can extract and separate the intended users' signals [104, 112, 119, 125]. In specific, we impede eavesdropping by broadcasting AN into the null of legitimate users, where the beamforming of AN in the null of users only depends on the legal user's CSI.

In addition to blurring the eavesdropped signal with AN, we can degrade its quality even more by transmitting downlink data streams using minimal power (i.e., enough to maintain QoS).

This strategy is especially relevant when the eavesdropper possesses a channel that is strongly correlated to a legitimate user link, thus allowing him to avoid AN. Hence, the contributions of this work can be summarized as:

- It is well-known that the estimated channel (the one used in AN precoding) contains estimation errors, which leads to an imperfect AN broadcasting scheme into the null space of users. This causes a portion of the AN to leak to legitimate users, reducing their QoS (illustrated by the impact on their SNR). To address this, we propose an optimization problem to maximize the security performance without sacrificing QoS. In fact, the optimization problem is formulated so as to first guarantee system QoS, then enhance the security. Specifically, the optimization problem determines the minimum power that guarantees system QoS and then dedicates the rest of the AP power budget to AN broadcasting. Moreover, this power allocation process is independent of the wiretap channel and depends only on the legal users' estimated channels.

- We propose a cooperative PLS algorithm, (**COP**), in which the APs cooperate to broadcast AN in the null of the users without the need for extra antennas. Here, the number of APs is greater than the number of users. However, this cooperation wastes some of the power dedicated to AN distribution. As such, an iterative power allocation algorithm must be in place, which introduces more computational complexity.

- We also propose an independent PLS algorithm (**IND**) that dispatches more AN than the **COP** algorithm. This is achieved by increasing the number of antennas at the APs, enabling them to independently broadcast AN. Besides, the additional antennas increase the beamforming gain in the AN channel, which actually enhances the security performance. Moreover, this technique reduces the computational complexity in terms of power allocation because there is no longer need for an iterative solution like the one seen in the case of the **COP** algorithm. However, this approach requires additional channel estimation, here a simple estimator has been consequently proposed to reduce the computational complexity applicable here.

- We investigate the security performance of the CF-MaMIMO system considering various factors such as the number of users and APs, QoS, as well as AN leakage. Furthermore, since the AN beamforming technique matrix is designed independently of those for user data streams, the proposed algorithms can be implemented with beamforming techniques traditionally used for user data streams (e.g., maximum ratio, zero-forcing, regular zero-forcing, or minimum mean square error. This work also analyzes the hardware and computational complexities of the proposed algorithms.

- We conducted extensive computer simulations, the results of which prove the capability of the proposed algorithms to enhance security in CF-MaMIMO systems. Moreover, the

Notation	Description
a, $\mathbf{a}$, $\mathbf{A}$	scalar, vector and matrix
$(.)^{\mathrm{T}}$, $(.)^{\mathrm{H}}$, $(.)^{-1}$	transpose, conjugate transpose, and inverse
$\mathbf{A}_{(i,j)}$, $\mathbf{A}^{*}_{(i,j)}$	the element (i,j) in the matrix $\mathbf{A}$ and its conjugate
$\mathbf{A}_{(i,:)}$	the i^{th} row in the matrix $\mathbf{A}$
$\mathbf{D}_{(:,i)}$	the i^{th} column in the matrix $\mathbf{A}$
$\mathscr{D}_{(i,:)}$	the diagonal matrix that contains in its diagonal the elements of the row $\mathbf{A}_{(i,:)}$
$\mathscr{D}_{(:,i)}$	the diagonal matrix that contains in its diagonal the elements of the column $\mathbf{A}_{(:,i)}$
$\mathbb{CN}(\mu,\sigma^2)$	complex Gaussian random variable distribution with mean μ and variance σ^2
$\mathbb{E}\{\cdot\}$	statistical expectations

Table B.2: Summary of notations

results indicate that the **IND** algorithm outperforms the **COP** algorithm in terms of security performance and computational overhead, of course at the expense of additional hardware maintenance and cost. Different parameters can impact security, such as the power budget, number of users, QoS, number of APs, and channel estimation accuracy. Factors such as an increased power budget, a greater number of APs and channel estimation accuracy leads to improved security, while increasing QoS or the number of users has a negative effect.

B.3 The Cell-Free Massive MIMO System

This section presents the CF-MaMIMO system model and discusses its transmission protocol, TDD [126]. Here, communication is carried out in three stages. In the first "uplink training" stage, all users broadcast their pilot sequences synchronously. In the second "estimation" stage, the links between the users and APs are estimated based on the transmitted uplink pilots. In the third "downlink transmission" stage, all APs precode the data streams and broadcast them to the users simultaneously. Therefore, in addition to the system model, this section discusses the channel estimation of the links between the APs and the users, which are crucial later on for the beamforming techniques that the APs can apply to minimize interference between the users.

B.3.1 System model

Fig. B.1 illustrates the CF-MaMIMO system, as described in [127], which consists of M single antenna APs. These APs are connected to a CPU that is not shown in this figure. The APs serve K single-antenna users simultaneously, where $M >> K$ and both the APs and users are randomly distributed over a wide area. Here, the propagation conditions include an NLoS environment with sufficient scattering between the APs and the terminals, and where different sets of scatters

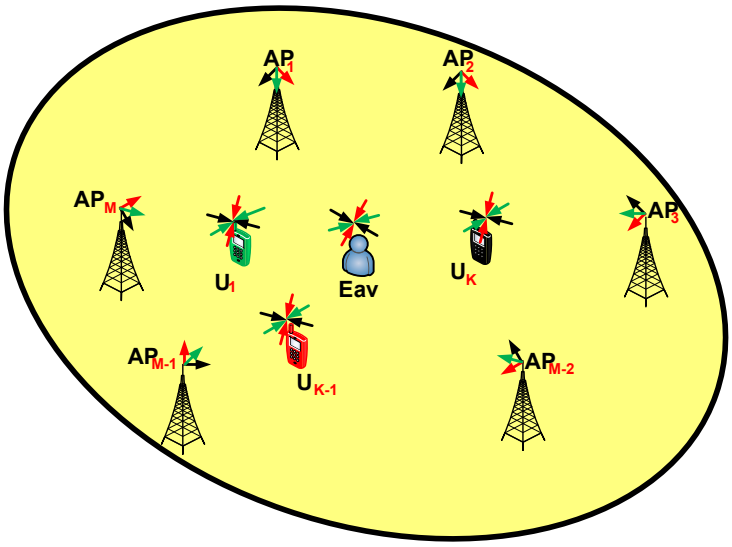

Figure B.1: Eavesdropping cell-free massive MIMO system model.

are likely to be for each AP and each user. Then the downlink signal reaches the receiver through many different NLOS paths and the superimposed received signals can either reinforce or cancel each other out. By the superposition principle and the central limit theorem, the channels between the APs and the terminals are modelled as circularly symmetric Gaussian. Moreover, the channel between the AP and a terminal comprises two components: The first part is a positive real number, termed the large-scale fading coefficient, which embodies distance-dependent path loss, shadowing, antenna gains, and penetration losses in NLoS propagation. This coefficient evolves slowly and can hence be accurately estimated and tracked. The second part is a complex-valued number, representing small-scale fading. It models range-dependent phase shift as well as constructive and destructive interference among different propagation paths. We assume that this coefficient is an independent and identically distributed (i.i.d) random variable that remains constant during a coherent interval and is independent across different coherent intervals.

The k^{th} user connects with the m^{th} AP through the wireless link h_{km} that suffers from flat fading for each orthogonal frequency division multiplexing (OFDM) subcarrier. In this case, the subcarrier's index is ignored for simplicity. The h_{km} link between the m^{th} AP and the k^{th} user is

$$h_{km} = \sqrt{\beta_{km}}\,\kappa_{km}, \tag{B.1}$$

where β_{km} is the large-scale fading coefficient while $\kappa_{km} \sim \mathbb{CN}(0,1)$ is the small-scale fading coefficient. Both coefficients are assumed to be i.i.d random variables, constant during a coherent interval and independent over different coherent intervals. The small-scale fading, in wide-band OFDM, is frequency-dependent and has a Nyquist sampling interval equal to the reciprocal of the channel delay-spread. On the other hand, the frequency-independent β_{km} coefficient changes slowly and can be estimated accurately by the CPU. This system also assumes that the area coverage is small enough to ensure that the maximum propagation time between any two APs is smaller than the duration of the OFDM cyclic prefix [120, 127, 128].

The transmitted signal from the m^{th} AP can be written as

$$x_m = \sqrt{p_d}\mathbf{G}_{(m,:)}\mathscr{D}^{\frac{1}{2}}_{(:,m)}\mathbf{s}, \tag{B.2}$$

where $\mathbf{s} \in \mathbb{C}^{K\times 1}$ is a vector of K symbols intended for K users with $\mathbb{E}\{\mathbf{s}\mathbf{s}^{\text{H}}\} = \mathbf{I}_K$ and $\mathbf{G} \in \mathbb{C}^{M\times K}$ is the downlink beamforming matrix. The diagonal matrix $\mathscr{D}_{(:,m)} \in \mathbb{R}^{K\times K}$ contains the power coefficients associated with the m^{th} AP, where those coefficients ensure that the total transmitted power of the AP is not greater than p_d, thus satisfying $\mathbb{TR}(\mathbf{G}_{(m,:)}\mathscr{D}_{(:,m)}\mathbf{G}^{\text{H}}_{(m,:)}) \leq 1\ \forall m$ and $\mathbb{E}\{|x_m|^2\} \leq p_d$. In the same context, the power coefficient matrix $\mathbf{D} \in \mathbb{R}^{K\times M}$ contains all the non-negative power control coefficients η_{km}.

Then, the received signal at the k^{th} user can be written as

$$y_k = \underbrace{\sqrt{p_d}\mathbf{H}_{(k,:)}\mathscr{D}^{\frac{1}{2}}_{(k,:)}\mathbf{G}_{(:,k)}s_k}_{\text{Desired Signal}} + \underbrace{\sqrt{p_d}\sum_{i=1,i\neq k}^{K}\mathbf{H}_{(k,:)}\mathscr{D}^{\frac{1}{2}}_{(i,:)}\mathbf{G}_{(:,i)}s_i}_{\text{Users' Interference}} + \underbrace{n_k}_{\text{noise}}, \tag{B.3}$$

where $\mathbf{H} \in \mathbb{C}^{K\times M}$ is the complex fading channel matrix between M APs and K users, $n_k \sim \mathbb{CN}(0,\sigma_k^2)$ is the additive white Gaussian noise (AWGN) at the k^{th} user, $\mathscr{D}_{(k,:)} \in \mathbb{C}^{M\times M}$ is a diagonal matrix that contains the power control coefficients η_{km} associated with the k^{th} user (i.e., the k^{th} row of the power coefficient matrix $\mathbf{D}$). Undergoing the normalization process at each coherence block allows the beamforming vector to satisfy $\mathbb{E}\{\|\mathbf{G}_{(:,k)}\|^2\} = 1$, and the allocated power to k^{th} user to become $p_d\sum_{m=1}^{M}\eta_{km}$.

A multiple-antenna passive eavesdropper taps the m^{th} AP through the wireless link $\mathbf{h}_{\text{e}m} \in \mathbb{C}^{M_{\text{E}}\times 1}$. Let $h^j_{\text{e}m}$ be the channel gain between the m^{th} AP and the j^{th} antenna at the eavesdropper. In that case,

$$h^j_{\text{e}m} = \sqrt{\beta_{\text{e}m}}\kappa^j_{\text{e}m} \quad j = 1,\cdots,M_{\text{E}}, \tag{B.4}$$

where $\beta_{\text{e}m}$ is the large-scale fading coefficient, and $\kappa^j_{\text{e}m} \sim \mathbb{CN}(0,1)$ is the small-scale fading coefficient. Finally, the eavesdropped signal can be expressed as

$$y_{\text{e}} = \sqrt{p_d}\sum_{m=1}^{M} h_{\text{e}m}\mathbf{G}_{(m,:)}\mathscr{D}^{\frac{1}{2}}_{(:,m)}\mathbf{s} + n_{\text{e}}, \tag{B.5}$$

where $\mathbf{n}_{\text{e}} \in \mathbb{C}^{M_{\text{E}}\times 1}$ is the independent and identically distributed (i.i.d) AWGN vector at the eavesdropper.

B.3.2 Uplink Training

At this stage, each k^{th} user transmits its pilot $\psi_k \in \mathbb{C}^{1\times\tau^{\text{p}}}$, with a sequence length of τ^{p}, in each coherent interval with unit-magnitude elements such that $||\psi_k||^2 = \psi_k\psi_k^{\text{H}} = \tau^{\text{p}}$. Then, the received signal sequence at the m^{th} AP is

$$y^{\text{p}}_m = \sqrt{p_u}\sum_{k=1}^{K} h_{km}\psi_k + n_m, \tag{B.6}$$

where $y^{\text{p}}_m \in \mathbb{C}^{1\times\tau^{\text{p}}}$, p_u is the uplink power and $n_m \sim \mathbb{CN}(0,\sigma_m^2)$ is the AWGN at the m^{th} AP.

B.3.3 Channel Estimation and Error Modeling

During the second stage, each AP estimates its channel with the k^{th} user by correlating its observation y_m^{p} with the pre-known pilot sequence ψ_k. As a result, the processed observation at the m^{th} AP is

$$y_{mk}^{\text{p}} = y_m^{\text{p}} \psi_k^{\text{H}} = \underbrace{\sqrt{p_u} h_{km} \psi_k \psi_k^{\text{H}}}_{\text{Desired Pilot}} + \underbrace{\sqrt{p_u} \sum_{i \neq k}^{K} h_{im} \psi_i \psi_k^{\text{H}}}_{\text{Pilot Contamination}} + \underbrace{n_m \psi_k^{\text{H}}}_{\text{Noise}}. \tag{B.7}$$

The second term represents estimation quality degradation due to pilot contamination and is determined by the inner product $\psi_i \psi_k^{\text{H}} = \tau^{\text{P}} I_{ik}$. The degree of pilot contamination is influenced by user mobility and pilot synchronization, where eliminating the contamination is possible in perfect pilot synchronization and low-speed mobility scenarios. In detail, pilot orthogonality can be achieved when a large number of perfectly synchronized and orthogonal pilots are available [127–129]. When the users' pilots are orthogonal (i.e., $I_{ik} = 0$), the corresponding pilot contamination is eliminated and therefore does not affect estimation quality. Moreover, some sources of estimation errors, such as outdated CSI, can trigger compounding errors that seriously degrade the quality of the estimation error.

In this system, the minimum mean square error (MMSE) estimator outputs the estimated channel $\hat{h}_{km} \sim \mathbb{CN}(0, \alpha_{km})$ by minimizing $\mathbb{E}\{||h_{km} - \hat{h}_{km}||^2\}$ as follows

$$\hat{h}_{km} = \left(\sqrt{p_u} \tau^{\text{p}} \beta_{km} y_{mk}^{\text{p}}\right) / \mathbb{E}\{y_{mk}^{\text{p}} (y_{mk}^{\text{p}})^{\text{H}}\}. \tag{B.8}$$

The variance of the estimated channel can be given as

$$\alpha_{km} = \left(p_u \tau^{\text{p}} \beta_{km}^2\right) / \left(p_u \tau \beta_{km} + p_u \tau^{\text{p}} \sum_{i \neq k}^{K} \beta_{im} I_{ik}^2 + \sigma_m^2\right). \tag{B.9}$$

Moreover, according to chapter (11) in [130], the estimation error $\tilde{h}_{km} = h_{km} - \hat{h}_{km}$ is a complex Gaussian distribution with $\tilde{h}_{km} \sim \mathbb{CN}(0, \beta_{km} - \alpha_{km})$, and is uncorrelated with the estimated channel $\hat{h}_{km}$.

B.3.4 Beamforming Techniques

The purpose of beamforming is to render the desired signal at each user much stronger than the sum of interfering signals and noise. Different techniques in (B.10) are used to beamform downlink data streams, each of which has an appropriate usage depending on a variety of factors. These factors vary in optimality, in computational complexity and in the degree to which we can analyze them mathematically [131].

B.3.4.1 Minimum Mean Squared Error Beamforming (MMSE)

MMSE beamforming the optimal technique for the maximization of signal-to-interference-plus-noise ratio (SINR). It determines the best balance between amplifying the desired signal and suppressing the interference in the spatial domain, however at the cost of a high computational complexity. This is due to the fact that computing an $M \times M$ matrix inverse requires a considerable amount of channel estimation.

B.3.4.2 Regularized Zero-Forcing Beamforming (RZF)

RZF beamforming is a simpler version of MMSE that can be used when good channel conditions exist and interfering signals are relatively weak. RZF requires inverting a $K \times K$ matrix instead of an $M \times M$ one, which reduces the amount of channel estimation needed, ultimately resulting in decreased computational complexity. Moreover, this technique judges whether to go for interference suppression or signal maximization by considering the regularization term [132, 133].

B.3.4.3 Zero-Forcing Beamforming (ZF)

When the signal-to-noise ratio (SNR) is sufficiently high, the RZF precoding matrix can be approximated to a ZF beamforming matrix, which usually exists in a CF-MaMIMO system because $M > K$. However, due to estimation error, it is more than likely that interference is not canceled completely. Above that, it is expected that the ZF scheme has a lower SNR than that of RZF because not all users exhibit high SNR in practice.

B.3.4.4 Maximum Ratio Beamforming (MR)

In contrast with the ZF and low SNR cases, the RZF precoding matrix can be approximated to a MR beamforming matrix, which does not require any matrix inversion. Since not every user exhibits a low SNR, it is expected that MR will provide a lower SINR than RZF [134].

The precoding matrices $\mathbf{W}$ of the discussed beamforming techniques can be written as

$$\mathbf{W} = \begin{cases} \mathbf{W}^{\mathrm{MMSE}} = \left(\hat{\mathbf{H}}^{\mathrm{H}}\mathbf{P}_u\hat{\mathbf{H}} + \sum_{k=1}^{K} p_u^k \mathbf{E}_k + \sigma_{\mathrm{UL}}^2 \mathbf{I}_M\right)^{-1}\hat{\mathbf{H}}^{\mathrm{H}}\mathbf{P}_u \\ \mathbf{W}^{\mathrm{RZF}} = \hat{\mathbf{H}}^{\mathrm{H}}\left(\hat{\mathbf{H}}\hat{\mathbf{H}}^{\mathrm{H}} + \sigma_{\mathrm{UL}}^2 \mathbf{P}_u^{-1}\right)^{-1} \\ \mathbf{W}^{\mathrm{ZF}} = \hat{\mathbf{H}}^{\mathrm{H}}\left(\hat{\mathbf{H}}\hat{\mathbf{H}}^{\mathrm{H}}\right)^{-1} \\ \mathbf{W}^{\mathrm{MR}} = \hat{\mathbf{H}}^{\mathrm{H}}, \end{cases} \tag{B.10}$$

where $\hat{\mathbf{H}} \in \mathbb{C}^{K \times M}$ is the estimated channel matrix between M APs and K users. $\mathbf{P}_u \in \mathbb{R}^{K \times K}$ is a diagonal matrix containing the transmission power from the users, $\mathbf{P}_u = p_u \mathbf{I}_K$, when they transmit using p_u. The diagonal matrix $\mathbf{E}_k \in \mathbb{C}^{M \times M}$ contains the channel estimation errors

$(\beta_{mk} - \alpha_{mk})$ between the k^{th} user and the APs. Finally, the normalized vector of the k^{th} user can be obtained as $\mathbf{G}_{(:,k)} = \mathbf{W}_{(:,k)} / \left\| \mathbf{W}_{(:,k)} \right\|$.

B.4 Cooperative Physical Layer Security Algorithm (COP)

This section investigates broadcasting AN in the null space of the users' channel matrix via cooperating APs. We include an AN beamforming matrix design, formulate a power allocation optimization problem, discuss its feasibility conditions, and present a solution to the optimization problem.

B.4.1 Adding the Artificial Noise

Now, when the m^{th} AP simultaneously broadcasts AN and the data stream, the transmitted signal in (B.2) can be written as

$$x_m = \underbrace{\sqrt{p_d}\mathbf{G}_{(m,:)}\mathscr{D}^{\frac{1}{2}}_{(:,m)}\mathbf{s}}_{\text{Users' Data}} + \underbrace{\sqrt{\bar{p}_d}\bar{\mathbf{G}}_{(m,:)}\bar{\mathbf{s}}}_{\text{AN}}, \tag{B.11}$$

where $\bar{\mathbf{s}} \in \mathbb{C}^{\bar{d}\times 1}$ such that $\bar{d}$ is the number of AN streams, $\bar{p}_d$ is the AN power, $\mathbb{E}\{\|\bar{s}\|^2\} = \mathbf{I}_{\bar{d}}$, and $\bar{\mathbf{G}} \in \mathbb{C}^{M\times \bar{d}}$ is the AN pre-coding matrix.

The signal tapped by the hidden eavesdropper is consequently distorted by the AN and received as

$$\mathbf{y}_{\text{e}} = \sqrt{p_d}\sum_{m=1}^{M}\mathbf{h}_{\text{e}m}\mathbf{G}_{(m,:)}\mathscr{D}^{\frac{1}{2}}_{(:,m)}\mathbf{s} + \sqrt{\bar{p}_d}\sum_{m=1}^{M}\mathbf{h}_{\text{e}m}\bar{G}_{(m,:)}\bar{\mathbf{s}} + \mathbf{n}_{\text{e}}. \tag{B.12}$$

Unfortunately, due to imperfect channel estimation, some of the power used to send out AN is leaked to the legitimate users. Based on that, the received signal in (B.3) becomes

$$y_k = \underbrace{\sqrt{p_d}\mathbf{H}_{(k,:)}\mathscr{D}^{\frac{1}{2}}_{(k,:)}\mathbf{G}_{(:,k)}s_k}_{\text{Desired Signal}} + \underbrace{\sqrt{p_d}\sum_{i=1,i\neq k}^{K}\mathbf{H}_{(k,:)}\mathscr{D}^{\frac{1}{2}}_{(i,:)}\mathbf{G}_{(:,i)}s_i}_{\text{Users' Interference}} + \underbrace{\sqrt{\bar{p}_d}\mathbf{H}_{(k,:)}\bar{\mathbf{G}}\bar{\mathbf{s}}}_{\text{AN leakage}} + \underbrace{n_k}_{\text{noise}}. \tag{B.13}$$

The desired signal of the k^{th} user propagates over the beamformed channel $\mathbf{H}_{(k,:)}\mathscr{D}^{\frac{1}{2}}_{(k,:)}\mathbf{G}_{(:,k)}$. Here, the user does not know the exact beamformed channel, but can approximate it to a mean value $\mathbb{E}\{\mathbf{H}_{(k,:)}\mathscr{D}^{\frac{1}{2}}_{(k,:)}\mathbf{G}_{(:,k)}\}$. Based on this, (B.13) can be rewritten as

$$\begin{aligned} y_k = {} & \underbrace{\sqrt{p_d}\mathbb{E}\{\mathbf{H}_{(k,:)}\mathscr{D}^{\frac{1}{2}}_{(k,:)}\mathbf{G}_{(:,k)}\}s_k}_{\text{Desired signal over average channel}} + \underbrace{\sqrt{p_d}\sum_{i=1,i\neq k}^{K}\mathbf{H}_{(k,:)}\mathscr{D}^{\frac{1}{2}}_{(i,:)}\mathbf{G}_{(:,i)}s_i}_{\text{Users' Interference}} \\ & + \underbrace{\sqrt{p_d}(\mathbf{H}_{(k,:)}\mathscr{D}^{\frac{1}{2}}_{(k,:)}\mathbf{G}_{(:,k)} - \mathbb{E}\{\mathbf{H}_{(k,:)}\mathscr{D}^{\frac{1}{2}}_{(k,:)}\mathbf{G}_{(:,k)}\})s_k}_{\text{Desired Signal over unknown channel}} + \underbrace{\sqrt{\bar{p}_d}\mathbf{H}_{(k,:)}\bar{\mathbf{G}}\bar{\mathbf{s}}}_{\text{AN leakage}} + \underbrace{n_k}_{\text{noise}}. \end{aligned} \tag{B.14}$$

$$\mathrm{SINR}_k = \frac{p_d \left| \mathbb{E}\left\{ \mathbf{H}_{(k,:)} \mathscr{D}_{(k,:)}^{\frac{1}{2}} \mathbf{G}_{(:,k)} \right\} \right|^2}{p_d \sum_{i=1}^{K} \mathbb{E}\left\{ \left| \mathbf{H}_{(k,:)} \mathscr{D}_{(i,:)}^{\frac{1}{2}} \mathbf{G}_{(:,i)} \right|^2 \right\} - p_d \left| \mathbb{E}\left\{ \mathbf{H}_{(k,:)} \mathscr{D}_{(k,:)}^{\frac{1}{2}} \mathbf{G}_{(:,k)} \right\} \right|^2 + \bar{p}_d \mathbb{E}\left\{ \left| \mathbf{H}_{(k,:)} \bar{\mathbf{G}} \right|^2 \right\} + \sigma_k^2}. \quad \text{(B.15)}$$

The first term in (B.14) presents the desired signal over the deterministic average beamformed channel, while the other terms are treated as noise.

Lemma B.4.1. *The ergodic channel capacity of the k^{th} user is lower-bounded using a hardening bound, that is*

$$R_k = \frac{\tau^d}{\tau^c} \log_2 \left(1 + SINR_k\right),$$

where τ^c is the number of samples per coherence block, τ^d is the number of downlink data samples per coherence block and $SINR_k$ can be given as in (B.15) in the top of the next page.

In this case, based on (B.12), the eavesdropper's data rate is

$$R_e = \frac{\tau^d}{\tau^c} \log_2 \left| \mathbf{I}_{M_E} + \left(p_d \sum_{m=1}^{M} \mathbf{h}_{em} \mathbf{G}_{(m,:)} \mathscr{D}_{(:,m)} \mathbf{G}_{(m,:)}^H \mathbf{h}_{em}^H \right) \times \left(\mathbf{Q}_e + \bar{p}_d \sum_{m=1}^{M} \mathbf{h}_{em} \bar{G}_{(m,:)} \bar{G}_{(m,:)}^H \mathbf{h}_{em}^H \right)^{-1} \right|, \quad \text{(B.16)}$$

where $\mathbf{Q}_\mathrm{e}$ is the covariance matrix of $\mathbf{n}_\mathrm{e}$.

B.4.2 Design and Feasibility Condition

To broadcast AN into the users' null space, the AN streams are pre-coded through the matrix $\bar{\mathbf{G}}$ which is chosen from the columns of the $\hat{\mathbf{H}}$ null space. This null space of $\hat{\mathbf{H}}$ exists when the number of transmitting antennas is larger than that of the receiving antennas. In the CF-MaMIMO systems, this typically occurs when the number of APs M is much higher than the number of users K. Moreover, to beamform the AN into the null space, the AN power $\bar{p}_d$ has to be a fixed number that is independent of the APs (i.e., all APs have the same $\bar{p}_d$ value) and achieves the following power constraint:

$$p_d \mathbf{G}_{(m,:)} \mathscr{D}_{(:,m)} \mathbf{G}_{(m,:)}^{\mathrm{H}} + \bar{p}_d \bar{\mathbf{G}}_{(m,:)} \bar{\mathbf{G}}_{(m,:)}^{\mathrm{H}} \leq p_d, \ \forall m, \quad \text{(B.17)}$$

where $\mathbb{E}\{\|\bar{\mathbf{G}}\|^2\}$=1. The proof can be found in the appendix B.9.1.

B.4.3 Power Allocation

From (B.16), decreasing the eavesdropper's data rate R_{e} requires boosting the AN power $\bar{p}_d$ and minimizing the signal power as much as possible. Unfortunately, the APs have to keep the transmission power at its limit to maintain the system's QoS. Denoting γ_k as the QoS (i.e., the minimum SINR_k) condition, the optimization problem $P1$ can be formulated as

$$P1: \min_{\eta_{km}} \sum_{m=1}^{M} \mathbf{G}_{(m,:)} \mathscr{D}_{(:,m)} \mathbf{G}_{(m,:)}^{\mathrm{H}} \tag{B.18a}$$

$$\text{s.t.}: \ \mathrm{SINR}_k \geq \gamma_k \quad \forall k, \tag{B.18b}$$

$$\eta_{km} \geq 0 \quad \forall k, m, \tag{B.18c}$$

$$p_d \mathbf{G}_{(m,:)} \mathscr{D}_{(:,m)} \mathbf{G}_{(m,:)}^{\mathrm{H}} + \bar{p}_d \bar{\mathbf{G}}_{(m,:)} \bar{\mathbf{G}}_{(m,:)}^{\mathrm{H}} \leq p_d \quad \forall m. \tag{B.18d}$$

Here, (B.18a) is the cost function that minimizes the transmission power of users' data, (B.18b) is the constraint that guarantees the user's QoS and (B.18d) is the power constraint. Now, we need to rewrite (B.18) in the standard form for semidefinite programming (SDP) problems so that it can be solved efficiently [125, 135].

Lemma B.4.2. *After some mathematical manipulations, the optimization problem $P1$ can be rewritten as*

$$P2: \min_{\mathbf{W}^{\eta}} \mathbb{TR}(\mathbf{W}^{\eta} \mathbf{V}^{0}), \tag{B.19a}$$

$$s.t.: \ p_d \mathbb{TR}(\mathbf{W}^{\eta} \mathbf{V}^{k}) \geq C_k^{(0)} \quad \forall k, \tag{B.19b}$$

$$\mathbf{W}^{\eta} \geq 0, \tag{B.19c}$$

$$p_d \mathbb{TR}\left(\left[\mathbf{W}^{\eta} \mathbf{V}^{0} \right]_{(L^{(m)}, L^{(m)})} \right) + \bar{p}_d \bar{\mathbf{G}}_{(m,:)} \bar{\mathbf{G}}_{(m,:)}^{H} \leq p_d \quad \forall m, \tag{B.19d}$$

where $\mathbf{w}_{\eta}$ is the power coefficient vector and $\mathbf{W}^{\eta} = \mathbf{w}_{\eta} \mathbf{w}_{\eta}^{T}$. Moreover, $\mathbf{V}^{0}$ is the matrix of constants that achieves the trace of the multiplication $\mathbf{W}^{\eta} \times \mathbf{V}^{0}$ representing the cost function, while $\mathbf{V}^{k}$ is the matrix of constants that makes the trace of the multiplication $\mathbf{W}^{\eta} \times \mathbf{V}^{k}$, which represents the QoS constraint for the k^{th} user. $p_d \mathbb{TR}\big(\left[\mathbf{W}^{\eta} \mathbf{V}^{0} \right]_{(L^{(m)}, L^{(m)})} \big)$ represents the data streams' power at the m^{th} AP and $C_k^{(0)}$ contains the power of the leakage AN and the AWGN. The conversion into SDP form can be found in Appendix B.9.2.

Lemma B.4.3. *When the power coefficients are only functions of the users (i.e., they are independent of the APs), $\eta_{k1} = \cdots = \eta_{kM} = \eta_k$, $\forall k$, and thus, $\mathscr{D}_{(k,:)} = \eta_k \mathbf{I}_M$, such that while using ZF, RZF and MMSE beamforming techniques, where the APs cooperate in beamforming the users' data streams and the power coefficients are functions only of k [127], the optimization problem $P1$ can be simplified to*

$$P3: \min_{\mathbf{w}_\eta} \mathbf{w}_\eta^T \mathbf{v}^0 \tag{B.20a}$$

$$s.t.: p_d \mathbf{w}_\eta^T \mathbf{v}^k \geq C_k^{(0)} \quad \forall k, \tag{B.20b}$$

$$\mathbf{w}_\eta^T \geq 0, \tag{B.20c}$$

$$p_d \sum_{k=1}^{K} \eta_k \xi_{km} + \bar{p}_d \bar{\mathbf{G}}_{(m,:)} \bar{\mathbf{G}}_{(m,:)}^H \leq p_d \quad \forall m, \tag{B.20d}$$

where the proof is in Appendix B.9.3. $P3$ is now a linear programming (LP) optimization problem and can be solved much more easily than the optimization problem $P2$.

However, these optimization problems are joint since they depend on two unknown parameters, the users' data stream power coefficients and the AN power $\bar{p}_d$. Therefore, the iterative optimization algorithm in [136] is used to separate such a problem into two distinct mathematical parts. In the first part, one of these parameters is fixed and the optimization problem is solved with respect to the other parameter. After that, the result of the previous optimization solution is utilized in determining the value of the second one. This process continues until the algorithm converges. We implement this technique when solving $P2/P3$.

First, the AN power $\bar{p}_d$ is fixed and set to zero as an initial value. Then, the power coefficient matrix is obtained from the optimization problem. After that, the values of the power coefficients are utilized to calculate $\bar{p}_d$, where this value of $\bar{p}_d$ is input into the optimization problem as a fixed value again and the process continues until the convergence 1. The value of $\bar{p}_d$ is calculated as

$$\bar{p}_d = \begin{cases} \mathbf{min}\{p_d\big(1 - \mathbb{TR}\big(\big[\mathbf{W}^\eta \mathbf{V}^0\big]_{(L^{(m)},L^{(m)})}\big)\big)/\big(\bar{\mathbf{G}}_{(m,:)} \bar{\mathbf{G}}_{(m,:)}^{\mathrm{H}}\big)\}, \ \forall m \text{ in } \mathbf{P2} \\ \mathbf{min}\{p_d\big(1 - \sum_{k=1}^{K} \eta_k \xi_{km}\big)/\big(\bar{\mathbf{G}}_{(m,:)} \bar{\mathbf{G}}_{(m,:)}^{\mathrm{H}}\big)\}, \ \forall m \text{ in } \mathbf{P3}. \end{cases} \tag{B.21}$$

However, when the system cannot achieve the QoS of all users, raising the users' data rates is prioritized, and, for simplicity, the power is allocated equally between them There are a few key details that should be noted about the algorithm:

- **Steps 5-6**: We select the value $\bar{p}$ that achieves the (B.19d)/(B.20d) constraint, and make the left side equal to p_d for at least one AP. However, a portion of this value is re-input into the optimization problem as the AN power $\bar{p}_d = f \times \bar{p}$, trying to leave an amount of $(1-f) \times \bar{p}$ power available to compensate for the QoS damage caused by the leaked AN power.
- **Steps 9-14**: The steps (5-6) are repeated so long as $(1-f) \times \bar{p}$ power can compensate the damage done to the QoS.
- **Steps 15-17**: If $(1-f) \times \bar{p}$ is unable to compensate the damage done to the QoS, the value of $f \times \bar{p}$ is decreased until the QoS is achieved.
- **Steps 19:** Here we have the system's energy efficiency constraint, where P_{EE} represents the maximum AN power that can be broadcast from the AP.

Algorithm 1 The iterative power allocation algorithm

Initialize $\bar{p}_d = 0$, $f = 0.5$, $\bar{p}_{d_{\text{last}}} = \bar{p}_d$
Compute $C_k^{(0)}$
if Problem $P2/P3$ is solved **then**
    Save $\mathbf{W}^{\eta}/\mathbf{w}^{\eta}$ and $\bar{p}_d = 0$
    Obtain $\bar{p}$ from (B.21).
    Calculate $\bar{p}_d = f \times \bar{p}$.
    Compute $C_k^{(0)}$
    Solve Problem $P2/P3$ and get $\mathbf{W}^{\eta}/\mathbf{w}^{\eta}$.
    if Problem $P2/P3$ is solved **then**
        Save $\mathbf{W}^{\eta}/\mathbf{w}^{\eta}$ and $\bar{p}_d$
        Define $\bar{p}_{d_{\text{last}}} = \bar{p}_d$
        Obtain $\bar{p}$ from (B.21).
        Define $f = 0.5$
        Calculate $\bar{p}_d = \bar{p}_{d_{\text{last}}} + f \times \bar{p}$.
    else
        Calculate$f = 0.5 \times f$
        Calculate $\bar{p}_d = \bar{p}_{d_{\text{last}}} + f \times \bar{p}$
    end if
    Go to step 7 **Until** $\bar{p}_d$ converge **OR** $\bar{p}_d \sum_{m=1}^{M} \bar{\mathbf{G}}_{(m,:)} \bar{\mathbf{G}}_{(m,:)}^{\mathrm{H}} \geq \mathrm{P_{EE}}$
    Return saved values.
else
    Equal power allocation
end if

B.5 Independent Physical Layer Security Algorithm (IND)

In this section, we present the **IND** PLS algorithm merely to boost AN distribution and enhance security performance. Considering the **COP** algorithm, the cooperation between APs imposes drawbacks because of the per AP power constraint problem: When any AP transmits data and fulfills its power budget, the other APs cannot boost their transmission power even if they have yet to reach their own power limit. In addition, the iterative algorithm increases the computational complexity of the system. The **IND** algorithm, on the other hand, adds $\overline{M}$ antennas to each AP, enabling each of them to independently broadcast AN from these $\overline{M}$ antennas, thereby increasing the total power dedicated to AN distribution and ultimately enhancing security. Besides, adding the AN antennas improves the beamforming gain of the AN channel between them and the hidden eavesdropper, which severely reduces the quality of the eavesdropped signal. Furthermore, the independent values of $\bar{p}_{d_m}$ reduce the complexity of the iterative power allocation process.

B.5.1 Adding the Artificial Noise

The transmitted signal from the m^{th} AP is given by

$$\mathbf{x}_m = \begin{bmatrix} \sqrt{p_d}\mathbf{G}_{(m,:)}\mathscr{D}_{(:,m)}^{\frac{1}{2}}\mathbf{s} \\ \sqrt{\bar{p}_{d_m}}\,\overline{\mathbf{G}}_m\bar{\mathbf{s}} \end{bmatrix},$$

while the received signals at the k^{th} user and the eavesdropper, respectively, are

$$\mathrm{SINR}_k = \frac{p_d \left| \mathbb{E}\left\{ \mathbf{H}_{(k,:)} \mathscr{D}_{(k,:)}^{\frac{1}{2}} \mathbf{G}_{(:,k)} \right\} \right|^2}{p_d \sum_{i=1}^{K} \mathbb{E}\left\{ \left| \mathbf{H}_{(k,:)} \mathscr{D}_{(i,:)}^{\frac{1}{2}} \mathbf{G}_{(:,i)} \right|^2 \right\} - p_d \left| \mathbb{E}\left\{ \mathbf{H}_{(k,:)} \mathscr{D}_{(k,:)}^{\frac{1}{2}} \mathbf{G}_{(:,k)} \right\} \right|^2 + p_d \sum_{m=1}^{M} \bar{c}_{km} - p_d \sum_{m=1}^{M} \sum_{i=1}^{K} \eta_{im} \bar{c}_{kim} + \sigma_k^2}, \tag{B.25}$$

$$y_k = \underbrace{\sqrt{p_d} \mathbf{H}_{(k,:)} \mathscr{D}_{(k,:)}^{\frac{1}{2}} \mathbf{G}_{(:,k)} s_k}_{\text{Desired Signal}} + \underbrace{\sqrt{p_d} \sum_{i=1, i\neq k}^{K} \mathbf{H}_{(k,:)} \mathscr{D}_{(i,:)}^{\frac{1}{2}} \mathbf{G}_{(:,i)} s_i}_{\text{Users' Interference}} + \underbrace{\sum_{m=1}^{M} \sqrt{\bar{p}_{d_m}} \overline{\mathbf{H}}_{mk} \overline{\mathbf{G}}_m \bar{\mathbf{s}}}_{\text{AN}} + \underbrace{n_k}_{\text{noise}}, \tag{B.22}$$

$$\mathbf{y}_{\mathrm{e}} = \sqrt{p_d} \sum_{m=1}^{M} \mathbf{h}_{em} \mathbf{G}_{(m,:)} \mathscr{D}_{(:,m)}^{\frac{1}{2}} \mathbf{s} + \sum_{m=1}^{M} \sqrt{\bar{p}_{d_m}} \overline{\mathbf{H}}_{em} \overline{\mathbf{G}}_m \bar{\mathbf{s}} + \mathbf{n}_{\mathrm{e}}, \tag{B.23}$$

where $\mathbf{s}$ is the vector symbol defined in Eq.(B.2), $\overline{\mathbf{G}}_m \in \mathbb{C}^{\overline{M} \times \bar{d}}$ is the AN precoding matrix at the m^{th} AP. The term $\overline{\mathbf{H}}_{mk} \in \mathbb{C}^{1 \times \overline{M}}$ represents the AN antenna links at the m^{th} AP and the kth user, while $\overline{\mathbf{H}}_{em} \in \mathbb{C}^{M_{\mathrm{E}} \times \overline{M}}$ is the link between the AN antennas at the m^{th} AP and the eavesdropper. Both $\overline{\mathbf{H}}_{mk}$ and $\overline{\mathbf{H}}_{em}$ are characterized by uncorrelated Rayleigh fading due to the rich scatter set mentioned in the system model. Accordingly, the channel gain between the j^{th} AN antenna element at the m^{th} AP and the k^{th} user is $\sim \mathbb{CN}(0, \beta_{km})$. Similarly, the channel gain between the same j^{th} element and the i^{th} element of the eavesdropper's antennas is $\sim \mathbb{CN}(0, \beta_{em})$.

The independent AN power $\bar{p}_{d_m}$ at the m^{th} AP is

$$\bar{p}_{d_m} = \mathbf{min}\left(p_d (1 - \mathbf{G}_{(m,:)} \mathscr{D}_{(:,m)} \mathbf{G}_{(m,:)}^{\mathrm{H}}), P_{\mathrm{EE}}/M \right) \ \forall m, \tag{B.24}$$

where P_{EE} represents the maximum AN power that can be broadcast from the AP, and is determined according to the system's energy efficiency constraint.

Lemma B.5.1. *The data rate at the k^{th} user can be bounded by the $SINR_k$ as follows in (B.25) in the top of the next page, while the eavesdropper's data rate can be calculated as*

$$R_e = \frac{\tau^d}{\tau^c} \log_2 \left| \mathbf{I}_{M_E} + \left(p_d \sum_{m=1}^{M} \mathbf{h}_{em} \mathbf{G}_{(m,:)} \mathscr{D}_{(:,m)} \mathbf{G}_{(m,:)}^{H} \mathbf{h}_{em}^{H} \right) \times \left(\mathbf{Q}_e + \sum_{m=1}^{M} \bar{p}_{d_m} \overline{\mathbf{H}}_{em} \overline{\mathbf{G}}_m \overline{\mathbf{G}}_m^{H} \overline{\mathbf{H}}_{em}^{H} \right)^{-1} \right|,$$

where $\bar{c}_{km}$, $\bar{c}_{kim}$, following the proofs in Appendix B.9.4.

B.5.2 Design and Feasibility Condition

The AN precoding matrix is selected from the null matrix, where the null matrix at the m^{th} AP is

$$\overline{\mathbf{W}}^m = \mathrm{null}\left\{ \left[\hat{\overline{\mathbf{H}}}_{m1}^{\mathrm{H}}, \hat{\overline{\mathbf{H}}}_{m2}^{\mathrm{H}}, \cdots, \hat{\overline{\mathbf{H}}}_{mK}^{\mathrm{H}} \right]^{\mathrm{H}} \right\},$$

and the AN precoding matrix is $\overline{\mathbf{G}}_m = \left(\overline{\mathbf{W}}^m_{(:,1:\bar{d})}\right) / \left\| \overline{\mathbf{W}}^m_{(:,1:\bar{d})} \right\|$. It is worth mentioning that the null matrix, and consequently the AN precoder matrix, exists for the m^{th} AP when the m^{th} AP is equipped with $\overline{M} > K$ antennas.

B.5.3 Power Allocation

Adding antennas at the APs leads to independent $\bar{p}_{d_m}$ at each AP, which makes the QoS (B.18b) and power (B.18d) constraints independent of the AN power as shown in Appendix B.9.4. Consequently, the joint optimization problem $P2$ becomes an individual optimization problem as follows

$$P4: \min_{\mathbf{W}^\eta} \mathbb{TR}(\mathbf{W}^\eta \mathbf{V}^0) \tag{B.26a}$$

$$\text{s.t.}: p_d \mathbb{TR}(\mathbf{W}^\eta \mathbf{V}^k) \geq C_k^{(0)} \quad \forall k, \tag{B.26b}$$

$$\mathbf{W}^\eta \geq 0, \tag{B.26c}$$

$$p_d \mathbb{TR}\left(\left[\mathbf{W}^\eta \mathbf{V}^0 \right]_{(L^{(m)}, L^{(m)})} \right) \leq p_d \quad \forall m. \tag{B.26d}$$

Applying the same idea to problem $P3$ gives

$$P5: \min_{\mathbf{w}_\eta} \mathbf{w}_\eta^{\mathrm{T}} \mathbf{v}^0 \tag{B.27a}$$

$$\text{s.t.}: p_d \mathbf{w}_\eta^{\mathrm{T}} \mathbf{v}^k \geq C_k^{(0)} \quad \forall k, \tag{B.27b}$$

$$\mathbf{w}_\eta^{\mathrm{T}} \geq 0, \tag{B.27c}$$

$$p_d \sum_{k=1}^{K} \eta_k \xi_{km} \leq p_d \quad \forall m. \tag{B.27d}$$

Now, the SDP and LP optimization problems $P4$ and $P5$ can be solved individually. The power used to broadcast AN, $\bar{p}_{d_m}$, is calculated from (B.24), removing the need for any iterative optimization algorithms and consequently decreasing the computational complexity of the system. Note that the structure of matrices $\mathbf{W}^\eta, \mathbf{V}^0$ and $\mathbf{V}^k$ is the same as in the optimization problem $P2$, and the structure of vectors $\mathbf{w}_\eta, \mathbf{v}^0$ and $\mathbf{v}^k$ is the same as in the optimization problem $P3$, but the values inside $\mathbf{V}^0, \mathbf{V}^k, \mathbf{v}^0, \mathbf{v}^k$ and $C_k^{(0)}$ are re-defined in Appendix B.9.4.

B.6 Hardware and Computational Complexities

This section investigates the additional hardware and computational complexities of the proposed algorithms, where the latter are evaluated by counting the number of arithmetic operations similar to those in works that discuss the computational complexity in massive MIMO and cell-free massive MIMO (i.e., those in [131, 137, 138]). Accordingly, this work evaluates the computational complexity for every access point as per the following: signal processing for channel estimation, signal processing for data reception and transmission, fronthaul signaling for data and CSI sharing, and power control optimization.

Hardware Complexity: It is quite evident that **COP** offers the simplest hardware of the two algorithms since no extra antennas are added to the system. This is not the case for the **IND** algorithm, where $\overline{M} = K + 1$ antennas are added at each AP. This is a reasonable number of antennas per AP. It is also applicable to CF-MaMIMO, where a number of works in the literature equipped each AP with a higher number of antennas than users. For example, in [139], the number of antennas per AP reached 64 antennas for 20 users.

Computational Complexity: There is no additional computational complexity due to fronthaul signaling for data and CSI sharing nor due to the signal processing for channel estimation. The reason for this is that the CPU utilizes the original users' CSI $\hat{\mathbf{H}}$ to design the AN beamforming matrix in the **COP** algorithm. Moreover, in the case of the **IND** algorithm, the AN beamforming matrix is built inside the AP not in the CPU, so there can be no additional security computational complexity due to fronthaul signaling for data and CSI sharing. However, building the AN precoding matrices in the **IND** algorithm requires estimating $\overline{\mathbf{H}}_{mk}$ for all m and k values, which intensifies the computational complexity. It can be concluded from Chapter 3 in [131] that the correlation process between the pilot ψ_k and $\mathbf{y}^{\mathrm{p}}_m = \sqrt{p_u}\sum_{k=1}^{K}\overline{\mathbf{H}}^{\mathrm{H}}_{mk}\psi_k + \mathbf{n}_m \in \mathbb{C}^{\overline{M}\times\tau^{\mathrm{p}}}$ requires $\overline{M}\times\tau^{\mathrm{p}} = K^2 + K$ mathematical operations, where $\overline{M} = K + 1$ is the minimum number of antennas to achieve the feasibility condition, and $\tau^{\mathrm{p}} = K$ ensures that orthogonality is achieved between pilots.

During the precoding design stage, the computational complexities of both algorithms are computed when the **null** is performed using singular value decomposition (SVD). From [140], the **IND** algorithm requires $K^3 + K^2$ mathematical operations performed by the AP while the **COP** requires only MK^2 operations performed by the CPU.

Furthermore, the CPU already optimizes the power allocation for the users' data streams. It does so based on different utility functions that determine the most appropriate approach to each optimization problem [138]. In this work, we just adopt a utility function that is suitable for security purposes, where it aims to minimize the transmission power to the amount that maintains the system's QoS, i.e., optimization problems $P2$ & $P3$. According to [141–143], the solutions of these problems using the interior-point method require $(KM)^{3.5}$ and $(K+M)^2K$ operations, respectively. Moreover, (B.21) and steps (5 & 12) in algorithm 1 require only M operations.

Consequently, the **IND** algorithm requires negligible computational complexity for AN power allocation since the AN power is calculated directly from Eq.(B.24), while the additional computational complexity in the case of the **COP** algorithm comes from solving the optimization problem N times to search for the AN power each time. Fortunately, the convergence of the iterative optimization algorithm is relatively quick, as seen in the simulation results section.

Considering all mentioned calculations, the **IND** performs $K(K+1)^2$ operations at the AP, which can be neglected (see Table 5 in [138]). Furthermore, the **COP** algorithm adds a very affordable computational complexity to the CPU, a unit that can comfortably perform the significant

number of operations mentioned in [138].

B.7 Discussion and Simulation Results

In this section, we evaluate the proposed PLS algorithms by applying them to the CF-MaMIMO system described in [127], where $M = 64$ single antenna APs and $K = 8$ single antenna users are uniformly distributed over a 1km×1km coverage area. To avoid boundary effects, and to imitate a network with an infinite area, the square area is wrapped around at the edges. The **Hata-COST** propagation model is used to model the large-scale coefficient as $10\log_{10}(\beta_{km}) = -136-35\log_{10}(d_{km})+X_{km}$, where d_{km} is the distance (in kilometers) between the m^{th} AP and the k^{th} user, and $X_{km} \sim \mathbb{N}(0, \sigma^2_{\text{shadow}})$ represents the shadow fading with $\sigma_{\text{shadow}} = 8$ dB. The AWGN variance at each receiver is $\sigma_w^2 = T_0 \times KB \times BW \times NF$, where $T_0 = 290$ (in Kelvin) is the noise temperature, $KB = 1.381\sqrt{ó}10^{\text{àí}23}$ (in Joules per Kelvin) is the Boltzmann constant, $BW = 20$ (in MHz) is the bandwidth and $NF = 9$ dB is the noise figure.

In this simulation, specifically during the uplink training stage, the user utilizes $p_u = 100$ mW to transmit an orthogonal pilot with sequence length τ^{P}, i.e., the case of low-speed mobility users. In the channel estimation stage, each AP estimates its channels with all users using the MMSE estimator, while in the downlink stage, all APs cooperate to serve the users simultaneously using the MMSE beamforming technique. The total downlink PT in the system is divided between the M APs equally such that p_d=$\frac{\text{PT}}{M}$. Then, p_d is allocated optimally, where the users' QoS is γ_k=4. The **IND** algorithm adds $\overline{M}$=9 antennas to broadcast an independent $\bar{p}_{d_m}$ for each AP. These specifications are the default unless otherwise mentioned.

In the same context, we used MATLAB to run all simulations. We built 250 different networks, each of which had a uniform geometrical distribution of APs and users. Within these networks, the eavesdropper occupied different locations, where it had distances to the APs in the range of [5−1330] m and distances to the users in the range of [15−1270] m. Moreover, in each network, we obtained the results by averaging 1000 random realizations for each distribution. The MATLAB toolbox 'CVX' in [144] was used to solve the optimization problems.

B.7.1 The Proposed Algorithms

To evaluate the improvements seen in security performance thanks to the proposed PLS algorithms, we compared them with two different scenarios. The first scenario, **Full**, transmits data streams with a complete PT that is equally divided between users. This scenario neither performs power control nor broadcasts any AN to enhance security. The second scenario, **QoS**, secures the transmission by performing optimal power control without broadcasting the AN [119–122]. Specifically, **QoS** transmits the data streams with only enough power to achieve the users,Äô QoS while minimizing the attainable data by the eavesdropper.

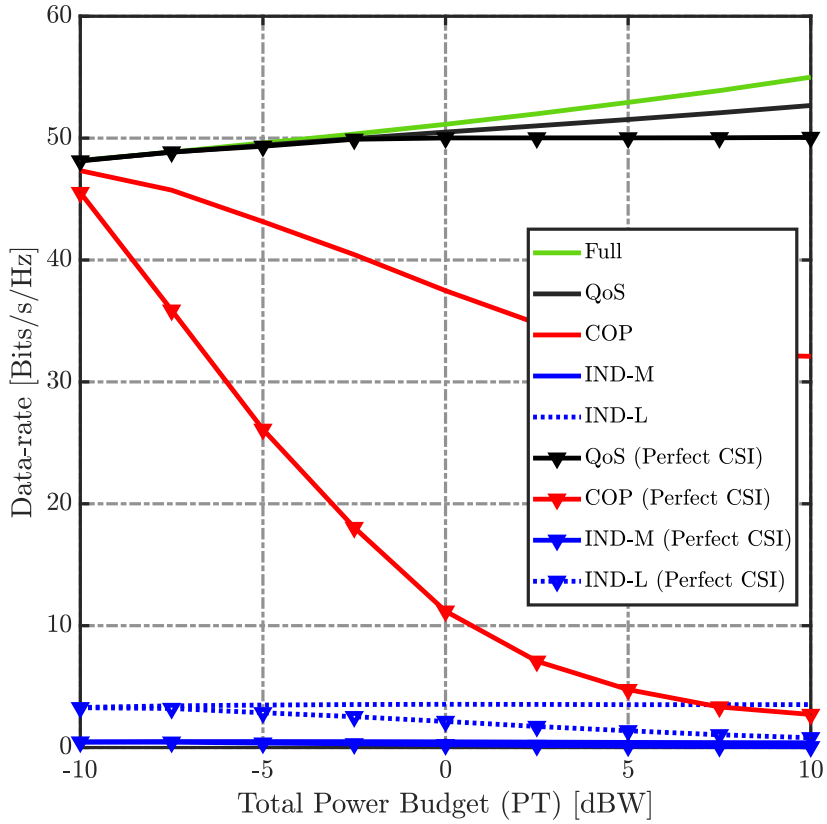

Figure B.2: Eavesdropper data rates versus the transmission schemes.

Moreover, we use the term **IND-M** to indicate a scenario that aims to maximize the security performance using the **IND** algorithm (i.e., by using the leftover component after achieving QoS to broadcast AN). On the other hand, we use **IND-L** to denote a scenario that prioritizes maintaining the desired energy efficiency simultaneously while enhancing the security performance. In this scenario, the **IND** algorithm limits the AN power to the amount that ensures that the energy efficiency in the system is accepted. Furthermore, for the **COP** algorithm, we always consider maximizing the security performance since the nature of the **COP** algorithm limits AN power.

Since this work investigates the PLS of CF-MaMIMO systems that aim to transmit a large amount of data, we present the secrecy performance in terms of the leaked data. More precisely, we use the number of tapped data streams i.e., the "eavesdropper data rate" as a benchmark to evaluate the security performance. As such, we present the concept of secrecy sum-rate as a way to represent the secured data, and we define it as the difference between the users' sum rate and the eavesdropped data streams [111, 113, 115, 116, 119].

Fig. B.2 presents the eavesdropper data associated with the different techniques proposed for securing the downlink of the CF-MaMIMO system. The figure demonstrates that as the system has accurate knowledge about users' CSI, the proposed algorithms become more efficient in securing the system. This occurs because the AN power is perfectly broadcast in the null of the

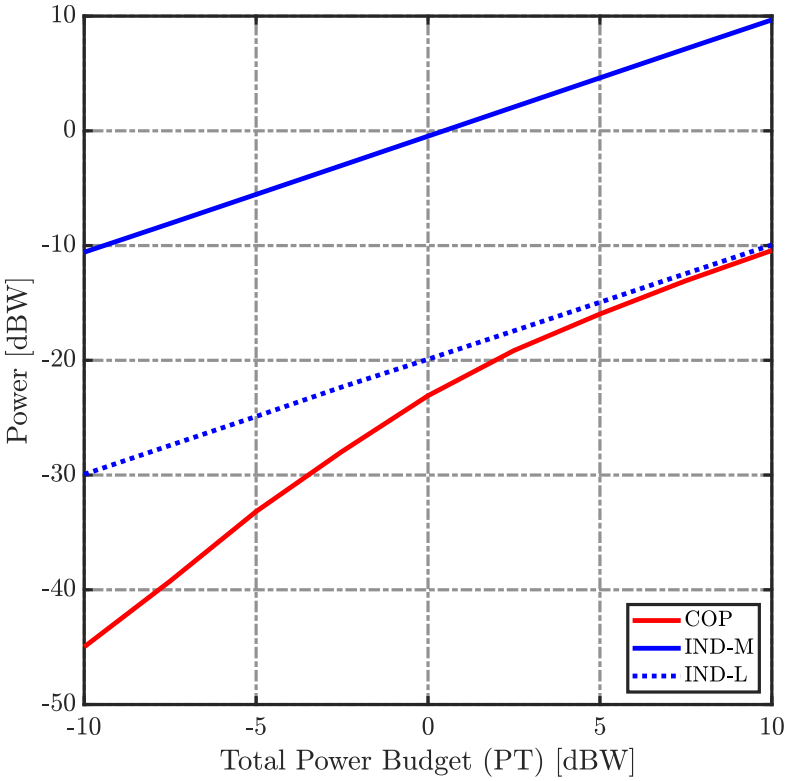

Figure B.3: AN powers of the proposed algorithms.

users and none of it leaks to the users. Consequently, the users' QoS is accomplished with a smaller amount of power and thus more is available for AN.

Moreover, Fig. B.2 shows, the **QoS** scheme more effectively limits the eavesdropper's data rate than the **Full** scheme by minimizing the users' data stream power to the amount that guarantees the QoS. While the **COP** and **IND** algorithms increase this limitation by broadcasting AN, the **IND** algorithm jamming has more of an effect than the **COP** algorithm.

Fig. B.3 interprets the reasons behind the advanced security performance of the **IND** algorithm over the **COP** algorithm. The first reason is that the amount of power dedicated to AN broadcasting is greater in the former than in the latter, because the cooperation between the APs in the **COP** scheme inevitably comes across an AP power constraint problem. When one AP point reaches its power constraint, the others cannot consume more power even if they are below their own power constraints, and hence the total consumed power in the **COP** cannot reach the PT. This constraint is relaxed when using the **IND** algorithm, meaning that the amount of consumed power reaches the PT because each AP has an independent AN power value $\bar{p}_{d_m}$, and thus consumes its PT completely as in (B.24) which maximizes the AN power.

The security performance is bolstered additionally by a multiple-antenna AN channel gain, which is achieved by using $\overline{M}$ antennas to broadcast the AN. Although the AN power of the **IND-L** is limited and approaches that of the **COP** algorithm, as seen in Fig. B.3, the security performance of the **IND-L** algorithm is still superior to that of **COP**, as seen in Fig. B.2. Consequently, we

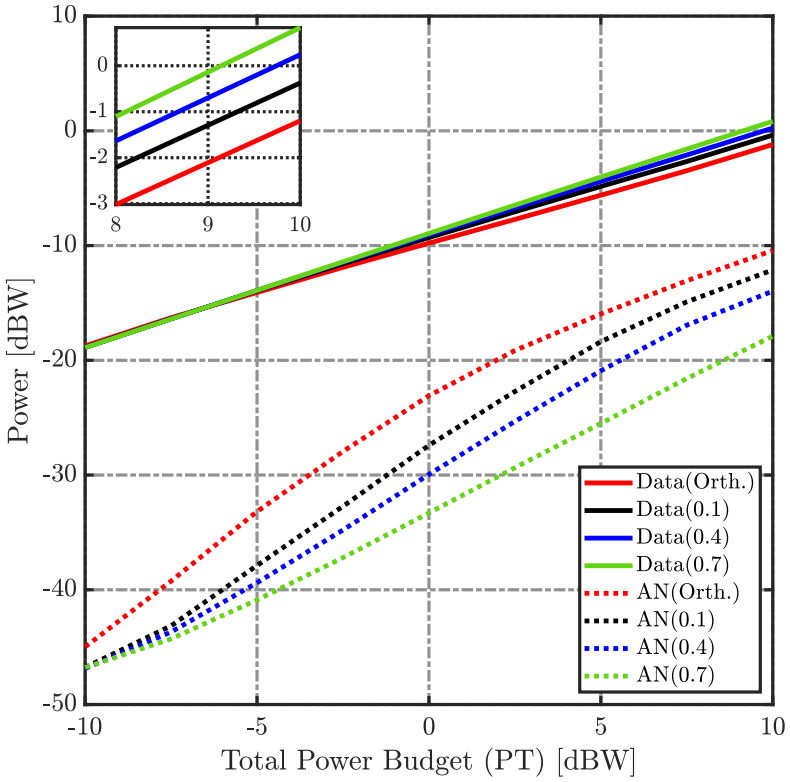

Figure B.4: **COP**. algorithm powers at different pilot contamination levels.

henceforth simulate and analyze while aiming to maximize the security performance, i.e we use the **IND-M** algorithm, where all the conclusions and analysis are applicable for the **IND-L** algorithm.

Figs. B.4 and B.5 illustrate the amount of power used to distribute user data and AN versus the PT for different levels of pilot contamination. It is worth noting that the extent of pilot contamination is determined by the users' mobility. In low-speed mobility scenarios, it is possible to achieve orthogonal pilot signals, which can reduce the impact of pilot contamination and improve channel estimation accuracy. Many points can be concluded from these figures. First, the amount of power used to stream user data is almost the same in both algorithms for each contamination level because both of them prioritize QoS. The small difference between them occurs because of the AN leakage, as was seen in Fig. B.6. Second, the channel estimation error has a minor effect on the AN power when using the **IND** algorithm, where almost the same AN power can be observed for all contamination levels. Third, at a low power budget ($PT < -2.5$ dBW), when the PTs are not enough to achieve the QoS, the data stream powers are approximately the same at all contamination levels because these PTs fail in achieving the QoS and thus equal power allocation is performed. Fourth, at a high power budget ($PT > -2.5$ dBW), when the PTs are enough to satisfy the QoS, the more accurate channel estimation accomplishes the QoS with a smaller amount of power, saving up more power to broadcast AN. This occurs because as the

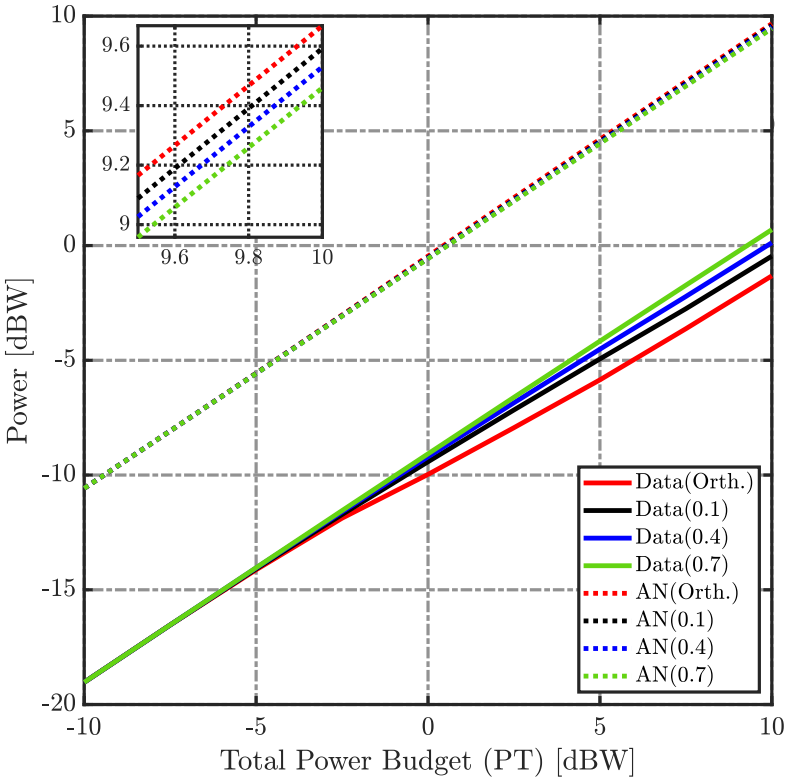

Figure B.5: **IND**. algorithm powers at different pilot contamination levels.

estimation becomes more accurate, the APs perform more accurate beamforming, which boosts the signal's power at the users and reduces the interference between them. The leaked AN is also decreased. Finally, we can conclude from these figures that AN power increases by boosting the PT, which also enhances security performance.

Fig. B.6 plots the leaked AN power, which is determined by the AN power and estimation error as in (B.15) and (B.25), against the PT. The results in this figure agree with the ones in Figs. B.4 and B.5, where for the **COP** algorithm, when PT < -7.5 dB, the estimation errors have a dominant role in determining the leaked AN power at the users. Moreover, when PT > -7.5 dB, the AN powers have different quantities at each pilot contamination value and thus have a dominant effect in the leaked AN power at the eavesdropper. On the other hand, for the **IND** algorithm, the AN power value is high and increases with estimation accuracy. Therefore, it has more of an effect on the leaked AN than the estimation errors (i.e., the leaked AN power is proportional to the AN power regardless of the pilot contamination).

As discussed before, the **IND** algorithm requires using a less complicated estimator. Fig. B.6 presents the difference between the leaked AN power when using the LS estimator in lieu of the MMSE one in conjunction with the **IND** algorithm. This figure confirms that the LS is less accurate than the MMSE at all pilot contamination levels. In addition, it shows that as pilot contamination increases, the amount of leaked AN intensifies, which implicitly leads to a greater degradation to the QoS. However, these variations in the amount of leaked AN between using the

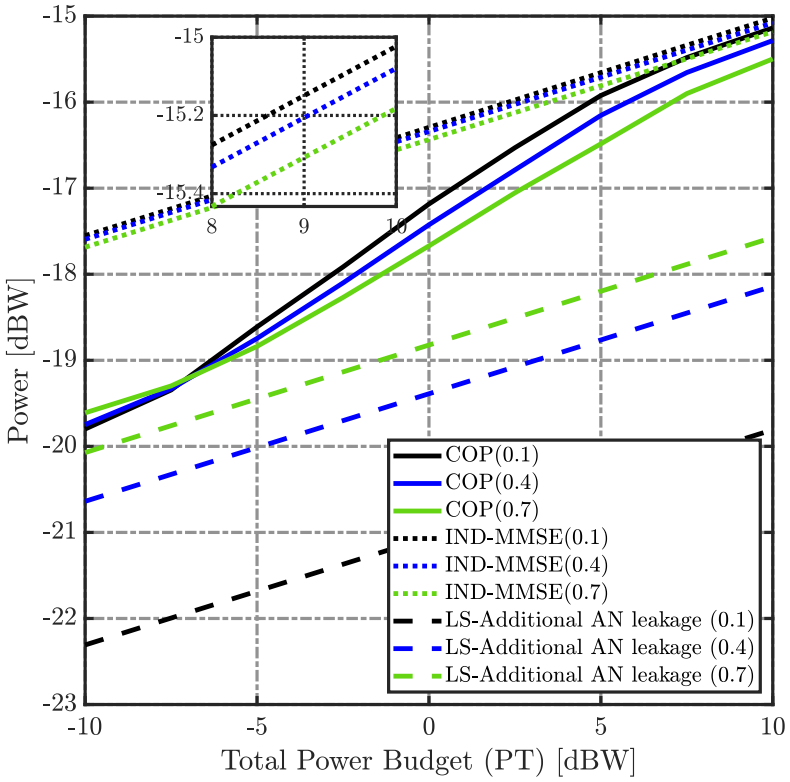

Figure B.6: AN Leakage power at different pilot contamination levels.

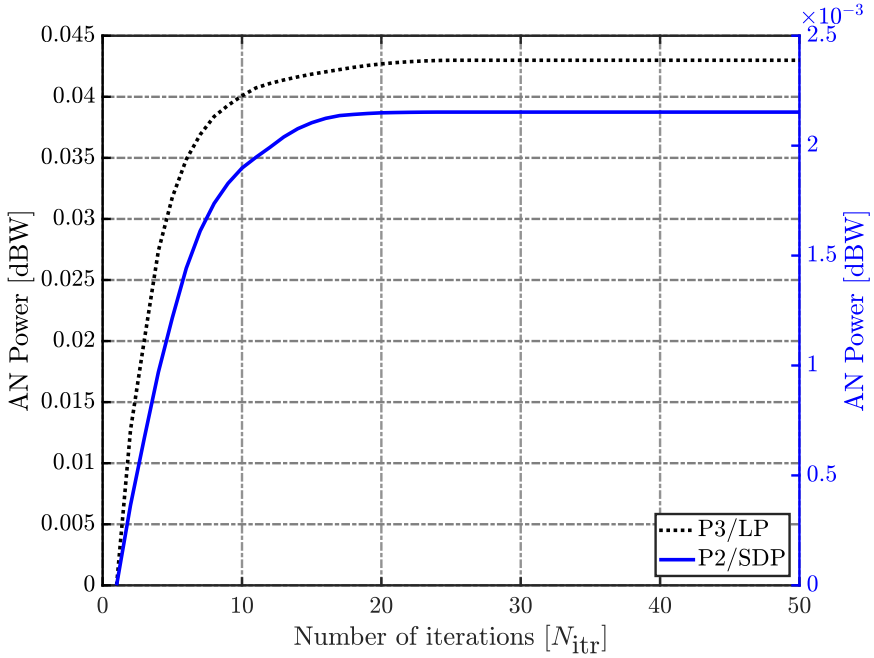

Figure B.7: Convergence time of algorithm 1.

MMSE estimator or the LS are negligible with respect to the amount of AN leakage seen in Fig. B.6.

Fig. B.7 presents the convergence of the algorithm (1) by plotting the AN power against the number of iterations when the pilot contamination has an inner product of 0.1. The iterative optimization algorithm converges to 90% of the steady-state in less than nine iterations and converges after two and four iterations to 60% from the final value of the AN power. It is clear that increasing the iterations boosts the AN power at the cost of increasing computational complexity. Therefore, the number of iterations can be two iterations when minimizing the computational complexity or nine when maximizing the security performance.

B.7.2 Network's Factors Impact on Security

Fig. B.8 illustrates the eavesdropper data rates at various numbers of users. This figure implies that the number of users determines the amount of power supplied to the users' data streams, thus also impacting the power reserved for AN distribution. The enhancement in security performance, measured by the degradation of eavesdropper's data-rate, becomes greater as the number of users decreases. It is evident that as the number of users increases, the amount of secured data decreases because more power is consumed when serving the users. This ultimately reduces the amount power dedicated to AN broadcasting. On another note, the secured data rate increases as the PT increases. Moreover, for the **IND** algorithm, as the number of users increases, the AN channel's beamforming gain also increases due to the elevated number of AN antennas. This can compensate for the degradation of the security performance because of the reduction in AN power. As a result, the reduction in security performance due to an increase in the number of users in the case of the **IND** case is limited in comparison to that of the **COP** case.

Fig. B.9 presents the role of the users' QoS on the security performance. As the users' QoS level increases along with the power used to stream the users' data, there is an increase in the amount of power received by the eavesdropper, which mitigates the effect of AN and undermines security performance. However, the **IND** algorithm demonstrates an excellent performance, where more AN power is exploited at all QoS levels which degrades the eavesdropper's performance. Specifically, this figure highlights an important feature regarding the **IND** algorithm in the presence of the per AP power constraint. When $\gamma_k = 8$, the eavesdropper's data rate associated with **QoS** scheme and **COP** algorithm, is approximately equal to that of the case of the **FULL** transmission scheme. This means that satisfying the system's QoS is accomplished by increasing the data streams' power until facing the per AP power constraint challenge, so the **COP** algorithm is unable to broadcast AN power. On the other hand, due to the independence property in the **IND** algorithm, it can exploit the remaining power at the APs after the per AP power constraint limit in broadcasting the AN power.

Fig.B.10 discusses the effect of the number of APs on security performance. The PT is fixed at 0 dBW to avoid its role in security performance. Although increasing the number of APs improves the connectivity of the users and the eavesdropper, the users' sum-rate (USR) in the **FULL** scheme increases with M while the eavesdropper's data rate (EDR) remains constant because of the beamforming techniques that maximize the power used for users and mitigate it otherwise.

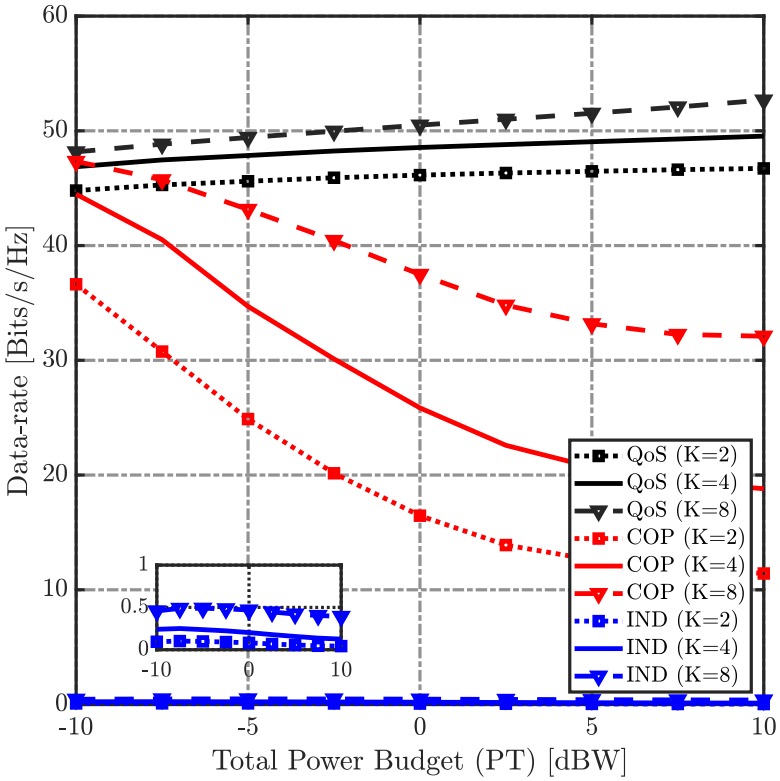

Figure B.8: Eavesdropper data rates at different number of users (K).

Besides, it is clear that the **QoS** scheme conserves the users' sum-rate above the lower bound and decreases the eavesdropper's data-rate because it bounds the power of the users' data streams. Moreover, since increasing the number of APs improves the connectivity, the **COP** and the **IND** algorithms achieve the QoS with a minimum amount of power, resulting in more power left over for the distribution of AN and ultimately decreasing the eavesdropper's data rates.

Fig. B.11 demonstrates the impact of the number of antennas ($\bar{M}$) on the secrecy performance when using the **IND** algorithm, where this impact depends on the channel estimation accuracy. Increasing the number of AN antennas amplifies the jamming signal at the eavesdropper. However, in the case of imperfect channel estimation, increasing the number of antennas exacerbates AN leakage to legitimate users, which in turn necessitates the use of more power to achieve the QoS, ultimately reducing the amount of broadcast AN. Moreover, enhancing the channel estimation accuracy leads to more effective security performance as the figure presents in the case of perfect CSI.

Fig.B.12 proves that beamforming the AN in the null of users is independent of the user's data stream beamforming techniques. Here, we secure the system when using different users' data beamforming techniques in the presence of pilot contamination with an inner product 0.1, where the AN beamformer is fixed with all of these users' data beamformers. The specifications of these different beamforming techniques can be noted in the figure, where the MR precoder

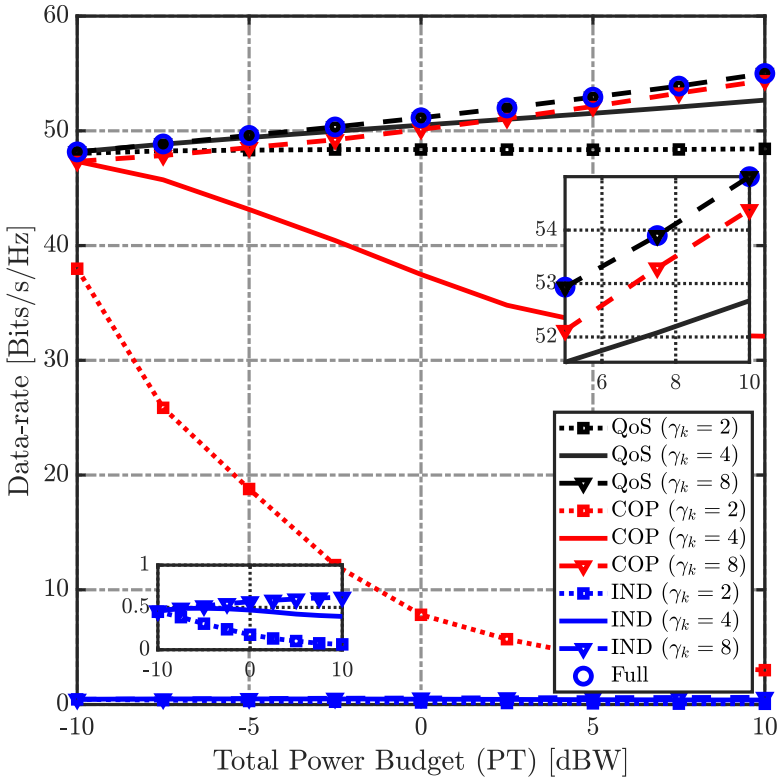

Figure B.9: Eavesdropper data rates at different QoS (γ_k) levels.

has the worst performance in these interfering environments and consumes more power than others to achieve the QoS, which degrades its security performance. However, the RZF and ZF beamforming techniques demonstrate performance approaching that of the MMSE technique.

B.8 Conclusion

In this paper, PLS is used to protect downlink data streams in CF-MaMIMO systems from passive eavesdropping. We broadcast both data streams and AN into the null of users. The **COP** algorithm achieves the feasibility conditions through the cooperation of APs; however, it prevents the APs from utilizing their total PTs. The **IND** algorithm achieves the AN feasibility conditions by increasing the number of AP antennas, which enables them to broadcast AN independently and allows them to consume their PTs completely. An optimization problem is formulated to maximize the AN power and to keep the QoS in a system affected by AN leakage due to estimation error. Both the hardware and the computational complexities of the proposed algorithms are compared, and then their security performances are evaluated regarding the number of users, number of APs, QoS, beamforming techniques, estimation errors and AN leakage. Our simulation results demonstrate that the proposed algorithms enhance the security of the system under multiple conditions. In future work, we plan to study the implementation of these proposed algorithms in the context of non-ideal transceivers at the BS and users. After that, the analysis in

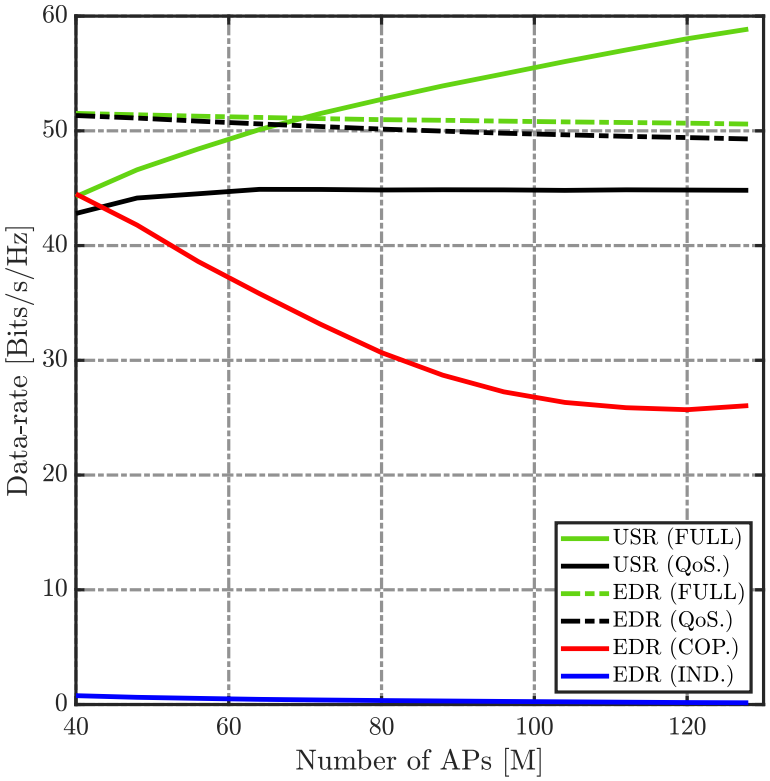

Figure B.10: Data-rate at different numbers of AP (M).

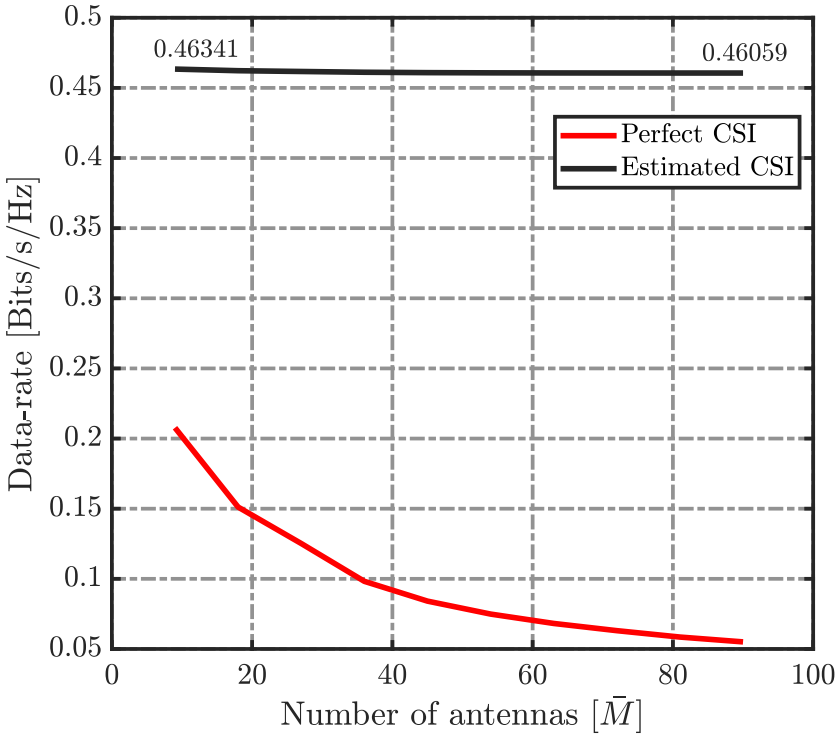

Figure B.11: Eavesdropper data rates versus the number of antennas ($\bar{M}$).

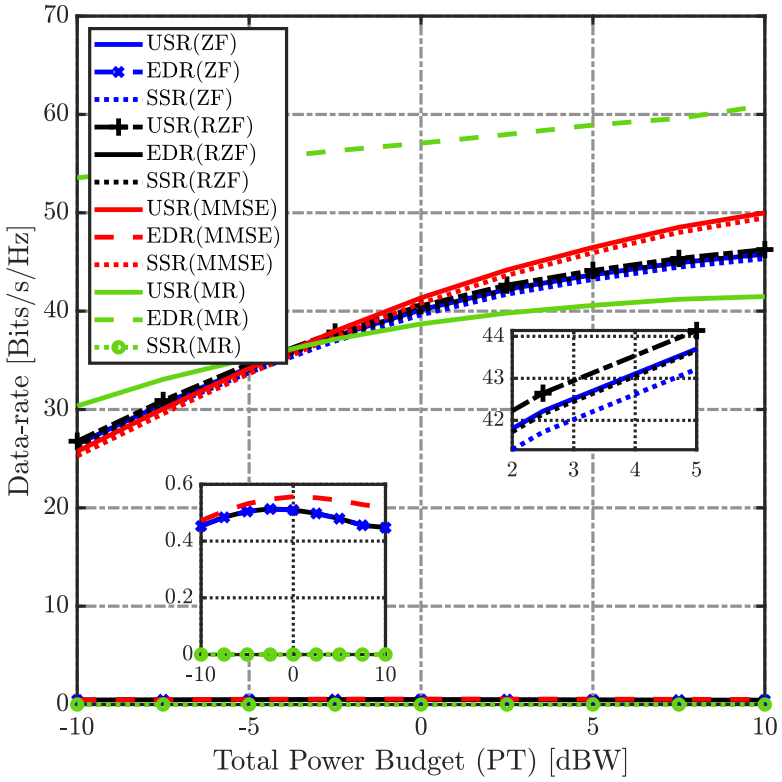

Figure B.12: secrecy sum-rate with different beamforming techniques.

terms of secrecy outage probability will be conducted to probe the possibility of satisfying system security requirements in the presence of non-ideal transceivers.

Acknowledgments

The authors would like to sincerely thank Laila Ikki for her diligent proofreading of this paper.

B.9 Appendices

B.9.1 Proof of the power constrain in (B.17).

Considering a system composed of K users and M APs, where $\mathbf{H} \in \mathbb{C}^{K\times M}$ is the channel matrix between the users and the APs, while the pre-coding matrix $\bar{\mathbf{G}} \in \mathbb{C}^{M\times 1}$ is chosen from the columns of the $\mathbf{null}(\mathbf{H})$ and thus $\mathbf{H}\bar{\mathbf{G}} = \mathbf{0}_{K\times 1}$.

The transmitted signal from the m^{th} AP

$$x_m = \underbrace{\sqrt{p_d}\mathbf{G}_{(m,:)}\mathscr{D}^{\frac{1}{2}}_{(:,m)}\mathbf{s}}_{\text{Users' Data}} + \underbrace{\sqrt{\bar{p}_m}\bar{\mathbf{G}}_{(m,:)}\bar{\mathbf{s}}}_{\text{AN}}, \tag{B.28}$$

and the received AN at the k^{th} user is

$$y_k^{\mathrm{AN}} = \underbrace{\sum_{m=1}^{M} \sqrt{\bar{p}_m}\mathbf{H}_{(k,m)}\bar{\mathbf{G}}_{(m,:)}\bar{\mathbf{s}}}_{\mathrm{AN}} = \underbrace{\begin{bmatrix} \mathbf{H}_{(k,1)} \\ \mathbf{H}_{(k,2)} \\ \vdots \\ \mathbf{H}_{(k,M)} \end{bmatrix}^{\mathrm{T}}}_{\mathbf{H}_{(k,:)}} \underbrace{\begin{bmatrix} \sqrt{\bar{p}_1} & 0 & \cdots & 0 \\ 0 & \sqrt{\bar{p}_2} & \cdots & 0 \\ \vdots & \cdots & \cdots & 0 \\ 0 & \cdots & 0 & \sqrt{\bar{p}_M} \end{bmatrix}}_{\mathbf{P}} \underbrace{\begin{bmatrix} \bar{\mathbf{G}}_{(1,:)} \\ \bar{\mathbf{G}}_{(2,:)} \\ \vdots \\ \bar{\mathbf{G}}_{(M,:)} \end{bmatrix}}_{\bar{\mathbf{G}}} \bar{\mathbf{s}}. \tag{B.29}$$

When $\sqrt{\bar{p}_1} = \sqrt{\bar{p}_2} = \cdots \sqrt{\bar{p}_M} = \sqrt{\bar{p}_d}$, then $\mathbf{P}\bar{\mathbf{G}} = \sqrt{\bar{p}_d}\bar{\mathbf{G}}$, and since $\mathbf{H}\bar{\mathbf{G}} = \mathbf{0}_{K\times 1}$, then $y_k^{\mathrm{AN}} = \sqrt{\bar{p}_d}\mathbf{H}_{(k,:)}\bar{\mathbf{G}}\bar{\mathbf{s}} = 0$. However, when $\sqrt{\bar{p}_1} \neq \sqrt{\bar{p}_2} \neq \cdots \neq \sqrt{\bar{p}_M}$, then $\mathbf{P}\bar{\mathbf{G}}$ results in new columns that are outside the space of the $\mathbf{null}(\mathbf{H})$ and thus the expression in (B.29) becomes $y_k^{\mathrm{AN}} = \mathbf{H}_{(k,:)}\mathbf{P}\bar{\mathbf{G}}\bar{\mathbf{s}} \neq 0$.

Consequently, to beamform the AN into the null space, the AN power $\bar{p}_d$ has to be a fixed number and the same in all APs. Thus, the power constraint at the m^{th} AP becomes

$$p_d\mathbf{G}_{(m,:)}\mathscr{D}_{(:,m)}\mathbf{G}_{(m,:)}^{\mathrm{H}} + \bar{p}_d\bar{\mathbf{G}}_{(m,:)}\bar{\mathbf{G}}_{(m,:)}^{\mathrm{H}} \leq p_d,\ \forall m. \tag{B.30}$$

B.9.2 Proof of Lemma B.4.2

The cost function of the optimization problem $P1$ is

$$\sum_{m=1}^{M}\mathbf{G}_{(m,:)}\mathscr{D}_{(:,m)}\mathbf{G}_{(m,:)}^{\mathrm{H}} = \sum_{m=1}^{M}\sum_{k=1}^{K}\eta_{km}\xi_{km}, \tag{B.31}$$

where $\xi_{mk} = \mathbf{G}_{(m,k)}\mathbf{G}_{(m,k)}^{*}$. Besides, the numerator of (B.15) can be simplified to

$$\begin{aligned}\left|\sqrt{p_d}\mathbb{E}\left\{\mathbf{H}_{(k,:)}\mathscr{D}_{(k,:)}^{\frac{1}{2}}\mathbf{G}_{(:,k)}\right\}\right|^2 &\triangleq p_d\Big(\sum_{m=1}^{M}\sqrt{\eta_{km}}\mathbb{E}\left\{\mathbf{G}_{(m,k)}\hat{\mathbf{H}}_{(k,m)}\right\}\Big)^2 \\ &= p_d\Big(\sum_{m=1}^{M}\sqrt{\eta_{km}}c_{km}\Big)^2 \\ &= p_d\sum_{m=1}^{M}\sum_{\dot{m}=1}^{M}\sqrt{\eta_{km}}\sqrt{\eta_{k\dot{m}}}\times c_{km}c_{k\dot{m}},\end{aligned}$$

where $c_{km} = \mathbb{E}\{\mathbf{G}_{(m,k)}\hat{\mathbf{H}}_{(k,m)}\}$ and ($\triangleq$) refers to the independence between the different random elements (i.e., channel estimate and the estimation error).

Correspondingly, the first term in the denominator of (B.15) can be simplified as

$$\begin{aligned}p_d\sum_{i=1}^{K}\mathbb{E}\left\{\left|\mathbf{H}_{(k,:)}\mathscr{D}_{(i,:)}^{\frac{1}{2}}\mathbf{G}_{(:,i)}\right|^2\right\} &\triangleq p_d\sum_{i=1}^{K}\mathbb{E}\left\{\left|\hat{\mathbf{H}}_{(k,:)}\mathscr{D}_{(i,:)}^{\frac{1}{2}}\mathbf{G}_{(:,i)}\right|^2\right\} + p_d\sum_{i=1}^{K}\mathbb{E}\left\{\left|\tilde{\mathbf{H}}_{(k,:)}\mathscr{D}_{(i,:)}^{\frac{1}{2}}\mathbf{G}_{(:,i)}\right|^2\right\} \\ &\triangleq p_d\sum_{i=1}^{K}\mathbb{E}\left\{\left|\sum_{m=1}^{M}\sqrt{\eta_{im}}\hat{\mathbf{H}}_{(k,m)}\mathbf{G}_{(m,i)}\right|^2\right\} + p_d\sum_{i=1}^{K}\sum_{m=1}^{M}\eta_{im}c_{kim} \\ &= p_d\sum_{i=1}^{K}\sum_{m=1}^{M}\sum_{\dot{m}=1}^{M}\sqrt{\eta_{im}\eta_{i\dot{m}}}c_{m\dot{m}}^{ki} + p_d\sum_{i=1}^{K}\sum_{m=1}^{M}\eta_{im}c_{kim},\end{aligned}$$

where $c_{m\dot{m}}^{ki} = \mathbb{E}\left\{\hat{\mathbf{H}}_{(k,m)}\mathbf{G}_{(m,i)}\hat{\mathbf{H}}_{(k,\dot{m})}^{*}\mathbf{G}_{(\dot{m},i)}^{*}\right\}$, and $c_{kim} = (\beta_{km} - \alpha_{km})\mathbb{E}\{|\mathbf{G}_{(m,i)}|^2\}$.

The third term in the denominator can also be presented as

$$\begin{aligned}
\bar{p}_d\mathbb{E}\left\{\left|\mathbf{H}_{(k,:)}\bar{\mathbf{G}}\right|^2\right\} &\triangleq \bar{p}_d\mathbb{E}\left\{\left|\tilde{\mathbf{H}}_{(k,:)}\bar{\mathbf{G}}\right|^2\right\} \\
&= \bar{p}_d\,\mathbb{TR}\left(\mathbb{E}\left\{\tilde{\mathbf{H}}_{(k,:)}^{\mathrm{H}}\tilde{\mathbf{H}}_{(k,:)}\bar{\mathbf{G}}\bar{\mathbf{G}}^{\mathrm{H}}\right\}\right) \\
&\triangleq \bar{p}_d\,\mathbb{TR}\left(\mathscr{E}_{(\beta_{km}-\alpha_{km})}\mathbb{E}\left\{\bar{\mathbf{G}}\bar{\mathbf{G}}^{\mathrm{H}}\right\}\right) \\
&= \bar{p}_d\sum_{m=1}^{M}\left(\beta_{km}-\alpha_{km}\right)\mathbb{E}\left\{\bar{\mathbf{G}}_{(m,:)}\bar{\mathbf{G}}_{(m,:)}^{\mathrm{H}}\right\} \\
&= \bar{p}_d c_k^{\mathrm{AN}},
\end{aligned}$$

where $\mathscr{E}_{(\beta_{km}-\alpha_{km})} \in \mathbb{C}^{M\times M}$ is a diagonal matrix that contains the variances of the channel estimation errors between the k^{th} user and the APs, and $(\triangleq)$ indicates the null effect, $\hat{\mathbf{H}}_{(k,:)}\bar{\mathbf{G}} = 0$. Now let us define the following terms

$$\begin{aligned}
&C_{\eta_{km}} = (1+\gamma_k)c_{km}^2 - \gamma_k(c_{mm}^{kk} + c_{kkm}), \\
&C_{\eta_{km\dot{m}}} = ((1+\gamma_k)c_{km}c_{k\dot{m}} - \gamma_k c_{m\dot{m}}^{kk}), \\
&\underline{C}_{\eta_{kim}} = -\gamma_k(c_{mm}^{ki} + c_{kim}), \\
&C_{\eta_{kim\dot{m}}} = -\gamma_k c_{m\dot{m}}^{ki}, \\
&\text{and} \\
&C_k^{(0)} = \gamma_k(\bar{p}_d c_k^{\mathrm{AN}} + \sigma_k^2),
\end{aligned}$$

meaning that constraint (B.18b) in the optimization problem $P1$ becomes

$$\sum_{m=1}^{M}\eta_{km}C_{\eta_{km}} + \sum_{m=1}^{M}\sum_{\substack{\dot{m}=1,\\ \dot{m}\neq m}}^{M}\sqrt{\eta_{km}\eta_{k\dot{m}}}C_{\eta_{km\dot{m}}} + \sum_{\substack{i=1,\\ i\neq k}}^{K}\sum_{m=1}^{M}\eta_{im}\underline{C}_{\eta_{kim}} + \sum_{\substack{i=1,\\ i\neq k}}^{K}\sum_{m=1}^{M}\sum_{\dot{m}=1,\dot{m}\neq m}^{M}\sqrt{\eta_{im}\eta_{i\dot{m}}}C_{\eta_{kim\dot{m}}} \geq C_k^{(0)}. \tag{B.32}$$

It is clear that the cost function in (B.31) and in the constraints of (B.32) are a sum of multiplications between the power coefficients and constants. Therefore, let's define

$$\mathbf{w}_\eta \in \mathbb{R}^{KM\times 1} = \left(\Big[\underbrace{\eta_{11},\eta_{21},\cdots,\eta_{K1}}_{\mathbf{D}_{(:,1)}},\underbrace{\eta_{12},\eta_{22},\cdots,\eta_{K2}}_{\mathbf{D}_{(:,2)}},\cdots,\underbrace{\eta_{1M},\eta_{2M},\cdots,\eta_{KM}}_{\mathbf{D}_{(:,M)}}\Big]^{\frac{1}{2}}\right)^{\mathrm{T}},$$

$$\mathbf{W}^{\eta} \in \mathbb{R}^{KM\times KM} = \mathbf{w}_{\eta}\mathbf{w}_{\eta}^{\mathrm{T}} = \begin{bmatrix} \eta_{11}, & \cdots \sqrt{\eta_{11}\eta_{K1}}, & \sqrt{\eta_{11}\eta_{12}} \cdots \sqrt{\eta_{11}\eta_{K2}} \cdots \sqrt{\eta_{11}\eta_{1M}} \cdots \sqrt{\eta_{11}\eta_{KM}} \\ \vdots & \ddots \quad \vdots & \vdots \quad \vdots \quad \vdots \quad \vdots \quad \vdots \quad \vdots \\ \sqrt{\eta_{K1}\eta_{11}} \cdots & \eta_{K1}, & \sqrt{\eta_{K1}\eta_{12}} \cdots \sqrt{\eta_{K1}\eta_{K2}} \cdots \sqrt{\eta_{K1}\eta_{1M}} \cdots \sqrt{\eta_{K1}\eta_{KM}} \\ \sqrt{\eta_{12}\eta_{11}} \cdots & \sqrt{\eta_{12}\eta_{K1}}, & \eta_{12} \quad \cdots \sqrt{\eta_{12}\eta_{K2}} \cdots \sqrt{\eta_{12}\eta_{1M}} \cdots \sqrt{\eta_{12}\eta_{KM}} \\ \vdots & \vdots \quad \vdots & \vdots \quad \ddots \quad \vdots \quad \vdots \quad \vdots \quad \vdots \quad \vdots \\ \sqrt{\eta_{K2}\eta_{11}} \cdots & \sqrt{\eta_{K2}\eta_{K1}}, & \sqrt{\eta_{K2}\eta_{12}} \cdots \quad \eta_{K2} \quad \cdots \sqrt{\eta_{K2}\eta_{1M}} \cdots \sqrt{\eta_{K2}\eta_{KM}} \\ \vdots & \vdots \quad \vdots & \vdots \quad \vdots \quad \vdots \quad \ddots \quad \vdots \quad \vdots \quad \vdots \\ \sqrt{\eta_{1M}\eta_{11}} \cdots & \sqrt{\eta_{1M}\eta_{K1}}, & \sqrt{\eta_{1M}\eta_{12}} \cdots \sqrt{\eta_{1M}\eta_{K2}} \cdots \quad \eta_{1M} \quad \cdots \sqrt{\eta_{1M}\eta_{KM}} \\ \vdots & \vdots \quad \vdots & \vdots \quad \vdots \quad \vdots \quad \vdots \quad \ddots \quad \vdots \\ \sqrt{\eta_{KM}\eta_{11}} \cdots & \sqrt{\eta_{KM}\eta_{K1}}, & \sqrt{\eta_{KM}\eta_{12}} \cdots \sqrt{\eta_{KM}\eta_{K2}} \cdots \sqrt{\eta_{KM}\eta_{1M}} \cdots \quad \eta_{KM} \end{bmatrix},$$

$$\mathbf{V}^{0} \in \mathbb{R}^{KM\times KM} = \begin{bmatrix} \xi_{11} & 0 & \cdots & \cdots & \cdots & \cdots & \cdots & \cdots & \cdots & 0 \\ 0 & \ddots & 0 & \vdots & \vdots & \vdots & \vdots & \vdots & \vdots & \vdots \\ \vdots & 0 & \xi_{K1} & 0 & \vdots & \vdots & \vdots & \vdots & \vdots & \vdots \\ \vdots & \vdots & 0 & \xi_{12} & 0 & \vdots & \vdots & \vdots & \vdots & \vdots \\ \vdots & \vdots & \vdots & 0 & \ddots & 0 & \vdots & \vdots & \vdots & \vdots \\ \vdots & \vdots & \vdots & \vdots & 0 & \xi_{K2} & 0 & \vdots & \vdots & \\ \vdots & \vdots & \vdots & \vdots & \vdots & 0 & \ddots & 0 & \vdots & \vdots \\ \vdots & \vdots & \vdots & \vdots & \vdots & \vdots & 0 & \xi_{1M} & 0 & \vdots \\ \vdots & \vdots & \vdots & \vdots & \vdots & \vdots & \vdots & 0 & \ddots & 0 \\ 0 & \cdots & \cdots & \cdots & \cdots & \cdots & \cdots & \cdots & 0 & \xi_{KM} \end{bmatrix}.$$

As a result, the cost function in (B.31) can be rewritten as

$$\sum_{m=1}^{M} \mathbf{G}_{(m,:)}\mathscr{D}_{(:,m)}\mathbf{G}_{(m,:)}^{\mathrm{H}} = \sum_{m=1}^{M}\sum_{k=1}^{K} \eta_{km}\xi_{km} = \mathbb{TR}\left(\mathbf{W}^{\eta}\mathbf{V}^{0}\right).$$

Note that the sum of the $L^{(m)} = [K(m-1)+1 : Km]$ elements in the diagonal line of $[\mathbf{W}^{\eta}\mathbf{V}^{0}]$ matrix, $p_d\,\mathbb{TR}\Big([\mathbf{W}^{\eta}\mathbf{V}^{0}]_{(L^{(m)},L^{(m)})}\Big)$, represents the power of the users' data stream at the m^{th} AP.

Following the same logic, constraint (B.32) can be written in matrix form by multiplying $\mathbf{W}^{\eta}$ by the $\mathbf{V}^{k} \in \mathbb{C}^{KM\times KM}$ matrices $\forall k$, where their elements are the coefficients of (**??**) and zeros. To explain this matrix form, we show a case study when $K = 2$ and $M = 3$ at $k = 1$ and $i = 2$ as follows

$$\mathbf{W}^{\eta_{=}}\begin{bmatrix} \eta_{11} & \sqrt{\eta_{11}\eta_{21}} & \sqrt{\eta_{11}\eta_{12}} & \sqrt{\eta_{11}\eta_{22}} & \sqrt{\eta_{11}\eta_{13}} & \sqrt{\eta_{11}\eta_{23}} \\ \sqrt{\eta_{21}\eta_{11}} & \eta_{21} & \sqrt{\eta_{21}\eta_{12}} & \sqrt{\eta_{21}\eta_{22}} & \sqrt{\eta_{21}\eta_{13}} & \sqrt{\eta_{21}\eta_{23}} \\ \sqrt{\eta_{12}\eta_{11}} & \sqrt{\eta_{12}\eta_{21}} & \eta_{12} & \sqrt{\eta_{12}\eta_{22}} & \sqrt{\eta_{12}\eta_{13}} & \sqrt{\eta_{12}\eta_{23}} \\ \sqrt{\eta_{22}\eta_{11}} & \sqrt{\eta_{22}\eta_{21}} & \sqrt{\eta_{22}\eta_{12}} & \eta_{22} & \sqrt{\eta_{22}\eta_{13}} & \sqrt{\eta_{22}\eta_{23}} \\ \sqrt{\eta_{13}\eta_{11}} & \sqrt{\eta_{13}\eta_{21}} & \sqrt{\eta_{13}\eta_{12}} & \sqrt{\eta_{13}\eta_{22}} & \eta_{13} & \sqrt{\eta_{13}\eta_{23}} \\ \sqrt{\eta_{23}\eta_{11}} & \sqrt{\eta_{23}\eta_{21}} & \sqrt{\eta_{23}\eta_{12}} & \sqrt{\eta_{23}\eta_{22}} & \sqrt{\eta_{23}\eta_{13}} & \eta_{23} \end{bmatrix},$$

$$\mathbf{V}^1 = \begin{bmatrix} C_{\eta_{11}} & 0 & C_{\eta_{121}} & 0 & C_{\eta_{131}} & 0 \\ 0 & \underline{C}_{\eta_{121}} & 0 & C_{\eta_{1221}} & 0 & C_{\eta_{1231}} \\ C_{\eta_{112}} & 0 & C_{\eta_{12}} & 0 & C_{\eta_{132}} & 0 \\ 0 & C_{\eta_{1212}} & 0 & \underline{C}_{\eta_{122}} & 0 & C_{\eta_{1232}} \\ C_{\eta_{113}} & 0 & C_{\eta_{123}} & 0 & C_{\eta_{13}} & 0 \\ 0 & C_{\eta_{1213}} & 0 & C_{\eta_{1223}} & 0 & \underline{C}_{\eta_{123}} \end{bmatrix}.$$

The other matrix $\mathbf{V}^2$ is derived in the same way. Now it is evident that

$$\begin{aligned} \mathbb{TR}\left(\mathbf{W}^{\eta}\mathbf{V}^1\right) = {} & \eta_{11}C_{\eta_{11}} + \eta_{12}C_{\eta_{12}} + \eta_{13}C_{\eta_{13}} + \sqrt{\eta_{11}\eta_{12}}C_{\eta_{112}} + \sqrt{\eta_{11}\eta_{13}}C_{\eta_{113}} \\ & + \sqrt{\eta_{12}\eta_{11}}C_{\eta_{121}} + \sqrt{\eta_{12}\eta_{13}}C_{\eta_{123}} + \sqrt{\eta_{13}\eta_{11}}C_{\eta_{131}} + \sqrt{\eta_{13}\eta_{12}}C_{\eta_{132}} \\ & + \eta_{21}\underline{C}_{\eta_{121}} + \eta_{22}\underline{C}_{\eta_{122}} + \eta_{23}\underline{C}_{\eta_{123}} + \sqrt{\eta_{21}\eta_{22}}C_{\eta_{1212}} + \sqrt{\eta_{21}\eta_{23}}C_{\eta_{1213}} \\ & + \sqrt{\eta_{22}\eta_{21}}C_{\eta_{1221}} + \sqrt{\eta_{22}\eta_{23}}C_{\eta_{1223}} + \sqrt{\eta_{23}\eta_{21}}C_{\eta_{1231}} + \sqrt{\eta_{23}\eta_{22}}C_{\eta_{1232}}. \end{aligned}$$

B.9.3 Proof of Lemma B.4.3

When $\eta_{k1} = \cdots = \eta_{kM} = \eta_k$, $\forall k$, $\mathscr{D}_{(k,:)} = \eta_{km}\mathbf{I}_M$, $\mathscr{D}_{(:,1)} = \mathscr{D}_{(:,2)} = \cdots = \mathscr{D}_{(:,M)}$, and thus, the cost function of the optimization problem $P1$ is

$$\sum_{m=1}^{M} \mathbf{G}_{(m,:)}\mathscr{D}_{(:,1)}\mathbf{G}^{\mathrm{H}}_{(m,:)} = \sum_{k=1}^{K}\eta_k \sum_{m=1}^{M}\xi_{km} = \mathbf{w}_{\eta}^{\mathrm{T}}\mathbf{v}^0,$$

where $\mathbf{w}_{\eta} \in \mathbb{C}^{K\times 1} = \left([\eta_1,\eta_2,\cdots,\eta_K]^{\frac{1}{2}}\right)^{\mathrm{T}}$, and $\mathbf{v}^0 \in \mathbb{C}^{K\times 1} = \left[\sum_{m=1}^{M}\xi_{m1}, \sum_{m=1}^{M}\xi_{m2}, \cdots, \sum_{m=1}^{M}\xi_{mK}\right]^{\mathrm{T}}$.

The numerator of (B.15) becomes

$$\left|\sqrt{p_d}\,\mathbb{E}\{\mathbf{H}_{(k,:)}\mathscr{D}^{\frac{1}{2}}_{(k,:)}\mathbf{G}_{(:,k)}\}\right|^2 = p_d\eta_k\sum_{m=1}^{M}\sum_{\dot{m}=1}^{M} c_{km}c_{k\dot{m}},$$

and the first term in the denominator of (B.15) becomes

$$p_d\sum_{i=1}^{K}\mathbb{E}\left\{\left|\mathbf{H}_{(k,:)}\mathscr{D}^{\frac{1}{2}}_{(i,:)}\mathbf{G}_{(:,i)}\right|^2\right\} = p_d\sum_{i=1}^{K}\eta_i\sum_{m=1}^{M}\sum_{\dot{m}=1}^{M} c^{ki}_{m\dot{m}} + p_d\sum_{i=1}^{K}\eta_i\sum_{m=1}^{M} c_{kim}.$$

However the third term in the denominator of (B.15) does not change. As such, the QoS constraint (B.32) is

$$\eta_k\Big(\sum_{m=1}^{M} C_{\eta_{km}} + \sum_{m=1}^{M}\sum_{\substack{\dot{m}=1,\\ \dot{m}\neq m}}^{M} C_{\eta_{km\dot{m}}}\Big) + \sum_{\substack{i=1,\\ i\neq k}}^{K}\eta_i\Big(\sum_{m=1}^{M}\underline{C}_{\eta_{kim}} + \sum_{m=1}^{M}\sum_{\substack{\dot{m}=1,\\ \dot{m}\neq m}}^{M} C_{\eta_{kim\dot{m}}}\Big) \geq C_k^{(0)}. \tag{B.33}$$

For an arbitrary desired user k, where the other users are interfering users, the multiplication of $\mathbf{w}_{\eta}^{\mathrm{T}}$ with $\mathbf{V}^k \in \mathbb{C}^{K\times 1}$, $(\mathbf{w}_{\eta}^{\mathrm{T}}\mathbf{v}^k)$, constructs the left side of constraint (B.33), where

$$\mathbf{V}^k \in \mathbb{C}^{K\times 1} = \begin{bmatrix} \sum_{m=1}^{M} \underline{C}_{\eta_{k1m}} + \sum_{m=1}^{M} \sum_{\substack{\grave{m}=1,\\ \grave{m}\neq m}}^{M} C_{\eta_{k1m\grave{m}}} \\ \vdots \\ \sum_{m=1}^{M} \underline{C}_{\eta_{k(k-1)m}} + \sum_{m=1}^{M} \sum_{\substack{\grave{m}=1,\\ \grave{m}\neq m}}^{M} C_{\eta_{k(k-1)m\grave{m}}} \\ \sum_{m=1}^{M} C_{\eta_{km}} + \sum_{m=1}^{M} \sum_{\substack{\grave{m}=1,\\ \grave{m}\neq m}}^{M} C_{\eta_{km\grave{m}}} \\ \sum_{m=1}^{M} \underline{C}_{\eta_{k(k+1)m}} + \sum_{m=1}^{M} \sum_{\substack{\grave{m}=1,\\ \grave{m}\neq m}}^{M} C_{\eta_{k(k+1)m\grave{m}}} \\ \vdots \\ \sum_{m=1}^{M} \underline{C}_{\eta_{kKm}} + \sum_{m=1}^{M} \sum_{\substack{\grave{m}=1,\\ \grave{m}\neq m}}^{M} C_{\eta_{kKm\grave{m}}} \end{bmatrix}.$$

B.9.4 Proof of Lemma B.5.1

Based on (B.22), the data rate at the k^{th} user is bounded by (B.25). By substituting (B.24) into the AN term, the latter becomes

$$\begin{aligned}\sum_{m=1}^{M} \mathbb{E}\{|\sqrt{\bar{p}_{d_m}}\,\overline{\mathbf{H}}_{mk}\overline{\mathbf{G}_m}|^2\} &\doteq p_d \sum_{m=1}^{M} \mathbb{E}\{|\tilde{\overline{\mathbf{H}}}_{mk}\overline{\mathbf{G}}_m|^2 \times (1-\mathbf{G}_{(m,:)}\mathscr{D}_{(:,m)}\mathbf{G}^{\mathrm{H}}_{(m,:)})\} \\ &= p_d \sum_{m=1}^{M} \bar{c}_{km} - p_d \sum_{m=1}^{M}\sum_{i=1}^{K} \eta_{im}\bar{c}_{kim},\end{aligned}$$

where $\bar{c}_{km} = \mathbb{E}\{|\tilde{\overline{\mathbf{H}}}_{mk}\,\overline{\mathbf{G}}_m|^2\}, \bar{c}_{kim} = \mathbb{E}\{|\tilde{\overline{\mathbf{H}}}_{mk}\,\overline{\mathbf{G}}_m\mathbf{G}_{(m,i)}|^2\}$. Then, the coefficients of the QoS constraint become independent of $\bar{p}_{d_m}$ and are given

$$\begin{aligned} C_{\eta_{km}} &= ((1+\gamma_k)c^2_{km} - \gamma_k(c^{kk}_{mm} + c_{kkm} - \bar{c}_{kkm}), \\ C_{\eta_{kim\grave{m}}} &= -\gamma_k c^{ki}_{m\grave{m}}, \\ C_{\eta_{km\grave{m}}} &= ((1+\gamma_k)c_{km}c_{k\grave{m}} - \gamma_k c^{kk}_{m\grave{m}}), \\ C_{\eta_{kim}} &= -\gamma_k(c^{ki}_{mm} + c_{kim} - \bar{c}_{kim}), \\ C^{(0)}_k &= \gamma_k(p_d \sum_{m=1}^{M} \bar{c}_{km} + \sigma^2_k). \end{aligned}$$

Moreover, since the AN power at the m^{th} APs is the remaining amount of the power (that is above the QoS power), then the constraint (B.18d) in the problem $P1$ becomes

$$p_d \mathbf{G}_{(m,:)}\mathscr{D}_{(:,m)}\mathbf{G}^{\mathrm{H}}_{(m,:)} + \bar{p}_{d_m} = p_d, \quad \forall m,$$

which leads to $p_d \mathbf{G}_{(m,:)}\mathscr{D}_{(:,m)}\mathbf{G}^{\mathrm{H}}_{(m,:)} \leq p_d, \quad \forall m$, and then the AN power, $\bar{p}_{d_m}$, is calculated from (B.24). Now, both the QoS and power constraints are independent of the AN power, which converts

the joint optimization problems $P2$ and $P3$ to the separated optimization problems $P4$ and $P5$, respectively.

BIBLIOGRAPHY

[1] A. Kupper, *Location-based Services Fundamentals and Operation*. The Atrium, Southern Gate, Chichester, West Sussex PO19 8SQ, England: John Wiley & Sons Ltdl, 2005.

[2] J. A. del Peral-Rosado, R. Raulefs, J. A. Lopez-Salcedo, and G. Seco-Granados, "Survey of cellular mobile radio localization methods: From 1G to 5G," *IEEE Communications Surveys Tutorials*, vol. 20, no. 2, pp. 1124–1148, 2018.

[3] C. Laoudias, A. Moreira, S. Kim, S. Lee, L. Wirola, and C. Fischione, "A survey of enabling technologies for network localization, tracking, and navigation," *IEEE Communications Surveys Tutorials*, vol. 20, no. 4, pp. 3607–3644, 2018.

[4] i-locate project, indoor/outdoor location and asset management through open geodata. Online. [Online]. Available: http://www.i-locate.eu/

[5] K. Moore and et al., "Older adults' experiences with using wearable devices: Qualitative systematic review and meta-synthesis," *JMIR mHealth and uHealth*, vol. 9, no. 6, 2021.

[6] S. Paiva, M. A. Ahad, G. Tripathi, N. Feroz, and G. Casalino, "Enabling technologies for urban smart mobility: Recent trends, opportunities and challenges," *Sensors (Basel)*, vol. 21, no. 6, 2021.

[7] D. McEntire, *Disaster response and recovery: strategies and tactics for resilience, second version*. Hoboken, New Jersey: John Wiley & sons Inc., 2015.

[8] E. c.L. Chan and G. Baciu, *Introduction to Wireless Localization: With iPhone SDK Examples*. Singapore Pte.: John Wiley & Sons Ltdl, 2012.

[9] Z. M. Abu-Shaban, "Towards the next generation of location-aware communications," Ph.D. dissertation, The Australian National University, 2018.

[10] F. Ghaseminajm, "Localization error bounds for 5G mm-wave systems under hardware impairments," Ph.D. dissertation, Lakehead University, PhD in Electrical Engineering, 2022.

[11] E. Bjornson, J. Hoydis, and L. Sanguinetti, *Massive MIMO Networks: Spectral, Energy, and Hardware Efficiency*. http://www.nowpublishers.com: now Publishers Inc., 2017, vol. 11.

[12] F. Horlin and A. Bourdoux, *Digital Compensation for Analog Front-Ends: A New Approach to Wireless Transceiver Design*. Wiley Telecom., 2008.

[13] T. Schenk, *RF imperfections in high-rate wireless systems:Impact and digital compensation*. Springer, 2008.

[14] G. Hueber and R. B. Staszewski, *RF Impairment Compensation for Future Radio Systems*, 2011, pp. 451–496.

[15] Z. Pi and F. Khan, "An introduction to millimeter-wave mobile broadband systems," *IEEE Communications Magazine*, vol. 49, no. 6, pp. 101–107, 2011.

[16] C. Kim, J.-S. Son, T. Kim, and J.-Y. Seol, "On the hybrid beamforming with shared array antenna for mmwave MIMO-OFDM systems," in *2014 IEEE Wireless Communications and Networking Conference (WCNC)*, 2014, pp. 335–340.

[17] A. Alkhateeb and R. W. Heath, "Frequency selective hybrid precoding for limited feedback millimeter wave systems," *IEEE Transactions on Communications*, vol. 64, no. 5, pp. 1801 – 1818, 2016.

[18] F. Sohrabi and W. Yu, "Hybrid analog and digital beamforming for mmwave OFDM large-scale antenna arrays," *IEEE Journal on Selected Areas in Communications*, vol. 35, no. 7, pp. 1432–1443, 2017.

[19] S. Trevlakis, A. Boulogeorgos, D. Pliatsios, K. Ntontin, P. Sarigiannidis, S. Chatzinotas, and M. Renzo, "Localization as a key enabler of 6G wireless systems: A comprehensive survey and an outlook," *IEEE Communications Surveys Tutorials*, vol. 35, no. 7, pp. 1432–1443, 2023.

[20] Z. Abu-Shaban, H. Wymeersch, T. Abhayapala, and G. Seco-Granados, "Single-anchor two-way localization bounds for 5G mmwave systems," *IEEE Transactions on Vehicular Technology*, vol. 69, no. 6, pp. 6388–6400, 2020.

[21] H. Wymeersch, J. He, B. Denis, A. Clemente, and M. Juntti, "Radio localization and mapping with reconfigurable intelligent surfaces: Challenges, opportunities, and research directions," *IEEE Vehicular Technology Magazine*, vol. 15, no. 4, pp. 52–61, 2020.

[22] R. Keating, M. Saily, J. Hulkkonen, and J. Karjalainen, "Overview of positioning in 5G new radio," in *2019 16th International Symposium on Wireless Communication Systems (ISWCS)*, 2019, pp. 320–324.

[23] K. Witrisal, P. Meissner, E. Leitinger, Y. Shen, C. Gustafson, F. Tufvesson, K. Haneda, D. Dardari, A. F. Molisch, A. Conti, and M. Z. Win, "High-accuracy localization for assisted living: 5G systems will turn multipath channels from foe to friend," *IEEE Signal Processing Magazine*, vol. 33, no. 2, pp. 59–70, 2016.

[24] K. Witrisal, P. Meissner, E. Leitinger, Y. Shen, C. Gustafson, F. Tufvesson, K. Haneda, D. Dardari, A. F. Molisch, A. Conti, and M. Win, "High-accuracy localization for assisted living: 5G systems will turn multipath channels from foe to friend," *IEEE Signal Processing Magazine*, vol. 33, no. 2, pp. 59–70, 2016.

[25] Z. Abu-Shaban, X. Zhou, T. D. Abhayapala, G. Seco-Granados, and H. Wymeersch, "Error bounds for uplink and downlink 3D localization in 5G mmWave systems," *IEEE Transactions on Wireless Communications*, vol. 17, no. 8, pp. 4939–4954, 2018.

[26] Z. Marzi, D. Ramasamy, and U. Madhow, "Compressive channel estimation and tracking for large arrays in mm-wave picocells," *IEEE Journal of Selected Topics in Signal Processing*, vol. 10, no. 3, p. 514,Äì527, Jan. 2016.

[27] A. Shahmansoori, G. E. Garcia, G. Destino, G. Seco-Granados, and H. Wymeersch, "Position and orientation estimation through mmWave MIMO in 5G systems," *IEEE Transactions on Wireless Communications*, vol. 17, no. 3, pp. 1822–1835, Dec. 2018.

[28] A. Fascista, A. D. Monte, A. Coluccia, H. Wymeersch, and G. Seco-Granados., "Low-complexity downlink channel estimation in mmwave multiple-input single-output systems," *IEEE Wireless Communications Letters*, pp. 1–5, 2021.

[29] B. Zhou, A. Liu, and V. Lau, "Successive localization and beamforming in 5G mmwave MIMO communication systems," *IEEE Transactions on Signal Processing*, vol. 67, no. 6, pp. 1620–1635, 2019.

[30] A. Fascista, A. Coluccia, H. Wymeersch, and G. Seco-Granados., "Downlink single-snapshot localization and mapping with a single-antenna receiver," *IEEE Transactions on Wireless Communications*, vol. 20, no. 7, pp. 4672–4684, 2021.

[31] F. Ghaseminajm, M. Alsmadi, D. Tubail, and S. S. Ikki, "RIS-aided mobile localization error bounds under hardware impairments," *IEEE Transactions on Communications*, vol. 70, no. 12, pp. 8331–8341, 2022.

[32] K. Keykhosravi, M. F. Keskin, G. Seco-Granados, P. Popovski, and H. Wymeersch, "RIS-enabled SISO localization under user mobility and spatial-wideband effects," *IEEE Journal of Selected Topics in Signal Processing*, 2022.

[33] A. Elzanaty, A. Guerra, F. Guidi, and M. Alouini, "Reconfigurable intelligent surfaces for localization: Position and orientation error bounds," *https://arxiv.org/abs/2009.02818*, Aug. 2020.

[34] J. He, H. Wymeersch, L. Kong, O. Silven, and M. Juntti, "Large intelligent surface for positioning in millimeter wave MIMO systems," in *IEEE 91st Vehicular Technology Conference (VTC2020-Spring)*, Antwerp, Belgium, May 2020, pp. 1–5.

[35] A. Fascista, M. Keskin, A. Coluccia, H. Wymeersch, and G. Seco-Granados, "RIS-aided joint localization and synchronization with a single-antenna receiver: Beamforming design and low-complexity estimation," *IEEE Journal of Selected Topics in Signal Processing*, 2022.

[36] A. Fascista, A. Coluccia, H. Wymeersch, and G. Seco-Granados, "RIS-aided joint localization and synchronization with a single-antenna MmWave receiver," in *2021 IEEE International Conference on Acoustics, Speech and Signal Processing (ICASSP)*, Toronto, ON, Canada, May 2021, pp. 4455–4459.

[37] M. Hellebrandt and R. Mathar, "Location tracking of mobiles in cellular radio networks," *IEEE Transactions on Vehicular Technology*, vol. 48, no. 5, pp. 1558–1562, 1999.

[38] M. Yongyi, Z. Ying, and Z. Kanglei, "A new tracking algorithm in cellular networks," in *2010 2nd International Conference on Future Computer and Communication*, vol. 2, 2010, pp. V2–459–V2–463.

[39] D. Fan, R. Zhang, and L. Jin, "Extended kalman filter location and tracking method using single base station in cellular network," in *2007 International Conference on Wireless Communications, Networking and Mobile Computing*, 2007, pp. 740–742.

[40] M. M. Olama, S. M. Djouadi, and C. D. Charalambous, "Position and velocity tracking in cellular networks using particle and kalman filtering with comparison," in *Proceedings of the 45th IEEE Conference on Decision and Control*, 2006, pp. 1315–1320.

[41] L. Mihaylova, D. Bull, D. Angelova, and N. Canagarajah, "Mobility tracking in cellular networks with sequential monte carlo filters," in *2005 7th International Conference on Information Fusion*, vol. 1, 2005, pp. 8 pp.–.

[42] L. Mihaylova, D. Angelova, S. Honary, D. R. Bull, C. N. Canagarajah, and B. Ristic, "Mobility tracking in cellular networks using particle filtering," *IEEE Transactions on Wireless Communications*, vol. 6, no. 10, pp. 3589–3599, 2007.

[43] M. Hernandez, B. Ristic, and A. Farina, "A performance bound for maneuvering target tracking using best-fitting gaussian distributions," in *2005 7th International Conference on Information Fusion*, vol. 1, 2005, pp. 8 pp.–.

[44] Y. Zhou, J. Li, and D. Wang, "Posterior Cramer-Rao lower bounds for target tracking in sensor networks with quantized range-only measurements," *IEEE Signal Processing Letters*, vol. 17, no. 2, pp. 157–160, 2010.

[45] C. Fritsche, A. Klein, and F. Gustafsson, "Bayesian Cramer-Rao bound for mobile terminal tracking in mixed LOS/NLOS environments," *IEEE Wireless Communications Letters*, vol. 2, no. 3, pp. 335–338, 2013.

[46] T. Brehard and J.-p. L. Cadre, "Closed-form posterior Cramer-Rao bound for a manoeuvring target in the bearings-only tracking context using best-fitting gaussian distribution," in *2006 9th International Conference on Information Fusion*, 2006, pp. 1–7.

[47] P. Zhu, H. Lin, J. Bao, J. Li, and D. Wang, "Beam tracking for distributed millimeter-wave massive MIMO systems based on the unscented kalman filter," *IEEE Wireless Communications Letters*, vol. 11, no. 4, pp. 712–716, 2022.

[48] F. Ghaseminajm, Z. Abu-Shaban, S. Ikki, H. Wymeersch, and C. R. Benson, "Localization error bounds for 5G mmwave systems under I/Q imbalance," *IEEE Transactions on Vehicular Technology*, vol. 69, no. 7, pp. 7971–7975, July 2020.

[49] C. Zhang, D. Guo, and P. Fan, "Tracking angles of departure and arrival in a mobile millimeter wave channel," in *IEEE International Conference on Communications (ICC)*, Kuala Lumpur, Malaysia, May 2016.

[50] Y. Yapici and f. Guvenc, "Low-complexity adaptive beam and channel tracking for mobile mmWave communications," in *2018 52nd Asilomar Conference on Signals, Systems, and Computers*, 2018, pp. 572–576.

[51] S. G. Larew and D. J. Love, "Adaptive beam tracking with the unscented kalman filter for millimeter wave communication," *IEEE Signal Processing Letters*, vol. 26, no. 11, pp. 1658–1662, 2019.

[52] Y. J. Kim and C. Y. Soo, "Beam-tracking technique for millimeter-wave cellular systems using subarray structures," *IEEE Transactions on Vehicular Technology*, vol. 67, no. 8, pp. 7806–7810, 2018.

[53] M. Robaei, R. Akl, R. Chataut, and U. K. Dey, "Adaptive millimeter-wave channel estimation and tracking," in *2021 23rd International Conference on Advanced Communication Technology (ICACT)*, 2021, pp. 23–28.

[54] P. Zhu, H. Lin, J. Bao, J. Li, and D. Wang, "Beam tracking for distributed millimeter-wave massive MIMO systems based on the unscented kalman filter," *IEEE Wireless Communications Letters*, vol. 11, no. 4, pp. 712–716, 2022.

[55] H. Li, Y. Zhang, J. Xi, and W. Guo, "3D beam tracking method based on reconfigurable intelligent surface assistant for blocking channel," in *Youth Academic Annual Conference of Chinese Association of Automation (YAC)*, Nanchang, China, May 2021.

[56] J. Yuan, G. C. Alexandropoulos, E. Kofidis, T. L. Jensen, and E. D. Carvalho, "Channel tracking for RIS-enabled multi-user SIMO systems in time-varying wireless channels," in *IEEE International Conference on Communications Workshops*, Seoul, Korea, May 2022.

[57] X. Wang, X. Zhao, Y. Zhang, Y. Liu, S. Li, S. Geng, X. Su, H. Qin, and S. Sun, "Codebook-based beam tracking for RIS assisted mobile MmWave networks," in *13th International Symposium on Antennas, Propagation and EM Theory (ISAPE)*, Zhuhai, China, Dec 2021.

[58] B. Teng, X. Yuan, R. Wang, and S. Jin, "Bayesian user localization and tracking for reconfigurable intelligent surface aided MIMO systems," *IEEE Journal of Selected Topics in Signal Processing*, 2022.

[59] B. Ceniklioglu, I. Develi, A. E. Canbilen, and M. Lafci, "Analysis of average bit error rate for OFDM-IM systems with hardware impairments over Nakagami-m and Weibull fading channels," *Accepted, International Conference on Computing, Communication, Security Intelligent Systems*, 2022.

[60] H. Mehrpouyan, M. Matthaiou, R. Wang, G. Karagiannidis, and Y. Hua, "Hybrid millimeter-wave systems: A novel paradigm for hetnets," *IEEE Communications Magazine*, vol. 53, no. 1, pp. 216–221, Jan. 2015.

[61] F. Ghaseminajm, Z. Abu-Shaban, S. S. Ikki, H. Wymeersch, and C. R. Benson, "Localization error bounds for 5G mmwave systems under I/Q imbalance," *IEEE Transactions on Vehicular Technology*, vol. 69, no. 7, pp. 7971–7975, 2020.

[62] F. Ghaseminajm, E. Saleh, M. M. Alsmadi, and S. Ikki, "Localization error bounds for 5G mmwave systems under hardware impairments," in *IEEE 32nd Annual International Symposium on Personal, Indoor, and Mobile Radio Communications*, Helsinki, Finland, Sep. 2021, pp. 1228–1233.

[63] D. Zhu, J. Choi, Q. Cheng, W. Xiao, and R. W. Heath, "High-resolution angle tracking for mobile wideband millimeter-wave systems with antenna array calibration," *IEEE Transactions on Wireless Communications*, vol. 17, no. 11, pp. 7173–7189, 2018.

[64] Y. Yang, S. Dang, M. Wen, S. Mumtaz, and M. Guizani, "Bayesian beamforming for mobile millimeter wave channel tracking in the presence of DOA uncertainty," *IEEE Transactions on Communications*, vol. 68, no. 12, pp. 7547–7562, 2020.

[65] O. S. Faragallah, H. S. El-Sayed, and M. G. El-Mashed, "Estimation and tracking for millimeter wave MIMO systems under phase noise problem," *IEEE Access*, vol. 8, pp. 228 009–228 023, 2020.

[66] F. Ghaseminajm, M. Alsamdi, and S. S. Ikki, "Error bounds for localization in mmwave MIMO systems: Effects of hardware impairments considering perfect and imperfect clock synchronization," *IEEE Systems Journal*, vol. 16, no. 4, pp. 6350–6359, 2022.

[67] C. Qing, W. Yu, S. Tang, C. Rao, and J. Wang, "ELM-based frame synchronization in nonlinear distortion scenario using superimposed training," *IEEE Access*, vol. 9, pp. 53 530–53 539, 2021.

[68] C. Qing, W. Yu, B. Cai, J. Wang, and C. Huang, "ELM-based frame synchronization in burst-mode communication systems with nonlinear distortion," *IEEE Wireless Communications Letters*, vol. 9, no. 6, pp. 915–919, 2020.

[69] C. Qing, L. Wang, L. Dong, and J. Wang, "Enhanced ELM based channel estimation for RIS-assisted OFDM systems with insufficient CP and imperfect hardware," *IEEE Communications Letters*, vol. 26, no. 1, pp. 153–157, 2022.

[70] C. Qing, L. Dong, L. Wang, J. Wang, and C. Huang, "Joint model and data-driven receiver design for data-dependent superimposed training scheme with imperfect hardware," *IEEE Transactions on Wireless Communications*, vol. 21, no. 6, pp. 3779–3791, 2022.

[71] A. Fascista, A. Coluccia, H. Wymeersch, and G. Seco-Granados, "Millimeter-wave downlink positioning with a single-antenna receiver," *IEEE Transactions on Wireless Communications*, vol. 18, no. 9, pp. 4479–4490, 2019.

[72] B. Zhou, R. Wichman, L. Zhang, and Z. Luo, "Simultaneous localization and channel estimation for 5G mmWave MIMO communications," in *IEEE* 32^{nd} *Annual International Symposium on Personal, Indoor and Mobile Radio Communications (PIMRC)*, Helsinki, Finland, Sept. 2021, p. 853,Äì858.

[73] E. Basar, M. Di Renzo, J. De Rosny, M. Debbah, M.-S. Alouini, and R. Zhang, "Wireless communications through reconfigurable intelligent surfaces," *IEEE Access*, vol. 7, pp. 116 753–116 773, 2019.

[74] A. A. Boulogeorgos and A. Alexiou, "How much do hardware imperfections affect the performance of reconfigurable intelligent surface-assisted systems?" *IEEE Open Journal of the Communications Society*, vol. 1, pp. 1185–1195, 2020.

[75] M. H. N. Shaikh, V. A. Bohara, A. Srivastava, and G. Ghatak, "Performance analysis of intelligent reflecting surface-assisted wireless system with non-ideal transceiver," *IEEE Open Journal of the Communications Society*, vol. 2, pp. 671–686, 2021.

[76] Z. Xing, R. Wang, J. Wu, and E. Liu, "Achievable rate analysis and phase shift optimization on intelligent reflecting surface with hardware impairments," *IEEE Transactions on Wireless Communications*, vol. 20, no. 9, pp. 5514–5530, 2021.

[77] Y. Liu, E. Liu, and R. Wang, "Energy efficiency analysis of intelligent reflecting surface system with hardware impairments," in *GLOBECOM 2020 - 2020 IEEE Global Communications Conference*, 2020, pp. 1–6.

[78] D. Li, "Ergodic capacity of intelligent reflecting surface-assisted communication systems with phase errors," *IEEE Communications Letters*, vol. 24, no. 8, pp. 1646–1650, 2020.

[79] S. Zhou, W. Xu, K. Wang, M. Di Renzo, and M.-S. Alouini, "Spectral and energy efficiency of IRS-assisted MISO communication with hardware impairments," *IEEE Wireless Communications Letters*, vol. 9, no. 9, pp. 1366–1369, 2020.

[80] E. Bjornson, J. Hoydis, M. Kountouris, and M. Debbah, "Massive MIMO systems with non-ideal hardware: Energy efficiency, estimation, and capacity limits," *IEEE Transactions on Information Theory*, vol. 60, no. 11, pp. 7112 – 7139, Nov. 2014.

[81] Q. C. Li, G. Wu, and T. S. Rappaport, "Channel model for millimeter-wave communications based on geometry statistics," in *2014 IEEE Globecom Workshops (GC Wkshps)*, 2014, pp. 427–432.

[82] Q. Li, H. Shirani-Mehr, T. Balercia, A. Papathanassiou, G. Wu, S. Sun, M. K. Samimi, and T. S. Rappaport, "Validation of a geometry-based statistical mmwave channel model using ray-tracing simulation," in *2015 IEEE 81st Vehicular Technology Conference (VTC Spring)*, 2015, pp. 1–5.

[83] A. Fascista, A. Coluccia, H. Wymeersch, and G. Seco-Granados, "Millimeter-wave downlink positioning with a single-antenna receiver," *IEEE Transactions on Wireless Communications*, vol. 18, no. 9, pp. 4479 – 4490, July 2019.

[84] T. S. Rappaport, S. Sun, R. Mayzus, H. Zhao, Y. Azar, K. Wang, G. N. Wong, J. K. Schulz, M. Samimi, and F. Gutierrez, "Millimeter wave mobile communications for 5G cellular: It will work!" *IEEE Access*, vol. 1, pp. 335–349, 2013.

[85] S. M. Kay, *Fundamentals of Statistical Signal Processing: Estimation Theory*. Englewood Cliffs, NJ: Prentice-hall, Mar. 1993, vol. 1.

[86] Y. Shen and M. Z. Win, "Fundamental limits of wideband localization- part I: A general framework," *IEEE Transactions on Information Theory*, vol. 56, no. 10, pp. 4956–4980, 2010.

[87] P. Tichavsky, C. H. Muravchik, and A. Nehorai, "Posterior Cramer-Rao bounds for discrete-time nonlinear filtering," *IEEE Transactions On Signal Processing*, vol. 46, no. 5, pp. 1386–1396, 1998.

[88] O. Simeone, *A Brief Introduction to Machine Learning for Engineers*, 2018.

[89] E. Cambria, G.-B. Huang, L. L. C. Kasun, H. Zhou, C. M. Vong, J. Lin, J. Yin, Z. Cai, Q. Liu, K. Li, V. C. Leung, L. Feng, Y.-S. Ong, M.-H. Lim, A. Akusok, A. Lendasse, F. Corona, R. Nian, Y. Miche, P. Gastaldo, R. Zunino, S. Decherchi, X. Yang, K. Mao, B.-S. Oh, J. Jeon, K.-A. Toh, A. B. J. Teoh, J. Kim, H. Yu, Y. Chen, and J. Liu, "Extreme learning machines [trends controversies]," *IEEE Intelligent Systems*, vol. 28, no. 6, pp. 30–59, 2013.

[90] Z. Xiao and Y. Zeng, "An overview on integrated localization and communication towards 6G," 2020.

[91] V. Sark, E. Grass, and J. Gutierrez, "Multi-way ranging with clock offset compensation," in *Advances in Wireless and Optical Communications (RTUWO)*, Riga, Latvia, Nov. 2015, pp. 1–5.

[92] F. Ghaseminajm, E. Saleh, M. Alsmadi, and S. S. Ikki, "Localization error bounds for 5G mmWave systems under hardware impairments," in *IEEE 32nd Annual Int. Symp. Personal, Indoor and Mobile Radio Commun. (PIMRC)*, 2021, pp. 1228–1233.

[93] C. N. Barati, A. Hosseini, M. Mezzavilla, T. Korakis, S. S. Panwar, S. Rangan, and M. Zorzi, "Initial access in millimeter wave cellular systems," *IEEE Transactions on Wireless Communications*, vol. 15, no. 12, pp. 7926 – 7940, 2016.

[94] B. Ceniklioglu, D. A. Tubail, A. E. Canbilen, I. Develi, and S. S. Ikki, "Error analysis of the joint localization and synchronization of RIS-assisted mm-wave MISO-OFDM under the effect of hardware impairments," *IEEE Open Journal of the Communications Society*, vol. 3, pp. 2151–2161, 2022.

[95] B. Anderson and J. Moore, *Optimal Filtering*. Prentice-Hall information and system sciences series, 1979.

[96] D. Tubail, B. Ceniklioglu, A. E. Canbilen, I. Develi, and S. S. Ikki, "The effect of hardware impairments on the error bounds of localization and maximum likelihood estimation of mm-wave MISO-OFDM systems," *IEEE Transactions on Vehicular Technology*, vol. 72, no. 3, pp. 4063–4067, 2023.

[97] D. A. Tubail, B. Ceniklioglu, A. E. Canbilen, I. Develi, and S. Ikki, "Error bounds for 3D localization and maximum likelihood estimation of mm-wave MISO OFDM systems in the presence of hardware impairments," *IEEE Communications Letters*, 2022.

[98] H. V. Nguyen, V. Nguyen, O. A. Dobre, S. K. Sharma, S. Chatzinotas, B. Ottersten, and O. Shin, "On the spectral and energy efficiencies of full-duplex cell-free massive MIMO," *IEEE Journal ON Selected Areas IN Communications*, June 2020.

[99] J. Zhang, Y. Wei, E. Bjornson, Y. Han, and S. Jin, "Performance analysis and power control of cell-free massive MIMO systems with hardware impairments," *IEEE Access*, vol. 6, pp. 55 302–55 314, Sep. 2018.

[100] J. Qiu, K. Xu, X. Xia, Z. Shen, and W. Xie, "Downlink power optimization for cell-free massive MIMO over spatially correlated rayleigh fading channels," *IEEE Access*, vol. 8, pp. 56 214–56 227, March 2020.

[101] Y. Zhao, I. Niemegeers, and S. Groot, "Power allocation in cell-free massive MIMO: A deep learning method," *IEEE Access*, vol. 8, pp. 87 185–87 200, May 2020.

[102] Y. Zhang, M. Zhou, Y. Cheng, L. Yang, and H. Zhu, "RF impairments and low-resolution ADCs for nonideal uplink cell-free massive MIMO systems," *IEEE Systems Journal*, pp. 1–12, May 2020.

[103] N. Yang, L. Wang, G. Geraci, M. Elkashlan, J. Yuan, and M. D. Renzo, "Safeguarding 5G wireless communication networks using physical layer security," *IEEE Communications Magazine*, vol. 53, no. 04, pp. 20–27, April 2015.

[104] D. Tubail, M. El-Absi, S. Ikki, W.Mesbah, and T. Kaiser, "Artificial noise based physical layer security in interference alignment multipair two-way relaying networks," *IEEE Access*, vol. 6, no. 1, p. 19073,Äì19085, 2018.

[105] A. D. Wyner, "The wire-tap channel," *The Bell System Technical Journal*, vol. 54, no. 8, pp. 1355–1387, Oct 1975.

[106] B. He, Y. She, and V. K. N. Lau, "Artificial noise injection for securing single-antenna systems," *IEEE Transactions on Vehicular Technology*, vol. 66, no. 10, pp. 9577–9581, 2017.

[107] A. Sikri, A. Mathur, M. Bhatnagar, G. Kaddoum, P. Saxena, and J. Nebhen, "Artificial noise injection,Äìbased secrecy improvement for fso systems," *IEEE Photonics Journal*, vol. 13, no. 2, pp. 1–12, 2021.

[108] S. Goel and R. Negi, "Guaranteeing secrecy using artificial noise," *IEEE Transactions on Wireless Communications*, vol. 7, no. 6, pp. 2180–2189, 2008.

[109] X. Chen, C. Yuen, and Z. Zhang, "Exploiting large-scale MIMO techniques for physical layer security with imperfect channel state information," in *2014 IEEE Global Communications Conference*, 2014, pp. 1648–1635.

[110] G. Geraci, M. Egan, J. Yuan, A. Razi, and I. B. Collings, "Secrecy sum-rates for multi-user MIMO regularized channel inversion precoding," *IEEE Transactions on Communications*, vol. 60, no. 11, pp. 3472–3482, 2012.

[111] E. Choi, M. Oh, J. Choi, J. Park, N. Lee, and N. Al-Dhahir, "Joint precoding and artificial noise design for MU-MIMO wiretap channels," *IEEE Transactions on Communications*, pp. 1–1, 2022.

[112] D. Tubail, M. El-Absi, S. Ikki, W. Mesbah, and T. Kaiser, "Secure interference alignment based multiuser relay system using artificial noise," *Proc. IEEE Globecom'17*, Dec. 2017.

[113] K. Neupane, R. Haddad, and D. Moore, "Secrecy analysis of massive MIMO systems with MRT precoding using normalization methods," in *SoutheastCon*, St. Petersburg, FL, April 2018, pp. 1–6.

[114] T. Yang, R. Zhang, X. Cheng, and L. Yang, "Secure massive MIMO under imperfect CSI: Performance analysis and channel prediction," *IEEE Transactions on Information Forensics and Security*, vol. 14, no. 06, pp. 1610–1623, June 2019.

[115] J. Zhu, R. Schober, and V. Bhargava, "Linear precoding of data and artificial noise in secure massive MIMO systems," *IEEE Transactions on Wireless Communications*, vol. 15, no. 3, pp. 2245–2261, March 2016.

[116] D. Kudathanthirige, S. Timilsina, and G. Baduge, "Secure communication in relay-assisted massive MIMO downlink with active pilot attacks," *IEEE Transactions on Information Forensics and Security*, vol. 14, no. 11, pp. 2819–2833, Nov. 2019.

[117] J. Chen, X. Chen, W. Gerstacker, and D. K. Ng, "Resource allocation for a massive MIMO relay aided secure communication," *IEEE Transactions on Information Forensics and Security*, vol. 11, no. 08, pp. 1700–1711, Aug. 2018.

[118] X. Wang, Y. Gao, G. Zhang, and M. Guo, "Security performance analysis of cell-free massive MIMO over spatially correlated rayleigh fading channels with active spoofing attack," in *2020 International Conference on Wireless Communications and Signal Processing (WCSP)*, Nanjing, China, Oct. 2020, pp. 1–6.

[119] S. Timilsina, D. Kudathanthirige, and G. Amarasuriya, "Physical layer security in cell-free massive MIMO," in *IEEE Global Communications Conference (GLOBECOM)*, Abu Dhabi, United Arab Emirates, Dec. 2018, pp. 1–7.

[120] X. Zhang, D. Guo, K. An, and B. Zhang, "Secure communications over cell-free massive MIMO networks with hardware impairments," *IEEE Systems Journal*, vol. 14, no. 2, pp. 1909–1920, June 2019.

[121] M. Alageli, A. Ikhlef, F. Alsifiany, M. Abdullah, G. Chen, and J. Chambers, "Optimal downlink transmission for cell-free SWIPT massive MIMO systems with active eavesdropping," *IEEE Transactions on Information Forensics and Security*, vol. 15, pp. 1–15, Nov. 2019.

[122] T. Hoang, H. Ngo, T. Duong, H. Tuan, and A. Marshall, "Cell-free massive MIMO networks: Optimal power control against active eavesdropping," *IEEE Transactions on Communications*, vol. 66, no. 10, pp. 4724–4737, Oct. 2018.

[123] F. Zhu, F. Gao, H. Lin, S. Jin, J. Zhao, and G. Qian, "Robust beamforming for physical layer security in BDMA massive MIMO," *IEEE Journal on Selected Areas in Communications*, vol. 36, no. 4, pp. 775–787, April 2018.

[124] D. Kapetanovi, G. Zheng, and F. Rusek, "Physical layer security for massive MIMO: An overview on passive eavesdropping and active attacks," *IEEE Communications Magazine*, vol. 53, no. 06, pp. 21–27, June 2015.

[125] M. Obeed and W. Mesbah, "An efficient physical layer security algorithm for two-way relay systems," in *in Proc. IEEE Wireless Communications and Networking Conference (WCNC)*, Qater, April 2016.

[126] T. L. Marzetta, "How much training is required for multiuser MIMO?" in *IEEE Asilomar Conference on Signals, Systems and Computers*, Oct. 2006, p. 359,Äì363.

[127] E. Nayebi, A. Ashikhmin, T. L. Marzetta, H. Yang, and B. D. Rao, "Precoding and power optimization in cell-free massive MIMO systems," *IEEE Transactions on Wireless Communications*, vol. 16, no. 7, pp. 4445–4459, July 2017.

[128] H. Q. Ngo, A. Ashikhmin, H. Yang, E. G. Larsson, and T. L. Marzetta, "Cell-free massive MIMO versus small cells," *IEEE Transactions on Wireless Communications*, vol. 16, no. 3, pp. 1834–1850, March 2017.

[129] T. L. Marzetta, E. G. Larsson, H. Yang, and H. Q. Ngo, *Fundamentals of Massive MIMO*. Cambridge CB2 8BS, United Kingdom: Cambridge University Press, 2016.

[130] S. M. Kay, *Fundamentals of statistical signal processing*. Upper Saddle River, New Jersey 07458: Prentice-Hall PTR, 1993, vol. I.

[131] E. Bjornson, J. Hoydis, and L. Sanguinetti, *Massive MIMO Networks: Spectral, Energy, and Hardware Efficiency*. http://www.nowpublishers.com: now Publishers Inc., 2017, vol. 11.

[132] D. H. Nguyen and T. Le-Ngoc, "MMSE precoding for multiuser MISO downlink transmission with non-homogeneous user SNR conditions," *EURASIP Journal on Advances in Signal Processing*, vol. 1, no. 85, pp. 1–12, 2014.

[133] F. Kaltenberger, M. Kountouris, L. Cardoso, R. Knopp, and D. Gesbert, "Capacity of linear multi-user MIMO precoding scheme with measured channel data," in *2008 IEEE 9th workshop on signal processing advanced in wireless communication*, Recife, Brazil, July 2008, pp. 1–5.

[134] J. H. Winters, "Optimum combining in digital mobile radio with cochannel interference," *IEEE Transactions on Vehicle Technology*, vol. 33, no. 3, pp. 144–155, Aug. 1984.

[135] S. Zhao, J. Liu,Ä†, Y. Shen, X. Jiang,Ä°, and N. Shiratori, "Secure and energy-efficient beamforming for MIMO two-way untrusted relay systems," in *IEEE Wireless Communications and Networking Conference (WCNC)*, Qater, April 2019.

[136] R. Zhang, C. C. Chai, and Y. Liang, "Joint beamforming and power control for multiantenna relay broadcast channel with QoS constraints," *IEEE Transactions on Signal Processing*, vol. 57, no. 2, pp. 726–737, Feb 2009.

[137] E. Bjornson and L. Sanguinetti, "Scalable cell-free massive MIMO systems," *IEEE Transactions on Communications*, vol. 68, no. 7, pp. 4247 – 4261, July 2020.

[138] S. Chen, J. Zhang, J. Zhang, E. Bjornson, and B. Ai, "A survey on user-centric cellfree massive MIMO systems," *Digital Communications and Networks*, 2022.

[139] G. Interdonato, M. Karlsson, E. Bjornson, and E. Larsson, "Downlink spectral efficiency of cell-free massive MIMO with full-pilot zero-forcing," in *IEEE Global Conference on Signal and Information Processing (GlobalSIP)*, Anaheim, CA, USA, Nov. 2018.

[140] S. Shishkin, A. Shalaginov, and S. Bopardikar, "Fast approximate truncated SVD," *Numerical Linear Algebra with Applications*, vol. 26, no. 04, pp. 1–18, August 2019.

[141] Z. Q. Luo, W. K. Ma, A. M. C. So, Y. Y. Ye, and S. Z. Zhang, "Semidefinite relaxation of quadratic optimization problems," *IEEE Signal Process. Mag.*, vol. 27, no. 03, pp. 20–34, May 2010.

[142] Y. Yang, C. Sun, H. Zhao, H. Long, and W. Wang, "Algorithms for secrecy guarantee with null space beamforming in two-way relay networks," *Signal Processing, IEEE Transactions*, vol. 62, no. 08, pp. 2111–2126, 2014.

[143] Y. YE, *Interior Point Algorithms. Theory and Analysis*. JOHN WILEY & SONS, INC., 1997.

[144] M. Grant and S. Boyd, *CVX: MATLAB Software for Disciplined Convex Programming, Version 2.1*, Available Online: http://cvxr.com/cvx, March 2014.